



THÈSE

PRÉSENTÉE A

L'UNIVERSITÉ BORDEAUX 1

ÉCOLE DOCTORALE DES SCIENCES à renseigner

Par **Ren-Wei, CHANG**

POUR OBTENIR LE GRADE DE

DOCTEUR

SPÉCIALITÉ : CHIMIE

Processus photoioniques au sein des architectures amphiphiles

Directeur de recherche :

Mme Reiko Oda, *Directeur de recherche, CBMN CNRS*

et

M. Nathan D. McClenaghan, *Chargé de Recherche, ISM CNRS*

Soutenue le : 25 Octobre 2011

Devant la commission d'examen formée de :

M. Bernard DESBAT, *Directeur de recherche, CBMN CNRS*

M. Amilra Prasanna DE SILVA, *Professeur, Queen's University of Belfast*

M. Julian EASTOE, *Professeur, University of Bristol*

M. Donal O'SHEA, *Professeur, University College Dublin*

Mme Reiko Oda, *Directeur de recherche, CBMN CNRS*

M. Nathan D. McClenaghan, *Chargé de Recherche, ISM CNRS*

Président

Rapporteur

Rapporteur

Examineur

Directeur de thèse

Directeur de thèse

Acknowledgement

I would like to show my sincere gratitude to my advisors: Dr. Reiko Oda (IECB) and Dr. Nathan D. McClenaghan (ISM) in University of Bordeaux. It is with their scientific instructions and consideration this thesis can be completed. During these three years in France, I have encountered numerous problems not only in science but also in daily life. Those problems depressed me and even once almost let me give up. I am honored and fortunate to have their encouragements and positive attitudes which inspired confidence in me and matured me to face those challenges.

Also, I would like to show my deepest appreciation to Dr. Bernard Desbat in IECB. His patient guidance in IR and surface analysis instruments allows me to learn more interdisciplinary knowledge and further polishes this study.

This PhD thesis was financed by the Region d'Aquitaine. Equally I acknowledge support from ERC (FP7/2007-2013) "Ideas" program, grant agreement N° 208702. All the work presented in this thesis corresponds to and directly contributed to the objectives of the latter project ("COMMOTION").

This interdisciplinary thesis involves biochemistry and photochemistry/physics thereby I am fortunate to work with different groups. In the biochemistry part under IECB, I would like to thank Dr. Brice Kauffmann who instructed me about SAXS and my coworkers Dr. Zahia Fezoua, Rumi Tamoto, Ha Phuong Ta, and Dima Dedovets.

In the photochemistry part under NEO group of ISM, I would like to thank: Guillaume Raffy who patiently instructed me about confocal laser microscopy; Guillaume Vives, Aurélie Lavie-Cambot and Aurélien Ducrot who provided me some preliminary compounds and shared the synthesis experience with me. Of course many thanks to all the professors and team members for creating great atmosphere in the group, sharing experience, and helping in daily life.

In the photophysics part, I want to thank Dr. Gediminas Jonusauskas and Pinar Batat for the measurements of time-resolved experiments.

Finally, I would like to thank my family and friends' support and care. Also, I am fortunate with my girlfriend Jennifer's accompanying during these years. Without their unconditioned love and supporting, I cannot go through these tough years.

Résumé

Pour effectuer des opérations de régulation et de signalisation, les systèmes naturels mettent à profit des processus ioniques et photoniques. Certains aspects de ces processus peuvent être reproduits dans des systèmes artificiels, en combinant senseurs et récepteurs moléculaires photoactifs dans des nanocapsules ou des membranes auto-assemblées. Une série de molécules photoactives amphiphiles et non-amphiphiles a été synthétisée, notamment pour la complexation et la libération d'ions calcium. Ces derniers processus ont été étudiés à l'aide de différentes spectroscopies incluant la fluorimétrie et l'infrarouge. Le couplage du processus photomodulé d'éjection d'ion et sa détection, dans des domaines nanoscopiques et à l'interface membrane / liquide, a été étudié pour connaître l'efficacité du transfert d'ion en solution et milieu organisé, notamment au sein de vésicules de tailles différents.

Abstract

Natural systems combine ionic and photonic processes in order to control, for example, signalling and regulation. Certain aspects of these processes can be achieved in artificial systems, on combining photoactive molecular sensors / switches, molecular receptors and self-assembled nanocapsules or membranes. A range of novel amphiphilic and non-amphiphilic synthetic photoactive molecules and molecular systems are reported, notably for the complexation and liberation of calcium ions. These processes are studied using a range of spectroscopies including fluorimetry, microscopy and IR-techniques. Coupling processes of photocontrolled ion ejection and detection in nanoscopic compartments and at liquid / membrane interfaces has been studied in order to assess the relative efficiency of intermolecular ion transfer in solution and organized media, notably in vesicle nanodomains.

Outline

Chapter 1	
General Introduction	
1.1 General introduction and outline.....	2
1.2 Supramolecular chemistry.....	4
1.3 Operating principle of photoactive ion-sensitive molecular probes.....	5
1.3.1 Ionophore.....	7
1.3.2 Molecular probes based on photoinduced electron transfer (PET).....	8
1.3.3 Fluorescence emission characteristics.....	10
1.4 Biomimetic nanodomains and organized media.....	12
1.4.1 Surfactants.....	13
1.4.2 The phospholipids.....	13
1.5 References.....	16
Chapter 2	
Photoactive Calcium Acceptors and Ejectors: Synthesis and Properties	
2.1 Introduction.....	20
2.1.1 Ca^{2+} -acceptors incorporating PET (photoinduced electron transfer).....	20
2.1.2 Ca^{2+} -donors (caged molecules).....	23
2.2 Synthesis of Ca^{2+} -acceptor and Ca^{2+} -ejector molecules.....	29
2.2.1 Synthesis of Ca^{2+} -acceptor molecules.....	29
2.2.1.1 Product BANI.....	30
2.2.1.2 Product BANI2.....	34
2.2.1.3 Product BANI3.....	37
2.2.1.4 Product BAPTAant.....	37
2.2.1.5 Product C15BAPTAant.....	39
2.2.2 Synthesis of Ca^{2+} -ejector molecules.....	40
2.3 Photophysical property of Ca^{2+} -acceptor and Ca^{2+} -ejector molecules.....	41
2.3.1 Photophysical properties of Ca^{2+} -acceptor molecules.....	41
2.3.1.1 Spectral measurement of trial compounds BAPTAant & C15BAPTAant.....	41
2.3.1.2 Spectral measurement of product BANI.....	43
2.3.1.3 Spectral measurement of product BANI2.....	46
2.3.1.4 Spectral measurement of product BANI3.....	54
2.3.1.5 Solvent effects on BANI2 & BANI3.....	55
2.3.1.6 Time-resolved fluorescence and transient absorption experiments.....	60
2.3.2 Photophysical measurement of Ca^{2+} -donor molecules.....	62
2.3.2.1 Spectral measurements of nitr-5.....	63

2.3.2.2 Spectral measurements of C15nitr-5.....	65
2.4 Conclusion.....	67
2.5 References.....	68

Chapter 3

Orientation and Morphology Study of BAPTA Compounds in Films	71
3.1 IR spectrum analysis.....	73
3.1.1 General band position.....	73
3.1.2 Carboxylic acid and carboxylate group.....	74
3.2 ATR-FTIR experiments for BAPTAhyd compound.....	76
3.2.1 Introduction to ATR-FTIR.....	76
3.2.2 ATR-FTIR experiment results for BAPTAhyd.....	78
3.3 Langmuir films & PM-IRRAS for C15BAPTAhyd compound.....	81
3.3.1 Introduction to PM-IRRAS.....	82
3.3.2 Introduction to Langmuir film.....	84
3.3.3 PM-IRRAS experiments of C15BAPTAhyd Langmuir film.....	85
3.4 Ellipsometry measurements for C15BAPTAhyd compound.....	89
3.4.1 Introduction to ellipsometry.....	90
3.4.2 Ellipsometry experiments of C15BAPTAhyd.....	91
3.5 Conclusion.....	102
3.6 References.....	103

Chapter 4

Implementation of Photocontrolled Ion-Shuttle in Nanodomains	105
4.1 Pretest of trial model compounds in multi-lamellar vesicles (MLVs).....	106
4.1.1 Introduction to small angle X-ray scattering (SAXs) for lamellar structure.....	106
4.1.2 Experimental section.....	107
4.2 Incorporation of synthesized Ca ²⁺ -acceptors into GUVs.....	113
4.2.1 Introduction to GUV.....	113
4.2.2 Experimental results of blending GUVs with fluoroionophores.....	115
4.3 Confocal microscopy and fluorescence-lifetime imaging microscopy.....	121
4.3.1 Introduction to fluorescence-lifetime imaging microscopy (FLIM).....	121
4.3.2 Experimental part.....	123
4.4 Fluoroionophores within small unilamellar vesicles (SUVs)	128
4.4.1 Pretest of EGTA additive in the SUVs solution.....	129
4.4.2 Dissociation constant (K_d) study of probes within different liposome environment.....	131
4.5 Photoinduced ion-shuttle in the free solution and SUVs nanodomains.....	140
4.5.1 Photoinduced ion-shuttle in the free solution.....	141
4.5.2 Photoactivated ion-shuttle confined in the vesicle matrix.....	150
4.6 Conclusion.....	168

4.7 References.....	169
---------------------	-----

<i>Summary and Conclusion</i>	171
--------------------------------------	------------

<i>Future development</i>	173
----------------------------------	------------

<i>Chapter 5</i>	
<i>Experimental Section</i>	175

5.1 Materials.....	176
5.2 Thin-layer chromatography and column.....	176
5.3 Nuclear magnetic resonance (NMR).....	176
5.4 Mass Spectrometry.....	176
5.5 UV-visible absorption Spectroscopy.....	176
5.6 Fluorescence spectroscopy.....	177
5.7 Irradiation systems.....	177
5.8 Calculation of fluorescence quantum yield.....	177
5.9 Determination of dissociation constants (K_d) with fluorimeter.....	177
5.10 Determination of dissociation constants (K_d) with UV/Visible absorption spectrometer.....	178
5.11 ATR-FTIR.....	179
5.12 Langmuir isotherms.....	179
5.13 PM-IRRAS.....	179
5.14 Ellipsometry measurement.....	180
5.15 Small angle X-ray scattering (SAXs)	180
5.16 Electroformation of giant unilamellar vesicles (GUVs).....	180
5.17 Preparation of small unilamellar vesicles (SUVs).....	181
5.18 Optical / fluorescence Microscopy.....	181
5.19 Confocal fluorescence microscope.....	181
5.20 Synthesis procedure.....	181
5.21 References.....	200

<i>Synthesized compound list</i>	201
---	------------

Chapter 1
General Introduction

1.1 General introduction and outline

Many vital processes are governed by ions and ion exchange. Cells use a wide variety of chemical messengers for signaling (Figure 1.1), and ionized calcium (Ca^{2+}) is the single most important information carrier.¹ The importance of Ca^{2+} inside cells was firmly established over 100 years ago by a series of key experiments by Ringer.² In the period 1940-70, various physiologists confirmed these ideas. In particular, direct injection of Ca^{2+} into muscle fibers and nerves cells definitively established that an increase in the intracellular Ca^{2+} concentration ($[\text{Ca}^{2+}]_i$) was the essential event for muscle contraction and nerve impulses.³

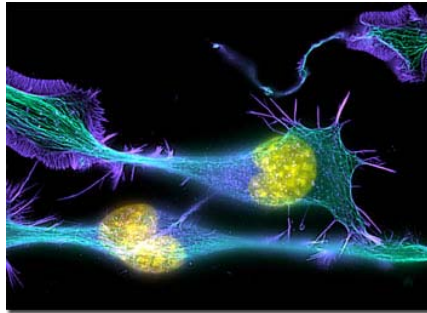


Figure 1.1 Ion-transfer is key in nerve cells and vision

We know that changes in $[\text{Ca}^{2+}]_i$ control a myriad of cells or cellular functions, including secretion of neurotransmitters and hormones, muscle contraction, synaptic plasticity, movement of cells (nonmuscle motility), gene transcription and cell death, wound healing, the activity of kinases and phosphatases and gating of ion channels.⁴ Often Ca^{2+} itself does not directly control a target protein, but a Ca^{2+} -activated calmodulin complex does. The majority of calcium is stored in the intracellular vesicles, the endoplasmic reticulum or mitochondria, and is released when necessary.⁵ Indeed, the resting intracellular calcium concentration is very low (100 nM) and its variation is harnessed in cell signaling.

	Intracellular concentration (mM)	Extracellular concentration (mM)
Na^+	5-15	145
K^+	140	5
Mg^{2+}	0.5	1-2
Ca^{2+}	10^{-4}	1-2
H^+	7×10^{-5}	4×10^{-5}

Table 1.1 Concentrations of different cations at the cellular level

The difficulty in establishing communication between distinct functional molecules is one major obstacle to the development of integrated molecular networks, which are much smaller than currently used solid-state equivalents. Previous attempts to effect communication have

been subjected to strong constraints: strategies based on magnetic coupling only function at low temperatures or are intramolecular⁶; systems based on the transfer of energy are limited by the energy-wasting downhill nature of the process⁷; long distance electron transfer processes are strongly distance dependent⁸ and sequential electron transfer processes are difficult to organize. Larger nanocomponents based on conventional microelectronic architectures such as nanotube bundles are comparable in size to those obtained by a “top-down” approach.⁹

The aim of this thesis is to combine photoactive ion-shuttle (Figure 1.2) and biomimetic host systems (nanocapsules, vesicles, etc.) to study photoinduced processes (ion ejection and detection) in nanoscopic compartments and at liquid / membrane interfaces to simulate cell-membrane environment as in nerve cells, thereby effecting communication between distinct functional molecules. The role of compartmentalization where the ionic processes are in membrane media, liquid-membrane interfaces or inside vesicles to modify efficiency and to direct ion-movement will be examined.

A schematic representation of a photoactive functional molecule-based ion-shuttle is shown in Figure 1.2: In this bistable system an ion, represented as a red sphere, alternates between two binding sites (shown in blue), under control of a light stimulus. Both serial and parallel operations of ion-shuttles can be envisaged. Light serves as a viable means of control and signaling of the different processes due to high temporal and spatial resolution afforded as well as ease of detection.

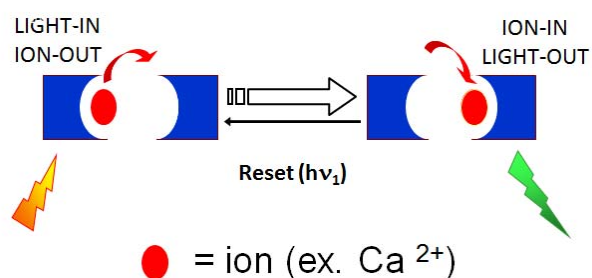


Figure 1.2 Representation of operation a bistable light driven ion-shuttle and associated processes

Further, in order to assure the message transfer between sites and enhance the efficiency of communication, organized media host for functional molecules will allow the execution and study of sequential processes, including inter-component ion-transfer in nanodomains on the order of a few nanometers.

The outline of the thesis with the five main chapters is:

Chapter 1 is a general introduction to supramolecular system, photochemistry mechanisms, and biomimetic self-assembled organized nanodomains.

Chapter 2 focuses on several different synthesized functional molecules involved in light-driven ion-shuttle development, notably fluorescent ion detections and photocontrolled ion ejectors both amphiphilic and non-amphiphilic variants are considered.

Chapter 3 is a basic study of lipid monolayer, membrane, and vesicle properties integrating ionophores by different techniques.

Chapter 4 considers the combination of the molecules presented in chapter 2 and materials of chapter 3 to build up biomimetic light-driven ion shuttles in vesicle matrices to study the compartmentalization effect of ion transfer.

Chapter 5 reports experiment details concerning synthetics, characterization and studies.

1.2 Supramolecular chemistry

One of the pioneers of supramolecular chemistry, Jean-Marie Lehn (Nobel Prize Chemistry 1987) surmised supramolecular chemistry being: " Beyond molecular chemistry based on the covalent bond, and an extended area which may be called supramolecular: the chemistry of molecular interactions, combinations of two or more chemical species, complexes, and intermolecular bonding."¹⁰

Supramolecular chemistry is an interdisciplinary science including chemical, physical and biological species with chemical molecular complexes that are related and organized through intermolecular interactions.¹¹ Early definitions of "supramolecular" chemistry focused mainly on the non-covalent interactions between "host" and "guest" molecules. Over the past decades, the rapid expansion of supramolecular chemistry has given rise to a large diversity of non-covalent chemical systems.¹² In addition to host-guest complexes, today supramolecular chemistry encompasses numerous designs of 2-D and 3-D architectures capable of various functionalities, including sensors,¹³⁻¹⁵ catalysts,¹⁶ switches,¹⁷ and signal amplification devices.¹⁸

Non-covalent interactions, which are the basis of supramolecular chemistry, are low energy interactions (between 1 and 70 kcal mol⁻¹, Table 1.2) compared to covalent bonds (between 35 and 110 kcal mol⁻¹).^{19,20}

The systems studied in this thesis are principally supramolecular systems which selectively recognize calcium ions and act as of Ca²⁺-ejectors and Ca²⁺-probes. Properties of these photochemically-active and biomimetic systems are considered. The molecular receptors and

ejectors involving supramolecular interactions to selectively complex / decomplex ions is presented and discussed in Chapter 2.

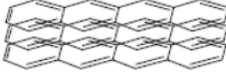
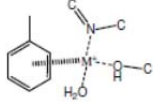
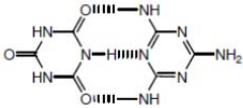
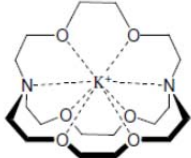
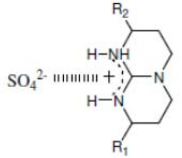
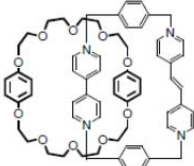
Type	Interaction strength Intensity (kcal·mol ⁻¹)	Example
Van der Waals interaction	< 2	
π-π interaction	0 – 12	
π-cation	1 – 20	
hydrogen bonding	1 – 30	
dipole-dipole interaction	1 – 12	
ion-dipole interaction	12 – 50	
ion-ion	50 - 70	
mechanical bonds	---	

Table 1.2 Summary of principal non-covalent interactions.

1.3 Operating principle of photoactive ion-sensitive molecular probes

While ion-recognition process can employ different transduction mechanisms, based on ion-selective electrodes²¹ for example, photoactive and notably fluorescent molecular sensors are particularly convenient. Indeed, these autonomous molecular species can be addressed

using light in a wide range of environments. Only photoactive species are considered for the rest of this thesis.

Photochemistry is the study of chemical reactions proceeding with the absorption of light by atoms or molecules. It includes the study of the nature of excited states after absorbing a photon and their evolution during a chemical transformation or photoinduced process²². The envisaged ion-shuttle systems photoswitch an ion between different molecular binding sites and harness key concepts in photochemistry, coordination and supramolecular chemistry.

For the Ca^{2+} -binding on recognition site in the ion-shuttle system, it is necessary to detect cations in different environments. Several approaches based on molecular probes have been developed using selective electrodes toward ions²³. To ensure high selectivity, it is necessary to use a molecular receptor which must meet several criteria recognition of the cation and reporting the event appropriately. Fluorescent sensors have the advantage of being sensitive, selective, having a fast response time and allowing a local observation of ion concentration. The ion-sensitive fluorescent probes typically consist of two parts, an ionophore, an entity sterically and chemically-adapted to selectively capture ions, and a fluorophore which generates the signal at the molecular level. (Figure 1.3 & 1.4)

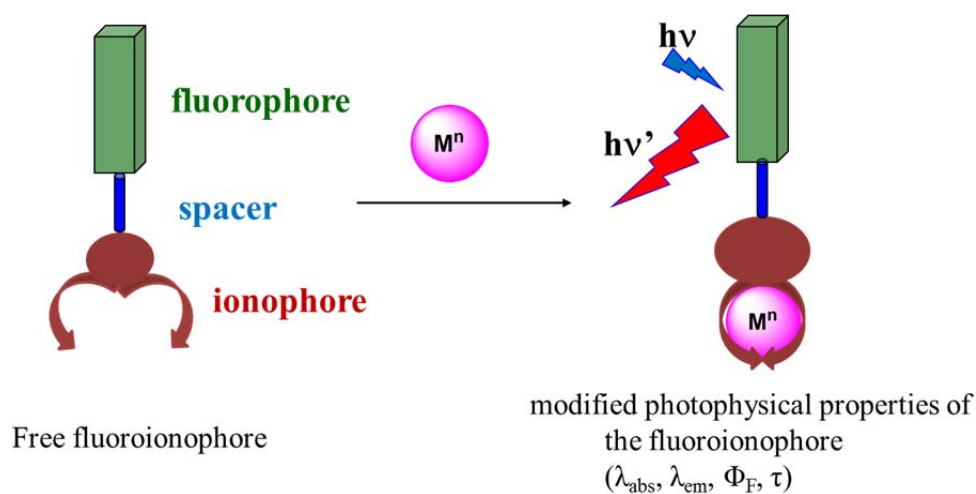


Figure 1.3 Principle of cation recognition and detection by fluoroionophore

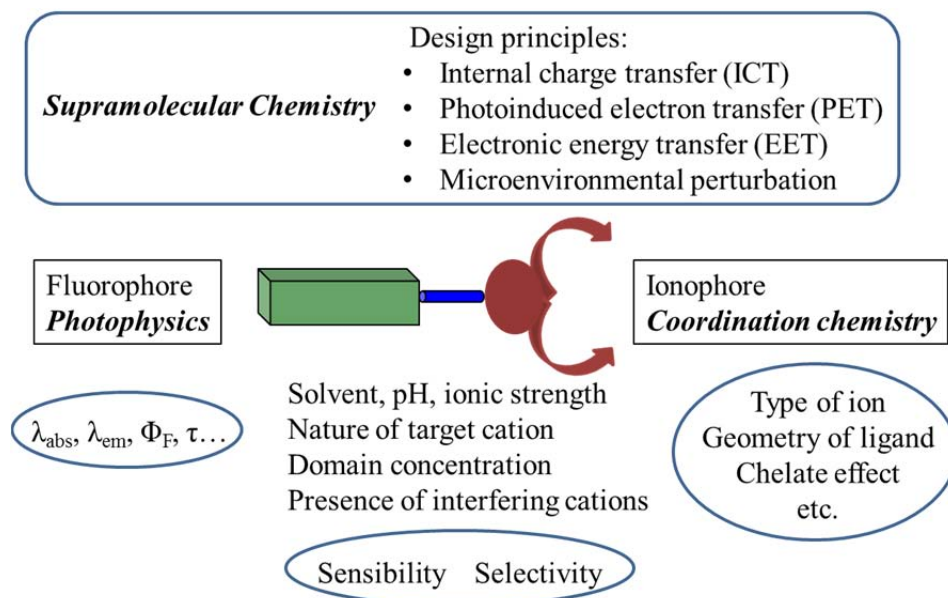


Figure 1.4 Summary of various considerations for the fluoroionophore

Complexation of the ion by the ionophore causes a change in the fluorophore behavior (emission lifetime, color and / or emission quantum yield) and will then allow the detection of the ion by optical means. This change is typically caused either by a photoinduced electron transfer (PET), or by photoinduced charge transfer (PCT) also called internal charge transfer (ICT).

1.3.1 Ionophore

As the name implies, the ionophore is a molecule capable of complexing ion. Typically, it is an organic chelating structure able to selectively bind ion substrates through weak ionic interactions and results in a supramolecular assembly¹¹. Ultimately it is the origin of ionophore which the selectivity and efficiency of the complex and depend on the topology of the ligand and the characteristics of the cation (ionic radius, charge density, coordination number, soft / hard nature) and the nature of the solvent (polarity, pH and ionic strength for ionic solutions).

The sensitivity of the ionophore, expressed by the dissociation constant (K_d) of the complex, must be adapted to the concentration range of the required cation. If the probe is too sensitive, it will be quickly saturated in the presence of a high concentration of cation, while a much less sensitive probe will not be able to detect low concentrations of cation.

K_d is defined as the dissociation constant of a complex $[LC]^+$, i.e. a 1:1 host-guest stoichiometry characterized by the equilibrium:



$$K_A = \frac{1}{K_d} = \frac{[LC]^+}{[C^+][L]} \quad \text{Equation 1.1}$$

Where L, the ligand; C⁺, the cation; K_A, the association constant, which is the reciprocal of dissociation constant

The evolution of a balance can be viewed from a thermodynamic aspect. The variation of free energy ΔG is the energy released by chemical reaction and operates in the following equation:

$$\text{Gibbs Equation : } \Delta G = \Delta H - T \Delta S \quad \text{Equation 1.2}$$

Where ΔG , the variation of Gibbs free energy; ΔH , the change of enthalpy, the global energy; ΔS , the change in entropy

The free energy can also be defined by the following equation:

$$\Delta G = \Delta G^\circ + RT \ln K_A \quad \text{Equation 1.3}$$

Where ΔG° , standard Gibbs energy

It is possible to predict the effectiveness of the exchange. Its evolution is evaluated by the standard Gibbs energy ΔG° . Spontaneous reactions have a negative ΔG° .

When the system reaches equilibrium, $\Delta G = 0$, and therefore $\Delta G^\circ = -RT \ln K_A$. This relationship is used to evaluate the energies of complexation from the spectral variations by varying the species concentrations in solution.

1.3.2 Molecular probes based on photoinduced electron transfer (PET)

Photoinduced electron transfer (PET) is the subject of intense research due largely a key role in photosynthesis.²⁴ This thermodynamic process can be incorporated into supramolecular molecules as probes, with a high degree of predictability. The electron transfer depends on the kinetic parameters and energy. Marcus theory²⁵ describes the rate of electron transfer from the outer layer, the speed at which an electron can be transferred between a donor D and an acceptor A. In this model, the potential energy of reactants R (complex A---D) and product (complex A⁻---D⁺) are represented by parabolas (Figure 1.5).

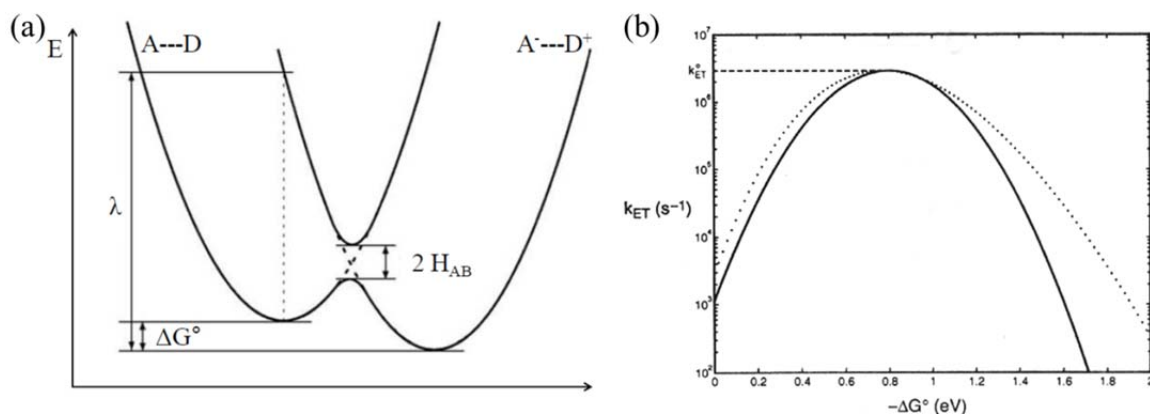


Figure 1.5 (a) Potential curves between the reactants and products. ΔG° , free energy of the system; H_{AB} , the electronic coupling between the initial and the final state; λ , the energy of reorganization (b) relationship between rate of electron transfer as a function of thermodynamic driving force, predicted by Marcus theory^{26,27}

Marcus theory relates the rate of electron transfer (k_{et}) to the free energy ΔG° of the system by the following equation:

$$k_{et} = \frac{2\pi}{h} \cdot |H_{AB}|^2 \cdot \frac{1}{\sqrt{4\pi\lambda k_b T}} \cdot \exp\left(-\frac{(\lambda + \Delta G^\circ)^2}{4\lambda k_b T}\right) \quad \text{Equation 1.4}$$

Where k_b , the Boltzmann constant ($1.380\ 66 \times 10^{-23}$ J/K)

When ΔG° is negative or slightly positive, the electron transfer from donor to acceptor can be very rapid.²⁸

Electron transfer can occur even in simple supramolecular receptor systems²⁹ when an ion-induced switching of fluorescence can be instilled (Figure 1.6). In this type of probe, the fluorophore and the ionophore are separated by an inert spacer which ensures the integrity of the intrinsic properties of each unit. In this case, the methylene group electronically isolates the redox active component in the ground state, yet allows an electron transfer between the ionophore (donor) and to the fluorophore in the excited state (acceptor). When the fluorophore is excited, the ionophore which includes a readily oxidizable group (tertiary amine) will transfer an electron to the fluorophore thereby preventing its fluorescence (Figure 1.6 left). As the probe complexes a cation, the blocking of the electron transfer will cause an enhancement of fluorescence of the probe (Figure 1.6 right).

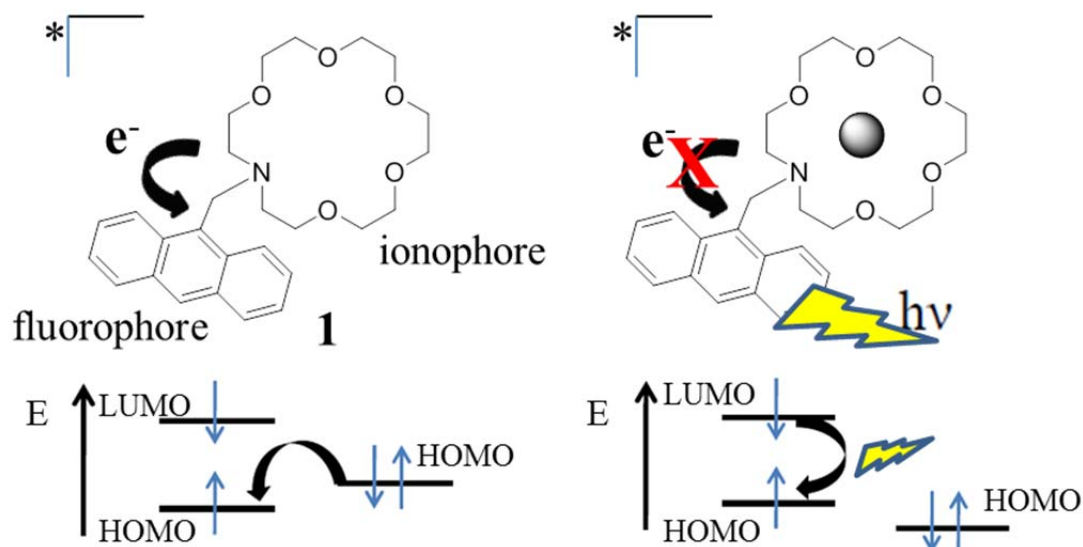


Figure 1.6 Example of a PET probe in the absence (left, fluorescence switched-off) and presence (right, switched-on) of a potassium ion with relevant frontier molecular orbital

The efficiency of electron transfer process can be estimated by the Rehm-Weller equation as shown below, respectively, taking into account the facility of oxidation receptor and the reduction of the fluorophore with the energy provided by light, while taking into account the radical pair following charge separation..

$$\Delta G^\circ = - E_{S, \text{fluor.}} - E_{\text{red.fluor.}} + E_{\text{ox. receptor}} - E_{\text{ion pair}} \quad \text{Equation 1.5}$$

$E_{S, \text{fluor.}}$: Energy of the excited state of the emissive fluorophore.

$E_{\text{red.fluor.}}$: Reduction potential of the fluorophore.

$E_{\text{OX. receptor}}$: oxidation potential of the receiver.

$E_{\text{ion pair}}$: coulombic interaction energy of the formed ion pair.

We will see more examples utilizing the PET mechanism as fluorescence probes in Chapter 2.

1.3.3 Fluorescence emission characteristics

Excited molecules are very reactive and tend to return to their ground state, the lifetime of the excited state is very short. A molecule in the excited singlet state (S_1) can relax rapidly radiative by fluorescence with a radiative constant k_F , or non-radiative by principally as internal conversion with a constant k_{IC} or intersystem crossing with a constant k_{ISC} . A constant k_{NR} is then defined based on the two non- radiative constant k_{ISC} and k_{IC} . A Jablonski-Perrin diagram allows the visualization of all possible processes after absorption of a photon (Figure 1.7).^{30,31}

It is worth mentioning that photoinduced electron transfer (PET) represents another process occurring in excited state while an electron can be transferred to another unit. Also when energetically and kinetically favorable, a transfer of energy to another molecule can also

occur.

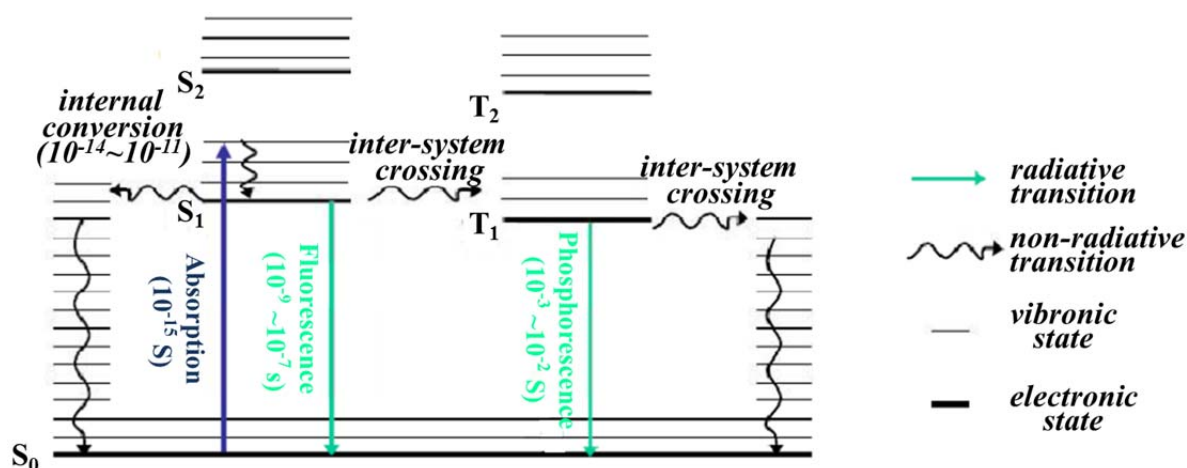


Figure 1.7 Jablonski-Perrin diagram for a typical molecular fluorophore

In the simplest case, a solution containing a fluorescent species M is excited by a short light pulse at $t = 0$, a certain proportion of these molecules is promoted to the excited state S_1 . The kinetics of processes following excitation follows the law:



$$\frac{-d[{}^1M^*]}{dt} = (k_F + k_{NR}) \cdot [{}^1M^*] \quad \text{Equation 1.6}$$

Where $[{}^1M^*]$ represents the population of M molecules in the excited state S_1 ; k_F , the rate constant of fluorescence decay and k_{NR} , the rate constant of overall non-radiative decay (sum of rate constants of internal conversion k_{IC} and inter-system crossing k_{ISC}).

The fluorescence intensity I_F measured at time t is proportional to the number of molecules in the excited state. The resolution of this differential equation implies exponential decay of the fluorescence intensity which is characterized by the lifetime τ of the excited state corresponding to the average time occupancy of the excited state S_1 . I_F can be defined as:

$$I_F(t) = k_F \cdot [M^*] = k_F \cdot [M^*]_0 \cdot e^{-\frac{t}{\tau}}$$

$$\tau = \frac{1}{k_F + k_{NR}} \quad \text{Equation 1.7}$$

Measuring the lifetime of a solution containing the chromophore is generally independent of the wavelength of excitation and emission.

The fluorescence quantum yield Φ_F is defined as the ratio of emitted fluorescence photons by the total number of absorbed photons.

$$\Phi_F = \frac{k_F}{k_F + k_{NR}} = k_F \cdot \tau \quad \text{Equation 1.8}$$

Knowing the values of Φ_F and lifetime τ , the values of different rate constants k_F and k_{NR} can be deduced. And they are important measurements in the fluorescence probes experiments.

1.4 Biomimetic nanodomains and organized media

The study of combined photoionic process in homogeneous solution as well as organized media can give important information on the photocontrol and efficiency of information transfer via ion messengers. The goal of this thesis is to incorporate and study functional molecular components in the organized and self-assembled host media. For example, molecular assemblies such as micelles and vesicles, which are formed by specific amphiphiles or surfactants in aqueous media. (Figure 1.8)

These systems, simulating cell-membrane environments, will serve as hosts for adapted functional molecules and evaluation of the potential role in directing the passage of a messenger ion, adding compartmental (as well as electrostatic) effects to favor binding listed. Such optimization of local concentration jumps, assuring ion / information transfer between sites, is reminiscent of the functioning of neuronal cells. Hosts for functional molecules will allow the execution and study of sequential processes, including inter-component ion transfer in nanodomains on the order of a few nm.

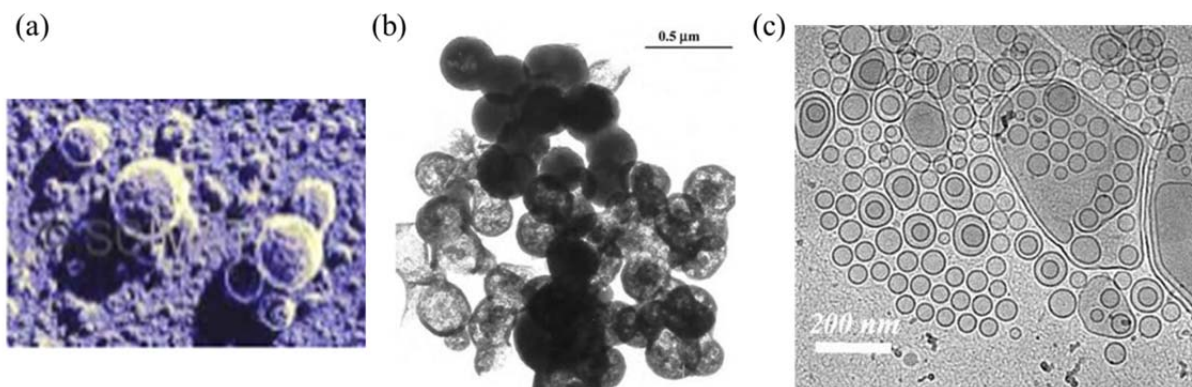


Figure 1.8 (a, b) vesicles and its transmission electron micrograph³² (b) vesicles (optical microscopy)

1.4.1 Surfactants

Surfactants are compounds that lower the surface tension of a liquid, the interfacial tension between two liquids, or that between a liquid and a solid. Surfactants may act as detergents, wetting agents, emulsifiers, foaming agents, and dispersants.

Lipids are a large and diverse group of naturally occurring organic compounds that are related by their solubility in nonpolar organic solvents and general insolubility in water.³³ The lipids have great structural variety, for example: fatty acid, phospholipid, terpene, steroids, etc.

In colloidal and surface chemistry, the critical micelle concentration (CMC) is defined as the concentration of surfactants above which micelles form and almost all additional surfactants added to the system become micelles (Figure 1.9).³⁴ The CMC is an important characteristic of a surfactant. Before reaching the CMC, the surface tension changes strongly with the concentration of the surfactant. After reaching the CMC, the surface tension remains relatively constant or changes with a lower slope. The value of the CMC for a given dispersant in a given medium depends on temperature, pressure, and (sometimes strongly) on the presence and concentration of other surface active substances and electrolytes. Micelles only form above critical micelle temperature.

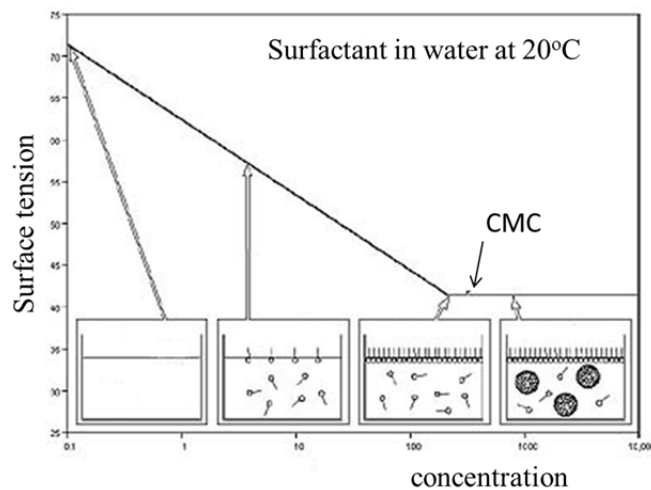


Figure 1.9 measuring surface tension as a function of surfactant concentration for determination of critical micelle concentration (CMC)

1.4.2 The phospholipids

In this thesis, phospholipids, which are omnipresent in nature as the main constituents of cell membranes are used principally. It has a structure as shown below:

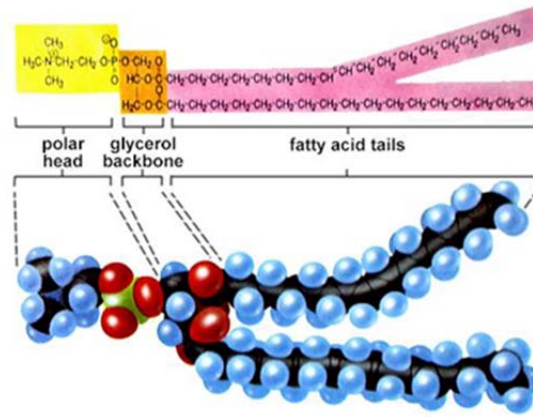


Figure 1.10 General structure of a phospholipid

As ionic amphiphiles, phospholipids aggregate or self-assemble when mixed with water, but in a different manner than soaps and detergents. Because of the two pendant alkyl chains present in phospholipids and the unusual mixed positive and negative charges in their head groups, micelle formation is unfavorable relative to a bilayer structure as shown in the Figure 1.11.

This bilayer membrane structure is also found in aggregate structures called *liposome*. Liposomes are microscopic vesicles consisting of an aqueous core enclosed in one or more phospholipid layers. They are formed when phospholipids are vigorously mixed with water. Unlike micelles, liposomes have both aqueous interiors and exteriors (Figure 1.11). Bilayers interact nonspecifically via long-range electrostatic, electrodynamic, and solvation forces. These colloidal forces are commonly recognized as van der Waals attraction, electric double-layer repulsion, and hydration repulsion. Other steric and structural interactions exist that are not yet clearly understood.³⁵

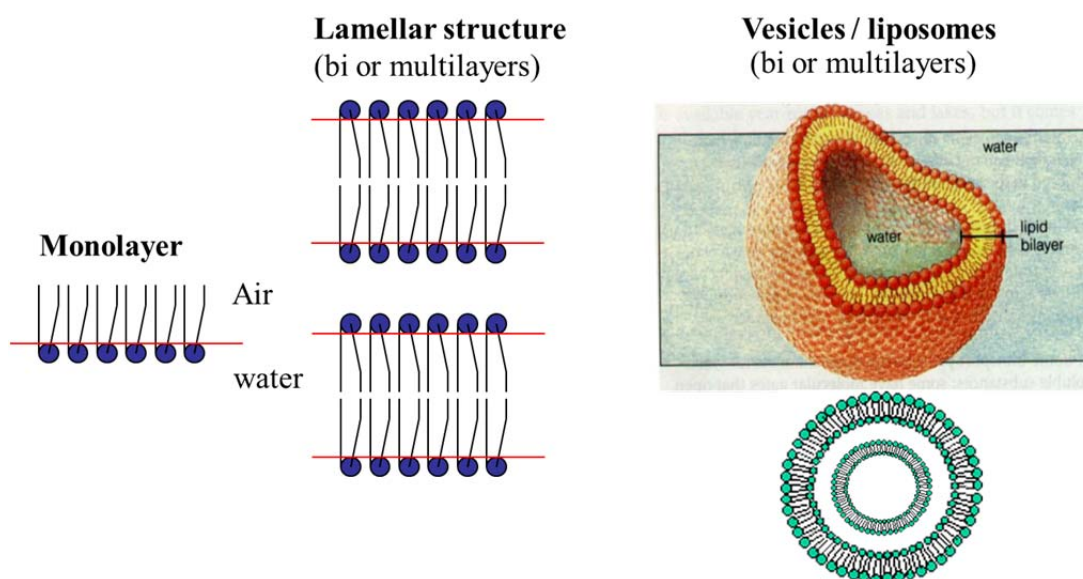


Figure 1.11 Phospholipid aggregates in the water

To distinguish vesicles by size, they can be small unilamellar vesicle (SUV, ~20 nm in radius, visible with an electron microscope), large unilamellar vesicle (LUV ~ μm , visible with optical microscope), giant unilamellar vesicle (GUV ~10-100 μm) and Multi-lamellar vesicles (MLV).

One of the most important properties of a lipid bilayer is the relative mobility (fluidity) of the individual lipid molecules and how this mobility changes with temperature. (Figure 1.12) This response is known as the phase behavior of the bilayer. Broadly, at a given temperature a lipid bilayer can exist in either a liquid or a solid phase. The solid phase is commonly referred to as a “gel” phase. All lipids have a characteristic temperature at which they undergo a transition (T_f) from the gel to liquid phase. In both phases the lipid molecules are constrained to the two dimensional plane of the membrane, but in liquid phase bilayers the molecules diffuse freely within this plane. Thus, in a liquid bilayer a given lipid will rapidly exchange locations with its neighbor millions of times a second and will through the process of a random walk and can migrate over relatively long distances^{36,37}

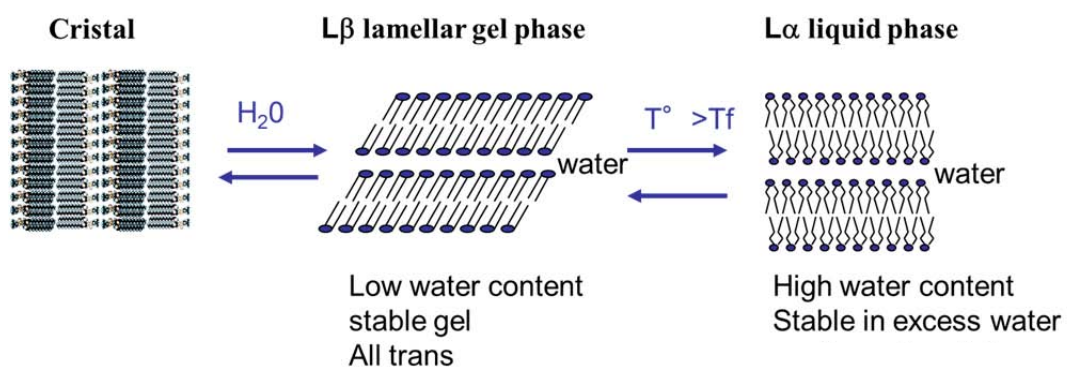


Figure 1.12 Phase transition of lipids

For the lipids and phospholipids, a range of instruments and measurement techniques are utilized and discussed in Chapter 3. These 3-D artificial capsules are employed as compartmental hosts in Chapter 4.

1.5 References

1. M. J. Berridge, P. Lipp, M. D. Bootman, *Nat. Rev. Mol. Cell Biol.* **2000**, *1*, 11.
2. S. Ringer, *J. Physiol.* **1883**, *4*, 222.
3. R. Miledi, *Proc. R. Soc. London, B: Biol. Sci.* **1973**, *183*, 421.
4. G. C. R. Ellis-Davies, *Chem.Rev.***2008**, *108*, 1603
5. L. Stryer, *Biochemistry*, Freeman, New York, 3rd ed., **1988**.
6. D. S. Marlin, E. Bill, T. Weyhermuller, E. Rentschler, K. Wieghardt, *Angew. Chem. Int. Ed.* **2002**, *41*, 4775
7. S. Speiser, *J. Luminescence*, **2003**, *102-3*, 267
8. Handbook of electron transfer in chemistry, Wiley-VCH, Weinheim, (2001), Vol. 1. (Editor-in-Chief: V. Balzani).
9. V. Derycke, R. Martel, J. Appenzeller, P. Avouris, *Nano lett.*, **2001**, *1*, 453
10. J-M Lehn, *Leçon inaugurale au Collège de France*, 7 mars 1980.
11. F. Vögtle, *Supramolecular Chemistry: An Introduction*, Wiley, **1993**, New York.
12. J.-M. Lehn, *Supramolecular Chemistry*, 1st ed., VCH, Weinheim, **1995**.
13. N. O. Mchedlov-Petrossyan, L. N. Vilкова, N. A. Vodolazkaya, A. G. Yakubovskaya, R. V. Rodik, V. I. Boyko, V. I. Kalchenko, *Sensors* **2006**, *6*, 962.
14. F. Faridbod, M. R. Ganjali, R. Dinarvand, P. Norouzi, S. Riahi, *Sensors* **2008**, *8*, 1645.
15. M. Becuwe, D. Landy, F. Delattre, F. Cazier, S. Fourmentin, *Sensors* **2008**, *8*, 3689.
16. Z. Yang, G. Liang, B. Xu, *Acc. Chem. Res.* **2008**, *41*, 315.
17. R. Pease, J. O. Jeppesen, J. F. Sroddart, Y. Lou, C. P. Collier, J. R. Heath, *Acc. Chem. Res.* **2001**, *34*, 433.
18. S. Matile, H. Tanaka, S. Litvinchuk, *Top. Curr. Chem.* **2007**, *277*, 219.
19. J-M Lehn, *La chimie supramoléculaire, concepts et perspectives*, De Boeck, **1997**, Bruxelles.
20. J. W. Steed, J. L. Atwood, *Supramolecular Chemistry, 2nd Ed.* Wiley & Sons, Chichester, **2009**.
21. A. J. Bard and L. Faulkner, *Electrochemical Methods: Fundamentals and Applications*. New York: Wiley. **2002**
22. J. D. Coyle, *Introduction to organic chemistry*, The Open University, Milton Keynes, **1989**
23. C. H. Fry, S. E. M. Langley, *Ion-selective electrodes for biological systems*, Hardwood, Academic Publishers, **2002**.
24. L. Stryer, *Biochemistry*, Freeman, New York, 3rd edn., **1988**
25. G. L. Closs, L. T. Calcaterra, N. J. Green, K. W. Penfield, J. R. Miller, *J. Phys. Chem.* **1986**, *90*, 3673
26. R. A. Marcus, *J. Chem. Phys.* **1965**, *43*, 679
27. H. B. Gray, J. R. Winkler, *Annu. Rev. Biochem.*, **1996**, *65*, 537
28. R.A. Marcus, *Angew. Chem. Int. Ed. Eng.*, **1993**, *32*, 1111.

29. A.P. de Silva, S. A. de Silva, *J. Chem. Soc., Chem. Commun.* **1986**, 1709.
30. B. Valeur, *Molecular Fluorescence. Principles and Applications*, Wiley-VCH, **2002**
31. J. B. Birks, *Photophysics of Aromatic Molecules*, Wiley, **1970**, London.
32. <http://what-when-how.com/nanoscience-and-nanotechnology/self-assembly-and-biocatalysis-of-polymers-and-polymer-ceramic-composites-part-1-nanotechnology/>
33. H. Heller, M. Schaefer, K. Schulten, *J. Phys. Chem.* **1993**, *97*, 8343
34. IUPAC. Compendium of Chemical Terminology, 2nd ed. (the "Gold Book"). Compiled by A. D. McNaught and A. Wilkinson. Blackwell Scientific Publications, Oxford (1997).
35. E. Evans, D. Needham, *J. Phys. Chem.* **1987**, *91*, 4219
36. H. C. Berg, "Random Walks in Biology". Extended Paperback Ed. ed. 1993, Princeton, NJ: Princeton University Press
37. A. E. Walsby, *Microbiological reviews*, **1994**, *58*, 94

Chapter 2

**Photoactive Calcium Acceptors and Ejectors: Synthesis and
Properties**

2.1 Introduction

As the goal and working mechanism mentioned in Chapter 1, the photoactive ion-shuttle which combines calcium acceptor and ejector is the key supramolecular system in this project. Here, Ca^{2+} -acceptor (fluorescence probes) and Ca^{2+} -ejector (cage compounds) will be discussed individually in terms of their synthesis and photophysical properties. First of all, general concept and examples of these two compositions will be introduced as follows.

2.1.1 Ca^{2+} -acceptors incorporating PET (photoinduced electron transfer)

Sensors for chemical species as well as physical properties continue to be in high demand because of existing and emerging needs from many areas of human activity, particularly concerning health and environmental monitorities.

The four main categories of molecular sensors have been described in Chapter 1.3, in the PET type sensors (Figure 2.1), the fluorophore-ionophore pair is selected to allow rapid PET between them on the basis of thermodynamically criteria. The rapidity is usually assured by sufficiently favorable PET thermodynamics and by using sufficiently short spacers in a media of sufficient polarity to favorize charge separation. As shown in the Figure 2.1, different sensors have the own chelating guest. Sensor **1** is one of the first and simplest crown PET sensors.² Its fluorescence quantum yield increases from 0.003 to 0.14 upon binding of K^+ in methanol. In sensor **2**,³ the crown contains four sulfur atoms and is known for its strong affinity towards Cu^{2+} . Notably, the other transition metal ions such as Mn^{2+} , Fe^{2+} , Co^{2+} , Ni^{2+} , have insignificant effect in ethanol solutions toward the sensor. As for sensor **3** and **4**,^{4,5} they are more selective towards alkali cations than macrocyclic structures. Sensor **5** can be used to bind Zn^{2+} and sensor **6** has selectivity for Cu^{2+} and Ni^{2+} .^{6,7}

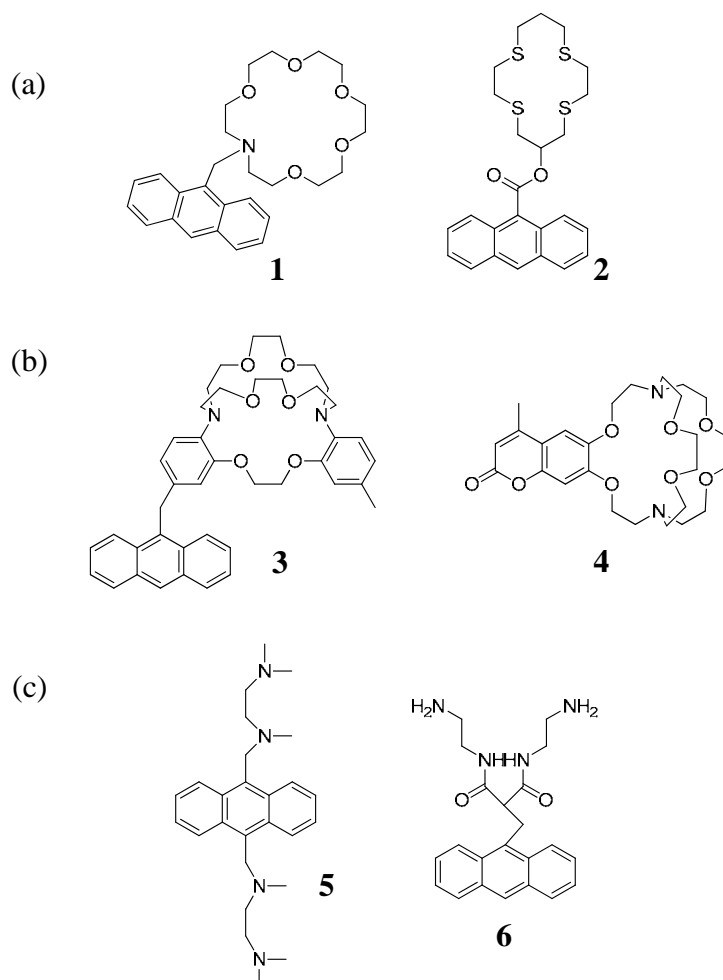


Figure 2.1 (a) Crown-containing PET sensors,¹⁻³ (b) Cryptand-based PET sensors,^{4,5} (c) Podand-based PET sensors^{6,7}

The chemical synthesis of effective fluorescent Ca^{2+} sensors in the period from 1980-1988 pre-staged the development and application of caged Ca^{2+} probes (will be presented in next section). These two pieces of chemical technology, in conjunction with other technologies such as patch clamp, laser-scanning confocal microscopy, microfluorimetry, genetic manipulation of proteins, etc., all combined to enable physiologists to start to obtain a detailed molecular picture of Ca^{2+} signaling cascades in many different cells.⁸

The chelating PET sensors (Figure 2.2) for selective calcium probes have been designed and developed by Tsien and coworkers for applications in cellular biology.^{9,10} i.e. for probing calcium concentrations in the micromolar range. Chelators with carboxylic groups are known to efficiently bind divalent hard cations like Ca^{2+} and Mg^{2+} . The so-called *BAPTA* (1,2-bis(o-aminophenoxy)ethane-N,N,N',N'-tetraacetic acid) recognition moiety resembles EGTA, but the nitrogen atoms are linked to a phenyl group in order to avoid pH sensitivity in physiological pH range. Most of them are not based exclusively on the PET switching principle. For example, the photophysical properties of Calcium Green (**7**) appears to be more complicated than the simple PET mechanism because ground-state conformational changes

upon calcium binding can be also involved.¹¹ In PET sensors, the changes in fluorescence quantum yield are accompanied with proportional changes in excited-state lifetime. Therefore, compounds **7** to **9** turned out to be suitable for fluorescence lifetime imaging of calcium.^{12,13}

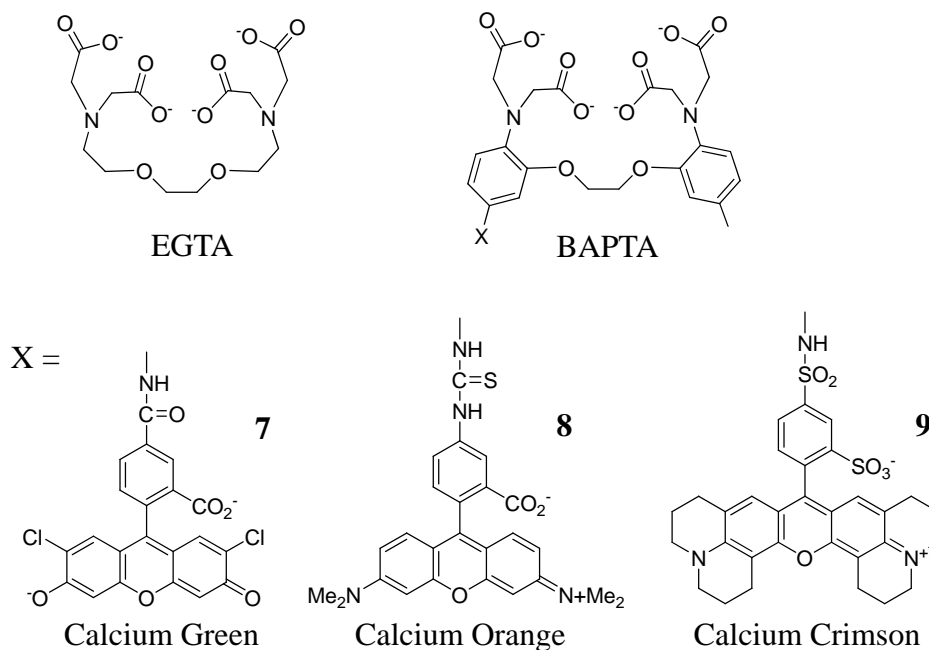


Figure 2.2 Chelating PET sensors

Except for the Calcium Green sensor, there are some important noteworthy sensors not based on the PET mechanism (Figure 2.3). For example fura-2 (**10**) is a ratiometric fluorescent dye which binds to free intracellular calcium. It was the first widely-used dye for calcium imaging, and remains very popular. At low concentrations of the indicator, use of the 340/380 nm excitation ratio for fura-2 allows accurate measurements of the intracellular Ca^{2+} concentration.¹⁴

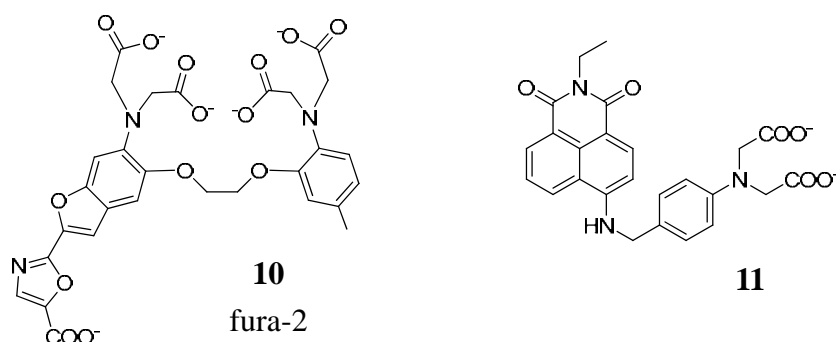


Figure 2.3 Calcium sensor fura-2 (**10**) and Zn^{2+} sensor (**11**) with naphthalimide fluorophore

Sensor **11**¹⁵, comprises the 4-amino-1,8-naphthalimide fluorophore. This fluorophore is widely used as active media for lasers. The spectral and luminescence properties of alkyl-substituted 4-aminonaphthalimide derivatives are determined by the solvent and the

nature of the amino group at the 4-position. Fluorescence of 4-aminonaphthalimide and its mono- 4-*N*-alkyl derivatives is characterized by high quantum yield in all examined solvents when auto-aggregation is not predominant. Moreover, strong influence of substitution in the amino group on the emission properties of 4-aminonaphthalimides is attributed to variation of the extent of the charge transfer in the excited state. For example, a considerable decrease in the quantum yield of the fluorescence in going from unsubstituted 4-aminonaphthalimide to 4-(dimethylamino)naphthalimide in polar solvents (by a factor of 28 in ethanol) is due to an increase in the efficiency of formation of the nonfluorescing charge transfer state with an increase in the electron-donor power of the amino group.¹⁶ Moreover, this fluorophore has the advantages of absorption and emission in the visible wavelength range, inert pH response, large Stokes' shift, high photostability, simple structure and easy approaches to synthetic modification. These are all favorable properties for the design of a fluorescent chemosensor.¹⁷

In the case of Zn^{2+} probe, it has an absorption band centred at 450 nm and emits in the green with $\lambda_{\text{max}} \sim 550$ nm (Figure 2.4). Also, it shows a high fluorescence quantum yield in aqueous media ($\Phi_{\text{free}} = 0.004$ to $\Phi_{\text{bound}} = 0.21$, 56-fold fluorescence enhancement).

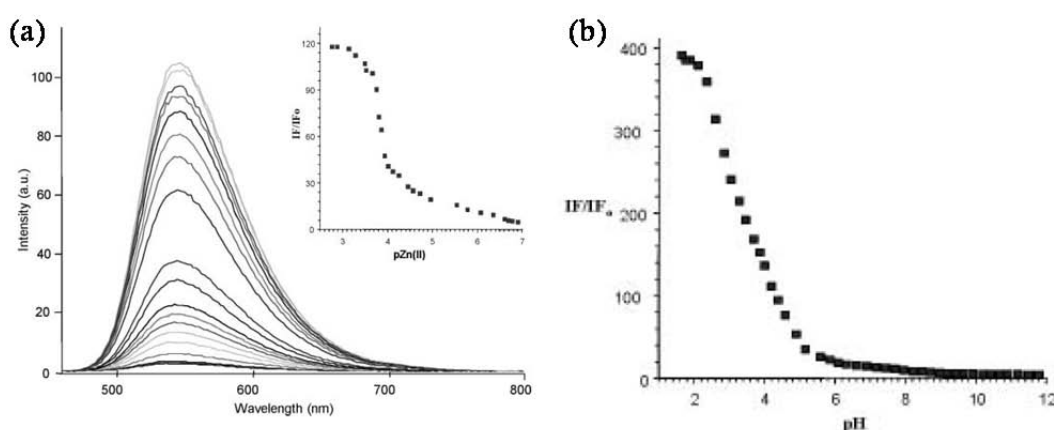


Figure 2.4 (a) Changes in the fluorescence emission spectra of **11** (1 μM) on addition of Zn^{2+} on excitation at 422 nm, at pH 7.4 [Zn^{2+}]: 1.2 nM-1.5 mM *Insert*: The changes at 550 nm as a function of $-\log[\text{Zn}^{2+}]$, pZn (b) Changes in fluorescence emission as a function of pH with **11** (1 μM)¹⁴

Due to the aforementioned advantages of *BAPTA ionophore* and *naphthalimide fluorophore*, in the coming synthesis part we will combine them together to fabricate biocompatible Ca^{2+} -acceptors, where fluorescence is switched on uniquely in the presence of Ca^{2+} .

2.1.2. Ca^{2+} -donors (caged molecules)

The other active component for construction of the photocontrolled ion-shuttle is the Ca^{2+} -donor which can be described as a “caged” compound. This term was created by physiologists to refer to the functional encapsulation of a biomolecule (ATP) by use of a

photochemical protecting group, which is uncaged upon irradiation.

Almost all chemical messengers used by cells are organic molecules, so they are caged by covalent modification of a crucial residue (e.g., the γ -phosphate of ATP). For a cation such as Ca^{2+} , this can be caged functionally by high affinity coordination, except the entire framework is not covalently bond. Thus, caged Ca^{2+} molecules are like the caged compounds with high affinity coordination of Ca^{2+} by photolabile chelators. For example, chromophore excitation leads to photolysis of a covalent bond, liberating the caged chemical messenger. As shown in Figure 2.5, Ca^{2+} uncaging is achieved by photolysis of **12** (NP-EGTA). Ca^{2+} is efficiently released by photolysis of the chelator backbone, converting a high affinity, tetracarboxylic acid chelator into two low affinity dicarboxylic acid molecules.

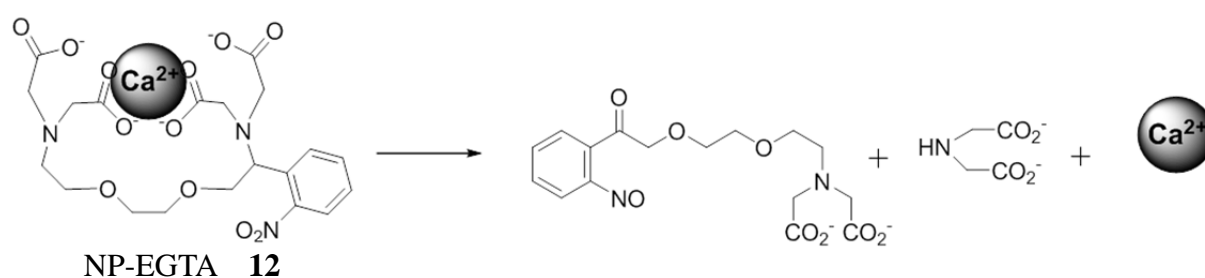


Figure 2.5 Ca^{2+} uncaging by photolysis of NP-EGTA.

The first caged Ca^{2+} compounds were developed independently by two groups during the period of 1986-1988.¹⁸⁻²⁰ Two of these probes (nitr-5 and DM-nitrophen, Figure 2.6) worked synthetically well to become commercially available.

The first published experiments with a Ca^{2+} cage highlighted almost all the strengths and weaknesses of caged Ca^{2+} biology and chemistry. During the period of development of fura-2, Tsien and co-workers also synthesized caged Ca^{2+} compounds, for example nitr-2 (**14**) and nitr-5 (**15**) in Figure 2.6.

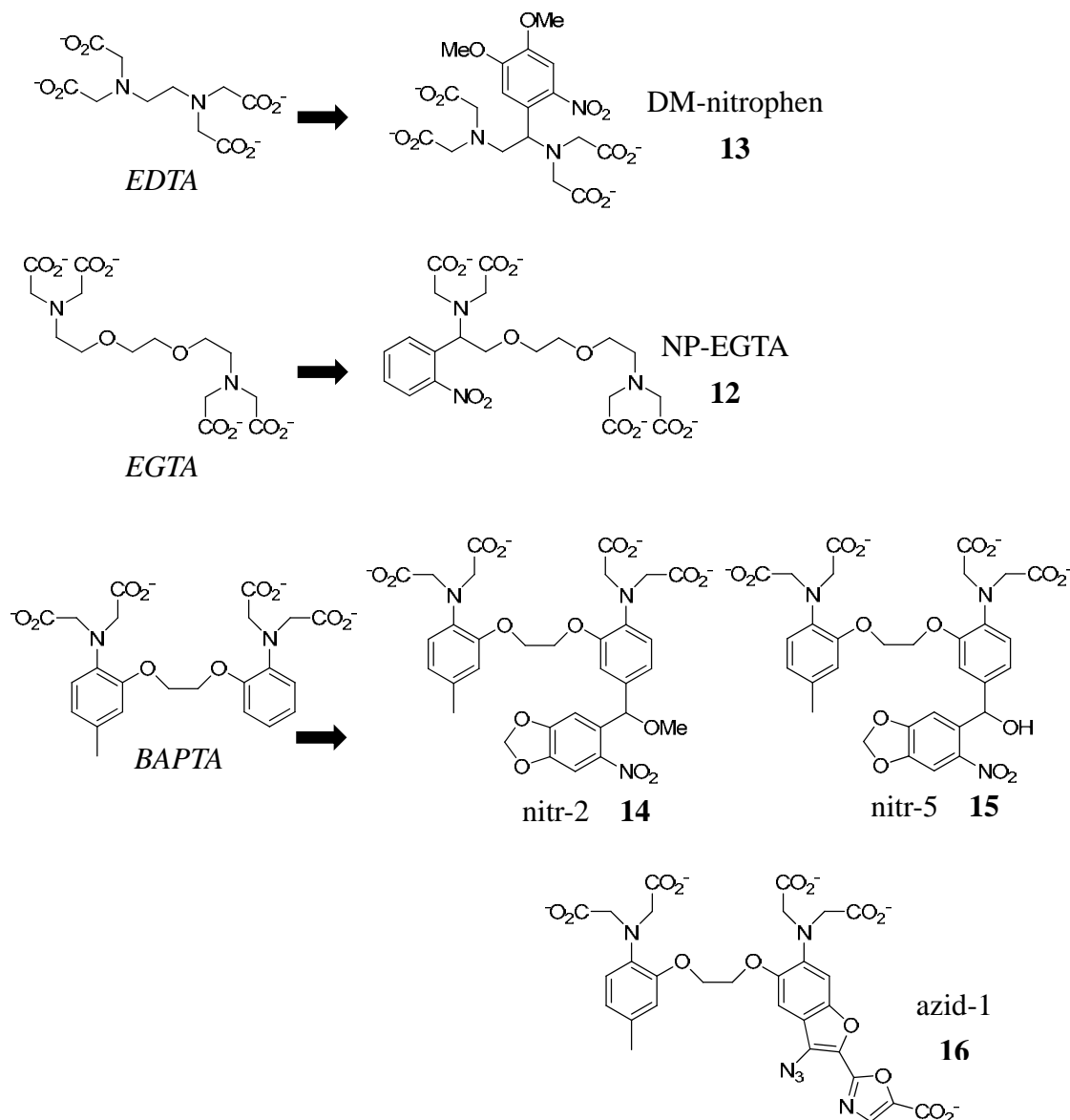


Figure 2.6 Structures of Ca^{2+} cages that have been used in living cells, with their parent chelators (EDTA, EGTA, and BAPTA).

The photoreaction of nitr-2 (**14**, Figure 2.7) eliminates methanol, creating a benzylic carbonyl functionality, and reduced the pK_a of the conjugated N atom. This chemistry changed the affinity towards calcium with values of dissociation constant (K_d) from 160 nM to circa 8 μM , thus some bound Ca^{2+} was released. The kinetically slow and photochemically inefficient release of Ca^{2+} by nitr-2 was seen as a potential problem for neurophysiological experiments, promoting development of improved caged Ca^{2+} compounds.

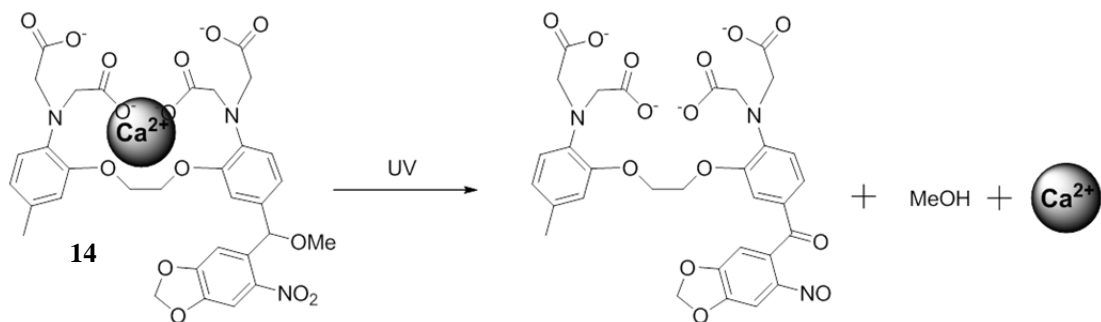


Figure 2.7 Photolysis of nitr-2 (**14**), lowering the affinity of the chelator for Ca^{2+} by creation of a conjugated electron withdrawing group on one aromatic ring.

The development of nitr-5 (**15**) was a significant improvement upon nitr-2.²⁰ Nitr-5 photolyzed in a similar way as nitr-2 (Figure 2.8), Photolysis at 365 nm in the absence of Ca^{2+} produced a major new absorbance peaking at 380 nm, consistent with the increased conjugation in the expected 4-amino-2'-nitrosobenzophenone (Figure 2.9a). Binding of Ca^{2+} now markedly reduced the 380 nm absorption band (Figure 2.9b), in close analogy to related chelators in which Ca^{2+} effectively decouples the amino groups from the rest of the chromophore. The affinities for Ca^{2+} were now 30-40-fold weaker than before photolysis, a large change easily explained by the negative mesomeric effect of the para carbonyl. The same end product was obtained whether Ca^{2+} was added before or after photolysis.

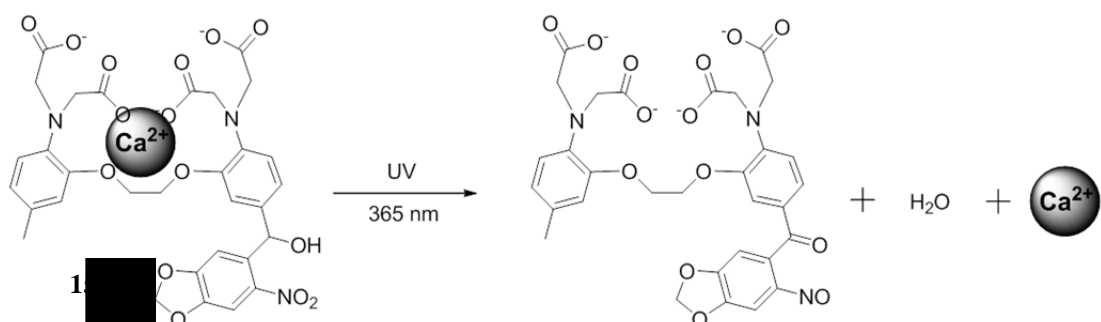


Figure 2.8 Photolysis of nitr-5 (**15**)

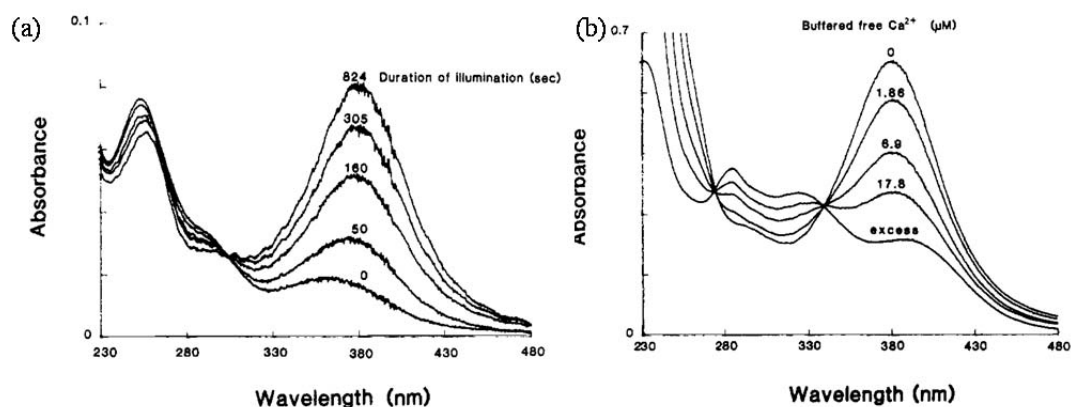


Figure 2.9 Electronic absorption spectra of nitr-5 undergoing photolysis in the absence of Ca^{2+} (a), and photolyzed nitr-5 as a function of free $[\text{Ca}^{2+}]$ (b).¹⁹

The nitr-series compounds have the advantage of being pH insensitive in the physiological range and show low affinities for Mg^{2+} (~ mM). Generally, these molecules are not ideal caged Ca^{2+} compounds because their disadvantage in releasing Ca^{2+} is (photo)chemically inefficient (Figure 2.10). However, these well characterized species can serve as effective models in proof of principle supramolecular systems.

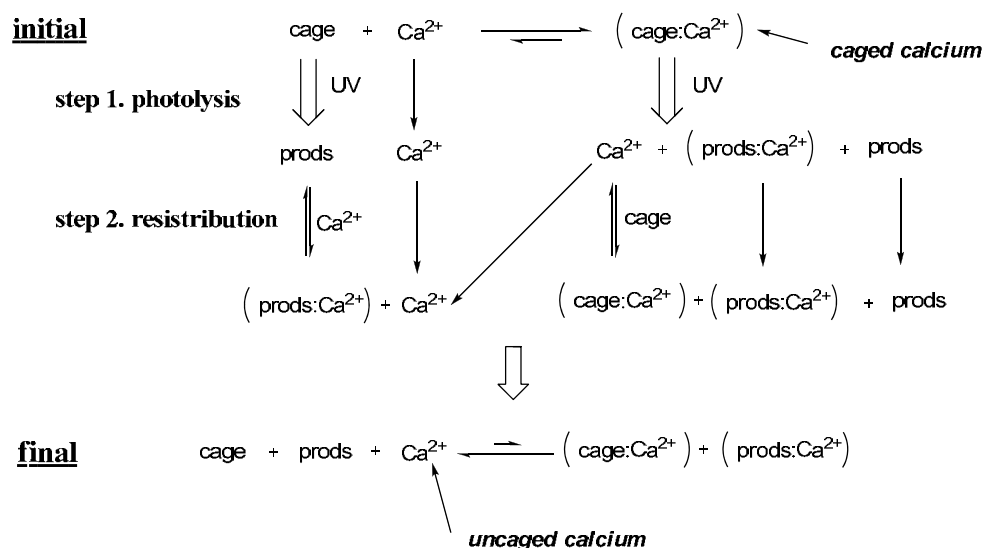


Figure 2.10 Changes involved in Ca^{2+} uncaging by photolysis of a high affinity Ca^{2+} chelator resulting in net Ca^{2+} liberation

As shown in the scheme, in the initial state, the equilibrium should lie to the right-hand side, favoring “caged Ca^{2+} ” (top line), and after photolysis, net release of Ca^{2+} will drive the equilibrium to the left-hand side in the final state. Note that the photoproducts will have a finite affinity for Ca^{2+} (Table 2.1) and so will chelate some photoreleased Ca^{2+} , reducing the overall chemical yield of uncaged Ca^{2+} .

at pH 7.2 100 mM KCl	K_d (cage) nM	K_d (prods) mM	ΔK_d x-fold	K_d (Mg^{2+}) mM	Extinction coefficient $M^{-1}cm^{-1}$	Rate of photolysis s^{-1}	Quantum yield of photolysis
EDTA	32	/	/	0.005	/	/	/
EGTA	150	/	/	12	/	/	/
DM-nitrophen	5	3	600,000	0.0025	4,300	8×10^4	0.18
NP-EGTA	80	1	12,500	9	975	5×10^5	0.23
BAPTA	110	/	/	/	/	/	/
nitr-5	145	0.0063	54	8.5	5,500	2.5×10^3	0.012
azid-1	230	0.12	520	8	33,000	/	1

Table 2.1 Properties of Ca^{2+} cage compounds / parent chelator

Therefore, chemical inefficiency of nitr compound imposes an upper limitation on the total amount of Ca^{2+} that can be uncaged. This limit for the nitr compounds stems both from the

modest changes in Ca^{2+} affinity arising from photolysis ($\Delta K_d \sim 40$ -fold) and from the relatively low affinity before photolysis. Since only bound Ca^{2+} can be uncaged, the K_d before photolysis sets the percentage loading of the photolabile chelator before the unbound or free $[\text{Ca}^{2+}]$ reaches the threshold. If the cage has $K_d = 140$ nM (nitr-5), then only 40% of the chelator complexes Ca^{2+} , leaving 60% free chelator.²¹ Net release of Ca^{2+} under these circumstances requires photolysis of $>60\%$ total cage; otherwise, uncaged Ca^{2+} will be recomplexed by unloaded, unphotolyzed cage. The modest change in affinity (ΔK_d) has an even more profound effect on the chemical efficiency of Ca^{2+} uncaging from photolabile nitr chelators. Since the photoproducts of uncaging of nitr compounds have affinities for Ca^{2+} in the range of 1-10 μM , most of the Ca^{2+} remains complexed after photolysis.

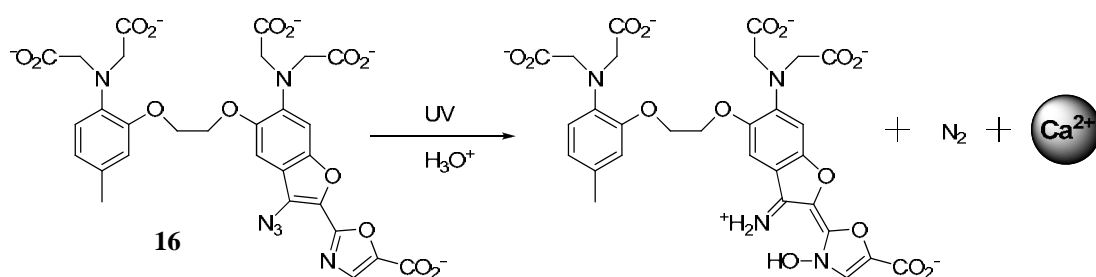


Figure 2.11 Photolysis of azid-1 (**16**)

Another cage compound with BAPTA parent chelator is azid-1 (**16**), a photosensitive derivative of fura-2 designed initially for photocross-linking the Ca^{2+} dye to cellular proteins. Illumination of this probe preserves the BAPTA coordination sphere (Figure 2.11) but not the fluorescence properties of the fura dye, as an amidoxime photoproduct is generated.²² This new electron withdrawing substituent reduces the molecule's affinity for Ca^{2+} more efficiently than any of the nitr cages. Combined with its superior photochemical properties (Table 2.1), this makes azid-1 more (photo)chemically efficient than any nitr cage at releasing Ca^{2+} . Besides, azid-1 is extremely efficient photochemically, having a quantum yield of photolysis of unity. A small two photon absorption cross-section offers the possibility of photo-decaging using NIR light, which penetrates deeper into tissue.

Compared to the chemistry of the nitr series, the other first generation cage compound DM-nitrophen (**13**) is cleaved during photolysis; this destroys the high affinity Ca^{2+} coordination sphere of the chelator as the example NP-EGTA (**12**) in Figure 2.1. This fragmentation approach to Ca^{2+} release inevitably produced much larger changes in ΔK_d than the modest 40-fold changes of nitr-5 (Table 2.1). Before photolysis, the K_d DM-nitrophen for Ca^{2+} is 5 nM, and the photoproducts have an average affinity of about 3 mM; thus, the ΔK_d is 600,000-fold at pH 7.2. However, since DM-nitrophen was based on EDTA, it shares similar Mg^{2+} and proton affinities with those of the parent chelator.^{20,23}

In the vital usage, the selectivity of cation binding is clearly an important property for any

Ca²⁺ cage. All the mentioned cages start with chelators that effectively discriminate for alkaline earth metals over alkali metals. Since intracellular [K⁺ + Na⁺] is >100 mM compared to 100 nM for Ca²⁺, this selectivity is a prerequisite for Ca²⁺ cages and rules out the use of crown ether chelators. Since intracellular [Mg²⁺] is about 1 mM, a Ca²⁺/Mg²⁺ selectivity of 10⁵ is required for a truly Ca²⁺ selective cage.

In conclusion, from the view of chemical yield of Ca²⁺, photolysis of DM-nitrophen is the most efficient cage, as this molecule has the highest affinity before photolysis and the lowest after. Thus, calculations suggest that DM-nitrophen may release an order of magnitude more Ca²⁺ than any other cage. As for the aspect of chromophore, in terms of light absorption, azid-1 is the best chromophore having a large extinction coefficient being based on fura-2. The other cages use the traditional nitrobenzyl (ex. nitr series) or dimethoxynitrobenzyl chromophore, which absorb light 5-34 times less efficiently than azid-1.

Finally, the pH insensitivity of the affinity for Ca²⁺ has been recognized as an important property for Ca²⁺ cages. Since the BAPTA type Ca²⁺-acceptor was chosen for our usage in photoinduced ion-shuttle, BAPTA-based Ca²⁺-ejector of caged compound such as nitr-series more preferred to EG(D)TA-based probes.

2.2 Synthesis of Ca²⁺-acceptor and Ca²⁺-ejector molecules

2.2.1 Synthesis of Ca²⁺-acceptor molecules

In order to compare the photoinduced ion-shuttle systems in free solution and in the vesicle matrix, five Ca²⁺-acceptor molecules were synthesized as fluorescence probes (Figure 2.12):

-BANI: With amide bond as spacer linkage between BAPTA chelator and 4-amino-1,8,-naphthalimide as chromophore.

-BANI2 & BANI3: Two similar compounds **BANI2** and **BANI3** to **BANI** having a shorter methylene group spacer. Moreover, **BANI2** has a long hydrocarbon chain (C₈H₁₇) on the chromophore but not in **BANI3**, therefore in principal a different behavior can be observed when probe molecules are fixed on the lipid bilayer membrane in the vesicle matrix or in free solution.

-BAPTAant & C15BAPTAant: Trial compounds to compare with **BANI** series.

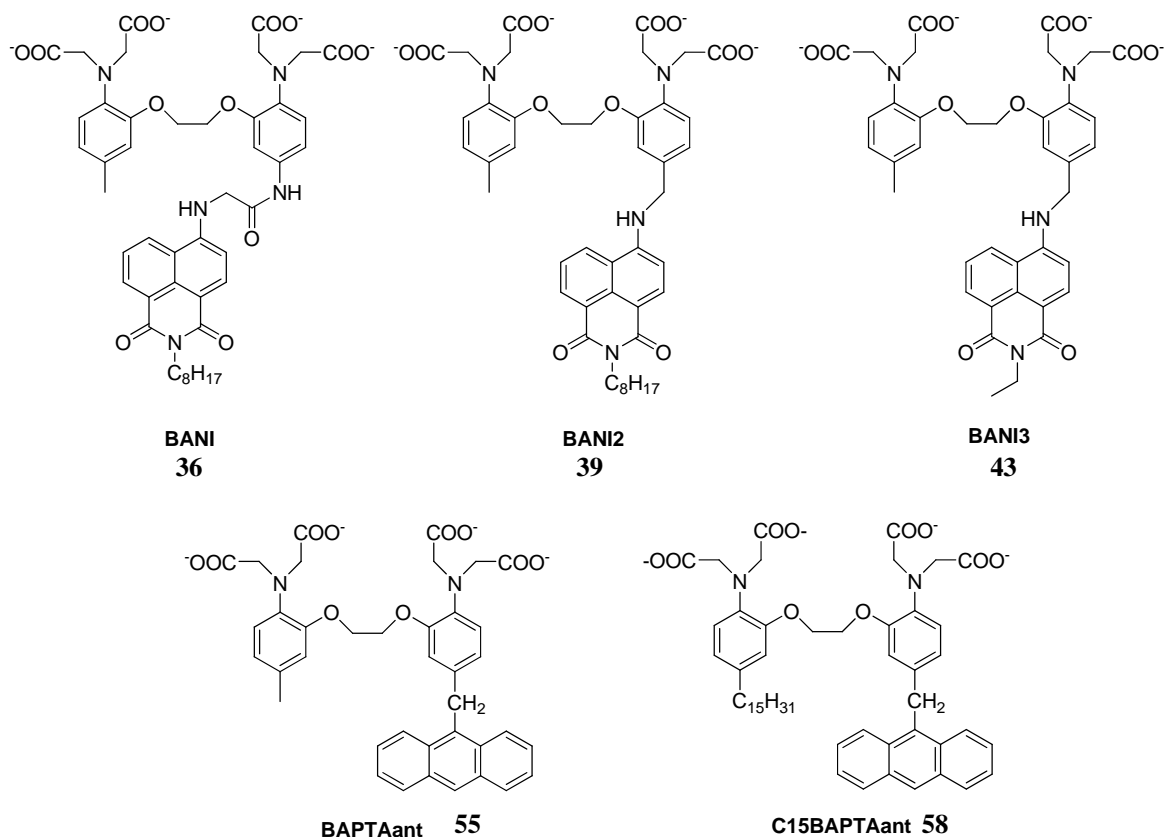


Figure 2.12 Synthesized Ca^{2+} -acceptor molecules / fluorescence probes

The following sections **2.2.1.1** to **2.2.1.5** are concern the synthetic route to those molecules and discussion of their behaviors:

2.2.1.1 Product BANI

<Synthesis route>

To obtain product **BANI**, a receptor moiety and the chromophore unit can be coupled by amide bond formation (Figure 2.13), In order to achieve this, two precursor compound, **24** and **30** were reported.

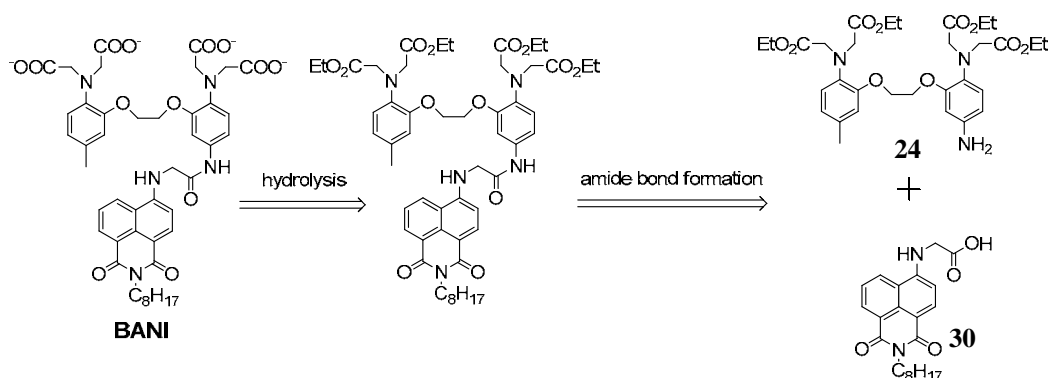


Figure 2.13 Amide bond formation giving **BANI**

Following the procedure published by Tsien in 1985¹⁴, compound **22** was successfully synthesized. After optimizing the stoichiometry (in the coming discussion part) to get one nitration compound **23**, compound **24** was obtained by palladium catalyzed reduction²⁸ (Figure 2.14).

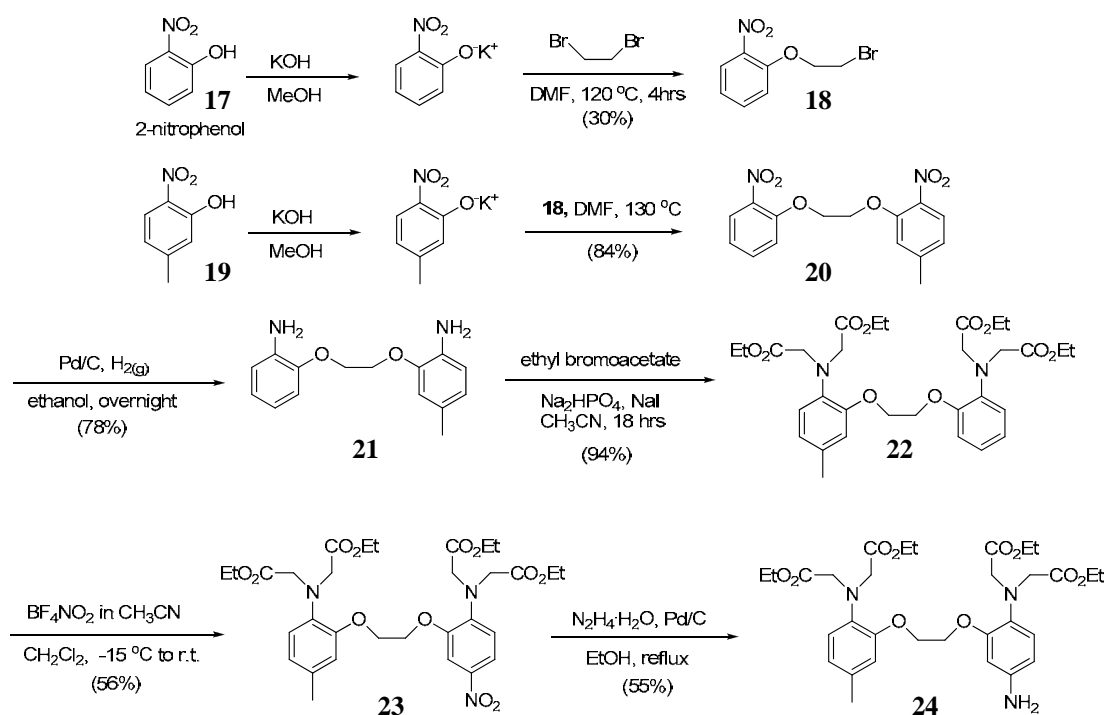


Figure 2.14 Synthesis of precursor compound **24**

Commercial compound 4-nitro-1,8-naphthalic anhydride served as a precursor for compound **30**. Intermediate **27** was obtained by refluxing with *n*-octylamine in ethanol. (Figure 2.15)

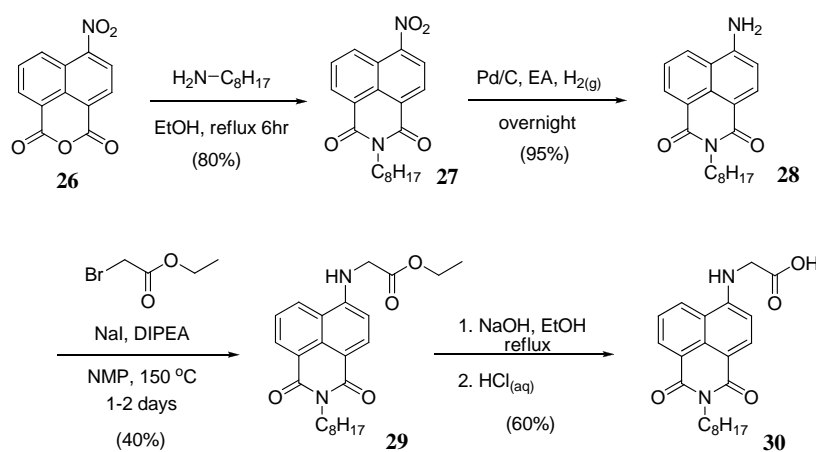


Figure 2.15 Synthesis of precursor compound **30**

After Pd-catalyst reduction overnight to obtain compound **28**, we utilized as S_N2 reaction with ethyl bromoacetate to get compound **29**. Followed by hydrolysis and acidification,

compound **30** can be obtained by collecting the yellow precipitation.

With two precursors in hand, making use of amide bond formation to couple compounds **24** and **30** allowed us to obtain compound **35** (Figure 2.16). After hydrolysis then acidification, we successfully got the final product **BANI** (compound **36**).

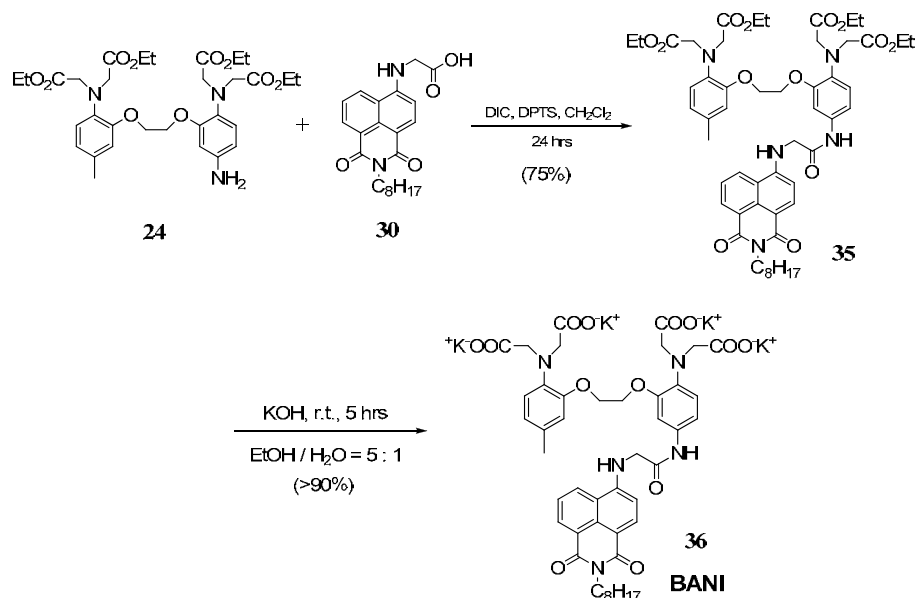


Figure 2.16 Synthesis of product **BANI** by precursors **24** and **30**

<Synthesis discussion>

In the synthesis route to **BANI**, some key reactions needed to be optimized to increase yield and/or avoid side product formation.

- compound **23**:

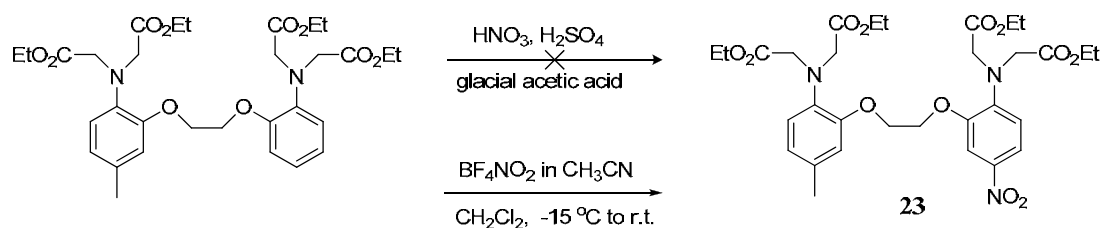


Figure 2.17 Synthesis of compound **23**

After failure of using the common nitration condition in strong acid, milder conditions were employed with nitronium tetrafluoroborate to obtain compound **23**.²⁴ For this step, the equivalents of BF₄NO₂ could decide the yield of product because of the difficulty to discriminate between the one-nitro and two-nitro compounds by column chromatography and TLC. The only way to characterize the nitration state is by NMR and Mass Spectrometry. In the end, the optimized stoichiometry (Table 2.2) was determined to be 1.5 equivalent of

Eq. of BF ₄ NO ₂	Results
1.1	S.M. not fully consumed, the yield of one-nitro product is 45 %
1.5	Adequate (purified by column then recrystallization, yield is 56%)
2	Two-nitro compound present

Table 2.2 Stoichiometry of nitrating agent

- compound **11**:

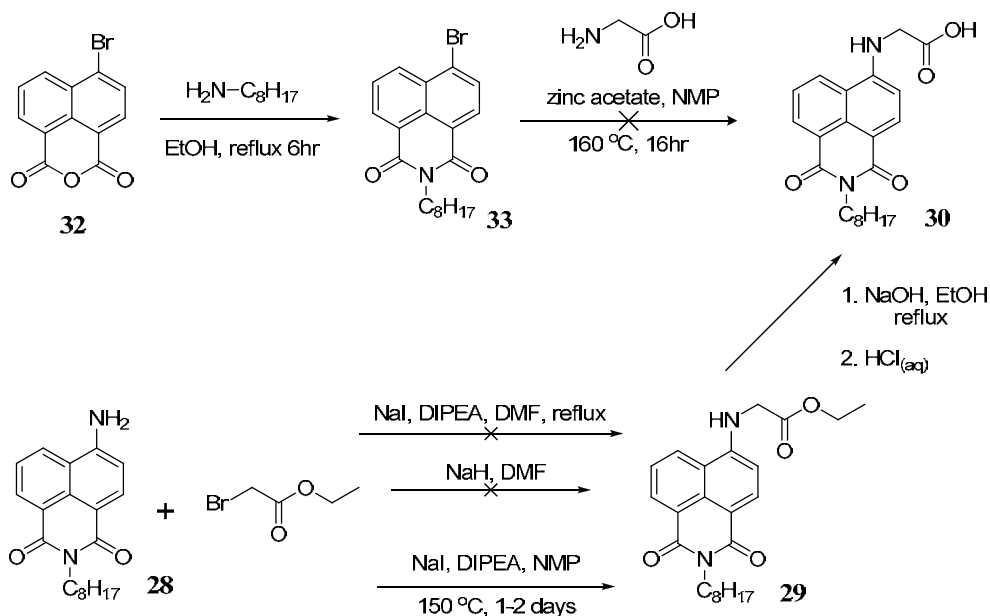


Figure 2.18 Synthesis of compound **30**

Initially, 4-bromo-1,8-naphthalic anhydride was used as starting material (**32**) to obtain compound **33** on reacting with octylamine. (Figure 2.18) After failure of the direct addition-elimination reaction with 2-aminoacetic acid to obtain **30**, we changed our route by using compound **28** with 2 steps to obtain compound **30**. Due to the low nucleophilicity of compound **28**, harsh S_N2 reaction conditions were chosen to get compound **29**. After several trial conditions such as changing different solvent and base, compound **29** was obtained with 35% yield, which was subsequently hydrolyzed to obtain compound **30**.

- Product **BANI (36)**:

At first sight the hydrolysis reaction, according to the literature procedure,¹⁴ this step seems clean and straightforward. Typically, the general procedure uses a strong base such as KOH or NaOH to hydrolyze the ester-compound. One should obtain the precipitate carboxylate acid product by slowly acidifying the aqueous phase solution or after further purified with ion-exchange resin column (Figure 2.19).

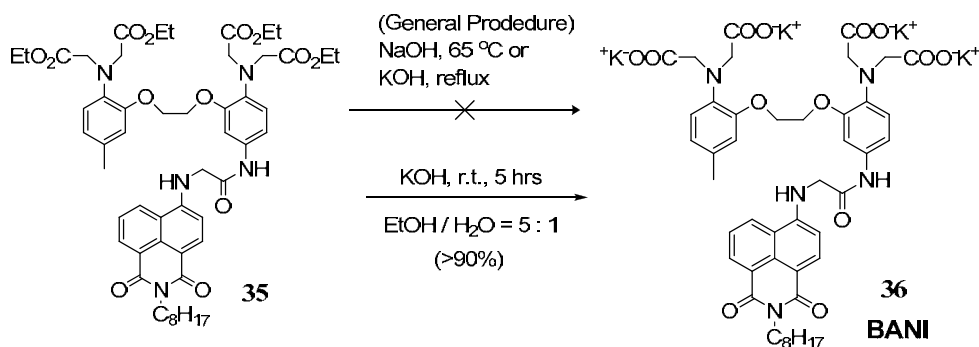


Figure 2.19 Synthesis of product **BANI**

All these conditions were tested and proved problematic for molecule **36**. First, compound **35** seems to decompose as raising the temperature in strongly basic conditions. Second, after hydrolysis we tried to obtain the product by carefully acidifying the aqueous crude to pH ~3 under 0 °C bath. No precipitate was observed even acidifying to pH ~1.5 (Note. such strongly acid condition may damage and decompose the product). Therefore, KOH was used as base to hydrolyze compound **35** for 5 hours under room temperature. The resultant solution was diluted with ice-water and 10 % HCl_(aq) was added slowly at 0 °C to pH = 7. After directly removing the solvents via freeze dry, as a mixture of **BANI** (52.5 w %) and KCl was obtained.

It should be mentioned that although in the end for product **BANI2** and **BANI3**, we hydrolyzed them with a very mild base LiOH·H₂O, and obtained the solid products by collecting the precipitates after acidification. We did not reproduce **BANI** with this milder condition; instead we directly used this mixture product (**BANI** 52.5 w % with KCl) to perform photophysical measurements and obtained these results as a stepping stone for products **BANI2** and **BANI3** which could be obtained in a more direct fashion.

2.2.1.2 Product **BANI2**

<Synthesis route>

In order to simplify the synthesis steps and introduce a shorter spacer between the BAPTA chelator and the chromophore to enhance PET mechanism, we synthesized **BANI2** by using a Schiff base reaction to couple the two precursors, compound **28** and **37**. (Figure 2.20)

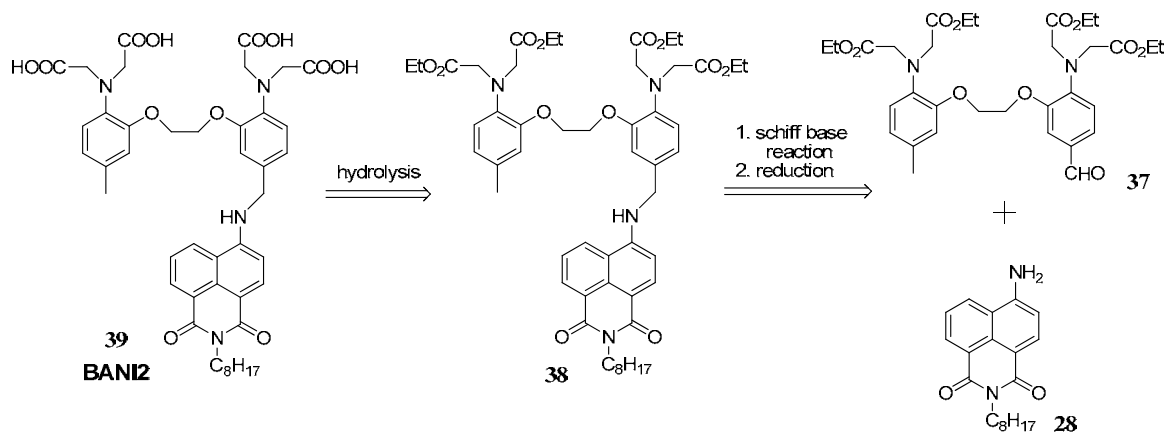


Figure 2.20 Schiff base reaction of **BAN12**

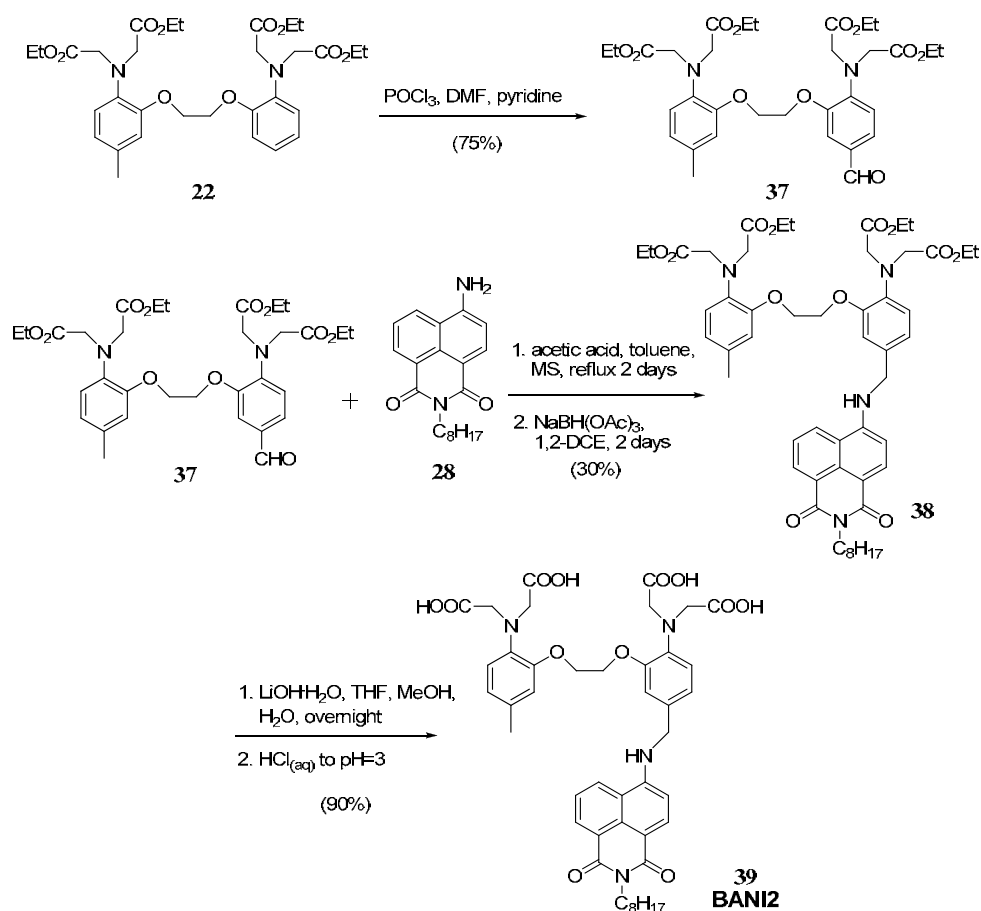


Figure 2.21 Synthesis of **BAN12**

As shown in Figure 2.21, we performed the formylation reaction with compound **22** to obtain the white powder compound **37** in 75% yield in the first stage. After the Schiff base reaction with the other precursor compound **28**, the chelator and chromophore were successfully coupled together to get compound **38** in an acceptable 30% yield. Following hydrolysis in mild conditions, final product **BAN12** (**39**) can be obtained by collecting the precipitates after careful acidification until pH~3 at 0 °C (Caution! Acidification pH~2 would damage the product).

<Synthesis discussion>

- compound **38**:

In the synthesis route of **BANI2**, the key reaction is Schiff base reaction allowing coupling compounds **28** and **37** together (Table 2.3).

<i>Reaction solvent and condition</i>	<i>result</i>
(a) ethyl acetate, equipped with Dean Stark	No reaction
(b) toluene, equipped with Dean Stark	Consuming of S.M. is low
(c) toluene, acetic acid as catalyst, molecular sieves	About 85% S.M. can be consumed, 30% over all yield in two steps

Table 2.3 Schiff base reaction of compound **38**

First, general reaction condition under refluxing in anhydrous ethyl acetate using a Dean Stark apparatus was tested.²⁵ Due to the low solubility of compound **28**, there was no reaction in these conditions. On changing the solvent to toluene, the consumption of starting material was still very low. In order to enhance the reaction acetic acid was used as catalyst and some molecular sieves were added to remove the water from reaction instead using a Dean Stark. Finally, after reduction compound **38** was obtained in 30% yield for two steps.

- Product **BANI2** (**27**):

With the test on **BANI** described in last paragraph of previous section, we found the hydrolysis condition with strong base such as KOH or NaOH would damage the compound in this case as well (Figure 2.22). Therefore, the instability towards strong acid or basic conditions is not necessarily from the amide bond linkage in product **BANI**, but more likely from the chromophore itself.

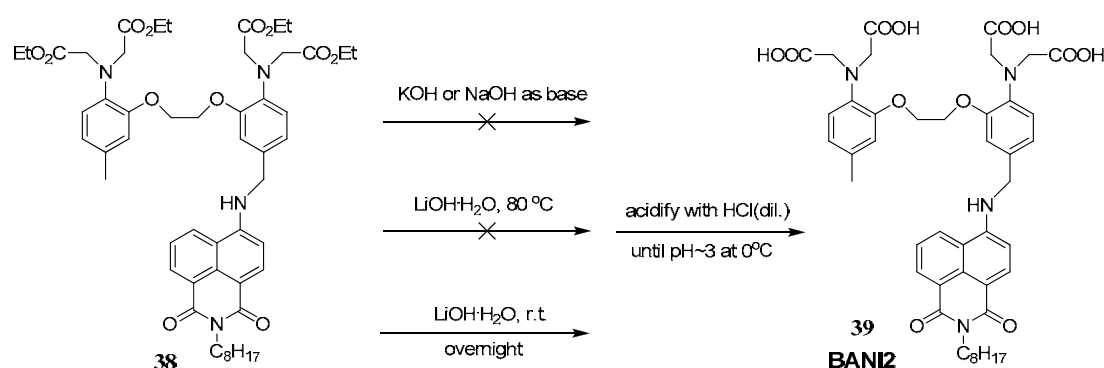


Figure 2.22 Hydrolysis of **BANI2**

Moreover, we found even using LiOH·H₂O under refluxing would damage the compound and make it harder to purify the product leading to a low yield as checked by NMR and reverse phase TLC. It was found that only using LiOH·H₂O under room temperature gives the pure and clean product without further purification. Followed by careful acidification to pH~3

at 0 °C, product **BANI2** can be obtained by collecting the precipitates from aqueous solution.

2.2.1.3. Product **BANI3**

For **BANI3**, the synthesis route is similar to product **BANI2**. The principal difference is the use of ethylamine instead of *n*-octylamine to obtain compound **40**. Following hydrogenation, precursor **41** was obtained in 95% yield. (Figure 2.23)

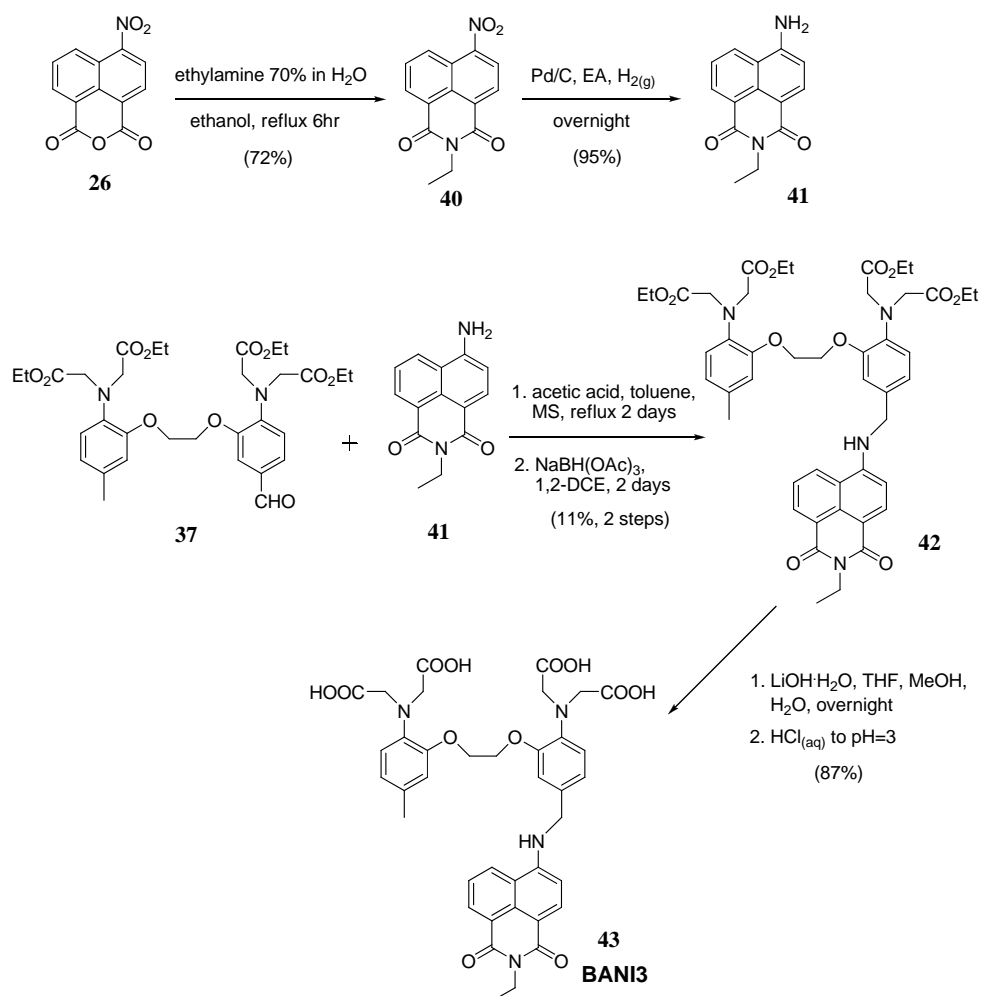


Figure 2.23 Synthesis of **BANI3**

In the same way, coupling precursors **37** and **41** with Schiff base reaction then reduction can obtain compound **42** in a lower yield than the case of **BANI2**. After hydrolysis, final product **BANI3** (**43**) was obtained in the same process as that used to acquire **BANI2**.

2.2.1.4. Product **BAPTAant**

As shown in Figure 2.24, synthesis of the product **51** was attempted with a long alkyl chain attached to anthracene chromophore. Following the synthesis route published by in the literature²⁶, precursor **49** was obtained from anthracene. Making use of Friedel-Crafts reaction

to couple the two precursors **22** and **49**, no reaction was found for this step at all. As a result, we synthesized the product **BAPTAant**, and another product **C15BAPTAant** (next section) with a long alkyl chain connected to the BAPTA unit to replace **51**.

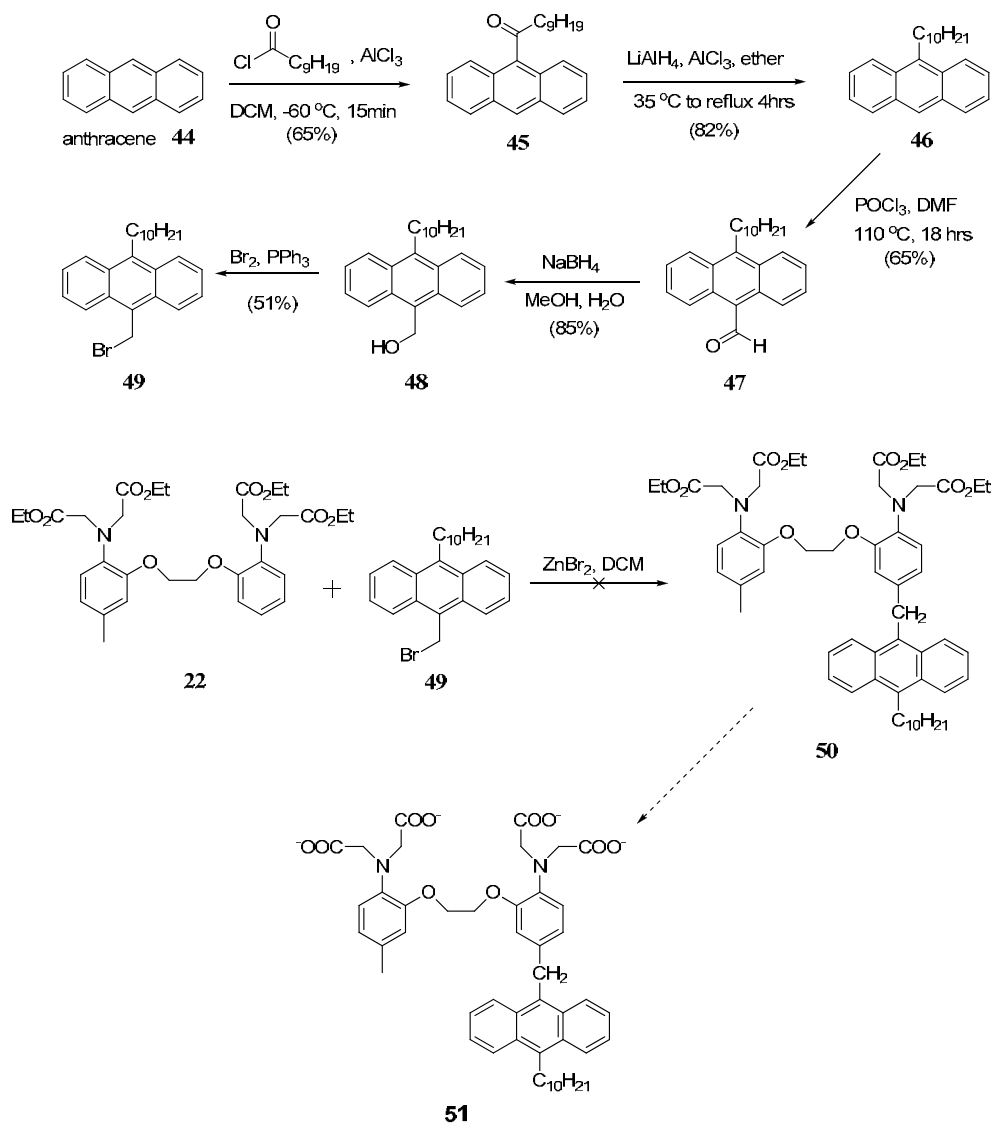


Figure 2.24 Synthesis routes of compound **51**

Directly, precursor **53** can be acquired by general halogenation from 9-methanol anthracene (Figure 2.25).²⁷ Using a Friedel-Crafts reaction to couple the two precursors **22** and **53**, compound **54** was obtained in 40 % yield. Since the anthracene chromophore is stable in acid or basic conditions, performing the hydrolysis with KOH and then acidifying it in normal methods allowed isolation of product **BAPTAant** (**55**) in 85% yield.

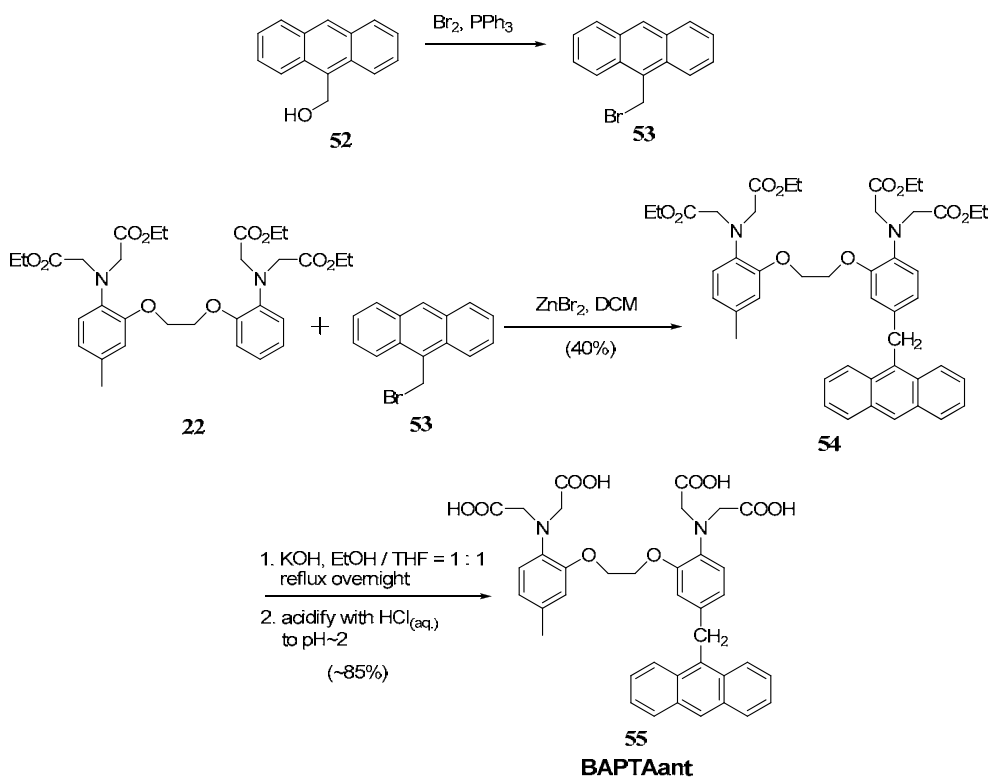


Figure 2.25 Synthesis route of **BAPTAant**

2.2.1.5 Product C15BAPTAant

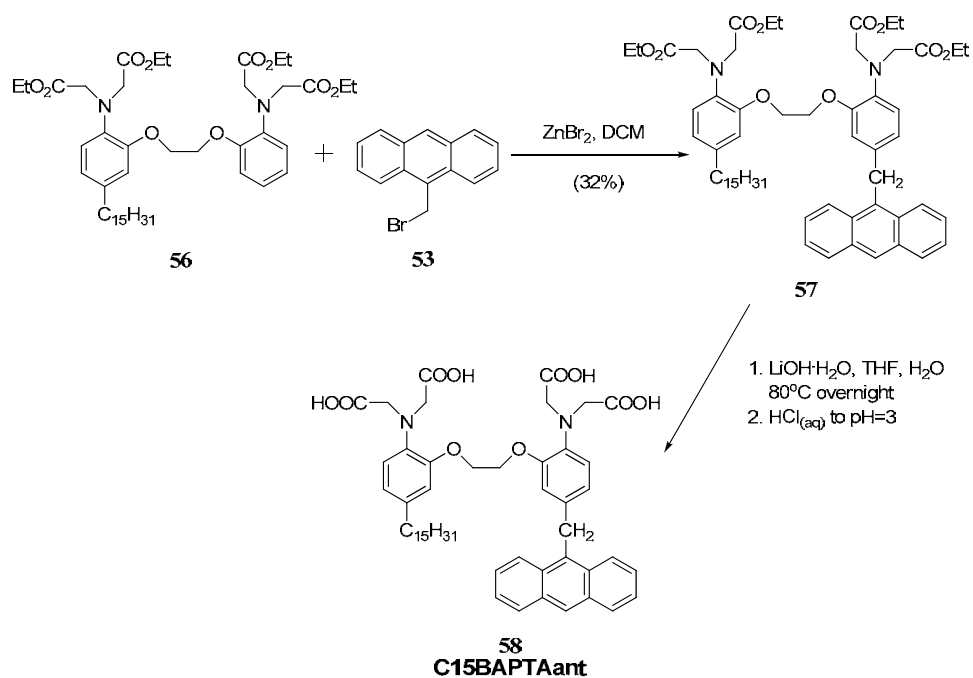


Figure 2.26 Synthesis of **C15BAPTAant**

With two precursors **53** and **56** (synthesis route is similar to compound **22**), compound **57** was obtained by coupling these two precursors together with Friedel-Crafts. The same, hydrolysis of compound **57** and then acidifying using methods described above allowed

isolation of product **C15BAPTAant (58)** in 85% yield. (Figure 2.26)

2.2.2 Synthesis of Ca^{2+} -ejector molecules

As a major goal mentioned in the introduction is to design a calcium donor-acceptor system, in this section we discuss the synthesis of **nitr-5** and **C15nitr-5** as Ca^{2+} -ejector molecules which differ in the hydrophobic part with or without long alkyl chains and can be compared in the free solution and the vesicle matrix.

Nitr-5 is a known compound published by Tsien et al.¹⁹ By using the same reactions, compound **59** was obtained in two steps (Figure 2.27), these two steps were combined in one pot reaction and purified it after deprotecting the –TMS group in 41% overall yield.

As for the subsequent hydrolysis, $\text{LiOH}\cdot\text{H}_2\text{O}$ which is a milder base than KOH or NaOH was used without heating to perform the hydrolysis. We found that the reaction is cleaner without damaging the molecular. Therefore, after acidification the yield of **nitr-5 (60)** is about 85% by collecting the precipitates with centrifugation without further purification.

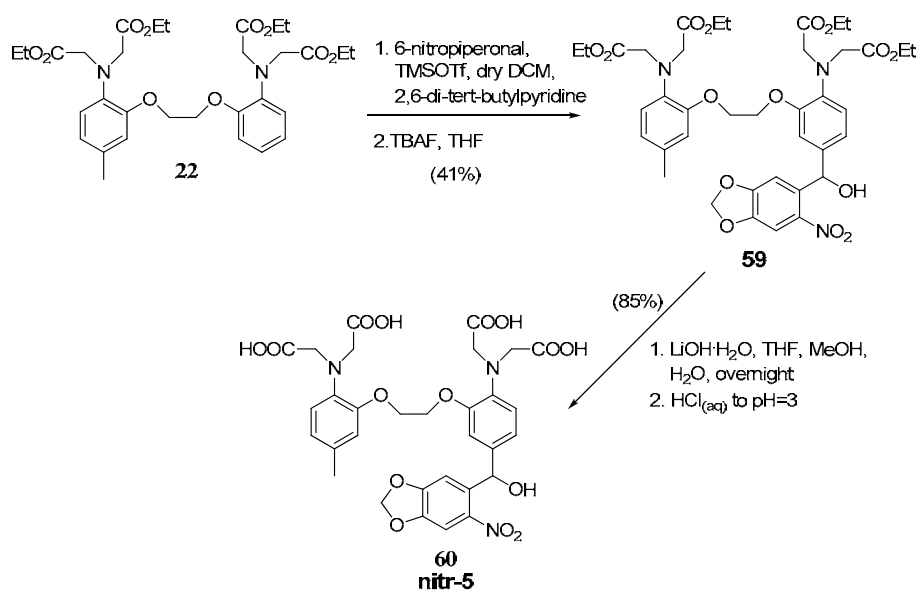


Figure 2.27 Synthesis of **nitr-5**

For the product **C15nitr-5**, compound **56** was employed as precursor using similar procedure for **nitr-5** to obtain compound **61** in 55% yield for the two steps (Figure 2.28). After hydrolysis and acidification, product **C15nitr-5 (62)** was obtained in 87% yield.

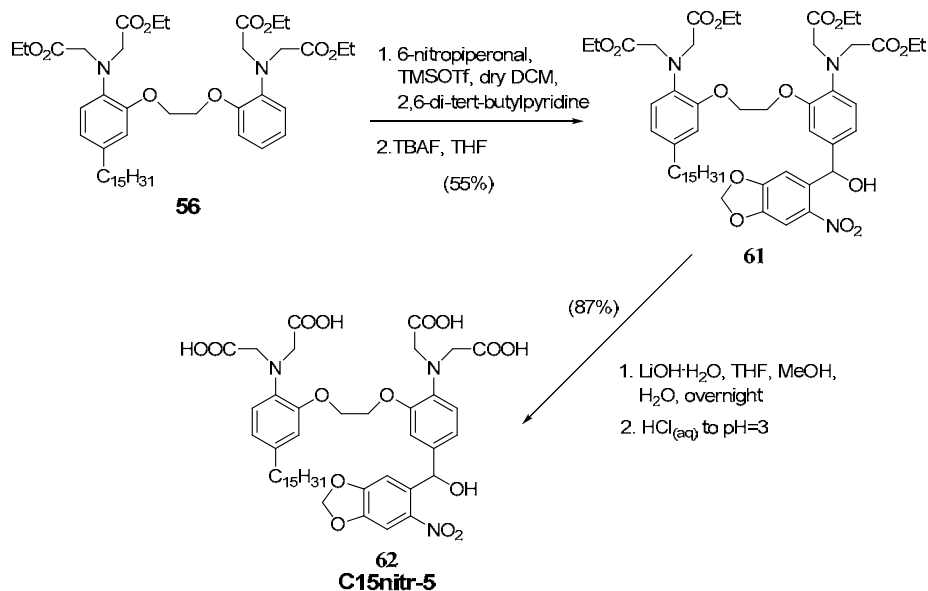


Figure 2.28 Synthesis of **C15nitr-5**

2.3 Photophysical property of Ca²⁺-acceptor and Ca²⁺-ejector molecules

Since our goal is to introduce and measure the photoionic transfer process in the amphiphile, in this chapter we will discuss the photophysical properties such as absorption and emission characters for these synthesized molecules. For Ca²⁺-acceptor molecules (fluorescence probes: **BANI1**, **BANI2 &3**, **BAPTAant**, **C15BAPTAant**), the main effort was acquiring their dissociation constant (K_d value) and also the switch on/off ability in chelating with calcium ion. As for the Ca²⁺-ejectors (**nitr-5** and **C15nitr-5**), we focused on their K_d value changing before and after photolysis which affect the cage/ release Ca²⁺ ability.

2.3.1 Photophysical properties of Ca²⁺-acceptor molecules

2.3.1.1 Spectral measurement of trial compounds **BAPTAant** & **C15BAPTAant**

As shown in Figure 2.29 for **BAPTAant** which is a known compound with a name QCa1²⁹, the switch-on/off ability triggered by Ca²⁺ was measured after hydrolysis by emission spectra in Milli-Q water without pH or ionic strength buffer. After chelating with large amount of Ca²⁺ ion, the fluorescence increase times is about 7.6-fold.

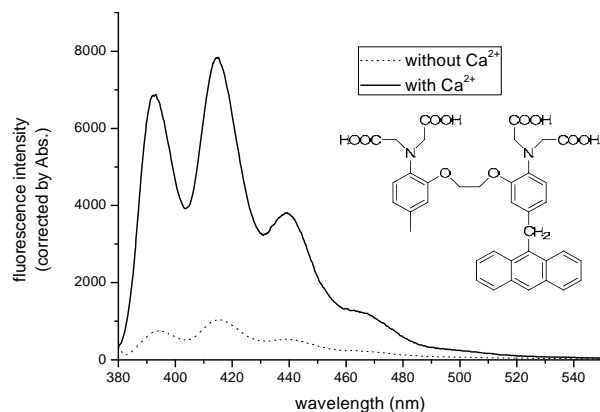


Figure 2.29 Fluorescence emission spectra (right) of **BAPTAant** in water with or without Ca^{2+} (excess equivalents)

On measuring **C15BAPTAant** (Figure 2.30) under similar conditions, differences arising from the hydrocarbon chain can be assessed. The absorption spectra shows that aggregation might occur after binding with Ca^{2+} as shown by light diffusion towards the red end of the spectrum and the increase of baseline. It would be anticipated that the excited dimer formation leads to a broad, structureless emission band at ~ 490 nm while the clear vibronic bands can be observed in the solution without Ca^{2+} . (Note. excited dimer (excimer) is a short-lived dimeric molecule formed from two species, at least one of which is in an electronic excited state. The lifetime of an excimer is very short.)

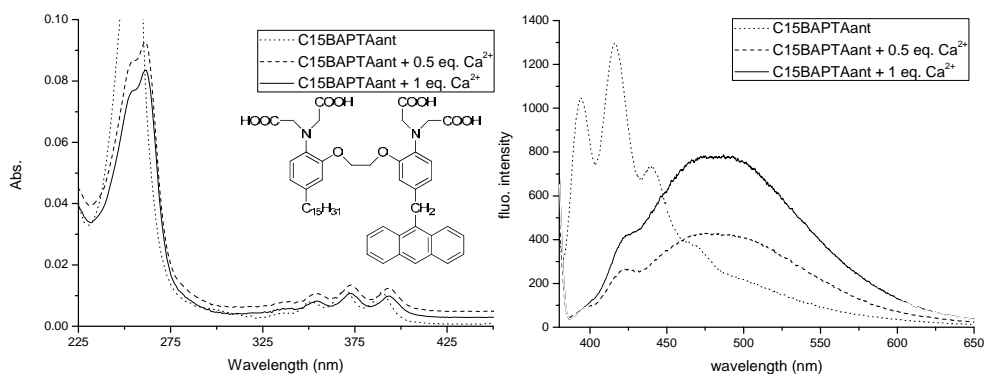


Figure 2.30 Electronic absorption spectra (left) and fluorescence emission spectra (right) of **C15BAPTAant** in water with or without Ca^{2+}

Comparing the preliminary photophysical results of these two trial molecules, we could say the nature of compound can affect the switch-on/off character due to the ease of aggregation or dimerization when strong van der Waals' forces or π - π interaction exist. This phenomenon will also be found in the **BANI** product in the coming discussion. Also, directly adding Ca^{2+} worked well to switch on the fluorescence of these two anthracene products in the Milli-Q water. As earlier mentioned, **BANI** series fluoroionophores are designed and will be mainly

studied. Therefore no further investigation was performed for anthracene systems; however with the results of **BAPTAant** and **C15BAPTAant** in mind, we will test the **BANI** series products from the method of direct Ca^{2+} addition in the Milli-Q water where the results are more complicated than anthracene compounds.

2.3.1.2 Spectral measurement of product BANI

For the novel compound **BANI**, initially it proved problematic to switch on the fluorescence by simply adding Ca^{2+} . It might be caused by the strong probe-probe interaction of π - π interaction and long alkyl chain of the chromophore part leading to aggregation-induced quenching or the H-bond interaction of the amide bond spacer enhancing vibrational quenching. For example, the fluorescence decreased after adding Ca^{2+} in the water/methanol = 4/1 solution (Figure 2.31).

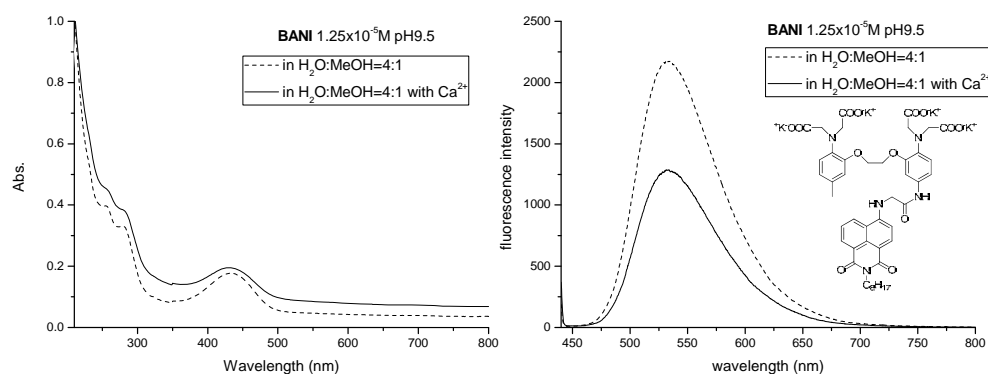


Figure 2.31 Electronic absorption spectra (left) and fluorescence emission spectra (right) of **BANI** in water/methanol = 4/1 v/v solution with or without Ca^{2+} (1 mM)

To investigate why the fluorescence decreased, the absorption and emission spectra of **BANI** were measured in water at different Ca^{2+} concentrations (Figure 2.32).

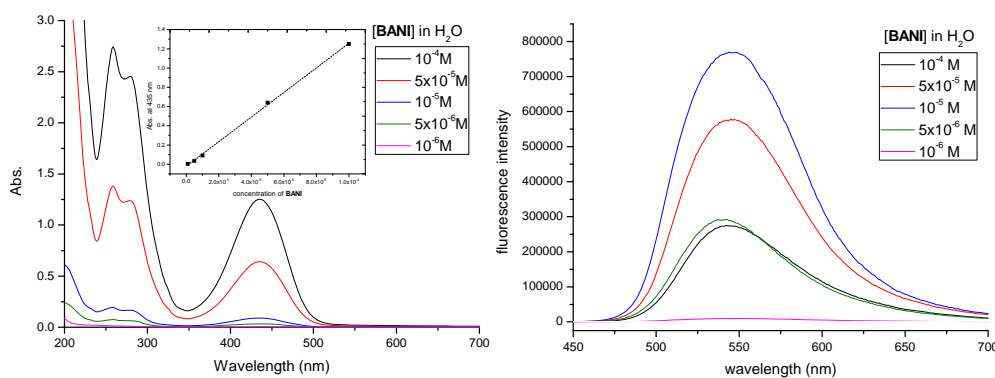


Figure 2.32 Electronic absorption spectra (left) and fluorescence emission spectra (right) of **BANI** in Milli-Q water without any buffer at different concentration of Ca^{2+}

The electronic absorption spectra showed the absorption is proportional to the concentration. The absorption spectrum of **BANI**, when recorded in Milli-Q water, showed two main absorption bands: between 260-300 nm, assigned to the π - π^* transition, and a second centered at 445 nm with a molar extinction coefficient ($\epsilon = 1.28 \times 10^4 \text{ M}^{-1} \text{ cm}^{-1}$) assigned to the internal charge transfer (ICT) character of the fluorophore, arising due to the push-pull nature of the donating amine and the withdrawing diimide. On the other hand, the fluorescence emission spectra started to decrease when the concentration was higher than 10^{-5} M (Figure 2.32right, blue curve).

To further understand the photophysical properties of the **BANI** molecules, pH vs. absorption titrations were examined (Figure 2.33). First, compound **64** (hydrolyzed compound **56**) was pretested to investigate the behavior of the aniline part of the BAPTA chelator (Figure 2.33a.). We found that the absorption increased at 300 nm when the pH decreases, which comes from the gradual protonation of the aniline part when the environment becomes acid. To identify the contributions of specific moieties in the **BANI** molecules, the absorption intensity vs. pH was plotted to separately investigate the aniline part (Figure 2.33c), chromophore part (425 nm, Figure 2.33d), and baseline (e.g. at 550 nm, Figure 2.33e). One can see that when pH decreases, **BANI** has the same trend as pretested compound **64** around 320 nm consistent with gradual protonation on the aniline part. However the baseline increased during acidification accompanied with the broadening and decreasing of chromophore absorption at 435 nm, which is consistent with aggregation.

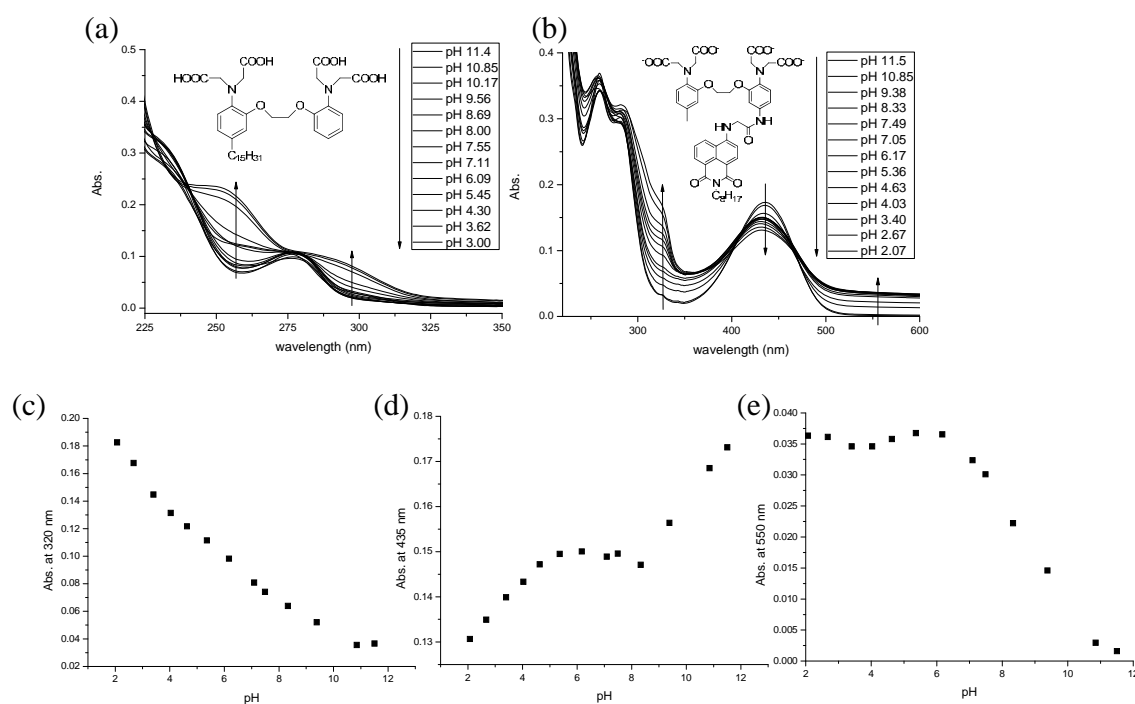


Figure 2.33 Electronic absorption spectra vs. pH for compound **64** (a) and **BANI** (b). Organized Abs. vs. pH trends of **BANI** at 320 nm <aniline part> (c), 435 nm <chromophore part> (d), 550 nm <baseline> (e)

In structurally similar fluorescence probes¹⁵, at high pH aqueous solution the molecular should be switched off with very weak fluorescence intensity and be switched on at low pH environment due to the blocking of the PET mechanism by protonation of the aniline part. Therefore, we also tested the pH vs. emission of **BANI** (Figure 2.34 right). However, **BANI** was unexpected already switched on at high pH value, and switched off at low pH.

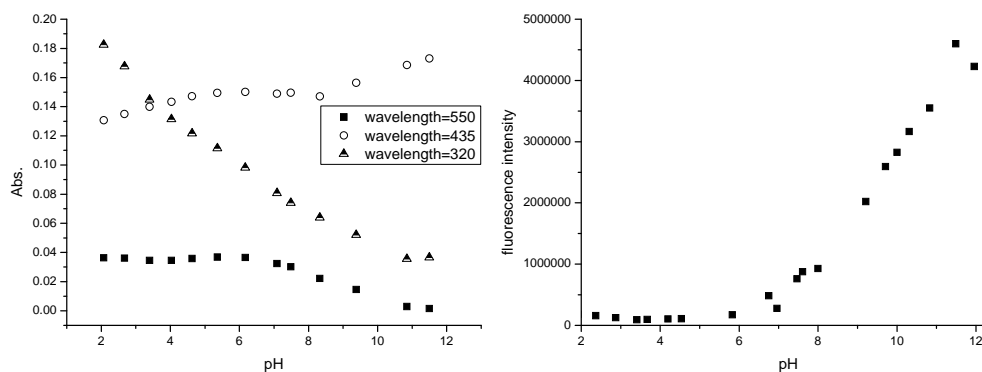


Figure 2.34 pH vs. absorption (left) and pH vs. emission (right) of **BANI** in aqueous solution ([**BANI**] = 1 μ M; [KCl] = 135 mM)

Combining the results of pH vs. absorbance graph (Figure 2.34 left) and pH vs. emission (Figure 2.34 right) with aforesaid results, it can be concluded that the difficulty in switching on the fluorescence by adding calcium might result from:

1. The aggregation of **BANI** in water by H-bonding of amide bond spacer, strong van der Waals' forces and π - π interaction of chromophore can lead to unusual properties.
2. The fluorescence probe was already partially chelated with Ca^{2+} from environment even if an ion-exchange column had already been used to purify it.

Finally, low concentration was employed to diminish the aggregation and also competitive chelator EGTA was added to eliminate the residual pollutant calcium ion present in the environment (Figure 2.35). The fluorescence increased ~ 6.5 -fold by adding Ca^{2+} but sequentially decreased after overdosing Ca^{2+} , which might be due to the aggregation of calcium ion and **BANI** interaction network. Indeed, EGTA proved an important additive to enhance switching the probe off-on.

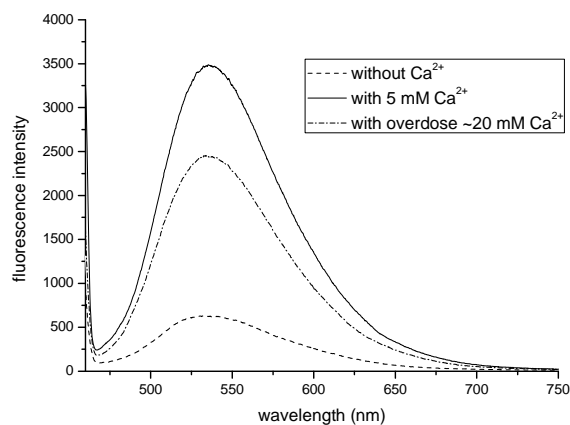


Figure 2.35 BANI (1 μM), 3-(N-morpholino)propanesulfonic acid (MOPS, 30mM), KCl (100mM), EGTA (10mM), pH=7.2 in milli-Q water solution with or without adding CaCl_2

2.3.1.3 Spectral measurement of product BANI2

After hydrolysis by strong base KOH, the emission enhancement as adding CaCl_2 into $1\mu\text{M}$ **BANI2** in milli-Q water without other additive as MOPS (3-(N-morpholino)- propanesulfonic acid) or KCl was verified. The fluorescence increased around 4 times and the emission profiles appeared to contain an artifact (Raman band) showing that absolute fluorescence intensity is low (Figure 2.36).

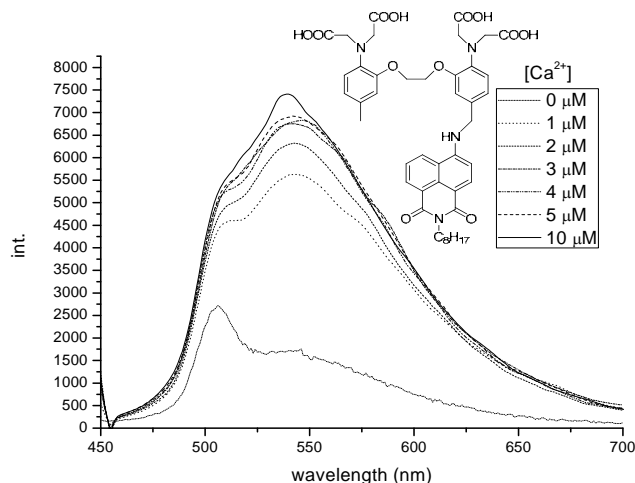


Figure 2.36 Fluorescence emission spectra after hydrolysis by KOH, **BANI2** (1 μM) in Milli-Q water with different concentrations of CaCl_2

Due to the unexpectedly low fluorescence enhancement, it was concluded that the hydrolysis procedure needed to be optimized. Perhaps the strong basic conditions caused some damage to the molecule. Therefore, milder base $\text{LiOH}\cdot\text{H}_2\text{O}$ was used instead of KOH and the absorption and emission spectra and switching on the fluorescence on adding calcium was retested (Figure 2.37).

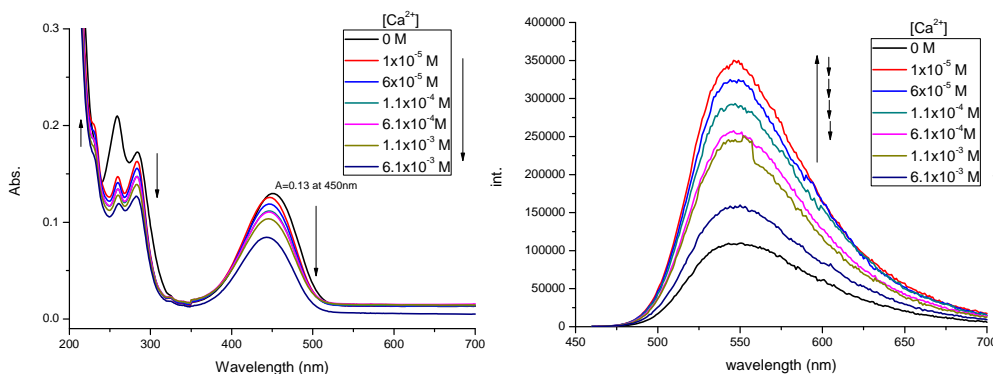


Figure 2.37 Electronic absorption spectra (left) and fluorescence emission (right) spectra of **BANI2** in Milli-Q water with different concentrations of Ca²⁺ after hydrolysis with LiOH:H₂O base

After this quick test of adding Ca²⁺ into the **BANI2** Milli-Q water solution, we observed that the fluorescence increases 3.2-fold at 550 nm. The off-on switching was anticipated to be higher, so in order to know the intrinsic photophysical character of **BANI2** in different solvating environments we tested the absorption and emission spectra of **BANI2** at different concentrations in the methanol (Figure 2.38a & b) and water (Figure 2.39a & b).

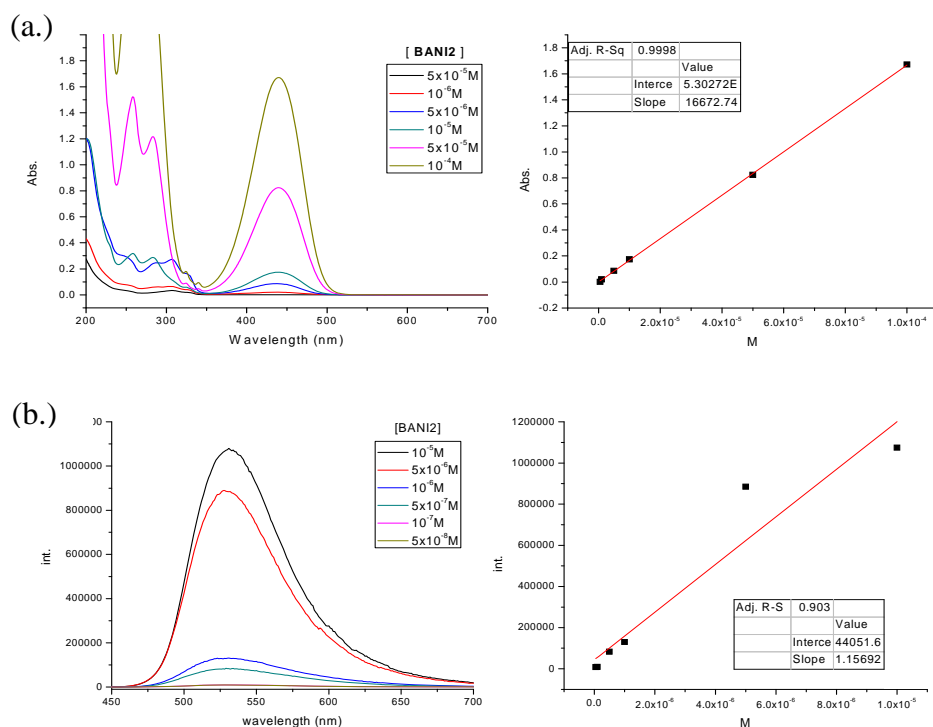


Figure 2.38 (a) Electronic absorption spectra of **BANI2** in methanol and profile of concentration vs. absorption at 445 nm; (b) emission spectra and profile of concentration vs. emission intensity at 545 nm

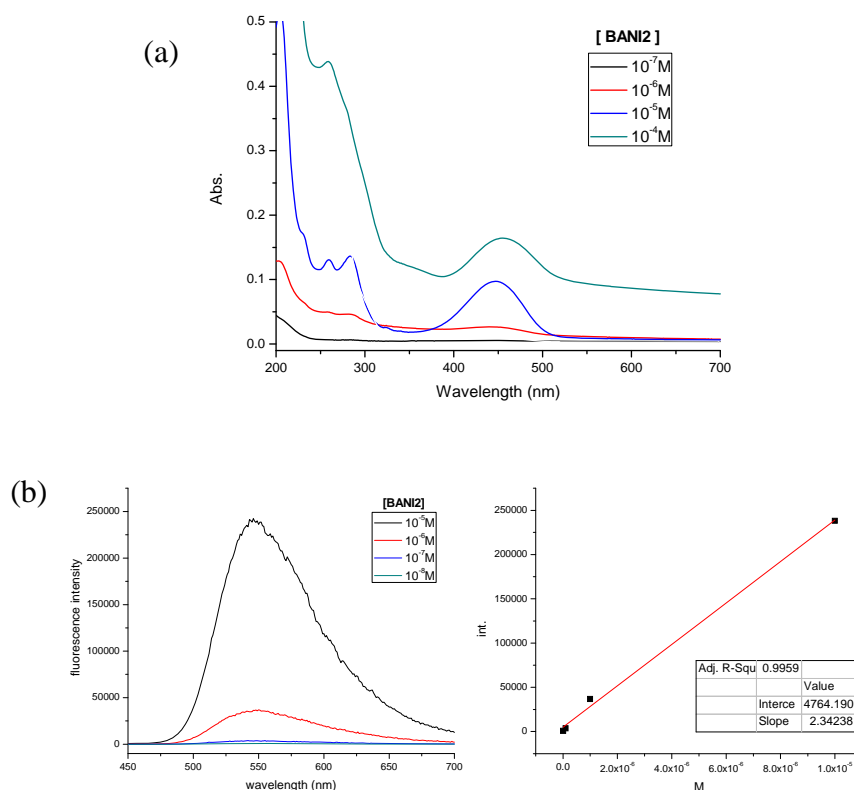


Figure 2.39 (a) Electronic absorption spectra of **BAN12** in milli-Q water; (b) emission spectra and profile of concentration vs. emission intensity at 545 nm

Comparing the results of **BAN12** in the methanol and water, we found that **BAN12** also tends to aggregate in water as in the case of product **BANI** and therefore leads to the baseline increase as raising the concentration. In the absorption spectra of **BAN12** in methanol or water solution, they showed two main spectral absorption bands 260-300 nm, assigned to the π - π^* transition, and a second band centered at 445 nm with extinction coefficient ($\epsilon = 1.67 \times 10^4 \text{ M}^{-1} \text{ cm}^{-1}$ obtained from the data of methanol solution) exactly the same with compound **BANI**. This structureless low energy absorption band is assigned to the fluorophore which shows internal charge transfer (ICT) character, arising due to the push-pull nature of the electron donating amine and the accepting withdrawing diimide.

As in the case of **BANI**, adding buffers helped the probe switch-off/on. Therefore we further performed the **BAN12** 10 μM water solution containing MOPS (30 mM), KCl (100 mM) to maintain the pH and ionic strength respectively and EGTA (10 mM) to switch off the fluorescence by eliminating the pollutant in the environment. In this way, the fluorescence could be completely switched-off by using EGTA in the beginning and then switched on about 67 times by gradually adding Ca^{2+} as shown in Figure 2.40.

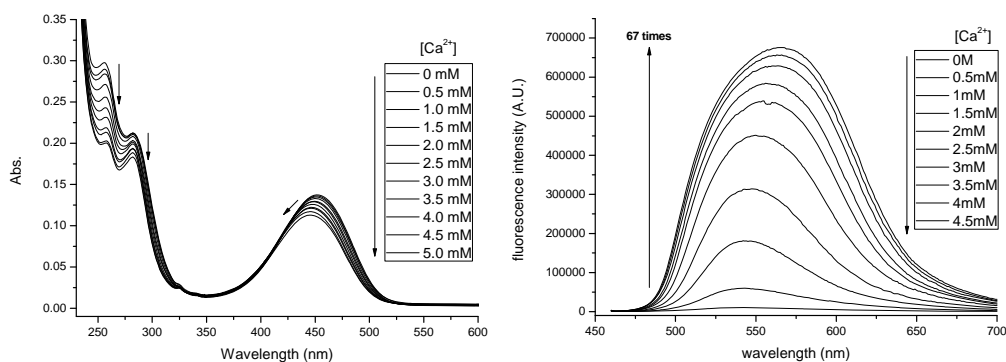


Figure 2.40 Electronic absorption spectra (left) and emission spectra (right) of calcium titration of **BAN12** in water at pH 7.2. [**BAN12**] = 10 μ M; [MOPS] = 30 mM; [KCl] = 100 mM; [EGTA] = 10 mM

To fully understand the origin of the enormous fluorescence switch difference with or without buffer, we performed the experiment stepwise, adding KCl, MOPS, and EGTA to observe which additive is crucial to help the fluorescence reaching maximum. As shown in Figure 2.41, we found only when EGTA was in the solution could the fluorescence be switched off and re-switched on, and have the fluorescence enhancement reached 124 times increase on adding Ca^{2+} .

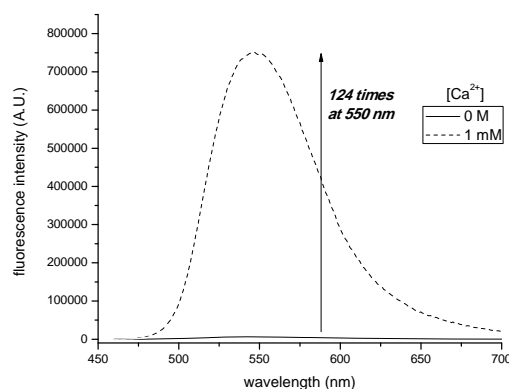


Figure 2.41 Emission spectra of **BAN12** (10 μ M) solution in presence of EGTA (10 mM) at pH 7.2 at different CaCl_2 concentrations

As a result it was confirmed that EGTA is the key additive to fully switch off/on the calcium probe molecule even if Milli-Q water is used to minimize the metal pollutants or the product was pre-treated and purified by strong acid ion-exchange column to eliminate the chelated alkaline earth metals or other heavy metals. As such this has to be taken into consideration in the implementation of the ion-shuttle.

Additionally **BAN12** is an unknown fluoroionophore having a C_8 -alkyl chain as hydrophobic part and comparatively Ca^{2+} -chelating site as hydrophilic part which leads to unusual photophysical behavior. For this reason, the pH titration was performed to study the

possible phenomenon such as aggregation, PET, etc. in the condition with or without EGTA trying to understand why EGTA could be the crucial additive in the switching-on/off of the probe.

As the absorption spectra of pH titration of 10 μM **BANI2** (Figure 2.42), one can see the compound in the basic pH range from 12 to 7 is not changing in Figure 2.42a, but the baseline at 600 nm and absorption band of the chromophore at 450 nm would change in the range pH 6 to 1.5 in Figure 2.42b. After the comparison of pH vs. absorption at 445 nm and 600 nm in Figure 2.42c & d, it was found that on gradually acidifying below pH = 6 the compound seemed to aggregate because of the baseline increase and the broadening while accompanying the decrease of the chromophore absorption band at 445 nm.

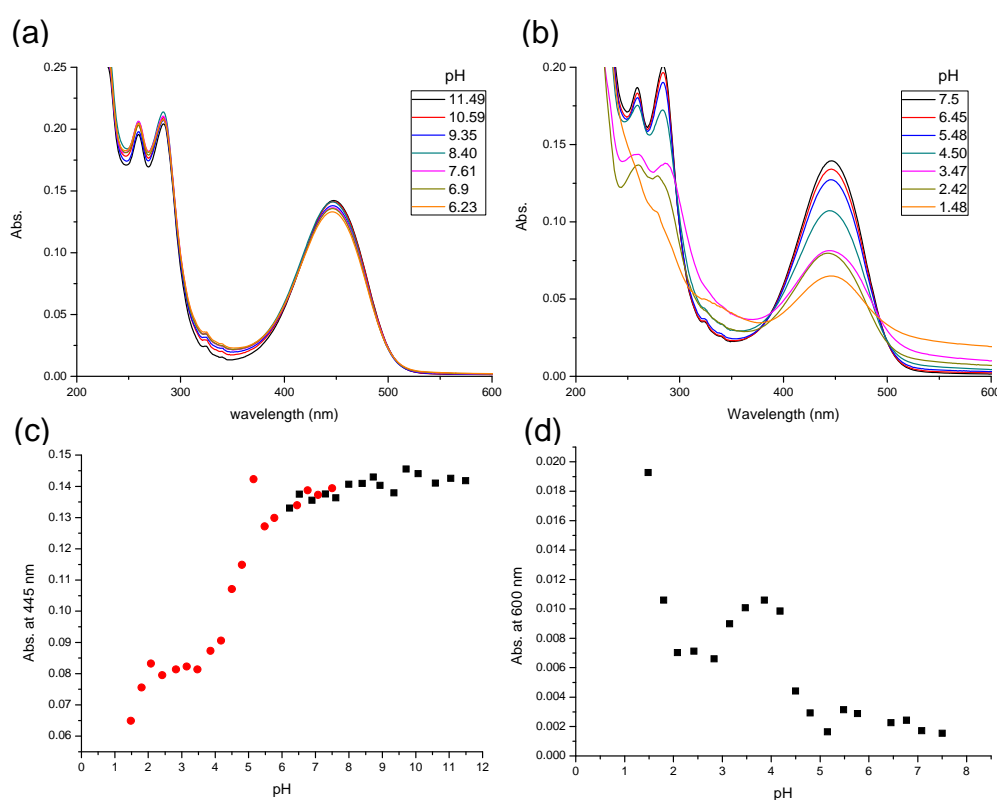


Figure 2.42 (a, b) Electronic absorption spectra of pH titration of **BANI2** ($c = 10 \mu\text{M}$); (c) chromophore absorption vs. pH at 445 nm, and (d) baseline changing at 600 nm

As for emission spectra (Figure 2.43), the fluorescence was already switched-on above pH = 6 and kept decreasing on acidifying the solution. It was not what we expected but is consistent with the results obtained in the case of **BANI**.

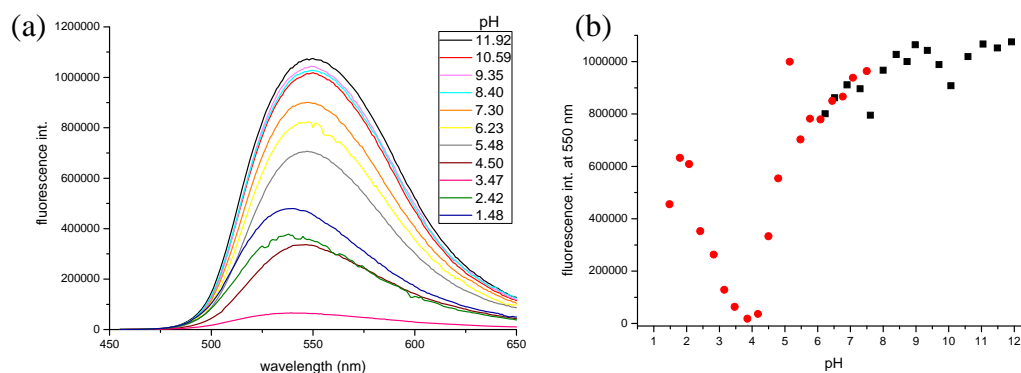


Figure 2.43 (a) Emission spectra of pH titration of **BANI2** ($c = 10 \mu\text{M}$) and (b) fluorescence intensity at 550 nm vs. pH

On the other hand, it is informative to determine what will happen when EGTA is present as an additive in the pH titration experiment. In the UV-Vis spectra of pH titration of $10 \mu\text{M}$ **BANI2** in the presence of 10 mM EGTA (Figure 2.44), we found the compound in the pH range from 12 to 5 presented no changes in absorption (Figure 2.44a), but from pH 5 to 1.5 (Figure 2.44b) the baseline and absorption band at 450 nm of the chromophore would shift. After the comparison of pH vs. absorption at 445 nm (chromophore part) and 600 nm (baseline) in Figure 2.44c & d, we found that in acid conditions below $\text{pH} = 5$, compound **BANI2** seemed to aggregate because of the baseline increase and at the same time the broadening and decrease of the absorption band at 445 nm. So the absorption trend basically is the same no matter whether the EGTA is present or not.

However, the observed hypsochromic shift in absorbance ~ 450 nm region upon titration with acid can be explained by the ICT excited state of the naphthalimide chromophore, which places a partial positive charge on the 4-amino moiety. This creates a repulsive interaction with the protonated *N*-acetate moiety of the chelator BAPTA part thus shifting the absorption spectra to lower wavelength.¹⁵

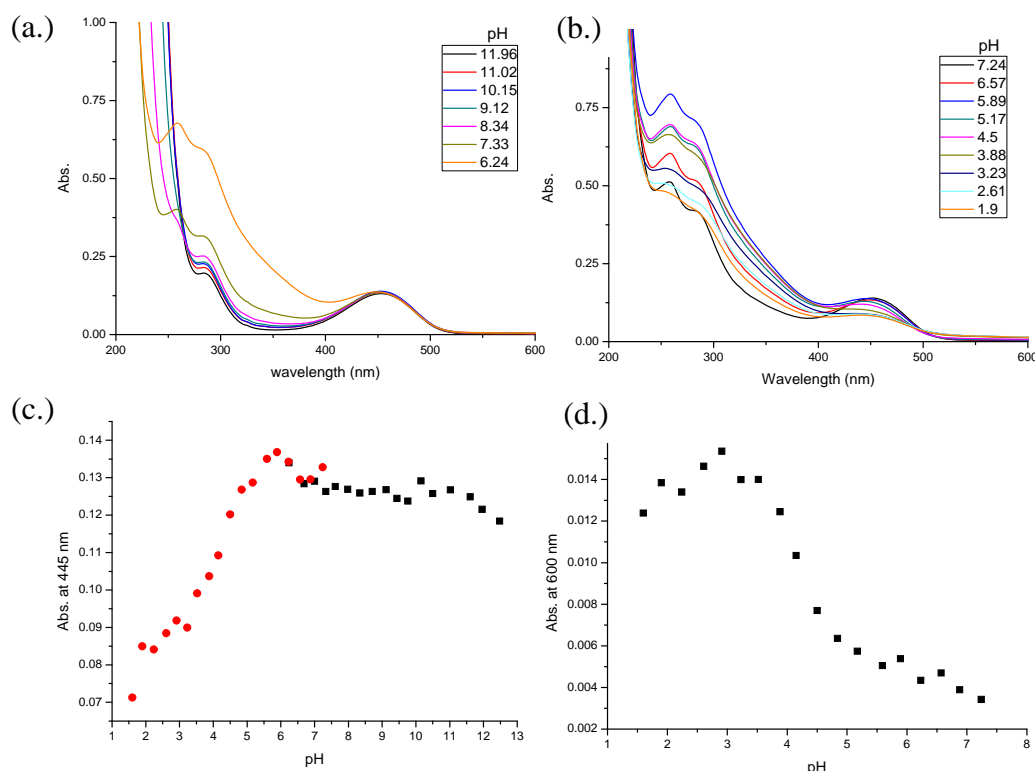


Figure 2.44 Electronic absorption spectra of pH titration of **BAN12** ($c = 10 \mu\text{M}$) in the presence of EGTA (10 mM) in basic range (a), acid range (b); Abs. vs. pH at 445 nm (c), baseline changing at 600 nm (d)

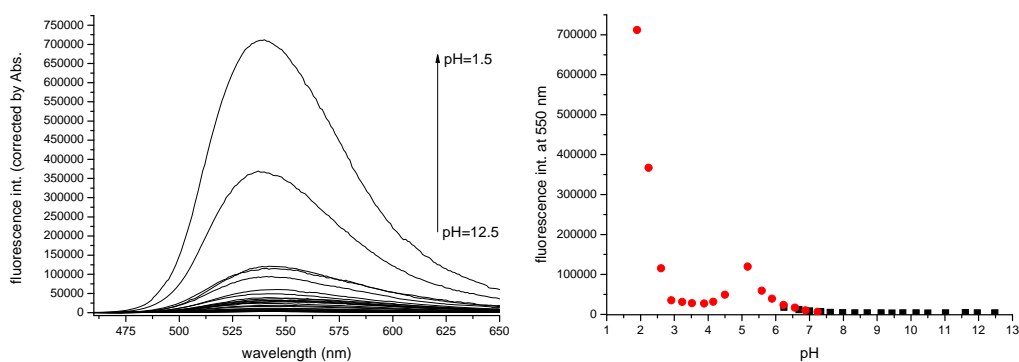


Figure 2.45 Emission spectra of pH titration of **BAN12** (10 μM) in presence of EGTA (10 mM) in the water (left), and fluorescence intensity at 550 nm vs. pH (right)

In the emission spectra of pH titration to **BAN12** with EGTA as additive on excitation of the ICT band at 450 nm (Figure 2.45), the ICT emission was observed at a long wavelength between 500–700 nm, with λ_{max} at 545 nm. The changes in the emission spectra of **BAN12** demonstrate that the observed emission is highly pH dependent; being “switched on” upon acidification, with large fluorescent enhancement. These changes were found to be reversible at $\text{pH} > 2.7$ (lower than 2.7 would damage the compound), demonstrating the suppression of any PET quenching from the electron rich receptor to the naphthalimide fluorophore upon

protonation of the aniline nitrogen of BAPTA chelator, which increases the oxidation potential of the receptors and hence makes PET thermodynamically unfavorable.

After the pH titration of the condition with or without EGTA, we observed certain differences when EGTA was added, which could explain the importance of EGTA in the switch-on/off ability in this Ca^{2+} probe system.

To quantitatively determine the affinity of **BANI2** towards free calcium, a buffered solution of **BANI2** (1 μM) containing 30 mM MOPS, 100 mM KCl and 10 mM EGTA was prepared (Figure 2.46) (Note. general procedure for the determination of K_d is described in the Chapter 5 Experimental Section).

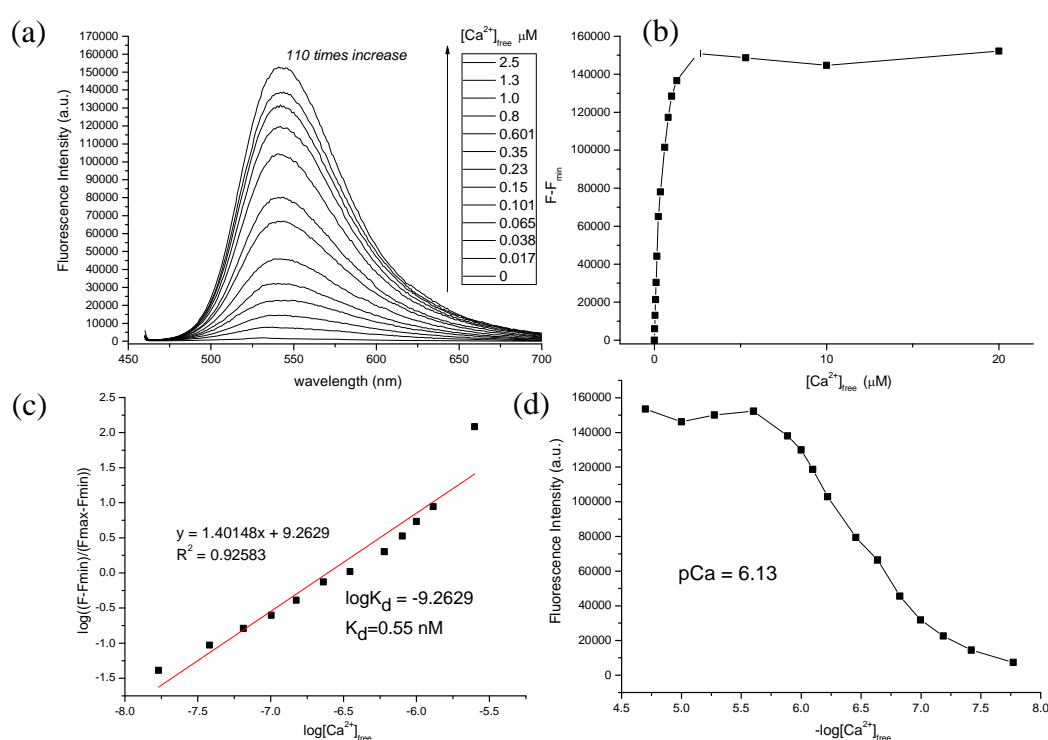


Figure 2.46 (a) Emission spectra of **BANI2** (1 μM) in MOPS (30 mM), KCl (100 mM), EGTA (10 mM) buffer at pH 7.2 in the presence of varying amounts of free Ca^{2+} . ($\lambda_{\text{ex}} = 450 \text{ nm}$) (b) Fluorescence intensity at 545 nm on varying amounts of free Ca^{2+} . (c) Hill plot for the complexation of **BANI2** with free Ca^{2+} . (d) Fluorescence titration curve for complexation with $-\log[\text{Ca}^{2+}]_{\text{free}}$

As shown in the graph, the fluorescence emission response was significantly affected, being switched on with fluorescence enhancements of 110-fold due to the blocking of the PET process by the complexation with the metal ion. From the Hill plot, for fluorescence changes a dissociation constant, K_d , was obtained as 0.55 nM, and also 1:1 stoichiometry for complexation between **BANI2** and Ca^{2+} was indicated.

2.3.1.4 Spectral measurement of product BANI3

The new Ca^{2+} -probe molecular **BANI3** (Figure 2.47) was synthesized in the similar way as **BANI2**. While a short ethyl chain connected to the chromophore, it was anticipated the switch-on/off ability would not be affected by aggregation as observed in the **BANI** or **BANI2** system. On the other hand, it is also designed to allow comparison of how the alkyl chain length would affect the character of the probes when they are confined in vesicles.

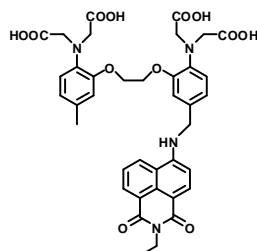


Figure 2.47 BANI3

For **BANI3**, the extinction coefficient was $1.48 \times 10^4 \text{ M}^{-1} \text{ cm}^{-1}$, calculated by the fitting shown in Figure 2.48.

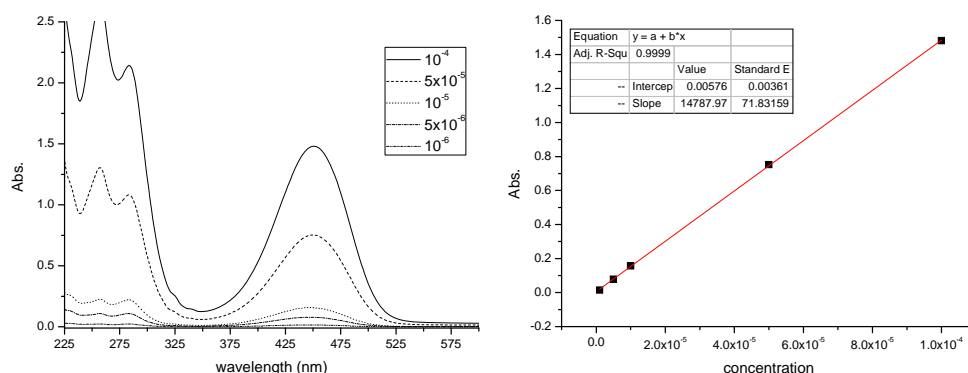


Figure 2.48 Electronic absorption spectra of different concentrations of **BANI3** in Milli-Q water

The affinity of **BANI3** towards free calcium was determined, on titrating a buffered solution of **BANI3** ($1 \mu\text{M}$) containing MOPS (30 mM), KCl (100 mM) and EGTA (10 mM) with Ca^{2+} (Figure 2.49). As shown in the graph, the fluorescence emission was switched on with fluorescence enhancement of 116-fold. By plotting the Hill plot using these changes a dissociation constant, K_d , was obtained as 5 nM. Also for Ca^{2+} binding with slopes ~ 1 indicated 1:1 complexation between **BANI3** and metal ion.

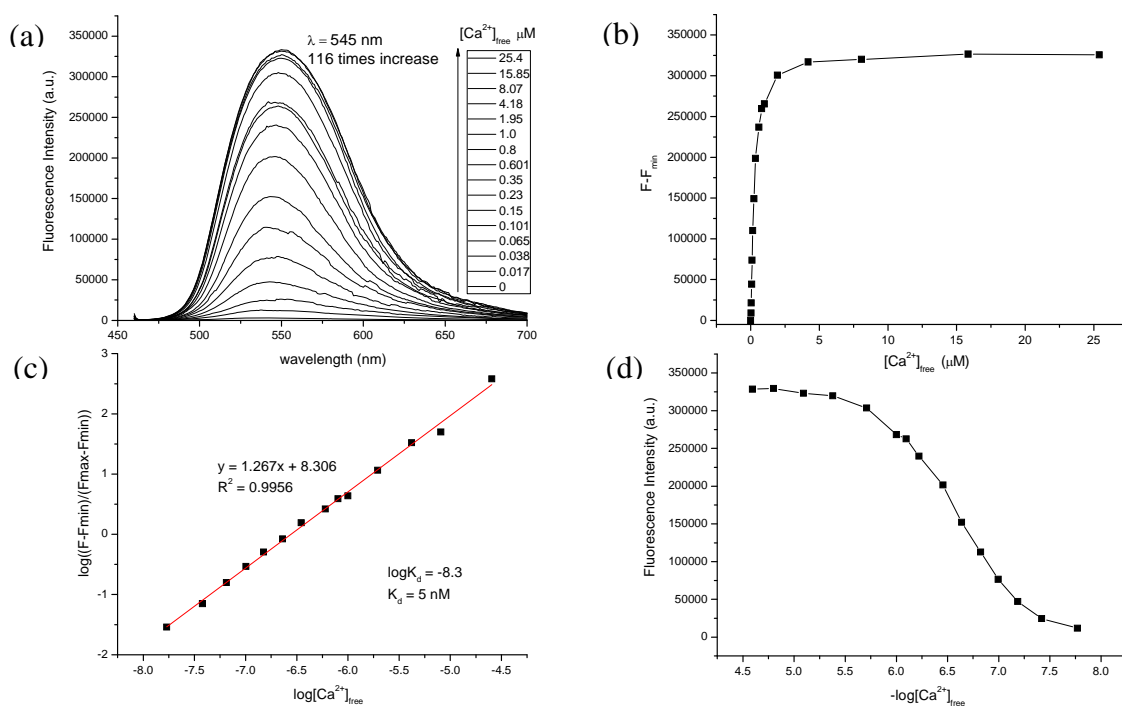


Figure 2.49 (a) Emission spectra of 1 μM **BANI3** in presence of MOPS (30 mM), KCl (100 mM), EGTA (10 mM) buffer at pH 7.2 in the presence of varying amounts of free Ca²⁺. ($\lambda_{\text{ex}} = 450 \text{ nm}$) (b) Fluorescence changes at 545 nm on complexing free Ca²⁺. (c) Hill plot for the complexation of **BANI3** with free Ca²⁺. (d) Fluorescence as a function of $-\log[\text{Ca}^{2+}]_{\text{free}}$

2.3.1.5 Solvent effects on BANI2 & BANI3

While the solvent polarity changes, the maxima of absorption and emission bands shift also. The positions, intensities and shapes of absorption and emission spectra can show the changes under the influence of the solvent surrounding the solute. The absorption and emission spectra of **BANI2** or its precursor ester-form compound **38** in different solvents showed gradual red shifts with the solvent polarity from non-polar to polar solvent (Figure 2.50) & (Table 2.4).

As shown in the figure and the data in Table 2.4, the quantum yield and fluorescence intensity in the low polarity solvents is lower due to the low solubility. Besides, by increasing the polarity of solvent, the red shifts of absorbance (397~450 nm) and emission (467~546 nm) are ca. 50 nm and 79 nm ($\Delta\omega = 3000 \text{ cm}^{-1}$ and 3100 cm^{-1} for absorption and emission, respectively). Therefore, the solvent effect to the absorption and emission shows the utility of **BANI2** as a polarity probe, which would give information about the location of the probe, i.e. in polar aqueous or less polar membrane. Also, the comparison of switch-on/off ability of **BANI2** by the difference of quantum yields shows the complexation with Ca²⁺ can increase the quantum yield in Milli-Q water about 480-fold.

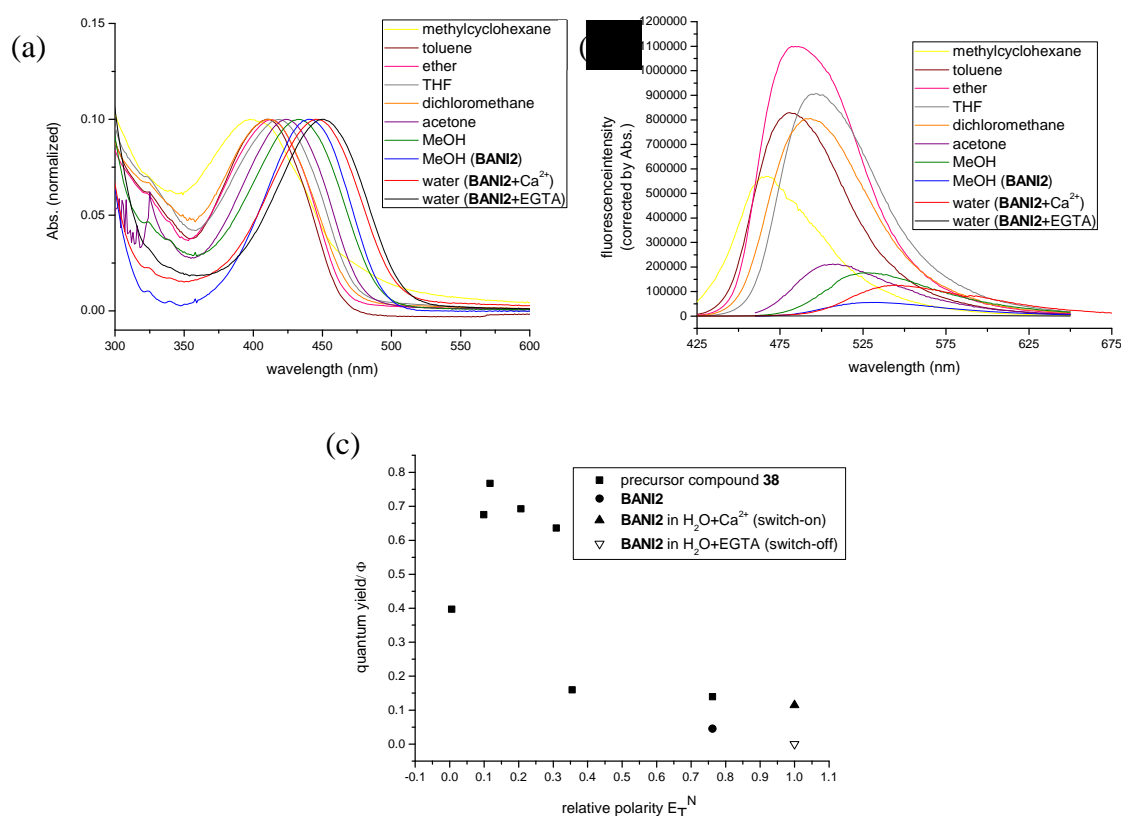


Figure 2.50 (a) Normalized electronic absorption spectra, (b) emission spectra corrected for absorption (c) quantum yield value as a function of the E_T^N (normalized values of $E_T(30)$ scale³⁰: with the help of the negative solvatochromic pyridinium-*N*-phenolate betaine dye $E_T(30)$ it was possible to measure the polarity of nearly 400 different solvents, through the longest-wavelength Vis/NIR absorption band at 25 °C and 1 bar if not otherwise mentioned. High $E_T(30)$ -values correspond to high solvent-polarity and vice versa) For these three graphs, the solvents methylcyclohexane, toluene, diethyl ether, tetrahydrofuran, dichloromethane, acetone, methanol are used for precursor compound **38**; methanol, water+ Ca²⁺ (1:1 to compound), water+ EGTA (10 mM) are used with **BANI2**.

Solvent (E_T^N)	compound 38 (ester-form precursor of BANI2)							BANI2 (hydrolyzed)		
	methyl-cyclohexane (0.006)	Toluene (0.099)	Ether (0.117)	THF (0.207)	CH ₂ Cl ₂ (0.309)	Acetone (0.355)	methanol (0.762)	methanol (0.762)	H ₂ O + Ca ²⁺ (1.000)	H ₂ O+ 10mM EGTA
quantum yield Φ^*	0.397	0.675	0.767	0.693	0.636	0.16	0.14	0.046	0.115	2.4x10 ⁻⁴
λ_{max} / nm (UV/Vis.)	397	411	413	411	418	423	432	441	446	450
λ_{max} / nm (emission)	467	480	484	497	493	507	526	530	545	546

Table 2.4 Photophysical properties of **BANI2** (or its precursor **38**) in various solvents (* the uncertainty of fluorescence quantum yield is $\pm 10\%$).

As for **BANI3** or its precursor ester-form compound **42** also showed gradual red shifts with the solvent polarity from non-polar to polar solvent (Figure 2.51). The data is tabulated in

Table 2.5.

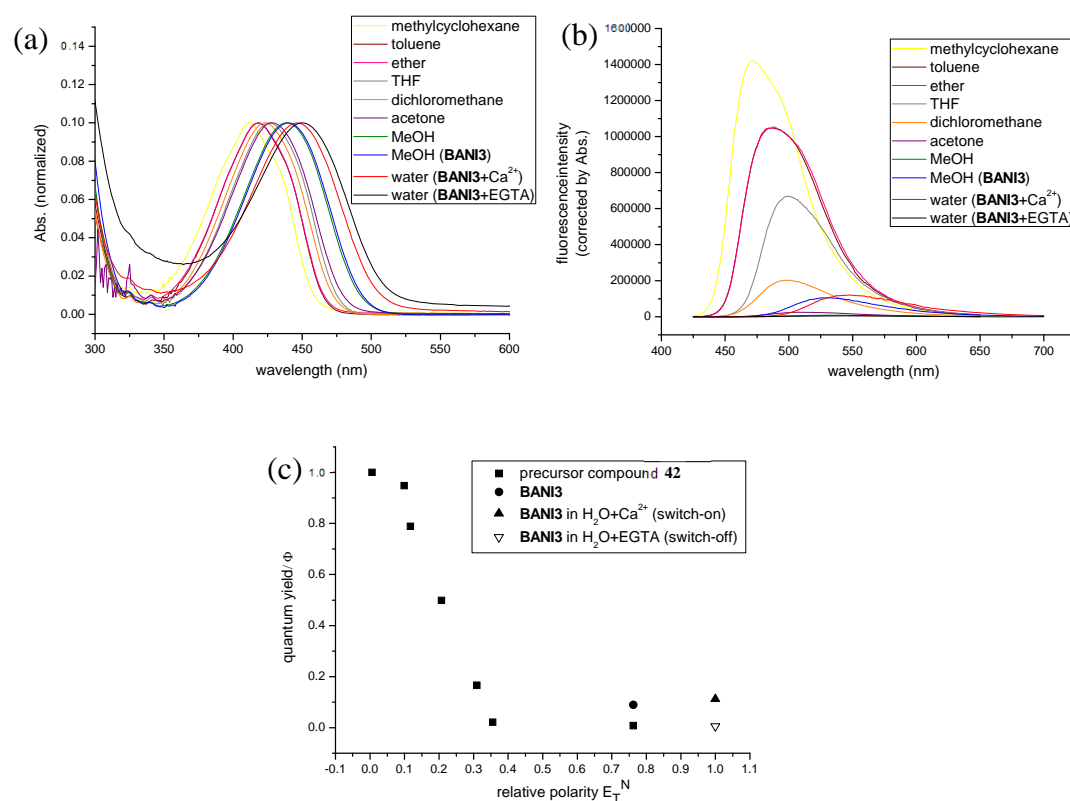


Figure 2.51 (a) Normalized electronic absorption spectra, (b) emission spectra corrected for absorption (c) quantum yield value as a function of the E_T^N (normalized values of ET(30) scale). For these three graphs, the solvents methylcyclohexane, toluene, diethyl ether, tetrahydrofuran, dichloromethane, acetone, methanol are with precursor compound **42**; methanol, water+ Ca^{2+} (1:1 to compound), water+ EGTA (10 mM) are with **BANI3**

Solvent (E_T^N)	compound 42 (ester-form precursor of BANI3)							BANI3 (hydrolyzed)		
	methyl-cyclohexane (0.006)	Toluene (0.099)	Ether (0.117)	THF (0.207)	CH_2Cl_2 (0.309)	Acetone (0.355)	methanol (0.762)	methanol (0.762)	$\text{H}_2\text{O} + \text{Ca}^{2+}$ (1.000)	$\text{H}_2\text{O} + 10\text{mM}$ EGTA
quantum yield Φ^*	1.0	0.948	0.789	0.499	0.166	0.021	0.008	0.09	0.112	0.005
λ_{max} / nm (UV/Vis.)	413	418	418	422	426	429	438	440	446	451
λ_{max} / nm (emission)	470	488	488	500	501	512	529	529	548	546

Table 2.5 Photophysical properties of **BANI3** (or its precursor) in various solvents (* The uncertainty of fluorescence quantum yield is $\pm 10\%$).

As shown in the figure and table, the effect was greater for the emission (~ 76 nm, $\Delta\omega = 2960$ cm^{-1}) than absorption spectra (~ 38 nm, $\Delta\omega = 2040$ cm^{-1}), thus indicating the utility of **BANI3** as a more polarity probe. In order to demonstrate this, it is necessary to estimate the change in the dipole moment from the ground state to the excited state ($\Delta\mu$).

The solvent effect arises the dipole moment of the molecules can be affected by the dipole moment of the solvents. The relationship between the Stokes shifts and the changes of the dipole moment of the molecule can be approximated to the energy difference (in cm^{-1}) which is a property of the refractive index (n) and dielectric constant (ϵ) of the solvent, and is described by the Lippert- Mataga equation:³¹

$$\Delta\nu = \nu_A - \nu_F = \frac{2}{hca^3} \left[\left(\frac{\epsilon-1}{2\epsilon+1} \right) - \left(\frac{n^2-1}{2n^2+1} \right) \right] (\mu_E - \mu_G)^2 \quad \text{Equation 2.1}$$

$$\Delta f = \left(\frac{\epsilon-1}{2\epsilon+1} \right) - \left(\frac{n^2-1}{2n^2+1} \right) \quad \text{Equation 2.2}$$

In this equation h ($= 6.6256 \times 10^{-27}$ ergs) is Planck's constant, c ($= 2.9979 \times 10^{10}$ cm/s) is the speed of light, and a is the radius of the solvent cavity in which the fluorophore resides (Onsager cavity radius) (3.61×10^{-8} cm was taken as half of the average size of naphthalimide moiety)³², ν_A and ν_F are the maxima of the absorption and emission in wavenumbers (cm^{-1}), respectively. The solvent sensitivity of a fluorophore can be estimated further by a Lippert plot as represented in Figure 2.52a for **BANI2** and its precursor, and in Figure 2.52b for **BANI3** and its precursor, and in Figure 2.53 for test compound **34** which bears a comparative phenyl ring generally giving a larger charge separation and higher solvent sensitivity. The data are represented in Table 2.6. These are the plot of $(\nu_A - \nu_F)$ versus the orientation polarizability (Δf) which is the term of Equation 2.2. The most sensitive fluorophores are those with the largest change in dipole moment upon excitation.

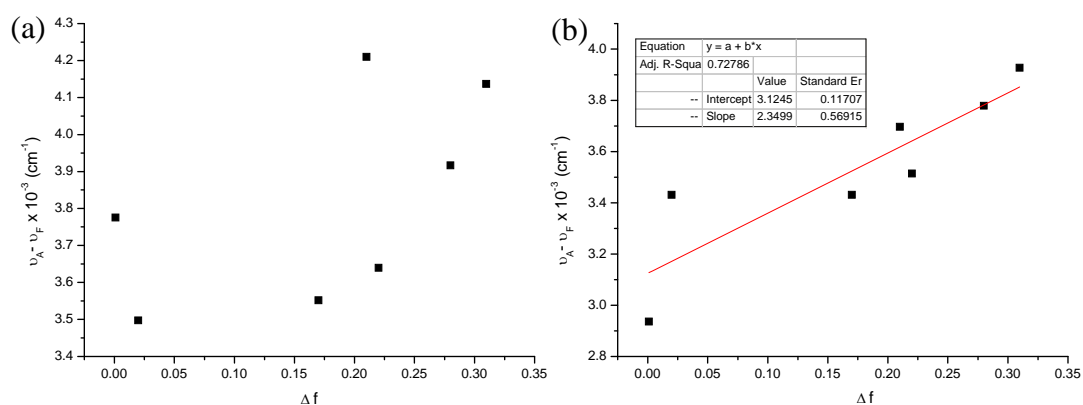


Figure 2.52 Lippert plot of $(\nu_A - \nu_F)$ versus the orientation polarizability (Δf) of **BANI2** (a), **BANI3** (b)

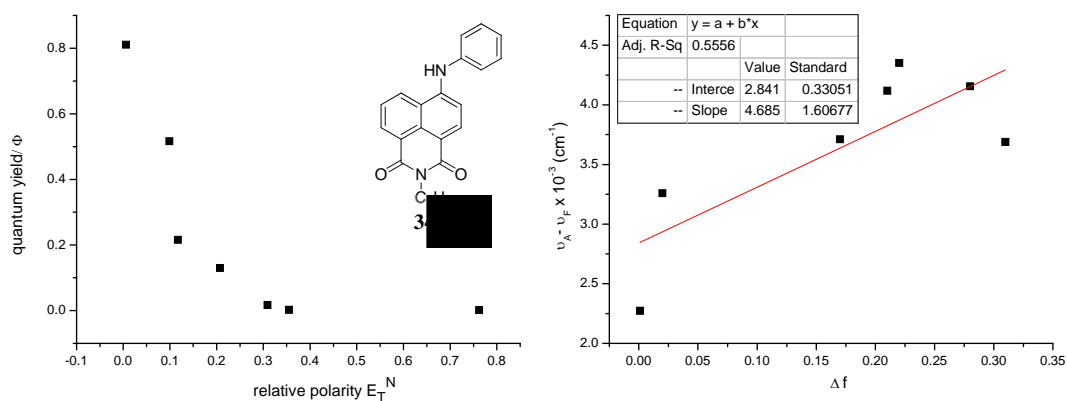


Figure 2.53 Test compound **34**: (a) quantum yield value as a function of the E_T^N , (b) Lippert plot of $(\nu_A - \nu_F)$ versus the orientation polarizability (Δf)

	Solvent (Δf)	Methyl cyclohexane (0.001)	Toluene (0.02)	Ether (0.17)	THF (0.21)	CH_2Cl_2 (0.22)	Acetone (0.28)	MeOH (0.3098)
 38 (Precursor of BANI2)	λ_{Abs} nm	397	411	413	411	418	423	432
	λ_{fluo} nm	467	480	484	497	493	507	526
	Φ_F	0.3973	0.6754	0.7672	0.6926	0.6358	0.1596	0.1395
	$\mu_A - \mu_G \times 10^{-3} \text{ cm}^{-1}$	3.7756	3.4976	3.5519	4.2102	3.6395	3.9168	4.1367
 42 (Precursor of BANI3)	λ_{Abs} nm	413	418	418	422	426	429	438
	λ_{fluo} nm	470	488	488	500	501	512	529
	Φ_F	1.0	0.948	0.7889	0.499	0.166	0.0213	0.008
	$\mu_A - \mu_G \times 10^{-3} \text{ cm}^{-1}$	2.9365	3.4316	3.4316	3.6967	3.5141	3.7788	3.9275
 34	λ_{Abs} nm	414	424	426	433	430	435	444
	λ_{fluo} nm	457	492	506	527	529	531	531
	Φ_F	0.811	0.517	0.216	0.13	0.017	0.00269	0.00203
	$\mu_A - \mu_G \times 10^{-3} \text{ cm}^{-1}$	2.2728	3.2597	3.7113	4.1194	4.3522	4.1561	3.6901

Table 2.6 Spectral properties of compound **38** (**BANI2** precursor), compound **42** (**BANI3** precursor) and test compound **34**

In Figure 2.52b the plot of $(\nu_A - \nu_F)$ versus Δf for **BANI3** is shown. From the slope (m) one can calculate the difference between the excited and ground state dipole moments. As given below in Equations 2.3:

$$m = \frac{2(\mu_E - \mu_G)^2}{hca^3} \quad \text{Equation 2.3}$$

The linearity of these plots is often regarded as evidence for the dominant importance of

general solvent effects in the spectral shifts. According to Lippert equations the difference of excited and ground state dipole moments of **BANI3** is found to be $10.48 D$ ($1D = 1.0 \times 10^{-18}$ esu cm), suggesting that the emission occurs from the locally excited state with large charge separation in the excited state. And the sensitivity of the fluorophore to solvent polarity is probably due to a charge shift from the amino group towards the electronegative imide group. As for test compound **34** the value is found to be $14.8 D$ which is bigger than **BANI3**, indicating that it is more sensitive to solvent polarity than **BANI3**. This result is expected due to the attachment of a phenyl group on the 4-amino-1,8-naphthalimide chromophore further increases the internal charge transfer in the excited state.

On the other hand, specific solvent effects lead to nonlinear Lippert plots as **BANI2** case, this could be caused from processes such as aggregation with probe-probe interactions leading to spectral variations.

2.3.1.6 Time-resolved fluorescence and transient absorption experiments

In order to look in more detail at the photophysical behavior of **BANI2** and **BANI3**, complementary preliminary pico- and femtosecond laser experiments were undertaken. Notably time-resolved fluorescence and transient absorption experiments were performed.

For the transient absorption experiments of **BANI3** in the absence of Ca^{2+} , complicated behavior of non-exponential decay kinetics was observed. This is related to fast processes including electron transfer through several pathways and solvent reorganization dynamics. Fluorescence emission also shows non-exponential decays. The observed fast non-exponential decay can be due to all of these factors. The following table shows several fast components for Ca^{2+} -free **BANI3** in different solvents including water, and their transient absorption are shown in Figure 2.54 & 55. The amine group of BAPTA makes hydrogen bonding in water and methanol, which possibly lowers the potential energy of the ground state of BAPTA. Thus observed decays have shorter lifetimes compared to acetonitrile. On binding calcium the situation is simplified and the data can be satisfactorily fitted to a monoexponential decay in the nanosecond rather than picosecond domain.

	Water (BANI3)	Methanol (BANI3)	Acetonitrile (compound 42 , precursor ester form of BANI3)
Without Ca^{2+}	1 ps, 26 ps, 190 ps	70 ps, 800ps, 5.5 ns	134 ps, 535 ps, 7ns
With Ca^{2+}	2.7 ns	5.5 ns	7ns

Table 2.7 Lifetime measurements of time-resolved fluorescence and transient absorption

The difference between corresponding components in the calcium-bound and calcium-free cases can give an estimation of the rate of intramolecular photoinduced electron transfer

according to the equation below (where τ and τ_0 represent the quenched and unquenched lifetime, respectively). Considering the longest component in the case without Ca^{2+} gives a lower value for the PET process.

$$k_{PET} = \frac{1}{\tau} - \frac{1}{\tau_0} \quad \text{Equation 2.4}$$

Thus a rate of PET of $> 4.9 \times 10^9 \text{ s}^{-1}$ can be estimated based on time-resolved fluorescence measurements.

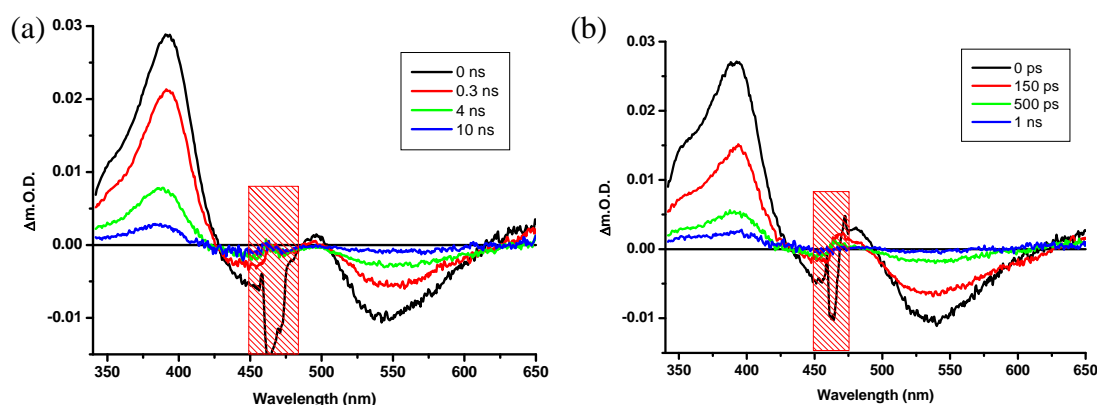


Figure 2.54 Transient absorption spectra of **BAN13** in methanol (a), and precursor ester form of **BAN13** (compound **42**) in acetonitrile (b) at different time delays in the absence of Ca^{2+} , see legend. $\lambda_{\text{ex}} = 460 \text{ nm}$. The rectangle region is the position where laser excites, which can be interfered.

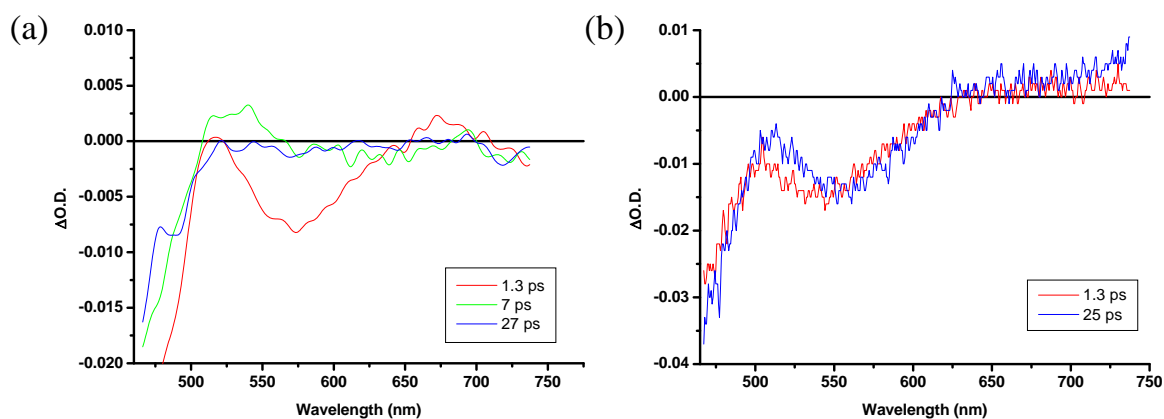


Figure 2.55 Transient absorption spectra of **BAN13** in water at different time delays in the absence (a) and presence (b) of Ca^{2+} , see legend. $\lambda_{\text{ex}} = 460 \text{ nm}$. Note. The stimulated emission band at 570 nm, faster decays in Ca^{2+} case compared to non- Ca^{2+} case. However In the presence of Ca^{2+} long components can be observed.

To summarize, similar behavior is observed in all three solvents (protic and non-protic),

particularly with regard to multiple short-lived components on the picosecond which become longer on binding calcium.

On the other hand, we also performed a preliminary measurement of **BANI2** in the DOPC small unilamellar vesicles (SUVs, about the introduction and preparation of vesicle will be detailed in Chapter 4). Through time-resolved fluorescence (Figure 2.56) we have observed non-monoexponential decay for the emission of **BANI2** in vesicle matrix. On fitting to a biexponential model the obtained lifetimes are $\tau_1=0.5$ ns and $\tau_2=5.2$ ns. By complex with Ca^{2+} , the fluorescence emission shows a mono-exponential decay with a lifetime of $\tau_1=8.4$ ns. The integrated fluorescence emission quantity represents a 200 % increase on addition of Ca^{2+} .

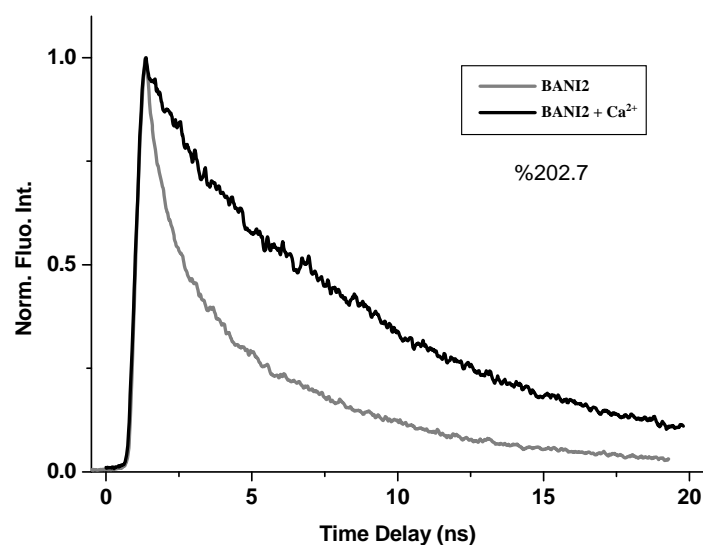


Figure 2.56 Fluorescence decay of **BANI2** in DOPC SUVs on exciting at 460 nm.

In the transient absorption experiment, the transient signal is perturbed by the non-homogeneity of the medium thus giving unusable spectra. Globally we can conclude that ion binding-induced switching of fluorescence is operational on the liposome bilayer as well as in homogeneous free solution.

2.3.2 Photophysical measurement of Ca^{2+} -donor molecules

For our goal to fabricate the photoinduced ion-shuttle system (which will be discussed in chapter 4), at first it is necessary to know the affinity change towards calcium before and after photolysis of the synthesized Ca^{2+} -donor molecules, **nitr-5** and **C15nitr-5**. Since **nitr-5** is a known compound described in the introduction, here we represent some measurements of the photophysical properties and effects of changing some experimental conditions for K_d determination which is adapted to the measurement environment of Ca^{2+} -acceptor compounds. For similar compound **C15nitr-5**, the same method was used to obtain the K_d value change

which could be further compared to **nitr-5** for implementation of the ion-shuttle in free aqueous solution or within a vesicle matrix.

2.3.2.1 Spectral measurements of **nitr-5**

The electronic absorption spectra of **nitr-5** with and without chelated with calcium ion and further photolyzed by irradiation with 365 nm UV light (see experimental part) for 15 minute as shown in Figure 2.57left. Before photolysis, the absorption spectra of **nitr-5** in the 330-400 nm region resembled that of an isolated nitropiperonyl group at 360 nm. Below 330 nm, the spectrum responded to the addition of Ca^{2+} , in a manner closely analogous to the response of the parent chelator, BAPTA, to Ca^{2+} . Thus the spectra of **nitr-5** before photolysis corresponds simply to the sum of the Ca^{2+} -insensitive absorbance of a nitropiperonyl group with a shorter-wavelength, Ca^{2+} -sensitive absorption spectrum of BAPTA. The observed simple superposition was expected because the BAPTA and the nitropiperonyl groups are linked through a saturated carbon atom, which should act as an electronic insulator.¹⁹

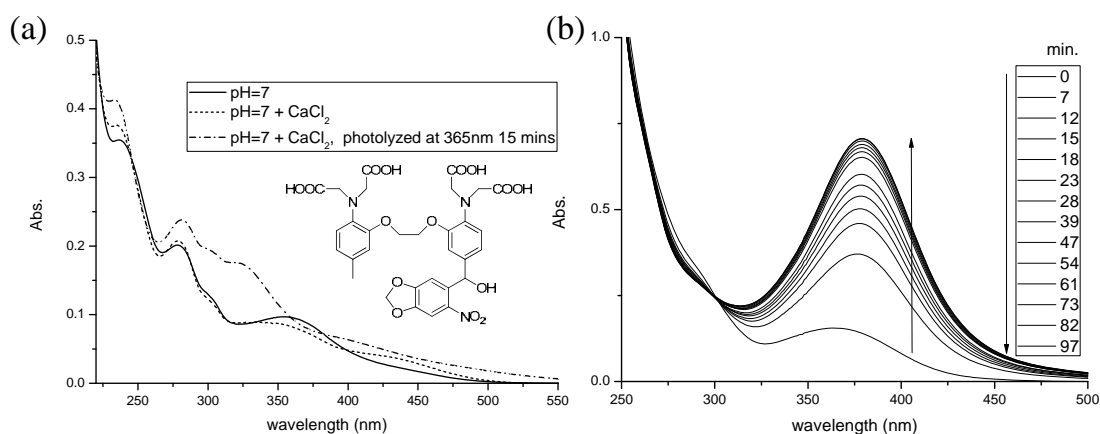


Figure 2.57 (a) Electronic absorption spectra of 1×10^{-5} M **nitr-5** alone, chelated with Ca^{2+} , and photolysis at 365 nm UV irradiation; (b) Photolysis of concentrated 3×10^{-5} M **nitr-5** solution without Ca^{2+} , then absorption spectra were collected at diluted 5×10^{-5} M solution

Photolysis increased the extinction coefficient of the 370 nm peak more than fourfold (Figure 2.57b). This increase is as expected for the generation of a benzophenone whose carbonyl group is in direct conjugation with the bis(carboxymethyl)amino group para to it. This large, long-wavelength UV absorbance should be diminished when Ca^{2+} binds (Figure 2.57a), since that would interfere with the ability of the amino group to donate electron density and conjugate with the carbonyl. Indeed, when **nitr-5** binds Ca^{2+} , the 370 nm absorbance was profoundly depressed, unlike that of **nitr-5** before photolysis.

The dissociation constant value for **nitr-5** published by Dr. Tsien et al was 0.145 μM and 6.3 μM after photolysis. The increase in the K_d value is about 40-fold for this molecule in 0.1

M KCl, 10 mM Tris·HCl, 10mM HEEDTA and at pH= 8.48. To measure the K_d value of this non-emissive compound, due to the detective limit of Electronic absorption spectrophotometer one need to use HEEDTA (2-[2-[bis-(carboxymethyl)amino]ethyl-(2-hydroxyethyl)amino]acetic acid) buffer instead of EGTA to obtain the bigger free $[Ca^{2+}]$ range (0 to 1400 μ M). In our case, we performed the K_d determination titration for unphotolyzed (Figure 2.58) and photolyzed (Figure 2.59) **nitr-5** (30 μ M) in 0.1 M KCl, 30 mM MOPS and 10 mM HEEDTA at pH= 7.3 aqueous solution. After the calculation by Hill-plot, we obtained the 1:1 complexation to calcium ion and K_d value were 0.4 nm and 17.2 after photolysis. The ΔK_d is about 43-fold, similar to the literature data.

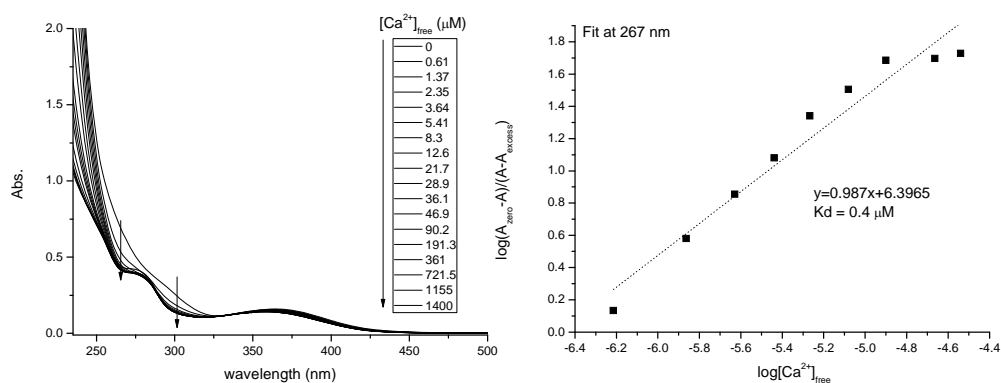


Figure 2.58 K_d determination: (left) electronic absorption spectra of **nitr-5** (30 μ M) in MOPS (30 mM), KCl (100 mM), HEEDTA (10 mM) buffer at pH 7.2 in the presence of varying amounts of free Ca^{2+} . (right) Hill plots for the variation of absorption at 267 nm accompanying complexation with free Ca^{2+}

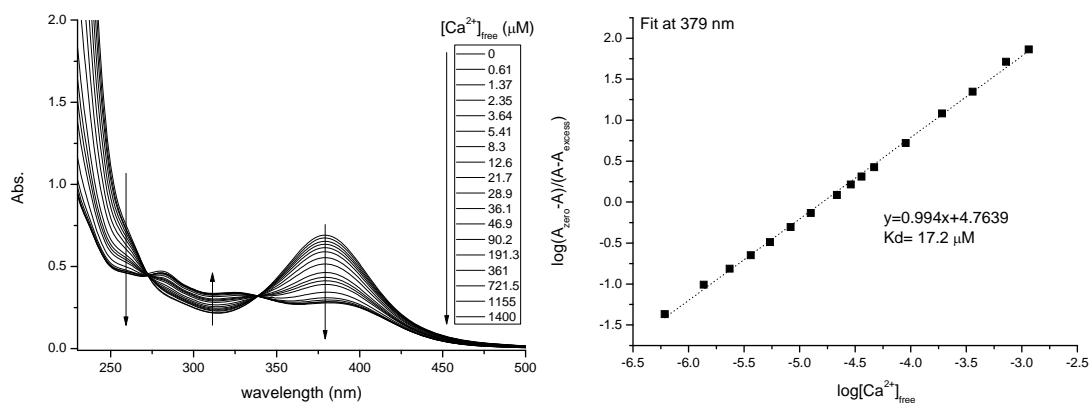


Figure 2.59 K_d determination: (left) electronic absorption spectra of photolyzed **nitr-5** (30 μ M) in MOPS (30 mM), KCl (100 mM), HEEDTA (10 mM) buffer at pH 7.2 in the presence of varying amounts of free Ca^{2+} . (right) Hill plots for the variation of absorption at 379 nm accompanying complexation with free Ca^{2+}

2.3.2.2 Spectral measurements of C15nitr-5

Since **C15nitr-5** is similar to **nitr-5** except for the presence of a long alkyl chain, it may be anticipated that the photophysical properties would be analogous in character to that described in the previous section. Before photolysis, the absorption spectra of **C15nitr-5** in the 330-400 nm region resembled that of an isolated nitropiperonyl group at 360 nm. Below 330 nm, the spectrum corresponded to the parent chelator, BAPTA (Figure 2.60). As seen in the figure, photolysis increased the extinction coefficient of the 370 nm peak about fourfold. This increase is expected and the same with **nitr-5**.

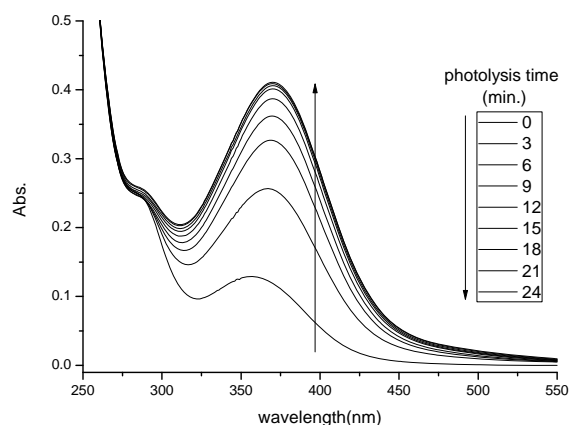


Figure 2.60 Electronic absorption spectra of photolysis of **C15nitr-5** (30 μM) in HEEDTA (10 mM), KCl (100 mM), and MOPS (30 mM) at pH 7.3

The dissociation constant value determination for **C15nitr-5** was also performed in the same manner as **nitr-5** in the previous section. The K_d determination titration for unphotolyzed and photolyzed **C15nitr-5** (30 μM) in 0.1 M KCl, 30 mM MOPS, 10 mM HEEDTA, and at pH= 7.3 aqueous solution are shown in Figure 2.61 & 2.62.

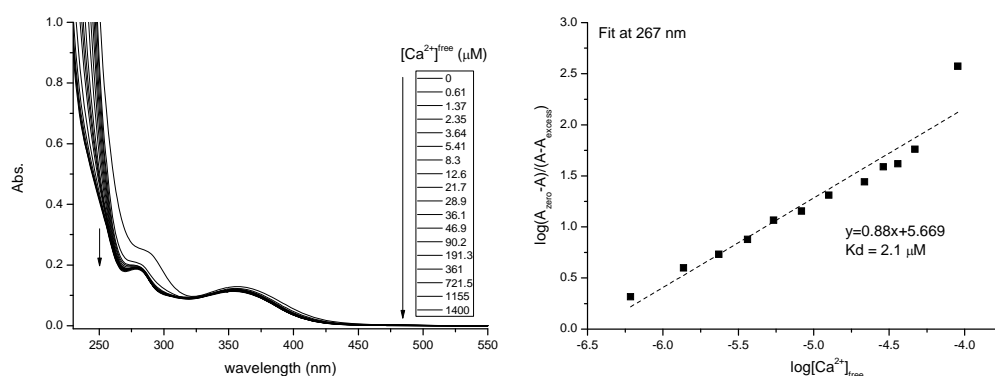


Figure 2.61 K_d determination: (left) Electronic absorption spectra of **C15nitr-5** (30 μM) in MOPS (30 mM), KCl (100 mM), HEEDTA (10 mM) buffer at pH 7.2 in the presence of varying amounts of free Ca^{2+} . (right) Hill plots for the variation of absorption at 267 nm accompanying complexation with free Ca^{2+}

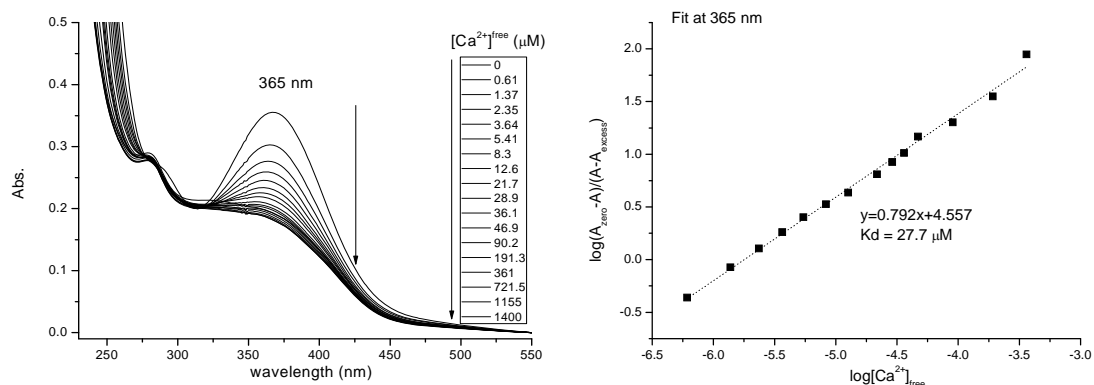


Figure 2.62 K_d determination: (left) Electronic absorption spectra of photolyzed **C15nitr-5** (30 μM) in MOPS (30 mM), KCl (100 mM), HEEDTA (10 mM) buffer at pH 7.2 in the presence of varying amounts of free Ca^{2+} . (right) Hill plots for the variation of absorption at 365 nm accompanying complexation with free Ca^{2+}

After Hill-plot, K_d values of 2.1 nM and 27.7 nM were obtained after photolysis (K_d increase is thus 13-fold). Comparing this result to **nitr-5** (K_d variation = 43-fold, 0.4 nM before & 17.2 nM after photolysis), it could be explained by:

1. Since the $-\text{OCH}_2\text{CH}_2\text{O}-$ carbon-carbon bond in BAPTA chelator is in anti-form in the absence of binding Ca^{2+} for a large proportion of molecules, in order to bind calcium ion by rotating to gauche-or eclipse-form would be harder with more rigid long hydrocarbon chain. Also the long alkyl chain could decrease the possibility for Ca^{2+} to approach due to a larger steric hindrance. As a result, the unphotolyzed K_d value of **C15nitr-5** (2.1 nM) is 5 times lower than **nitr-5** (0.4 nM).
2. Comparing the absorption performing of **nitr-5** and **C15nitr-5** after photolysis, in the profile of **nitr-5** one can see there are two isosbestic points at 273 and 339 nm, but not in the profile of **C15nitr-5**. It might be due to the accompanying of other mechanism such as forming aggregates by polarity decrease while chelating with calcium ion.

2.4 Conclusion

1. Five Ca^{2+} -acceptor fluorescence probes were successfully synthesized with parent BAPTA chelator, they are trial compounds **BAPTAant** and **C15BAPTAant** having an anthracene chromophore and **BANI**, **BANI2** and **BANI3** with naphthalimide as fluorophore. Different photophysical properties were anticipated for each type.
2. For the Ca^{2+} -donor, two photocontrolled calcium releasing products with and without a long alkyl chain were developed, which are the known **nitr-5** and unknown **C15nitr-5**.
3. For further usage in the photoinduced ion-shuttle system (Chapter 4), the dissociation constant K_d value of **BANI2** and **BANI3** Ca^{2+} -acceptors was determined, giving value of 0.55 nM and 5 nM with fluorescence switch-on/off ability at around 110-fold; as for Ca^{2+} -donors **nitr-5** and **C15nitr-5**, the K_d values of **nitr-5** are 0.4 nM and 17.2 nM after photolysis ($\Delta K_d = 43$ -fold) while **C15nitr-5** has $\Delta K_d = 13$ -fold, 2.1 nM before & 27.7 nM after photolysis).
4. Since the solvent effect plays an important role in governing the fluorescence quantum yield, dipole moment change and predicting the environment polarity when compartmentalized in vesicle matrix, absorption and emission measurements for **BANI2** and **BANI3** in different solvents were performed. The results showed these two fluoroionophores are polar probes and significantly sensitive to the solvent/environment polarity.
5. The aggregation phenomenon was found in many cases, for Ca^{2+} -acceptors **C15BAPTAant**, **BANI** and **BANI2** the switch-on/off abilities were found to be dramatically affected. On the other hand, aggregation also affected the Ca^{2+} -donor **C15nitr-5** binding of calcium ion which presented in smaller dissociation constant change resulting from photolysis.

2.5 References

1. A.P. de Silva, B. McCaughan, B.O.F. McKinney, M. Querol, *Dalton Trans.*, **2003**, 1902.
2. A.P. de Silva, S.A. de Silva, *J. Chem. Soc, Chem. Commun* **1986**, 1709.
3. G. De Santis, L. Fabbrizzi, M. Lichelli, C. Mangano, D. Sacchi, N. Sardone, *Inorg. Chim. Acta*, **1997**, 257, 69.
4. A.P. de Silva, H.Q.N. Gunaratne, K.R.A.S. Sandanayake, *Tetrahedron Lett.* **1990**, 31, 5193.
5. K. Golchini, M. Mackovic-Basic, S.A. Gharib, D. Masilamani, M.E. Lucas, I. Kurtz, *Am. J. Physiol.* **1990**, 258, F438.
6. M.E. Huston, K.W. Haider, A.W. Czarnik, *J. Am. Chem. Soc.* **1988**, 110, 4460.
7. L. Fabbrizzi, M. Lichelli, P. Pallavicini, A. Perotti, D. Sacchi, *Angew. Chem. Int. Ed. Engl.* **1994**, 33, 1975.
8. G.C.R. Ellis-Davies, *Chem. Rev.* **2008**, 108, 1603.
9. R.Y. Tsien, *Annu. Rev. Neurosci.* **1989**, 12, 227.
10. R.Y. Tsien, *Methods in Cell Biology*, **1989**, 30, 127.
11. L. Schouteten, P. Denjean, J. Faure, D. Pansu, C. Bernard, R. Pansu, *Chem. Phys.* **1999**, 1, 2463.
12. J.R. Lakowicz, H. Szmazinski, K. Nowaczyk, M.L. Johnson, *J. Fluoresc.* **1992**, 47.
13. B. Valeur, I. Leray, *Coordination Chemistry*, **2000**, 205, 3.
14. G. Grynkiewicz, M. Poenie, R. Y. Tsien, *J. Biological Chemistry*, **1985**, 6, 3440.
15. R. Parkesh, T.C. Lee, T. Gunnlaugsson, *Org. Biomol. Chem.*, **2007**, 5, 310.
16. Yu. A. Mednykh, Yu. A. Manaev, V.V. Volchkov, and B. M. Uzhinov, *Russian Journal of General Chemistry*, **2004**, 74, 1728.
17. J. Wang, Y. Xiao, Z. Zhang, X. Qian, Y. Yang and Q. Xu, *J. Mater. Chem.*, **2005**, 15, 2836.
18. R.Y. Tsien, R.S. Zucker, *Biophys. J.* **1986**, 50, 843.
19. S.R. Adams, J. P. Y. Kao, G. Grynkiewicz, A. Minta, R.Y. Tsien, *J. Am. Chem. Soc.* **1988**, 110, 3212.
20. J. H. Kaplan, G.C.R. Ellis-Davies, *Proc. Natl. Acad. Sci. U. S. A.* **1988**, 85, 6571.
21. G.C.R. Ellis-Davies, *Methods Enzymol.* **2003**, 360, 226.
22. S.R. Adams, V. Lev-Ram, R.Y. Tsien, *Chem. Biol.* **1997**, 4, 867.
23. E. Grell, E. Lewitzki, H. Ruf, E. Bamberg, G.C.R. Ellis-Davies, J.H. Kaplan, P. de Weer, *Cell. Mol. Biol.* **1989**, 35, 515.
24. O. Reany, T. Gunnlaugsson, D. Parker, *Perkin Trans.* **2000**, 2, 1819.
25. P.S. Mohan, C.S. Lim, Y.S. Tian, W.Y. Roh, J.H. Lee, B.R. Cho, *Chem. Commun*, **2009**, 5365.
26. F.H.C. Stewart, *Australian Journal of Chemistry*, **1960**, 13, 478.
27. F. Effenberger, S. Heid, R. Merkle, P. Zimmermann, *Synthesis*, **1995**, 1115.
28. S. Kemp, N.J. Wheate, D.P. Buck, M. Nikac, J.G. Collins, J.R. Aldrich-Wright, *J. Inorg.*

- Biochem*, **2007**, *101*, 1049.
29. A.P. de Silva, H. Q. Nimal Gunaratne, *J. Chem. Soc, Chem. Commun* **1990**, 186.
 30. (a) J.Y. Choi, E.J. Park, S.H. Chang, T.J. Kang, *Bull. Korean Chem. Soc.* **2009**, *30*, 1452.
(b) Z.W. Li, Q. Yang, R. Chang, G. Ma, M. Chen, W. Zhang, *Dyes and Pigments*, **2011**, *88*, 307.
 31. Joseph R. Lakowicz, *Principles of fluorescence spectroscopy third edition*, Springer, chapter 6.
 32. D.W. Choa, M. Fujitsuka, U.C. Yoon, T. Majimaa, *Journal of Photochemistry and Photobiology A: Chemistry*, **2007**, *190*, 101.

Chapter 3

Orientation and Morphology Study of BAPTA Compounds

in Films

As detailed in previous chapters, the BAPTA parent ionophore is mainly utilized in our photoinduced Ca^{2+} -donor / acceptor system. In order to assess and understand the relative efficiency and ion-chelating behavior of intermolecular ion transfer accompanying complexation and decomplexation in solution and organized media / lipid bilayer membrane nanodomains. It will be important to investigate the conformational and orientation change of the Ca^{2+} -binding site of BAPTA (four acid chelating ligands) as well as the related interfacial calcium affinity change.

Infrared spectroscopy is a powerful technique for detecting conformational changes by recording spectral differences before and after perturbations. Polarized infrared measurements on oriented membrane samples have revealed valuable information on the orientation of molecules and substructures within membrane molecules, which is difficult to obtain by other methods.

In this chapter, several techniques will be introduced and utilized in the coming sections to gain extra information as shown in Table 3.1. Using Langmuir monolayers at the air-water interface, different aspects of monolayer properties can be obtained. For example, surface compression isotherms provide macroscopic phase information about monolayers under constant compression; ellipsometry provides visual images of film morphologies in different phases; and polarization-modulated infrared reflection absorption spectroscopy (PM-IRRAS) not only helps in determining which molecules are at air-water surface but also provides molecular structural information such as the molecular conformation and chain orientation via spectral analysis.

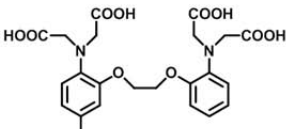
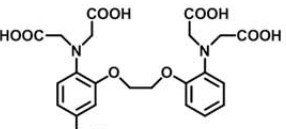
	 <p style="text-align: center;">63 BAPTAhyd</p>	 <p style="text-align: center;">64 C15BAPTAhyd</p>
To mimic:	BANI compounds in free solution	BANI compounds in the vesicle membrane bilayer surface
Techniques:	ATR-FTIR (attenuated total reflection Fourier-transform infrared spectroscopy)	Langmuir Film PM-IRRAS (polarization-modulated infrared reflection-absorption spectroscopy) ellipsometry

Table 3.1 Molecules and Techniques for mimicking **BANI** compounds in the free solution or liposome membrane

1. ATR-FTIR (attenuated total reflection Fourier-transform infrared spectroscopy) was

used to detect structure and orientation changes of **BAPTAhyd** (compound **63**) while complexation with calcium allowed mimicking the **BANI** series compounds in the free water solution.

2. In the other hand, Langmuir films of **C15BAPTAhyd** (compound **64**) can mimic the **BANI** compounds equipped with long alkyl chain when they are immobile on the liposome membrane. In order to observe the orientation and morphology change of this ionophore, PM-IRRAS combined in-situ with different techniques such as Langmuir film or ellipsometry allowed us to collect the infrared information of the ligand in the monolayer structure and compare them with the results of free solution.

3.1 IR spectrum analysis

3.1.1 General band position

IR spectra of large molecules are generally very complex and not well resolved in many regions of the spectrum. However, despite this complexity, absorption bands at distinct group frequencies can be assigned to various functional groups in protein, lipid and water molecules. Chemical compounds absorb in many different regions of the IR spectrum. Approximate frequencies of some important vibrational modes are listed in Table 3.2.

Assignment		Approximate wavenumbers (cm ⁻¹) ^a	Estimated direction of dipole moment
CH₃ antisymmetric stretch (choline)	(v _{as})	3038 (w)	
CH₃ antisymmetric stretch	(v _{as})	2956 (s)	
CH₂ antisymmetric stretch	(v _{as})	2920 (s)	⊥ to bisector of HCH angle
CH₃ symmetric stretch	(v _s)	2870 (s)	
CH₂ symmetric stretch	(v _s)	2850 (s)	∥ to bisector of HCH angle
C=O stretch	(v)	1730 (s)	~ ∥ to C=O bond
NH₃⁺ antisymmetric bend	(δ _{as})	1630 (m)	
COO⁻ antisymmetric stretch	(v _{as})	1623 (s)	
NH₃⁺ symmetric bend	(δ _s)	1571 (m)	
CH₂ scissoring (triclinic)	(δ)	1473 (m)	
CH₂ scissoring (hexagonal)	(δ)	1468 (m)	∥ to bisector of HCH angle
CH₂ scissoring (orthorhombic)	(δ)	1472 (m) 1463 (m)	
CH₃ antisymmetric bend	(δ _{as})	1460 (m)	
CH₃ symmetric bend	(δ _s)	1378 (m)	
CH₂ wagging band progression	(w)	1200-1400 (w)	∥ to hydrocarbon chain (alltrans)

Table 3.2 Important infrared absorption bands. ^a s, strong; m, medium; w, weak.

The exact frequencies of the absorption bands that are associated with methylene vibrations of the fatty acyl chains depend on the physical state of these chains. Therefore, precise measurements of CH₂ stretching, scissoring, and rocking band progressions can be used to probe the physical state of lipids or amphiphiles under various conditions. The ester carbonyl stretching band is very sensitive to hydrogen-bonding and, therefore, has been used to monitor hydration at the membrane-water interface.¹

The infrared absorption frequencies of H₂O, HOD, and D₂O are listed in Table 3.3.¹

Assignment		H ₂ O	HOD	D ₂ O
O-X stretching	(ν_{as})	3490 (s) ^a	3380 ^b (s)	2540 (s)
	(ν_s)	3280 (s)	2500 ^c (s)	2450 (s)
Combination	(ν_A)	2125 (w)	-	1555 (w)
Bending	(δ)	1645 (m)	1450 (m)	1210 (s)

Table 3.3 Infrared absorption bands of liquid H₂O, HOD, and D₂O (in cm⁻¹),^a s, strong; m, medium; w, weak. ^b O-H. ^c O-D

The H₂O bending mode at ~1645 cm⁻¹ and the HOD bending mode (present in mixed D₂O/H₂O samples) at ~1455 cm⁻¹ overlaps with the CH₂ scissoring mode of lipid fatty acyl chains (see Table 3.3). The D₂O combination band is at ~1555 cm⁻¹ and D₂O bending is at ~1215 cm⁻¹. Therefore, the choice of solvent depends on the spectral region of interest in each sample and its proper selection is important.

3.1.2 Carboxylic acid and carboxylate group

Carboxylic acid and carboxylate containing molecules at both the air-water and the solid-liquid interface have received much interest over the last two decades from surface specific techniques. The carboxyl group gives rise to vibrations at ~1730 and ~1700 cm⁻¹ and ~1623-1520 cm⁻¹ in the protonated (COOH) and ionized (COO⁻) forms, respectively. They shift slightly in different cases but generally are located in the spectral region shown in the example by ATR-FTIR in Figure 3.1.² The relative intensities of these two bands can be used in pH titrations to determine the apparent pK in lipid bilayers.³ Also, these two absorption bands will be the key information for us to observe the behavior of BAPTA parent molecules in the free solution or mimicking membrane environment by ATR-FTIR or PM-IRRAS techniques.

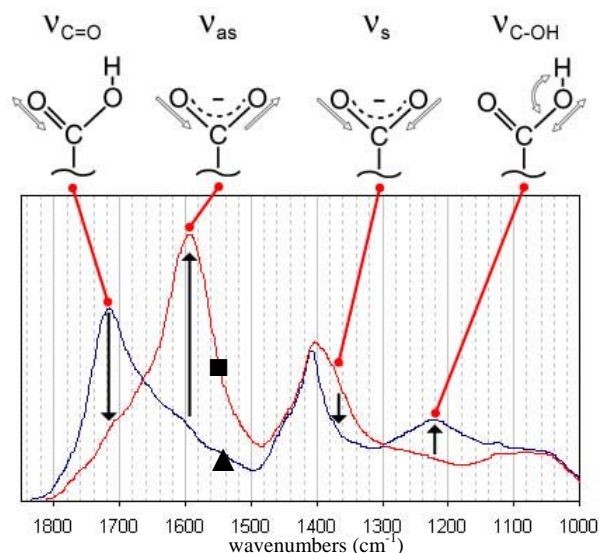


Figure 3.1 IR spectra of soil fulvic acid at pH= 2 (blue, ▲) and 6 (red, ■). The black arrows indicate the spectral changes that occur on deprotonation, namely the disappearance of the carbonyl and C-OH bands, and appearance of bands corresponding to the asymmetric and symmetric modes of the carboxylate anion.²

When long chain fatty acid amphiphiles are spread and form the monolayer, the ratio of neutral carboxylic acid and charged carboxylate in the monolayer depends on the pH value of the subphase. Previous work⁴ by Johann et al. used PM-IRRAS to study similar monolayers as a function of pH is summarized as follows:

1. The carboxylic acid bonding situation depends on the surface pressure of monolayer and the packing density of the molecules.
2. The head groups of neutral fatty acids on aqueous subphase (pH=5.6) are hydrated and the water molecules are bound to the head groups via hydrogen-bonding to the carbonyl oxygen.
3. In addition, neighboring fatty acids may be hydrogen-bridged. The possibility that there is only hydrogen bonding between fatty acids and not between fatty acids and water is unlikely, since hydrogen bonding also occurs with ester and in that case it must be with water.
4. At pH= 9 in the monolayer, nearly half of the lipids are dissociated, acid–anion dimers of carboxyl and carboxylate have formed and a fraction of about 20% of carboxyl is bonded to water. Also, and up to pH= 12 almost all the molecules are dissociated.

Other IRRAS work by Gericke and coworkers focused on long chain carboxylic acids using a number of different metals to study binding effects and monolayer conformation.⁵ While both of these studies were able to see splitting of the C=O vibrational mode into three

distinct peaks due to hydrogen-bonding, limited information is available about how the charged carboxylate head group was solvated at the air-water interface. Additionally, splitting of the asymmetric and symmetric carboxylate vibrational modes was seen by Johann et al., but there was no explanation as to why this occurred. Miranda and co-workers studied long chain carboxylic acids with vibrational sum frequency spectroscopy (VSFS) at the air-water interface and found that the surface pK_a is much different than what is normally found in bulk liquid.⁶ Also, they found at low pH values the monolayer is neutral and the surface water structure is disordered by hydrogen-bonding of water molecules with the acid head-groups. At high pH values, acid head-groups are ionized and the resulting surface field helps the surface water molecules form a more ordered hydrogen-bonding network. At pH=3, a small change in pH leads to a reorientation of the acid OH groups while the alkyl chains remain conformationally ordered at all pH values.

Allen and co-workers completed a study of carboxylic acids at the air-water interface in the presence of Na^+ and K^+ . They found that the palmitic acid ($C_{15}H_{31}COOH$) monolayer could effectively induce the very opposite binding characteristics of K^+ and Na^+ at the interface as compared with the observed binding behaviors of these two ions to the short-chain carboxylate groups in the bulk. Palmitic acid monolayer is mostly protonated at the aqueous surface at neutral pH (~ 6). However, various degrees of deprotonation are initiated by the introduction of Na^+ and K^+ that results in the complexation of $K^+:COO^-$ and solvent separated $Na^+:COO^-$ in neutral pH. Evidence in several spectral regions indicates that K^+ exhibits stronger ionic binding affinity to the carboxylate anion relative to Na^+ .⁷ Le Calvez and co-workers have demonstrated by PM-IRRAS that the apparent pK_a shift depend on the Gouy-Chapmann theory of the 2D charged surfaces, modulated by the type of cation in the aqueous subphase.⁸

Therefore, the intensity and position of carboxylic acid bands can be affected by pH value, counter ion, and surface pressure of monolayer situation. With the information in mind, it allows us to perform and determine the much more complicated structure of BAPTA (with four carboxylic acid groups and two aniline groups in one molecular) in free bulk solution or monolayer environment.

3.2 ATR-FTIR experiments for BAPTAhyd compound

3.2.1 Introduction to ATR-FTIR

IR spectroscopy is an analytical technique to acquire spectra from a very wide range of solids, liquids and gases. Traditionally IR spectrometers transmit the infrared radiation directly through the sample where the sample is in a liquid or solid form. Typically the sample

thickness cannot be more than a few tens of microns and therefore determines the intensity of the spectrum.

Attenuated total reflection using infrared Fourier transform (ATR) spectroscopy has become increasingly popular for membrane spectroscopy and revolutionized solid or liquid sample analyses. Also, it is considered as one of the simplest, and most direct, flexible and sensitive *in situ* infrared technique for substances dissolved in aqueous solutions. ATR-FTIR spectroscopy has several advantages:

1. Information can be obtained not only on the secondary structure, but also on the orientation of membrane molecules from measurements with polarized light.
2. The technique is very sensitive, requiring only sub-milligram quantities for sample preparation and detection.
3. Conformational states can be measured in aqueous environments.
4. The physiological conditions of a sample can be varied *in situ*.
5. Absorption due to water and other molecules in the bulk solution is greatly reduced.
6. Molecular orientations can be determined in oriented samples with polarized light.

ATR-FTIR operates by measuring the changes that occur in a totally internally reflected infrared beam when the beam comes into contact with a sample (Figure 3.2).

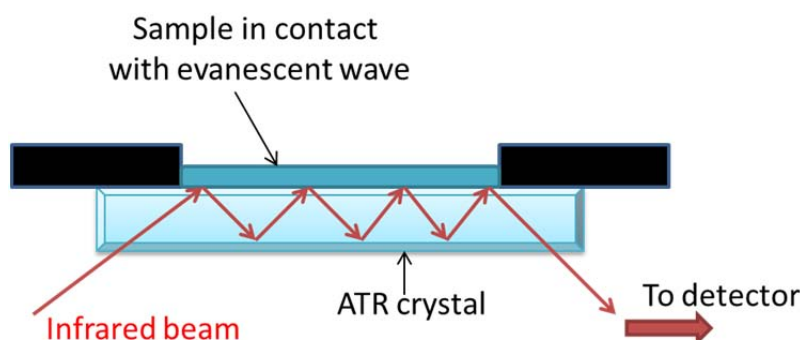


Figure 3.2 Multiple reflection ATR-FTIR system

An infrared beam is directed onto an optically dense crystal with a high refractive index at a certain angle (2.38 to 4.01 at 2000 cm^{-1}). The refractive index of the crystal must be significantly greater than that of the sample or else internal reflectance will not occur. This internal reflectance creates an evanescent wave that extends beyond the surface of the crystal into the sample held in contact with the crystal. This evanescent wave protrudes only a few microns ($0.5\text{ }\mu\text{m} - 5\text{ }\mu\text{m}$) beyond the crystal prism surface and into the sample so the sample must be in direct contact with the ATR crystal. In the infrared spectrum regions where the energy is absorbed by aqueous sample, the evanescent wave will be attenuated. The attenuated energy from each evanescent wave is passed back to the IR beam, which then exits

the opposite end of the crystal and is collected by the IR spectrometer. The system then generates an infrared spectrum. This method may solve problems associated with transmission infrared spectroscopy, such as path length and concentration.^{9,10}

In this internal reflection spectroscopy, the IR beam is reflected within an IR-transparent internal reflection element. An evanescent wave of the same frequency as the incoming IR light is set up in the optically rarer medium, such as an aqueous solution that is adjacent to the interface. The amplitude of the electric field, E , falls off exponentially with distance, z , from the interface:

$$E = E_0 e^{-z/d_p} \quad \text{Equation 3.1}$$

with a characteristic decay length (depth of penetration),

$$d_p = \frac{\lambda/n_1}{2\pi\sqrt{[\sin^2\gamma - (n_3/n_1)^2]}}, \quad \text{Equation 3.2}$$

where λ denotes the wavelength of the IR light, n_1 and n_3 are the refractive indices of the internal reflection element and water, respectively, and γ is the angle of incidence.

Because d_p is the order of only a few hundred nm in many typical applications, internal reflection spectroscopy is a surface-sensitive technique. Samples, such as membranes, that are deposited at the solid/liquid (or solid/gas) interface absorb electromagnetic radiation of the evanescent wave, and thereby reduce the intensity of the reflected light. Hence, the technique is referred to as attenuated total reflection spectroscopy.¹

We used circular ATR crystals of 1.5 mm and 5 mm diameters depending of the number of reflections (1 to 3). When measuring solid sample, it is necessary to ensure good optical contact between the sample and the crystal. The best and frequently used small crystal material is diamond because it has the best durability and chemical inertness. These small area ATR crystal top-plates generally provide only a single reflection but this is sufficient, given the very low noise level.

3.2.2 ATR-FTIR experiment results for BAPTAhyd

In order to understand the different behavior as a function of the K_d value and Ca^{2+} affinity of BAPTA series molecules in the aqueous solution or confined in the vesicle membrane. We have used ATR-FTIR spectroscopy to observe the character of the Ca^{2+} -ion binding site (four acid chelating ligands) in the **BAPTAhyd** molecule (Figure 3.3) to mimic the free solution.

We also compare with the ellipsometry and PM-IRRAS results of **C15BAPTAhyd** monolayer which mimics the liposome membrane environment will be presented in the coming sections.

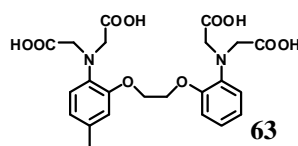


Figure 3.3 BAPTAhyd molecular structure

As shown in Figure 3.4, at the low subphase pH condition (pH~2), the spectrum only presents absorption bands related to the acid form, i.e., the C=O stretching vibration (ν C=O) located at 1720 cm^{-1} . The frequency position of the ν C=O is characteristic of a hydrogen-bonded carbonyl group and is positively oriented with respect to the baseline. During the increase of subphase basicity, the acetic acid groups are progressively deprotonated as indicated by the appearance and the increase in the carboxylate antisymmetric (ν_a COO⁻) located around at 1570 cm^{-1} . This band is correlated with the decrease in the ν C=O band. As a result, the pK_a can be deduced to be about 6~7 corresponding with the value of BAPTA series compounds' results in Chapter 2.

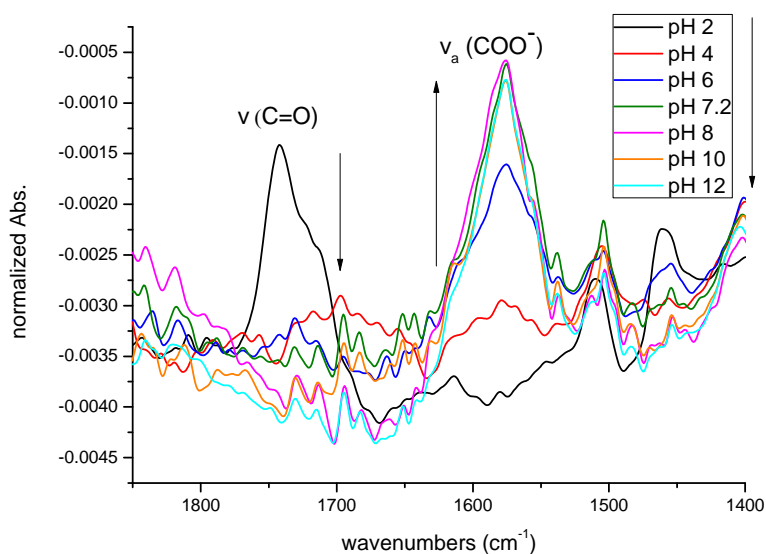


Figure 3.4 ATR spectra of BAPTAhyd (5 mg/ml) from pH = 2 to 12 in Milli-Q water

After having established the pH effect for the chelating ligands of the acetic acid (COOH) and ionized carboxylate (COO⁻) forms, the calcium chelating effect was further examined in a similar manner at a fixed pH value. The variation of ν_a COO⁻ and ν C=O bands with different concentrations of added Ca²⁺ is shown in Figure 3.5 (pH 7.2) and Figure 3.6 (pH 4). As we have seen in Chapter 2, BAPTA chelates Ca²⁺ in a 1:1 stoichiometry. Here we also observed that roughly one equivalent of Ca²⁺ in the subphase could totally deprotonate the acetic acid

group to the carboxylate which is observed by the increase in the $\nu_a \text{COO}^-$ and correlated with the decrease in the $\nu \text{C=O}$ band. Another interesting observation in these profiles is at high Ca^{2+} concentration at 500 equivalents, the shift and unsymmetrical spectra might come from the salt perturbation.

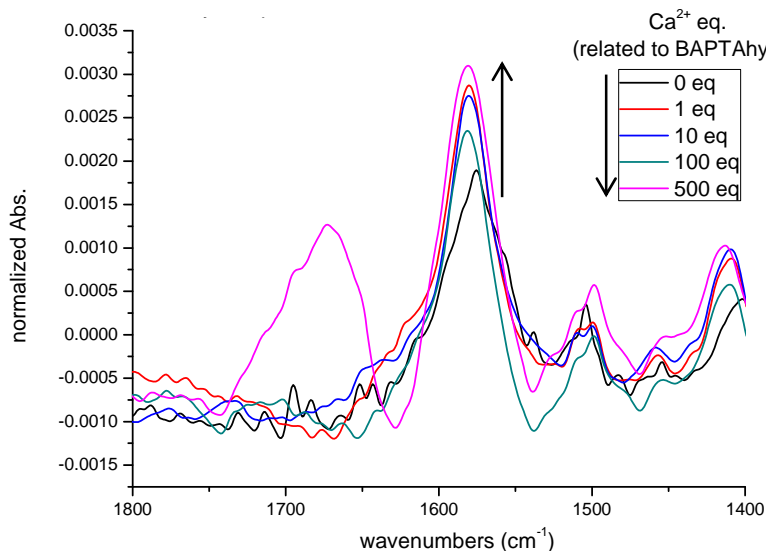


Figure 3.5 ATR spectra of BAPTAhyd (5 mg/ml) at pH = 7.2 with Ca^{2+} (0 to 500 equivalents) in Milli-Q water

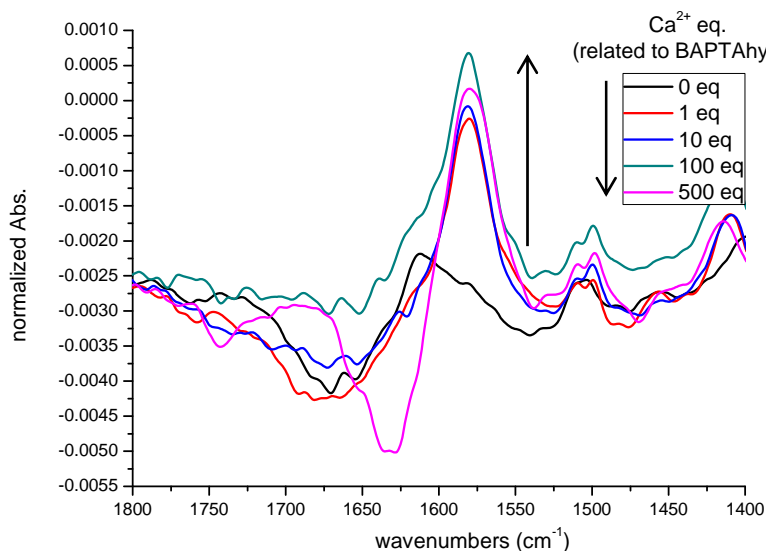


Figure 3.6 ATR spectra of BAPTAhyd at pH = 4 with Ca^{2+} (0 to 500 equivalents) in Milli-Q water

As represented in Figure 3.4 and 3.6, in the pH= 4 subphase neither the $\nu_a \text{COO}^-$ band nor the $\nu \text{C=O}$ band can be seen. This could be due to the interaction between BAPTA and H_2O

which makes the subtraction of the H₂O spectrum more delicate. Therefore, we performed the pH= 4 solution in D₂O (Figure 3.7, pH adjusted by adding DCI_(aq)) and found the 1720 cm⁻¹ ν C=O band appeared without Ca²⁺ ion in the subphase. As the quantity of the Ca²⁺ ion in the solution is increased, the ν C=O band disappeared but without obvious increase of the ν_a COO⁻ band.

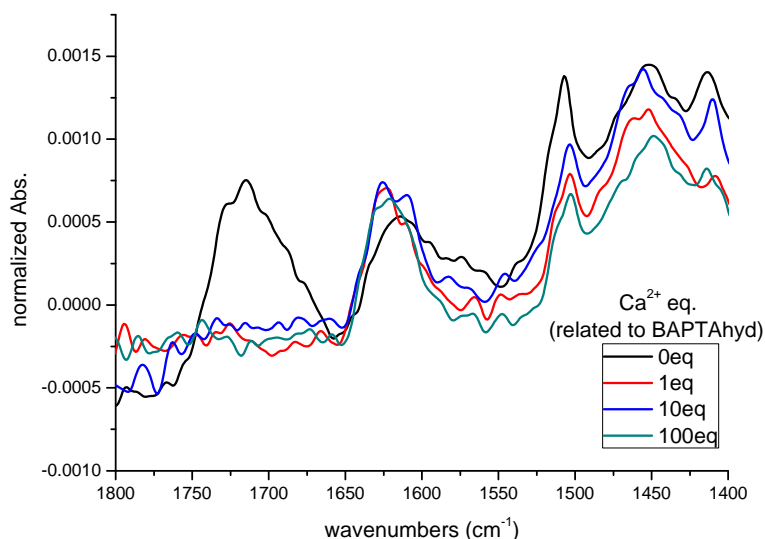


Figure 3.7 ATR spectra of BAPTAhyd at pH = 4 in D₂O with Ca²⁺ (0 to 100 equivalents)

The results of these series experiments can be summarized as follows:

1. At pH= 4, ν C=O band of carbonyl group is shifted from ~1740 to ~1700 cm⁻¹ and broadened (Figure 3.4 & 3.7). This might be because the CO group should be in interaction with oxonium species H₃O⁺ via hydrogen bond.
2. One can see at high Ca²⁺ concentration, the shift and unsymmetrical spectra might come from the salt perturbation.
3. Two observations can be made upon changing solvent from H₂O to D₂O (Figure 3.7): First, ν C=O band of carbonyl group at 1700 cm⁻¹ can be seen without calcium and the shift of ν_a COO⁻ to >1600 cm⁻¹. Second, by increasing the Ca²⁺ concentration the carboxylate antisymmetric band increase accompanied with the decrease in the ν C=O band is visible. Complete deprotonation is observed with one equivalent of Ca²⁺.

3.3 Langmuir films & PM-IRRAS for C15BAPTAhyd compound

In this section, the properties of C15BAPTAhyd monolayer mimicking the lipid bilayers

environment were studied. The result of PM-IRRAS will be compared with ATR-FTIR result of **BAPTAhyd**.

3.3.1 Introduction to PM-IRRAS¹¹⁻¹³

PM-IRRAS is a highly surface-specific FT-IR method that is capable of detecting chemical compositions from interfacial films down to one molecule-thick film. The PM-IRRAS technique allows enhanced detection on substrates and measurements from the air-water interface. Changes in the PM-IRRAS signal intensity and position can be used to infer molecular absorption/desorption behavior and kinetics, molecular packing, phase transitions, hydration, hydrogen-bonding and different surface reactions in a thin film. Additionally in PM-IRRAS the properties of the polarized light can be used to determine the molecular orientation in a film.

Infrared reflection absorption spectroscopy (IRRAS) is an established analytical technique for the characterization of adsorbed matter and thin layers on metal surfaces. In IRRAS experiments, the sample is investigated in reflection geometry under grazing incidence (typically 80°). At an interface p-polarized light is preferentially adsorbed during reflection, but s-polarized light is reflected almost completely, unlike in isotropic media where the adsorption is independent of polarization. So any differences in measured p- and s-polarized light can be attributed to surface specific adsorptions at the interface. In practice the IRRAS technique requires that four spectra be recorded, both p- and s-polarized spectra for background and of the sample itself. This makes IRRAS challenging due to slightly changing environmental factors like CO₂, water vapor, and instrumental noise like drifting of the interferometer over time. Any of these factors changing will affect the spectral resolution, and when measuring spectra from nano to micrometer thick systems the effects can dominate over the desired signals.

The sensitivity of this method can be significantly enhanced by employing the polarization modulation technique (PM). In particular the disturbing atmospheric absorptions, caused by water vapour and CO₂, are thereby eliminated. In PM-IRRAS the incoming IR-light polarization is modulated at high frequency, which allows the simultaneous collection of the surface specific spectra with one experiment. As the spectra are measured simultaneously, the environmental effects and instrument drift over time are almost completely removed. This is especially effective when measuring floating monolayers on water where the reflectivity is relatively small and there is a lot of interfering water vapor present during the measurement.

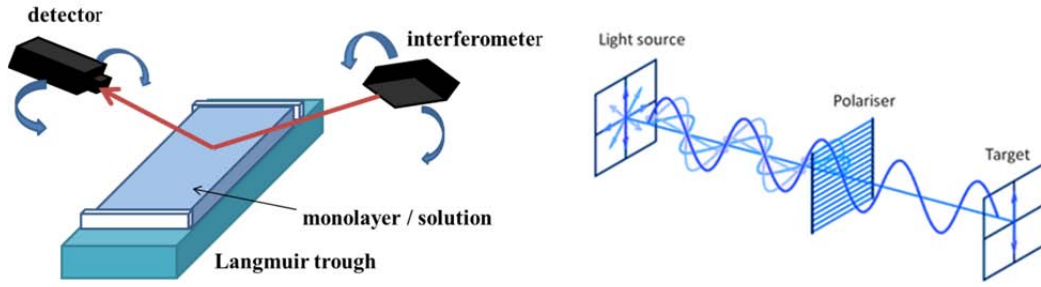


Figure 3.8 Schematic representations of PM-IRRAS

PM-IRRAS studies the high-frequency modulation between s- and p-polarization, allowing the simultaneous measurement of two signals: 1. the difference spectrum between s- and p-polarized light and 2. the corresponding sum spectrum. Also, the PM-IRRAS method allows determination of the molecular orientation of the functional groups and the whole molecule. In floating monolayers the PM-IRRAS has a strong incident angle dependency, and this can be used to determine the orientation. Also the relative peak ratios of functional groups of known orientation can be used to determine the tilt of the molecules compared to the surface. In short, the surface selection rule indicates positive bands for transition moments lying in the surface plane whereas negative bands are attributed to transition moments perpendicular to the surface. For an intermediate orientation of the transition dipole moment, the two contributions are competing, and the absorption band vanishes when the transition dipole moment is tilted 39° from the surface normal of the water subphase. The PM-IRRAS device allows us to obtain the differential reflectivity spectrum¹⁴

As mentioned, in a PM-IRRAS experiment the signal at the detector output can be electronically split into a part carrying only the intensity modulation at frequency ω_i introduced by the interferometer:

$$I_+ = [(R_p + R_s) + J_0(R_p - R_s)]I_0(\omega_i) \quad \text{Equation 3.3}$$

And a second part

$$I_- = [J_2(R_p - R_s)]I_0(\omega_i) \cos 2\omega_m t \quad \text{Equation 3.4}$$

That in addition contains the polarization modulation $2\omega_m$ induced by the photoelastic modulator. J_2 and J_0 are the second and zero-order Bessel functions of the maximum dephasing introduced by the photoelastic modulator. After demodulation, the ratio of these two parts (positive and negative bands) gives the PM-IRRAS signal:

$$S = \frac{J_2(R_p - R_s)}{(R_p + R_s) + J_0(R_p - R_s)} \quad \text{Equation 3.5}$$

With an ultrathin film deposited on a dielectric substrate, optimization of the PM-IRRAS

detection of the surface absorption is non-trivial. Indeed, depending on the angle of incidence, R_p may be very different from R_s and Equation 3.5 cannot be simplified. Moreover, the electric field at the surface has an in-plane component; absorptions with a transition moment parallel to the subphase are detected. Finally, a dielectric substrate has a large, specific and spectral-dependent contribution to the PM-IRRAS signal and, consequently, comparison with the bare substrate spectrum is necessary to extract the tiny signal from the deposited monolayer.

To remove the contribution of the subphase absorption and the dependence on the Bessel function, the film spectra are divided by that of the subphase to get the normalized PM-IRRAS signal. The weak water vapor contribution to the film spectra is removed by subtraction of the water vapor spectrum. The intensity of the absorbance bands is proportional to the surface concentration (N/A) and the orientation of the transition moment $f(\alpha)$.

$$I \propto \frac{N}{A} f(\alpha) \quad \text{Equation 3.6}$$

To obtain spectra independent of the surface concentration due to area reduction, spectra are multiplied by the surface area available for the film.

3.3.2 Introduction to Langmuir film

The study of amphiphiles at the air-water interface can be done through a variety of methods in which the measurement of the Langmuir isotherm is one of the most common techniques. The principle is to form a water surface area of a known surfactant monolayer, and progressively reduce the area of the monolayer accompanied with the change of surface tension. Figure 3.9 shows a typical Langmuir isotherm and schematic representations of surfactants on the water surface at different stages of the experiment.¹⁵

The amphiphile is dissolved in an organic solvent and subsequently spread at the air-water interface. The solvent evaporates and a monolayer of the amphiphile at the air-water interface is then produced. These so called Langmuir monolayers can be further manipulated by means of a moveable barrier which allows us to control the area per molecule.

Surface tension is measured by using various devices, the method of Wilhemy plate shown in Figure 3.9 is one of the most common. This method is based on measuring the force acting on a vertical plate of defined area in contact with the water surface. The Langmuir isotherm is usually represented as surface pressure, π , defined as the difference between the surface tension of pure water and the measured voltage.

$$\pi = \gamma_0 - \gamma \quad \text{Equation 3.7}$$

The experiment starts at *stage A* while the surfactant molecules are mutually too far away to interact with each other and to influence the surface pressure, which is called "gas phase". The mobile barriers are moving slowly to gradually reduce the area per molecule. The surface pressure then continuously increases, *stage B* during the increase of surface pressure is called the "liquid phase". *Stage C* is called the "solid phase" which shows the surface pressure increase more rapidly. In the end, the monolayer film will be destroyed (collapse) when the area allocated to each surfactant molecule is no longer sufficient to maintain a stable film.

The Langmuir isotherm allows us to obtain the data in terms of area per molecule at the interface. The shape of the isotherms, the point of threshold (P_0), the point of the physiological membranes (P_{25} , ~ 25 mN/m), and the collapse point (P_c) can be the basis of interpretations for the following discussion.

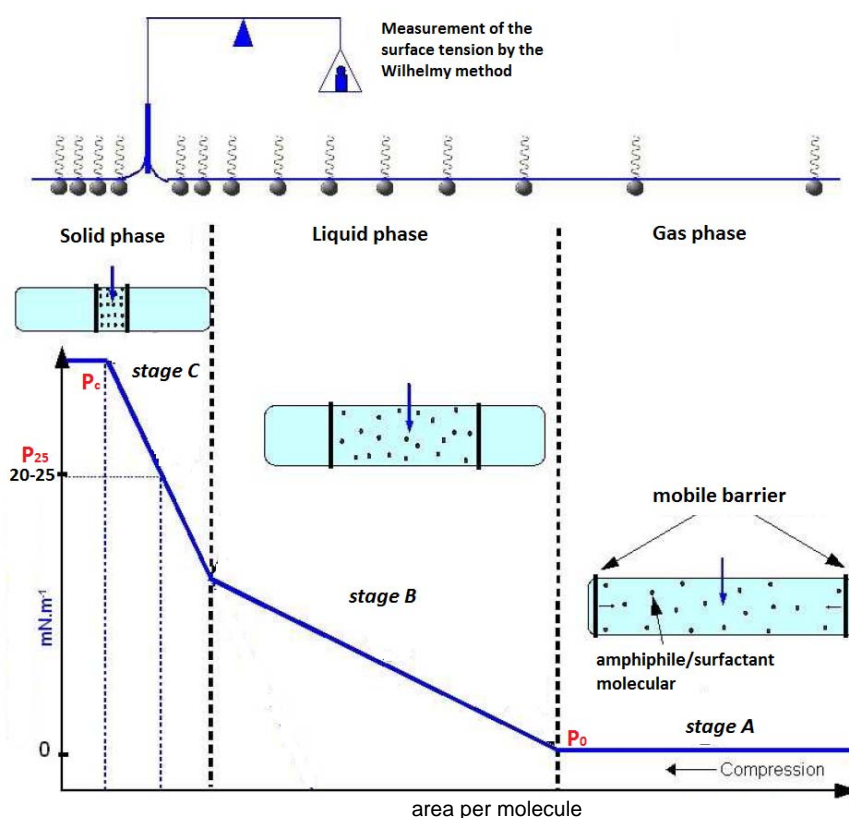


Figure 3.9 Schematic representation of Langmuir isotherm¹⁵

3.3.3 PM-IRRAS experiments of C15BAPTAhyd Langmuir film

To compare with the results of ATR-FTIR of **BAPTAhyd** which mimic the **BANI** series of molecules in aqueous solution, PM-IRRAS is used to observe **C15BAPTAhyd** in the

monolayer morphology on water subphase mimicking **BANI** series (especially **BANI2**) on the confined liposome membrane. We observe the C=O stretching vibration band (ν C=O) at 1720 cm^{-1} and the carboxylate antisymmetric (ν_a COO⁻) at about 1540 cm^{-1} during the compressing process of Langmuir film.

First, the effect on the IR absorption of carboxylic acid groups by changing pH was performed and presented in Figure 3.10 and Figure 3.11. Langmuir isotherms show the area per molecule would decrease by raising the pH of the bulk solution in the trough. At pH= 7 or 10, the area per molecular of P_c (collapse point) is $\sim 20\text{ \AA}^2/\text{molecular}$, which is roughly equal to one alkyl chain space area. Therefore the molecules have the most condensed arrangement with vertical direction of the alkyl chain and water surface. Decreasing pH can lead to a higher space requirement which comes from the tilt angle of the alkyl chain to the water surface. This phenomenon can be explained also in the coming ellipsometry experiment part, the film thickness will decrease by the alkyl chain shifting from perpendicular to tilt angle with the water surface.

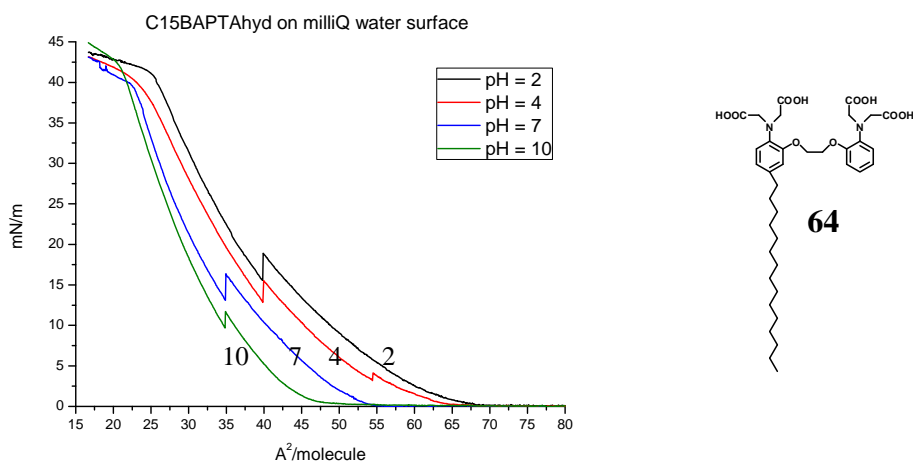


Figure 3.10 PM-IRRAS experiment: isotherms of **C15BAPTAhyd** on the different pH water surface

As for the IR absorbance result in Figure 3.11, the C=O stretching vibration band (ν C=O) at 1720 cm^{-1} cannot be observed in all pH conditions. Moreover, the results of this series were not able to see splitting of the C=O vibrational mode. Instead, they just show the general peak position of carbonyl absorbance. The possible speculations can be:

1. The disappearance of ν C=O at 1720 cm^{-1} may be due to the transition moments of these groups which are oriented near the magic angle.¹⁶
2. The ν_s COO⁻ at 1400 cm^{-1} cannot be observed probably due to the disturbance of CO₂ and water vapor or the orientation at magic angle.⁸

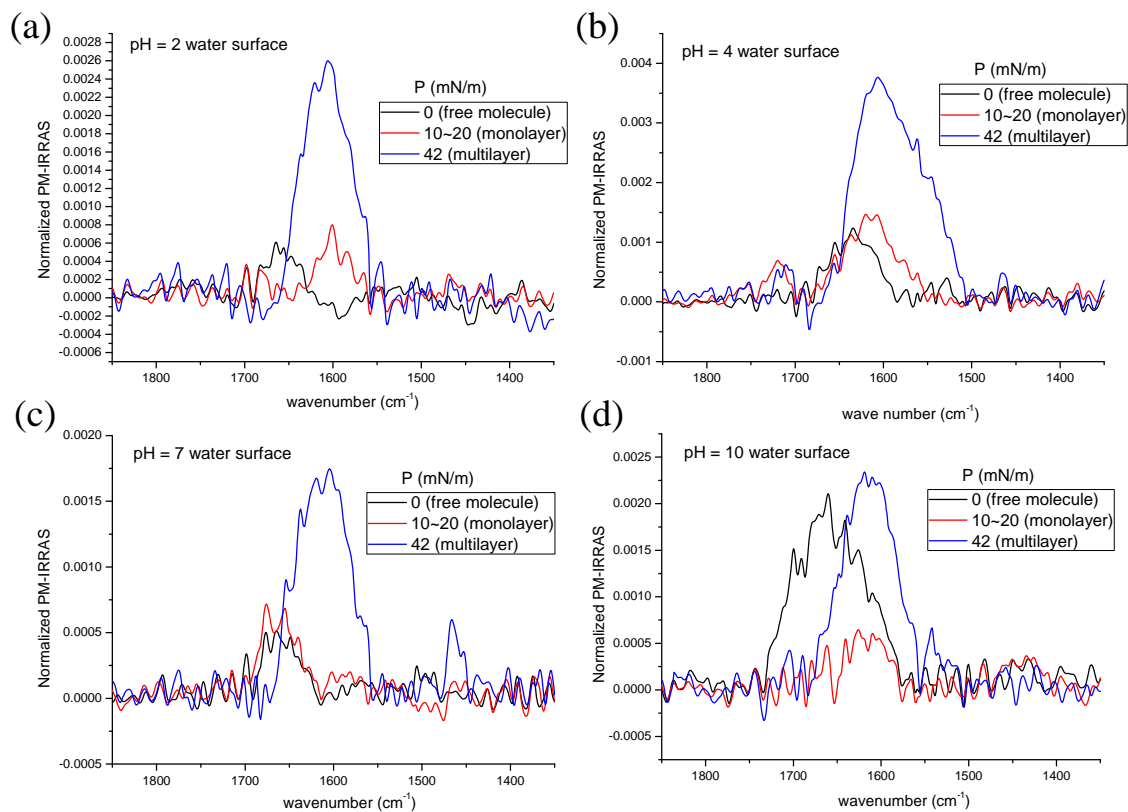


Figure 3.11 PM-IRRAS experiments of **C15BAPTAhyd** on the pure water at different surface pressure: (a) pH = 2, (b) pH = 4, (c) pH = 7, (d) pH = 10

As a result, we performed the experiments in the de- $\text{CO}_2(\text{g})$ environment on the D_2O subphase trying to eliminate the disturbance (Figure 3.12). In this series of tests, the round trough with 5.2 cm inside-diameter was used when a known volume sample was directly injected on the subphase in order to obtain the monolayer with pre-calculated surface pressure ($P \sim 30$ mN/m). After improvement, the spectra are able to be seen the bands of the $\nu_s \text{COO}^-$ at 1400 cm^{-1} and $\nu_a \text{COO}^-$ at about 1580 cm^{-1} , but still not for the $\nu \text{C}=\text{O}$ at 1720 cm^{-1} , which might be due to the magic angle orientation as in Figure 3.11.

Moreover, the absorption shift of $\nu_a \text{COO}^-$ from 1540 to 1580 cm^{-1} or higher frequency happened in both Figure 3.11 and 3.12. As the D_2O subphase case in the ATR results, the decrease of hydrogen exchange speed of $\text{COOH} \leftrightarrow \text{COO}^-$ resonance in D_2O solvent or monolayer / multilayers environments could be a tentative explanation. Despite the disappearance of the $1720 \text{ cm}^{-1} \nu \text{C}=\text{O}$ band, the important result of Figure 3.12 is, the intensity of $1580 \text{ cm}^{-1} \nu_a \text{COO}^-$ band increase from pH 2 to 10 with reaching maximum at pH 7 as the ATR result of **BAPTAhyd** in free solution. Hence, the pK_a values for **BAPTAhyd** in free solution and **C15BAPTAhyd** in monolayer ($P \sim 30$ mN/m) environment are similar at about 6-7 by the preliminary infrared results.

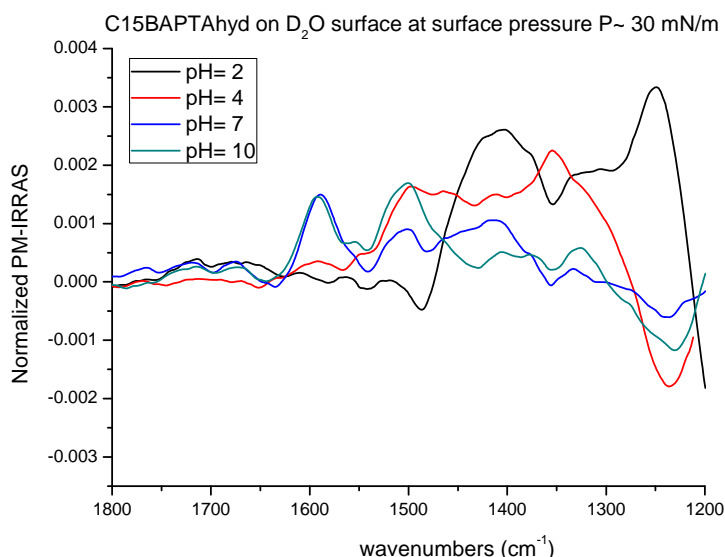


Figure 3.12 PM-IRRAS experiment: **C15BAPTAhyd** monolayer at different pH D_2O surface in the $de-CO_{2(g)}$ environment at surface pressure $P \sim 30$ mN/m

After knowing the pH effect for the carboxylic acid of **C15BAPTAhyd** monolayer, the calcium chelating effect was further examined. The Ca^{2+} chelating effect of **C15BAPTAhyd** monolayer at pH= 4 was directly examined (Figure 3.13).

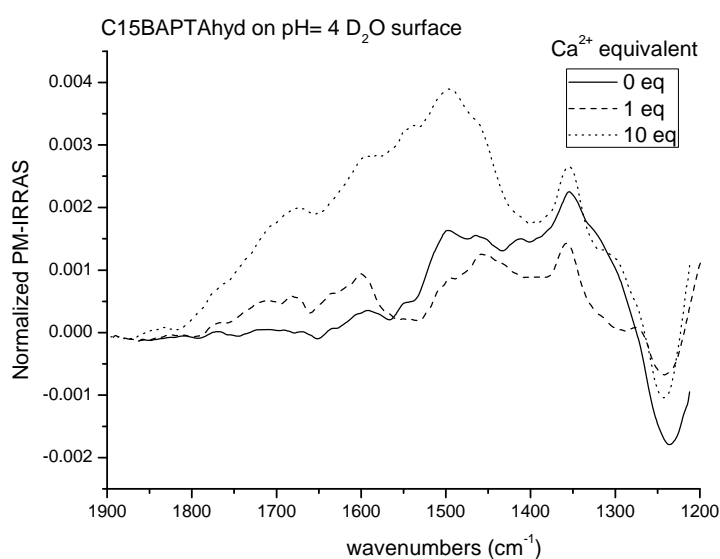


Figure 3.13 PM-IRRAS experiment: **C15BAPTAhyd** monolayer with different calcium equivalents on D_2O surface in the $de-CO_{2(g)}$ environment at surface pressure $P = 15 \sim 20$ mN/m

Unlike the ATR result of **BAPTAhyd** in free solution, for **C15BAPTAhyd** monolayer we found that 10 equivalents of Ca^{2+} could totally deprotonate the acetic acid group to carboxylate as the increase in the $\nu_a COO^-$. It corresponds to the K_d experiments of BAPTA parent fluoroionophores in the free solution vs. vesicle matrix solution. The affinity to Ca^{2+} would be lower when the fluoroionophores are fixed on the liposome membranes.

We then analyzed the CH₂ stretching modes to investigate the hydrophobic part of the molecule. Figure 3.14 shows the PM-IRRAS spectra in the CH stretching region of **C15BAPTAhyd** monolayers at different pH, subphase, and surface pressure. The frequencies of the CH₂ stretching modes indicate an apparent physical state of a hydrocarbon chain. As seen in Figure 3.14, at each surface pressure and pH value of the monolayer on the H₂O or D₂O, the asymmetric methylene stretching mode ν_{as} (CH₂) is found at 2923 cm⁻¹ and the symmetric mode ν_a (CH₂) at 2853 cm⁻¹. It means the methylene stretching modes are characteristic for a hydrocarbon chain existing in a liquid disordered state, having a numerous of gauche conformations.¹⁷

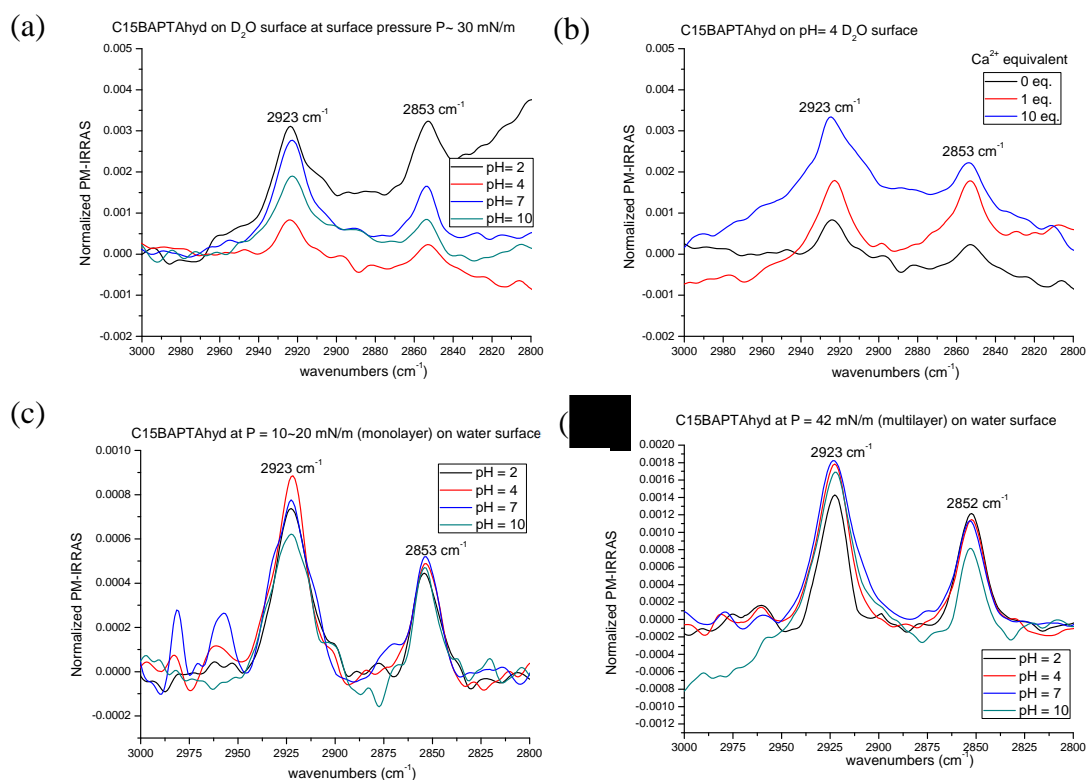


Figure 3.14 PM-IRRAS experiment of **C15BAPTAhyd** at: (a) different pH D₂O surface in the de-CO_{2(g)} environment at surface pressure P~ 30 mN/m monolayer; (b) different calcium equivalent on D₂O surface in the de-CO_{2(g)} environment at surface pressure P= 15~20 mN/m monolayer; (c) pure water with different pH at P= 10~20 mN/m monolayer; (d) pure water with different pH at P= 42 mN/m multilayers

3.4 Ellipsometry measurements for C15BAPTAhyd compound

As mentioned in the beginning of this chapter, it is important to know the morphology of Langmuir film during the compression. The monolayer pressure range of Langmuir film can be simultaneously observed by ellipsometry while performing the isotherm surface pressure measurement. The information of surface morphology such as film thickness, surface pressure and roughness will then be controlled with the precise information at molecular level by

PM-IRRAS.

We use ellipsometry measurements and PMIRRAS to determine the morphological and structural properties of monolayers at the air-water interface. Ellipsometry images allow the visualization of the morphology of lipid or amphiphile domains at the air-water interface, as well as changes in monolayer organization after binding ion, with a spatial resolution on the micrometer order. The variations of measured ellipsometric angles allow the evaluation of the thickness of the layers present at the air-water interface. PMIRRAS gives access to the structure of the amphiphile monolayer and its orientation at the air-water interface.

3.4.1 Introduction to ellipsometry^{14,18,19}

Langmuir films at the air-water interface possess a large number of phases which may exhibit a different orientation, tilt azimuth or rotational degrees of freedom of the molecules. These features can be visualized by means of ellipsometry (Figure 3.15). Ellipsometry is an optical technique for the investigation of the optical properties (complex refractive index or dielectric function) of thin films, which is a very sensitive measurement technique and provides unequalled capabilities for thin film metrology which is non-destructive and contactless.

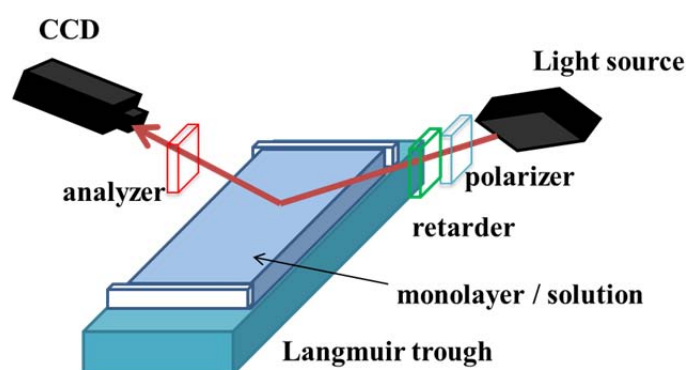


Figure 3.15 Schematic representation of ellipsometry for air-water interface film experiment

Analysis of the change of polarization of light reflected off a sample, ellipsometry can yield information about layers that are thinner than the wavelength of the incident light, even down to a single atomic layer. Ellipsometry can probe the refractive index or dielectric function tensor, which gives access to fundamental physical parameters and is related to a variety of sample properties, including morphology, crystal quality, chemical composition, or electrical conductivity. It is commonly used to characterize film thickness for single layers or multilayers.

Ellipsometry measures the change of polarization shape upon reflection or transmission on plane multilayers. The exact nature of the polarization change is determined by the sample

properties (thickness, complex refractive index or dielectric function tensor). Although optical techniques are inherently diffraction limited, ellipsometry exploits phase information and the polarization state of light, and can achieve angstrom resolution of thickness. Basically, it measures the complex reflectance ratio, ρ , which can be varied by Ψ and Δ . The polarization state of the light incident upon the sample may be decomposed into an s and a p component (the s component is oscillating perpendicular to the plane of incidence and parallel to the sample surface, and the p component is oscillating parallel to the plane of incidence). The amplitudes of the s and p components, after reflection and normalized to their initial value, are denoted by r_s and r_p , respectively. Ellipsometry measures the complex reflectance ratio, ρ (a complex quantity), which is the ratio of r_p over r_s :

$$\rho = \frac{r_p}{r_s} = \tan(\Psi)e^{i\Delta} \quad \text{Equation 3.9}$$

Thus, $\tan(\Psi)$ is the amplitude ratio upon reflection, and Δ is the phase shift between p and s polarization (difference). Since ellipsometry is measuring the ratio of two values (Ψ and Δ) it is very robust, accurate, and reproducible. For instance, it is relatively insensitive to scatter and fluctuations, and requires no standard sample or reference beam.

In situ ellipsometry during the growth of a thin film process is also possible by changing the mechanical setup which can include additional optical elements (mirrors, prisms, or lenses) for redirecting or focusing the light beam. In situ ellipsometry becomes more and more important as process control technique for thin film deposition and modification tools. Spectroscopic in situ ellipsometry uses multichannel detectors, for instance CCD detectors, which measure the ellipsometric parameters for all wavelength in the studied spectral range simultaneously.

3.4.2 Ellipsometry experiments of C15BAPTAhyd

To understand the behavior of BAPTA-series molecules bearing long alkyl hydrocarbon chains on the liposome bilayers membrane by ellipsometry, at first we tested the film of **C15BAPTAhyd** compound with Langmuir trough of the ellipsometry instrument by differing the number of Ca^{2+} equivalents in the MOPS and KCl bulk solution which was the same with the K_d determination experiment in the Chapter 2 and Chapter 4.

Figure 3.16 shows the required space per molecule would decrease by raising the Ca^{2+} ion concentration in the bulk solution in the trough. Which means once the **C15BAPTAhyd** molecular is paired with Ca^{2+} ion, the complexed molecules have less volume than uncomplexed ones. This could be explained by the crystal structures of the BAPTA ionophore before and after Ca^{2+} chelation as shown in Figure 3.17 and Figure 3.18. Interestingly, the

area per molecule can be lowered without KCl in the buffer constituent (Figure 3.16b), implying that the K^+ ion has an interaction with BAPTA acetic acid groups and will be examined and discussed later.

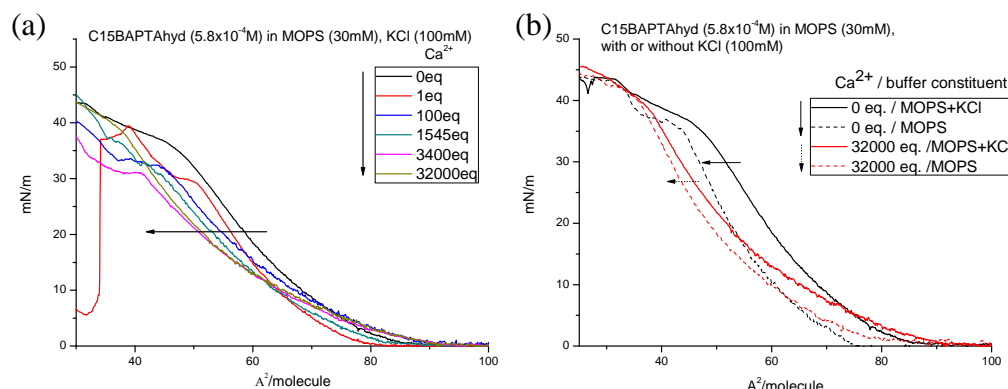


Figure 3.16 Langmuir film experiment: isotherms of **C15-BAPTAhyd** on MOPS (30 mM), KCl (100 mM) solution (a); on the MOPS (30 mM) with or without KCl (100 mM) (b)

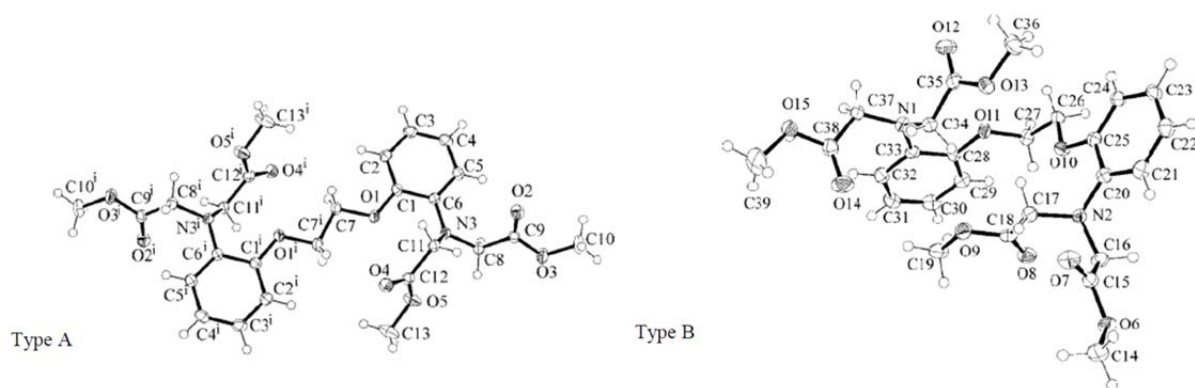


Figure 3.17 The two crystallographic forms A and B methyl ester of BAPTA.

The ester form of BAPTA crystallizes in two different crystallographic forms (Figure 3.17).²⁰ The first crystal form (type A) has a center inversion located between C7-C7i (symmetry code $i: -x, -y, -z$), and atoms N3, N3i, O1, O1i, C7, C7i are coplanar with the aromatic rings. At the half ethylene glycol center, the torsion angle of O1-C7-C7i-O1i is 179.89° which indicates that it is a trans conformation. For the second crystal form (type B), atoms N2, O10 and the composed aromatic ring of atoms C20-C25 are coplanar; atoms N1, O11 and the constituting second aromatic ring C28-C33 are also coplanar. The angle between two planes is 88° . For this conformation, the torsion angle of O10-C26-C27-O11 is 78.99° .

When paired with Ca^{2+} ion (Figure 3.18)²¹, the BAPTA octacoordinates calcium ion with a cis conformation through two nitrogen atoms N1 and N2 and two central ether oxygen O5 and O10 but with four carboxylates as shown in X-ray structure of the fluorinated derivative of BAPTA. Here, the torsion angle of O10-C12-C11-O5 is 60.8° .

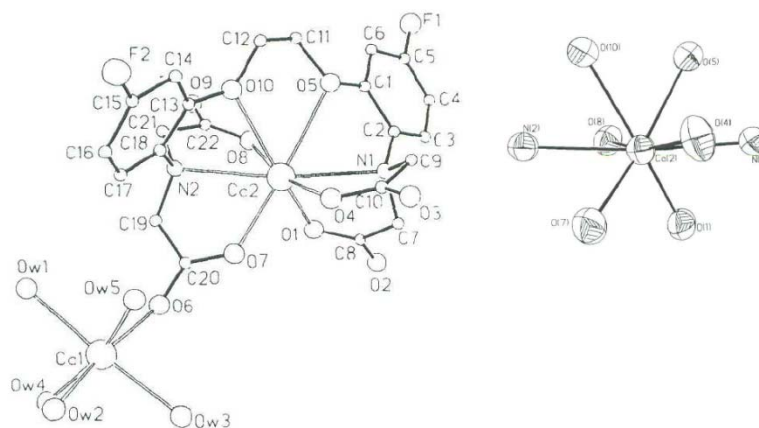


Figure 3.18 The X-ray structure of $\text{Ca}(\text{CaFBAPTA})\cdot 5\text{H}_2\text{O}$ is characterized by inequivalent Ca1 and Ca2 (left). Calcium is octacoordinated chelated by BAPTA (right)

Even if the X-ray structures are not exact conformations of molecules in the solution or monolayer environment, they still can be the reference for the trans to cis conformation trend in chelating with Ca^{2+} , and correlated with the decrease in the required area per molecule. Also, the KCl additive would increase the required area per molecule at the same surface pressure. This might be due to the exchange of the hydrogen and potassium counterion of the acetic acid ligands on the BAPTA molecules.

Ellipsometry and Langmuir film can be performed simultaneously and allow us to observe the surface morphology and thickness information when the **C15BAPTAhyd** is on the aqueous surface compressed from free molecule dispersion, monolayer, to multilayers. First, the ellipsometry experiments of **C15BAPTAhyd** on the different pH bulk solution are shown in Figure 3.19. And the deduced thickness profile which is described in the introduction is shown in Figure 3.19c.

From the Langmuir isotherms of the experiments with **C15BAPTAhyd** molecules on the different pH bulk solution, one can notice that neutral and basic bulk solution can give lower area per molecule than in acid subphase. At $\text{pH} = 7$, the area per molecule of P_c (collapse point) is $\sim 20 \text{ \AA}^2/\text{molecule}$, which is roughly equal to one alkyl chain area. Therefore the molecules have the most condense arrangement with vertical direction of the alkyl chain and water surface which gives the thickest monolayer. The observed minimum area per molecule at $\text{pH} = 7$ can be due to the fast exchange of hydrogen of four acetic acid group in the neutral environment without positive or negative electrostatic repulsion. On the other hand, increasing or decreasing pH would both lead to higher molecular areas and thinner monolayer thickness which result in bigger tilting of alkyl chain.

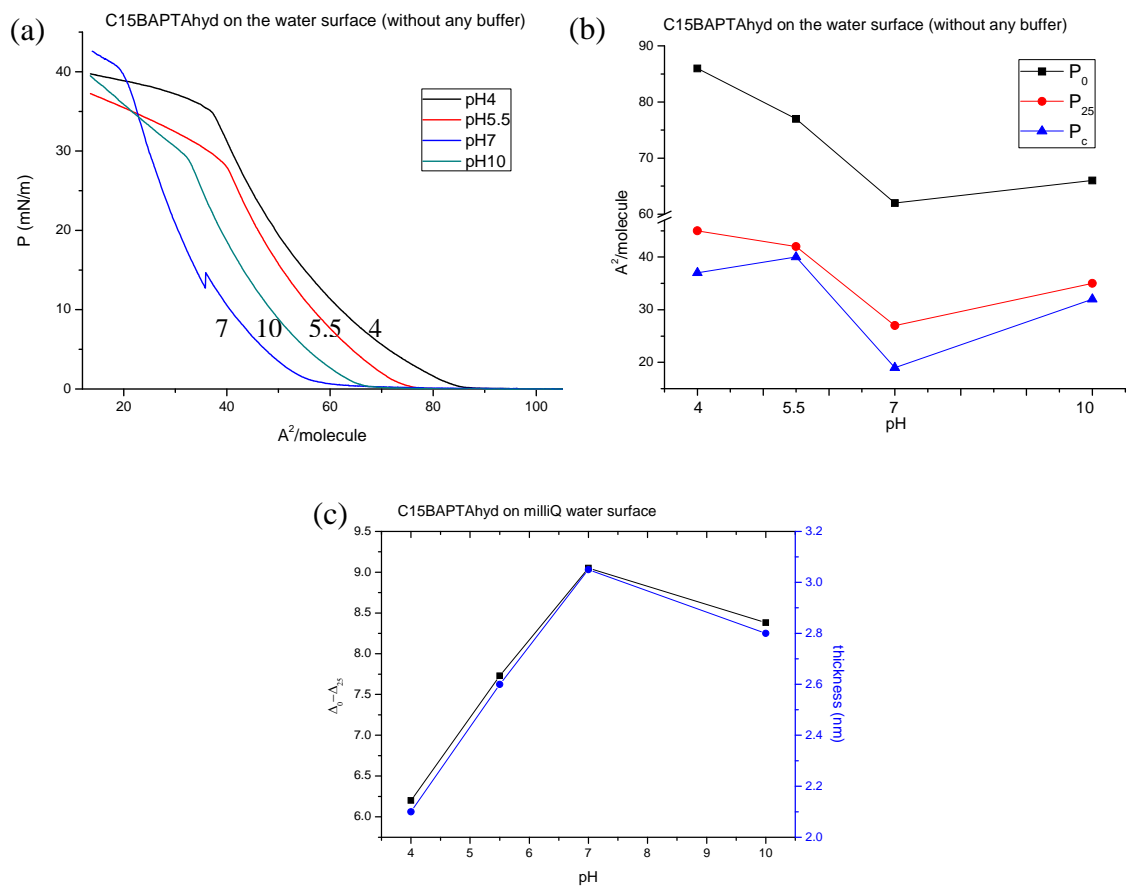


Figure 3.19 BAM experiment of **C15BAPTAhyd** on the water surface: (a) isotherms, (b) pH vs. area per molecule graph, (c) pH versus thickness profile at P_{25} . (ps. P_0 , P_{25} and P_c represent the points of surface pressure are 0, 25, and reaching collapse point)

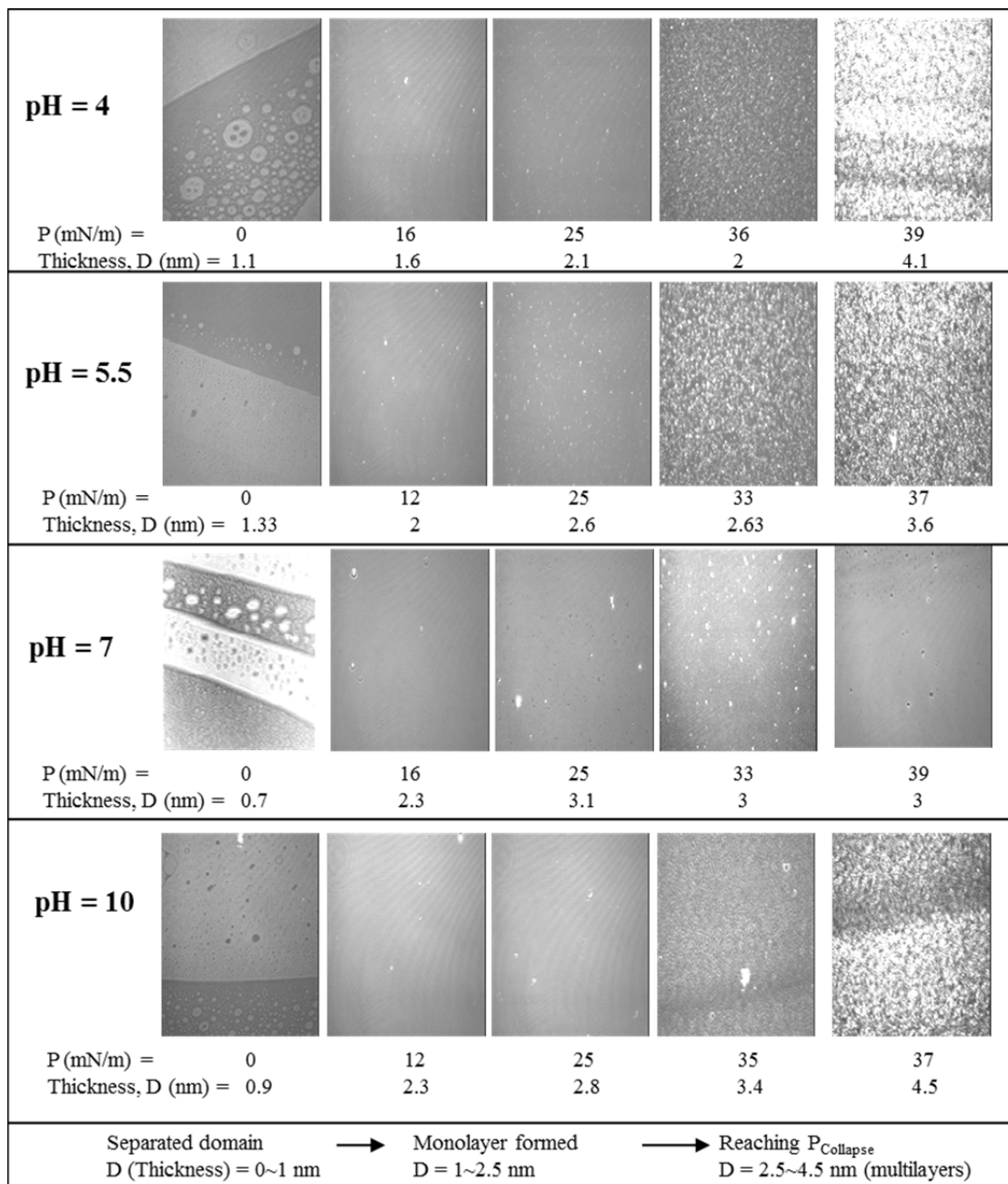


Figure 3.20 Ellipsometry measurements of surface image of **C15BAPTAhyd** on the water surface: from separate monolayer domain ($P = 0$ mN/m), continuous uniform monolayer ($P = 12\sim 30$ mN/m, gray level is higher therefore the brightness is needed to be lower to avoid camera saturation, to multilayers ($P > P_c$))

The observed surface morphology images by ellipsometry during the compression process are shown in Figure 3.20. Generally, in any pH conditions, **C15BAPTAhyd** compounds at $P = 0$ mN/m are freely dispersed with irregular domains. At $P = 12\sim 25$ mN/m, the molecules start to form continuous uniform monolayer with flat morphology. After $P > 33\sim 40$ mN/m, they reach the collapse point and form the multilayer morphology with irregular domain or aggregation.

After having a general idea of pH effect on the **C15BAPTAhyd** monolayer, we then

investigated the effect of buffer and added salt in the subphase as the experimental condition in the K_d determination or photoinduced ion-shuttle system (30 mM MOPS and 100 mM KCl buffer solution). The results are shown in Figure 3.21 and the morphology images are shown in the Figure 3.22 to Figure 3.24.

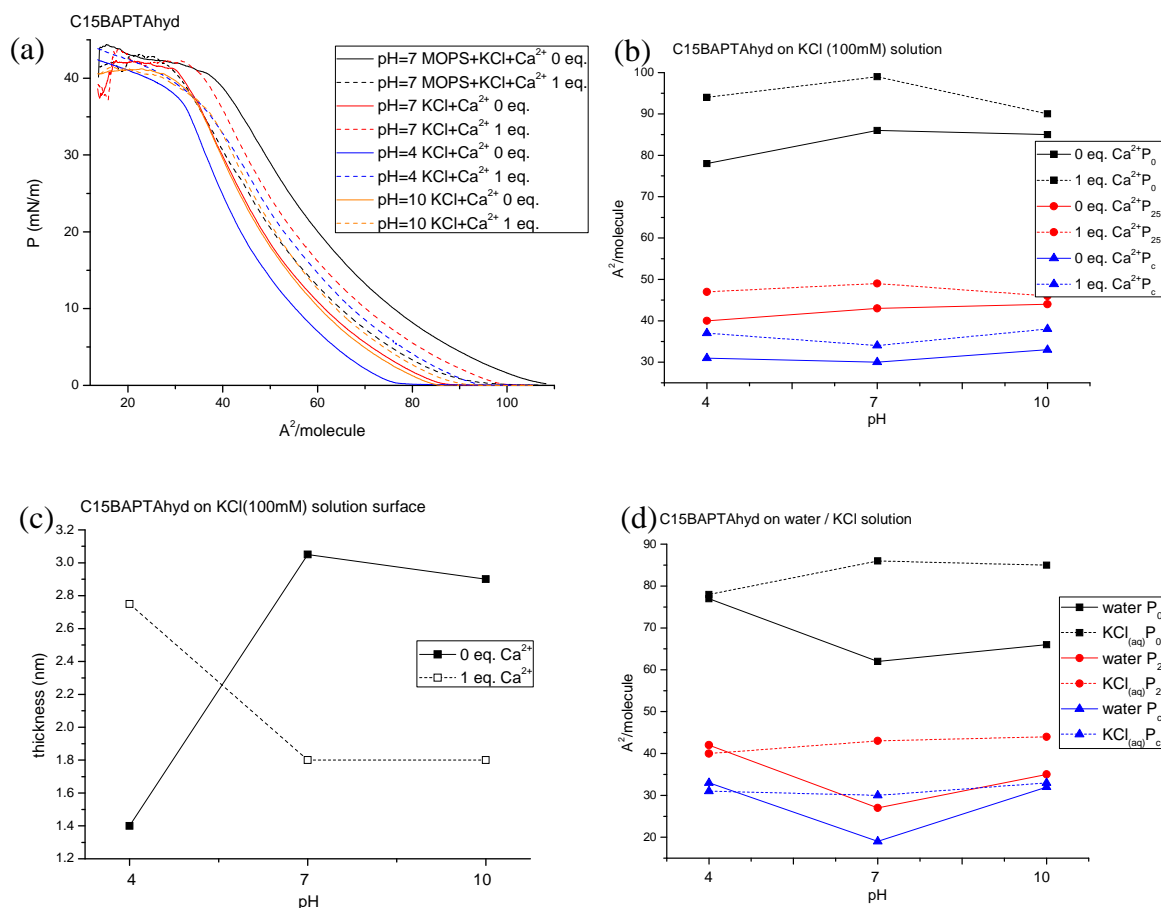


Figure 3.21 Ellipsometry measurements of **C15BAPTAhyd**: (a) isotherm on buffer (MOPS or KCl) solution; (b) graph of pH vs. area per molecule on KCl bulk solution surface; (c) pH vs. monolayer thickness on KCl bulk solution at $P = 25$ mN/m; (d) comparison of pH vs. area per molecular graph with or without KCl in the bulk solution

At first, when the subphase contains 30 mM 3-(N-morpholino)propanesulfonic acid (MOPS, pH buffer) and 100 mM KCl (ionic strength stabilizer) as shown in Figure 3.21a (black solid curve), the **C15BAPTAhyd** monolayer has a larger required area per molecule than the bulk solution with 100 mM KCl without MOPS (red solid curve). This means MOPS molecules would interfere with **C15BAPTAhyd** forming closest packing. When one equivalent of CaCl₂ is present with MOPS bulk solution (black dotted curve), it tends to lower the required area per molecular. This comes from the deprotonation and binding with Ca²⁺ by octacoordination as aforesaid explanation of X-ray.

The trend was changed when the bulk solution contains KCl without MOPS, as seen in the isotherms the required area per molecule increased for all pH value after adding Ca²⁺.

Moreover, the effect is most significant at pH 4 than pH 7 or 10 (Figure 3.21b) and the thickness versus pH diagram shows the adding of Ca^{2+} can decrease the monolayer thickness at pH 7 and 10 but reversed at pH 4 (Figure 3.21c). The trend difference with or without MOPS and the thickness change could be tentatively explained by:

1. In Figure 3.21d, the potassium ion can deprotonate the COOH groups at pH 7 and 10, this is due to the deprotonation of COOH and the increase of the repulsion between the head groups. At pH 10 the acetic acid groups are already deprotonated, that is why one can see the greater effect at pH 7. On the other hand, at pH 4 the potassium ion cannot deprotonate the carboxylic acid groups⁷, the effect of deprotonation by potassium ion is less and even reverse due to the acid environment
2. As mentioned, adding Ca^{2+} or forming an octacoordinate complex with Ca^{2+} should decrease the area per molecule of the monolayer with MOPS and KCl. Normally, existence of MOPS can increase the area per molecule to a certain distance thereby adding Ca^{2+} can really show the effect on decreasing area per molecule. The inverse tendency in the subphase without MOPS (Figure 3.21b) showed the adding Ca^{2+} leads to increases of area per molecule and has an apparent influence at pH 4 than that at pH 7 or 10. Supposedly, the space of **C15BAPTAhyd** seems inadequate in this case, therefore **C15BAPTAhyd** cannot really octacoordinate with Ca^{2+} to lower the area per molecule. As a result, adding Ca^{2+} in this subphase without MOPS might just further deprotonate the COOH; thereby increase the area per molecule as with MOPS.
3. Increasing area per molecule can lead to thickness decrease, but at pH 4 the result shows the opposite trend (thickness is increased, Figure 3.21c). At pH lower than pK_a or pK_a of aniline, hydrogen bond is more dominative by protonation of nitrogen of aniline group of BAPTA.
4. Compared to ATR-FTIR and PM-IRRAS result, adding Ca^{2+} has the biggest effect at pH 4 is reproduced in here (Figure 3.21b).

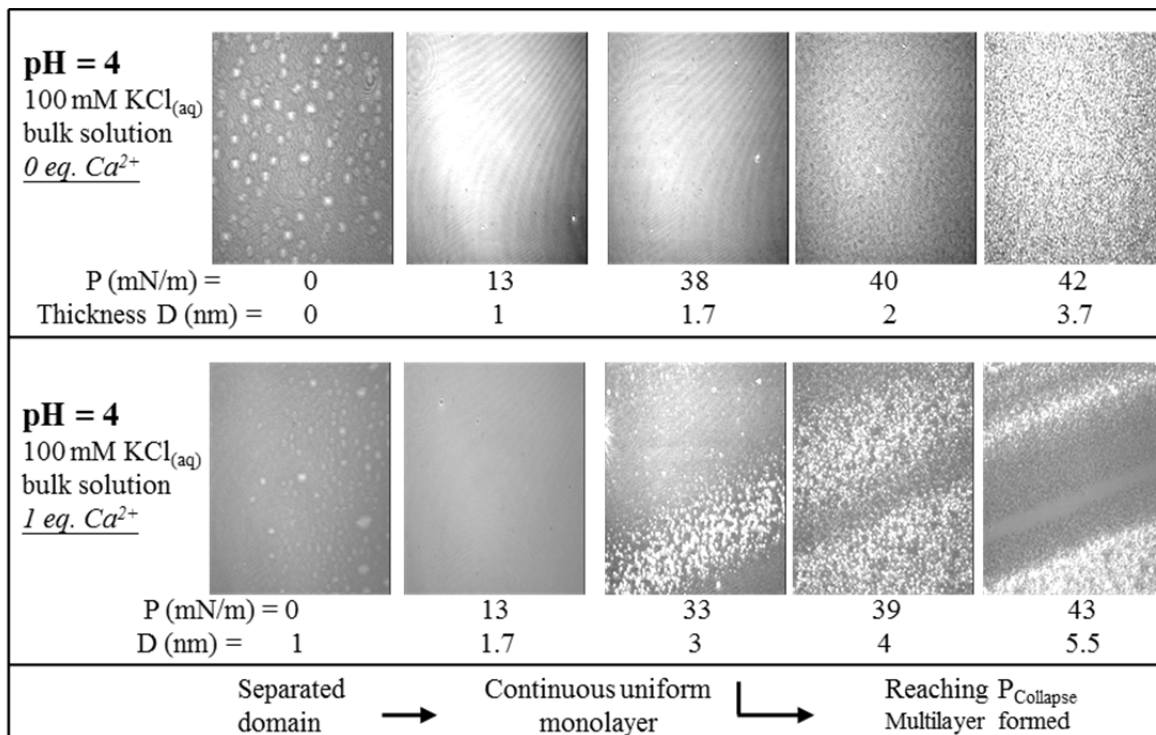


Figure 3.22 Ellipsometry measurements of surface image of **C15BAPTAhyd** on pH = 4, 100 mM $\text{KCl}_{(\text{aq})}$ solution

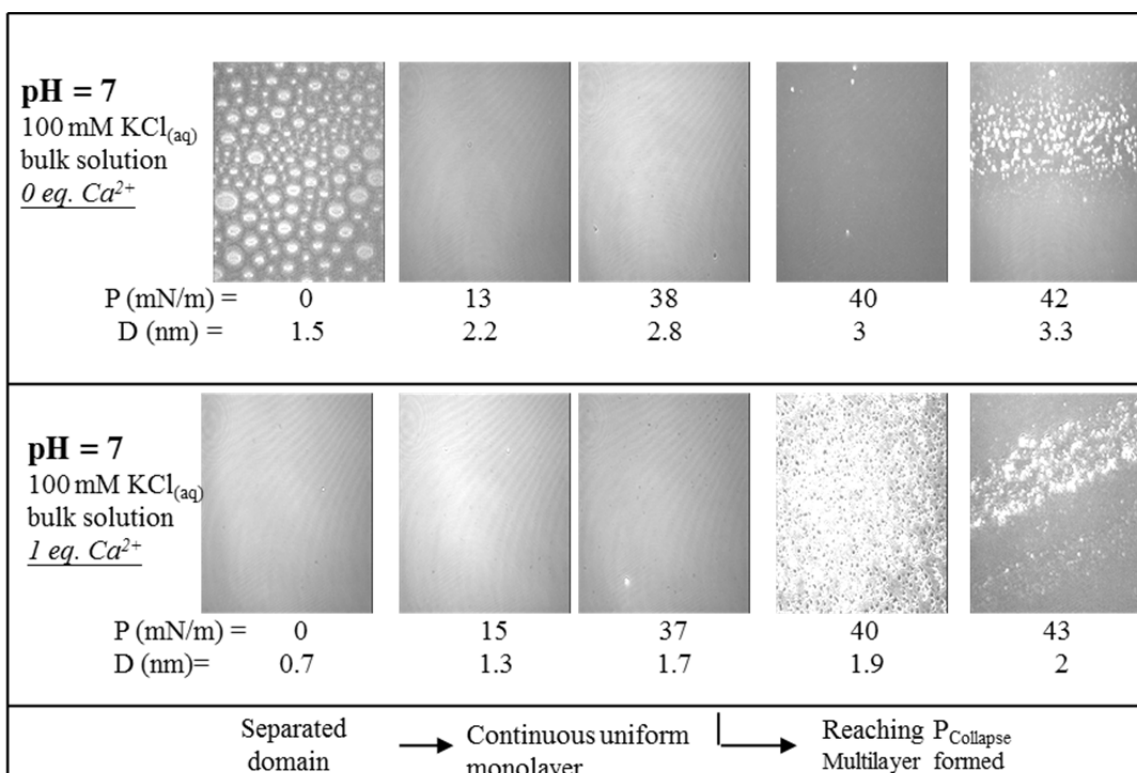


Figure 3.23 Ellipsometry measurements of surface image of **C15BAPTAhyd** on pH = 7, 100 mM $\text{KCl}_{(\text{aq})}$ solution

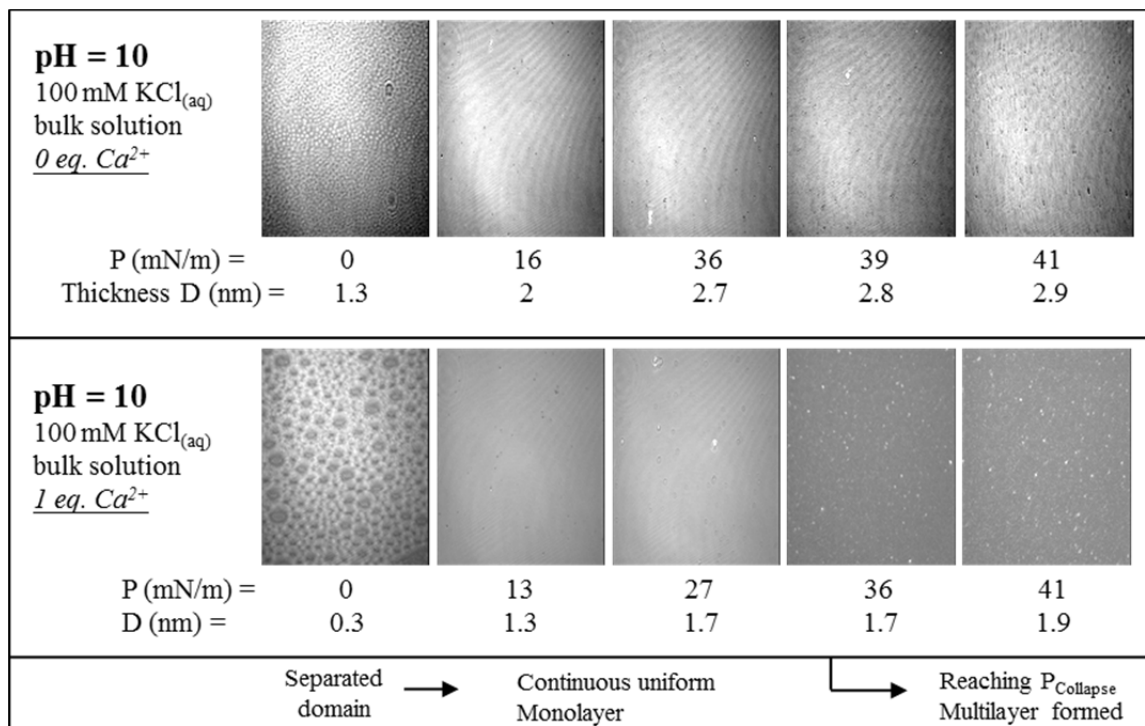


Figure 3.24 Ellipsometry measurements of surface image of **C15BAPTAhyd** on pH = 10, 100 mM KCl_(aq) solution

To conclude the effect of adding KCl, MOPS, and different Ca²⁺ concentration on the monolayer at pH 7 are shown in Figure 3.25a. The trend was obtained and shown in Figure 3.25b, with morphology images in Figure 3.26.

As mentioned above, changing the bulk solution from water to 100 mM KCl_(aq) can increase the required area per molecule by deprotonation and weakening the H-bond through the strong binding of potassium ion. Moreover, we observe that 30 mM MOPS as additive in the bulk solution can increase the area per molecule to the maximum. This indicates that the MOPS molecules interact with **C15BAPTAhyd** at the air-water interface. Therefore one can see the area increase by changing the bulk solution at first three points in the Figure 3.25b. Followed by adding Ca²⁺ from 0 to 5000 equivalents in the bulk, forming octa-coordinate structure starts to lower the space demanding and combined with thickness increase (Figure 3.25b & c). Even though the spacial demands, reach a stationary value with one equivalent of Ca²⁺, one can see the thickness of monolayer at 25 mN/m surface pressure is still increasing and reaching the maximum after 100 equivalents of Ca²⁺. It can be deduced that one equivalent of Ca²⁺ is not enough for Ca²⁺ binding of **C15BAPTAhyd** monolayer. The thickness increase may be due to the alkyl chain shift from tilt to perpendicular to the bulk surface during the conformational change occurred by Ca²⁺ complexation. If we compare these results with those obtained by ATR and PM-IRRAS, we can conclude that the affinity toward calcium is less in the monolayer situation as the observed higher K_d value while **BANI**-series fluoroionophores in the vesicle matrix. Noteworthy, **C15BAPTAhyd** forms star-shape aggregation morphology while compressing the Langmuir film to multilayers

situation under the buffered subphase without calcium as shown in Figure 3.26.

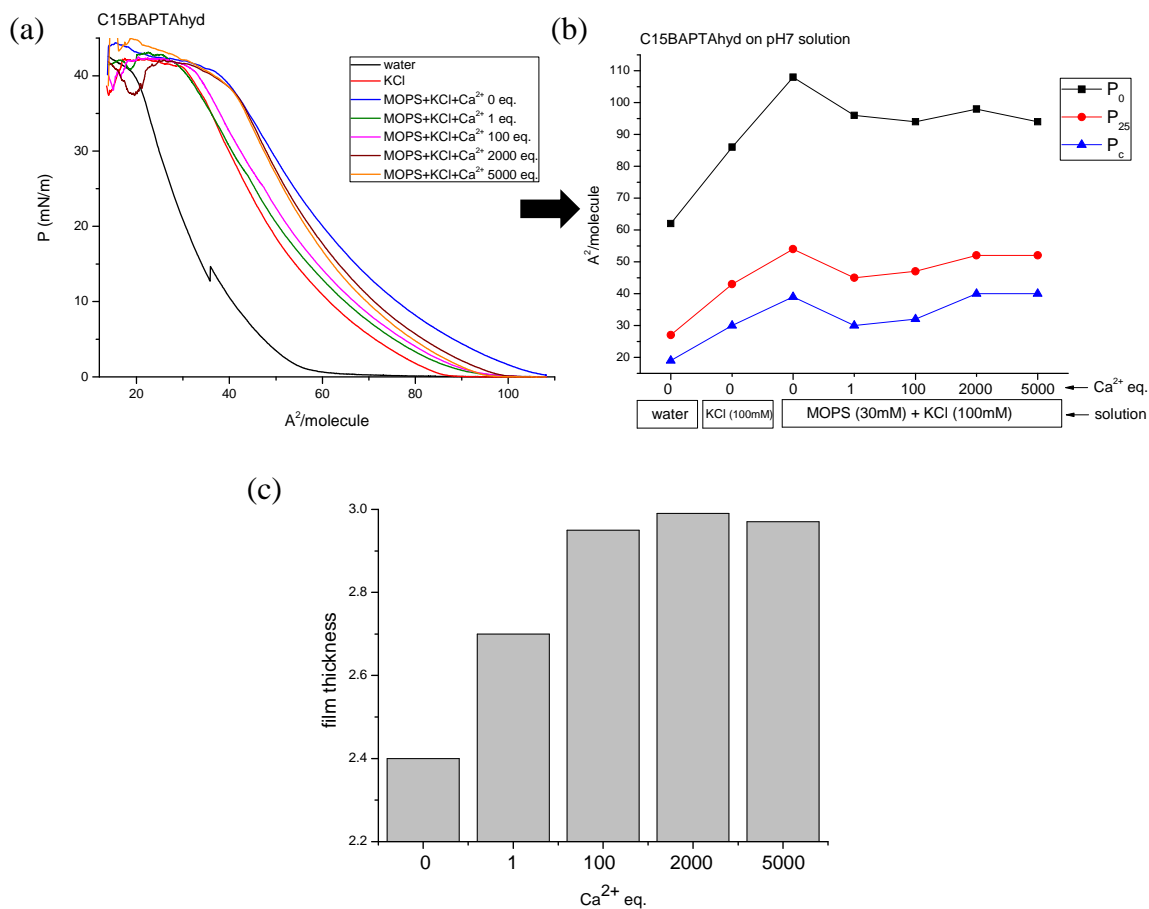


Figure 3.25 Surface pressure isotherm of **C15BAPTAhyd**: (a) isotherms of water, 100 mM KCl, 30 mM MOPS + 100 mM KCl + Ca²⁺ as bulk solution; (b) Ca²⁺ eq. vs. area per molecule graph on water, KCl, MOPS + KCl bulk solution at pH = 7; (c) Ca²⁺ eq. vs. thickness (nm) at P= 25 mN/m monolayer on MOPS + KCl bulk solution at pH = 7

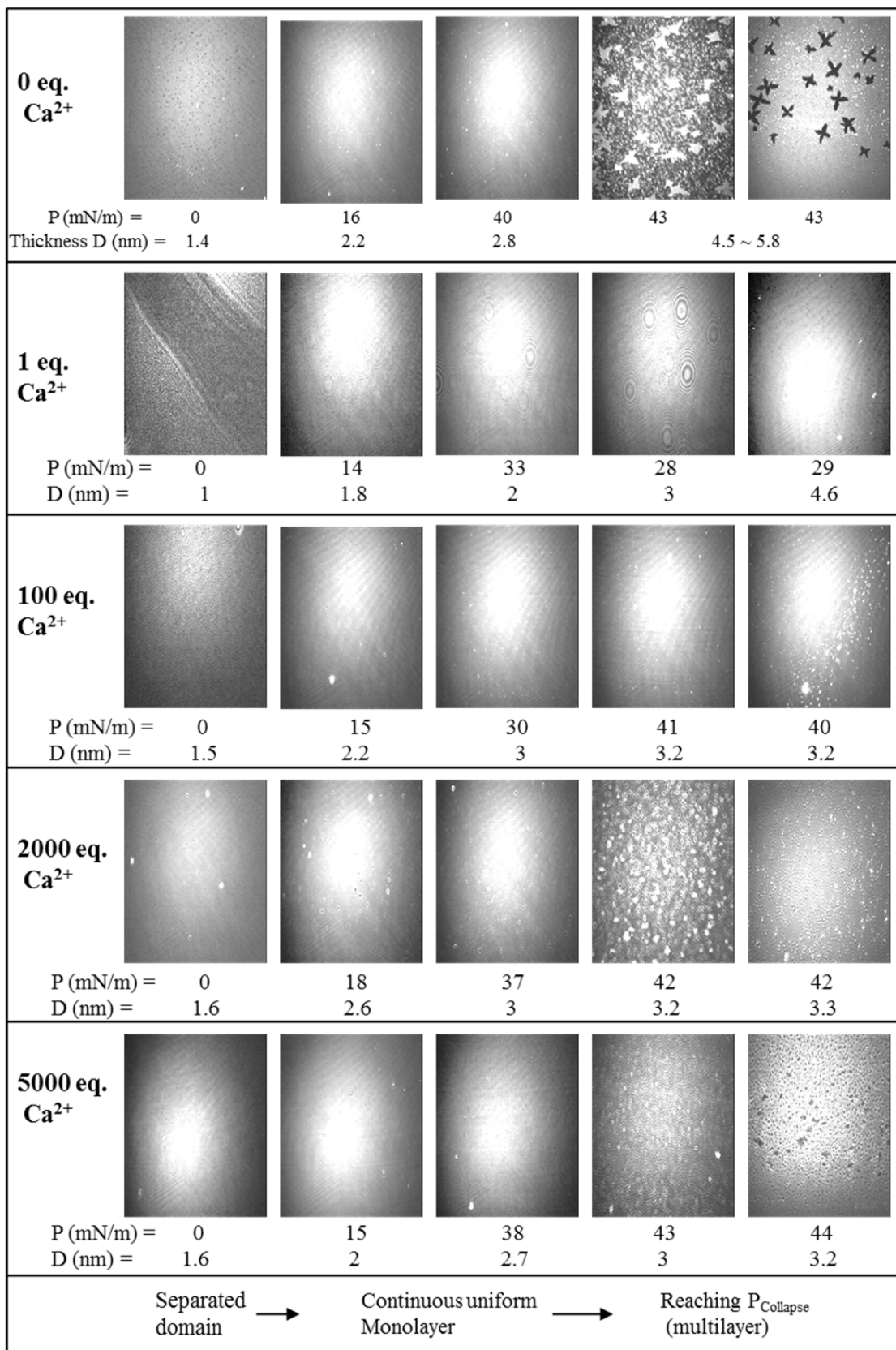


Figure 3.26 Ellipsometry measurements of surface image of **C15BAPTAhyd** on MOPS (30 mM) + KCl (100 mM) solution at pH = 7 with different equivalent of Ca²⁺

3.5 Conclusion

1. Two model compounds, **BAPTAhyd** and **C15BAPTAhyd**, were used to mimic the octa-coordinate Ca^{2+} chelating behavior of synthesized BAPTA parent compounds in free solution and in the vesicle liposome bilayers matrix, respectively.
2. Making use of IR techniques, ATR-FTIR was utilized to measure the properties of **BAPTAhyd** in the free solution. On the other hand, PM-IRRAS and ellipsometry combining with Langmuir isotherms allow us to measure **C15BAPTAhyd** compound while forming monolayer / multilayers accompanied with their surface morphology changing.
3. ATR-FTIR and PM-IRRAS results show that the pK_a values of these two BAPTA compounds are similar at ~ 6 , but the affinity towards to Ca^{2+} is about 10~100-fold less in the monolayer environment. For **BAPTAhyd** in the free solution, one equivalent of Ca^{2+} is enough to form a $\text{Ca}^{2+}:\text{BAPTA}$ pair, but a larger number of equivalents is needed for the **C15BAPTAhyd** monolayer.
4. Generally, the existence of additives (ex. buffering compounds: KCl, MOPS) can increase the required area per molecule of **C15BAPTAhyd** monolayer. The deprotonation along with conformational change by adding Ca^{2+} can lead to the decrease of area per molecule and increase of monolayer thickness.
5. The existence of potassium and calcium ions can help to deprotonate the carboxylic acid group by observing the infrared band and Langmuir isotherm, but the hydrogen bond can dominate in the low pH bulk solution, especially low enough to protonate the nitrogen of aniline group in the BAPTA parent. This leads to unusual behavior differing from neutral or basic pH condition while adding Ca^{2+} .

3.6 References

1. L. K. Tamm, S. A. Tatulian, *Quarterly Reviews of Biophysics*, **1997**, *30*, 365.
2. Probing the structural environment of carboxyl groups in natural organic molecules using infrared spectroscopy (<http://geoweb.princeton.edu/research/geochemistry/research/>)
3. F. López-García, J. Villalaín, J. C. Gómez-Fernández, P. J. Quinn, *Biophys. J.* **1994**, *66*, 1991.
4. R. Johann, D. Vollhardt, H. Mohwald, *Colloids Surf. A* **2001**, *182*, 311.
5. (a) D. K. Beaman, E. J. Robertson, G. L. Richmond, *J. Phys. Chem. C*, **2011**, *115* (25), 12508. (b) J. Kutscher, A. Gericke, H. Huhnerfuss, *Langmuir* **1996**, *12*, 1027.
6. P. B. Miranda, Q. Du, Y. R. Shen, *Chem. Phys. Lett.* **1998**, *286*, 1.
7. C. Y. Tang, H. C. Allen, *J. Phys. Chem. A* **2009**, *113*, 7383.
8. E. Le Calvez, D. Blaudez, T. Buffeteau, B. Desbat, *Langmuir*, **2001**, *17*, 670.
9. T. Tanaka, S. Nagao, H. Ogawa, *Analytical Sciences*, **2001**, *17*, i1081.
10. www.perkinelmer.com, PerkinElmer Life and Analytical Sciences
11. P. Griffiths, and J. Haseeth, *Chemical Analysis 83: Fourier Transformation Infrared Spectrometry*, Wiley, **1983**.
12. V. Zamlynny, I. Zawisza, J. Lipkowski, *Langmuir*, **2003**, *19*, 133.
13. (a) D. Blaudez, J-M. Turllet, H. Dufourcq, D. Bard, T. Buffeteau, and B. Desbat, *J. Chem. Soc. Faraday Trans.*, **1996**, *92*, 525. (b) Technology introduction guide of Bruker Optics. (c) Technology introduction guide of KSV NIMA.
14. A. Banc, B. Desbat, D. Renard, Y. Popineau, C. Mangavel, L. Navailles, *Langmuir*, **2007**, *23*, 13066.
15. S. Manet, R. Oda, *doctorate thesis of Bordeaux I university*, **2007**, 3472.
16. W. Hubner, H. H. Mantsch, F. Paltauf, & H. Hauser, *Biochemistry*, **1994**, *33*, 320.
17. M. Röefzaad, T. Klüner, I. Brand, *Phys. Chem. Chem. Phys.*, **2009**, *11*, 10140.
18. R. M. A. Azzam and N. M. Bashara, *Ellipsometry and Polarized Light*, Elsevier Science Pub Co, **1987**.
19. I. Ohlidal and D. Franta, *Progress in Optics*, **2000**, *41*, 181.
20. M. Rademeyer, D. A. Barkhuizen, G. E. M. Maguire, *Acta Cryst.* **2004**, *E60*, o213.
21. J. T. Gerig, P. Singh, L. A. Levy, R. E. London, *J. Inorg. Biochem.*, **1987**, *31*, 113.

Chapter 4

Implementation of Photocontrolled Ion-Shuttle in Nanodomains

A range of novel amphiphilic and non-amphiphilic synthetic photoactive molecules were characterized and reported in Chapter 2, notably for the complexation and liberation of calcium ions. Model compounds were also studied in the last chapter using a range of techniques including Langmuir films, surface analysis and infrared spectroscopies. In order to implement the photoactivated ion-shuttle system in nanoscopic compartments such as vesicles, in this chapter several approaches will be introduced and utilized to accomplish this goal:

- *Chapter 4.1*, organic compounds in multi-lamellar vesicle (MLV) matrices will be studied at first by means of small angle X-ray scattering.
- *Chapter 4.2*, combining synthetic Ca^{2+} -acceptors, **BANI** series fluoroionophores, with different methods of giant unilamellar vesicles (GUVs) are described and detected by fluorescence microscopy.
- *Chapter 4.3*, confocal scanning laser microscopy with fluorescence-lifetime imaging microscopy (FLIM) is utilized to investigate the lifetime of prepared fluorescent GUVs where the **BANI** fluoroionophore is confined on lipid bilayers.
- *Chapter 4.4*, K_d measurements of synthetic Ca^{2+} -acceptors (**BANI2** and **BANI3**) in the small unilamellar vesicles (SUVs) are performed to understand the influence on Ca^{2+} affinity in different hydrophobic liposome environments.
- *Chapter 4.5*, individual components are assembled to achieve the goal of photoactivated ion-shuttle systems inside or outside SUV liposome matrix solution.

4.1 Pretest of trial model compounds in multi-lamellar vesicles (MLVs)

4.1.1 Introduction to small angle X-ray scattering (SAXS) for lamellar structure

Small angle X-ray scattering (SAXS) is a remarkably informative technique for probing macromolecular structure. SAXS provides information about the size, shape, compactness, and molecular weight of macromolecules in solution. In contrast to X-ray crystallography, its structural information is low resolution, $\sim 10 \text{ \AA}$. The power of this approach lies in reporting functional (e.g., unconstrained) conformations and dynamics.¹

A schematic of a typical SAXS experiment is shown in Figure 4.1. Each electron in the sample reradiates a spherical wave upon excitation by the electric field of the incident X-ray beam. For regular SAXS, we consider elastic scattering into angles within a few degrees of the $\theta = 0$, or forward, direction. The amplitude of the scattered wave is computed by

considering phase differences between all waves scattered into a particular direction, characterized by the angle 2θ or the momentum transfer:

$$q = 4\pi \sin\theta / \lambda \quad \text{Equation 4.1}$$

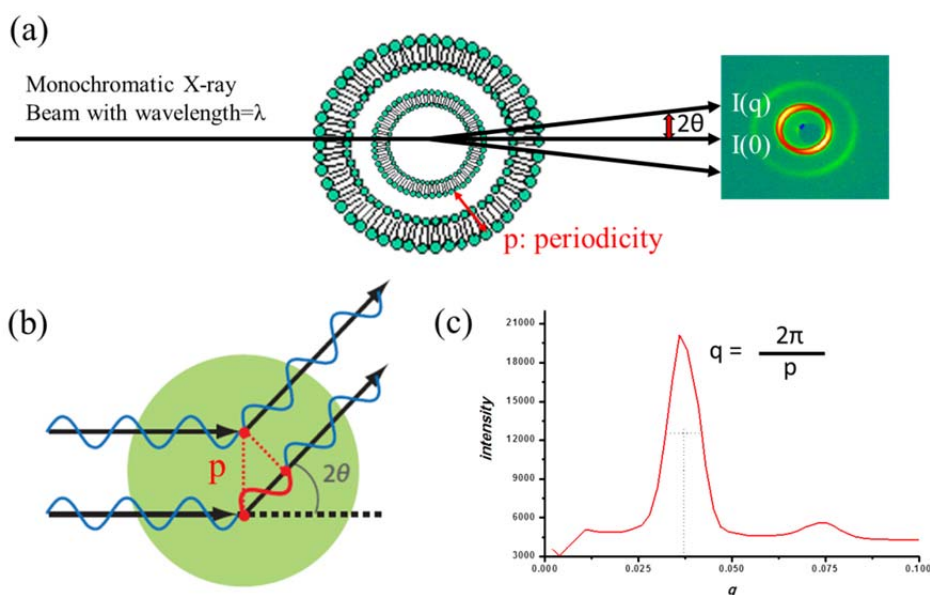


Figure 4.1 (a) Schematic of a SAXS experiment; (b) The phase difference between scattered waves (showed in red wave) when scattering angle is 2θ ; (c) Example of lamellar vesicle data, periodicity can be deduced by observed q value

The difference between the scattered waves caused by the distance r of two scatterers is $q \cdot r$. Once a sample has a periodic arrangement structure (ex. multi-lamellar vesicle, MLV), one can observe an apparent interference fringe at the place where $q \cdot r$ value is 2π . Therefore, by observing the interference angle or q value, the internal periodicity, p , of the lamellar structure material can be deduced:

$$p = 2\pi / q \quad \text{Equation 4.2}$$

4.1.2 Experimental section

Some amphiphiles form multi-lamellar vesicles, MLVs, above certain concentration percentage of amphiphiles in the water. Amphiphilic compounds, $(C_{12})_2Ac$, $(C_{14})_2Ac$, $(C_{16})_2Ac$, and **12-2-12 FF** (structures are shown in the top of Figure 4.2 & 4.3) were mixed with water (5 to 50 wt%) and were investigated by SAXs to determine in which concentration range they form MLVs. The detectable concentration for $(C_{12})_2Ac$, $(C_{14})_2Ac$, and $(C_{16})_2Ac$ is from 10 % to 50 %, as shown in Figure 4.2 and Figure 4.3. The deduced periodicity values by Equation 4.2 are shown in Figure 4.4. With the experimental setup we have used, we could not detect peaks under 0.02 \AA^{-1} . In the cases of $(C_{16})_2Ac$ and **12-2-12 FF**, it is likely to have lamella peaks for 10 and 20 wt %, but only at $q < 0.02 \text{ \AA}^{-1}$ ($p > 300 \text{ \AA}$). We are now repeating

experiments with a new setup which will allows us to detect these peaks.

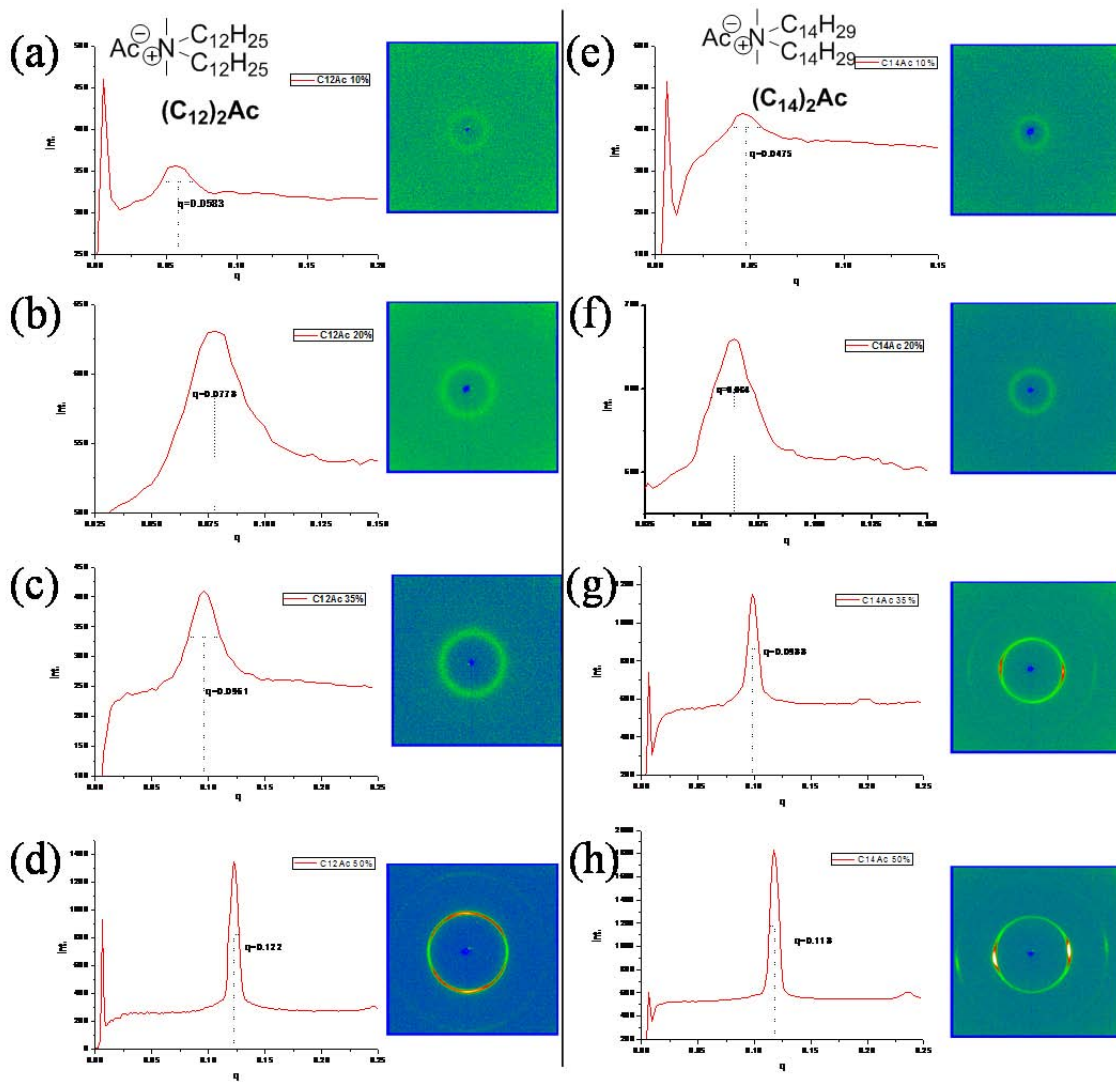


Figure 4.2 SAXS experiment: $(C_{12})_2Ac$ amphiphile forms MLV in the water at concentration of (a)10 wt%, (b) 20 wt%, (c) 35 wt%, (d) 50 wt%; $(C_{14})_2Ac$ amphiphile at (e)10 wt%, (f) 20 wt%, (g) 35 wt%, (h) 50 wt%

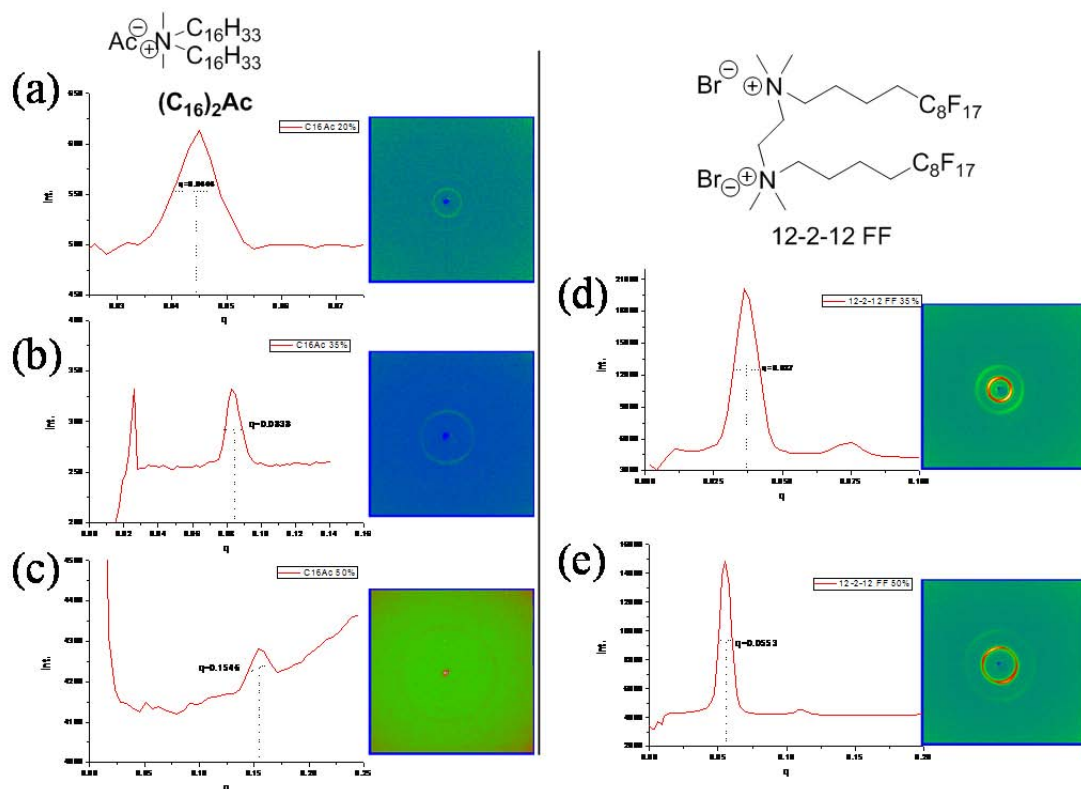


Figure 4.3 SAXS experiment: $(C_{16})_2Ac$ amphiphile forms MLV in the water at concentration of (a) 20 wt%, (b) 35 wt%, (c) 50 wt%; **12-2-12 FF** amphiphile at (d) 35 wt%, (e) 50 wt%

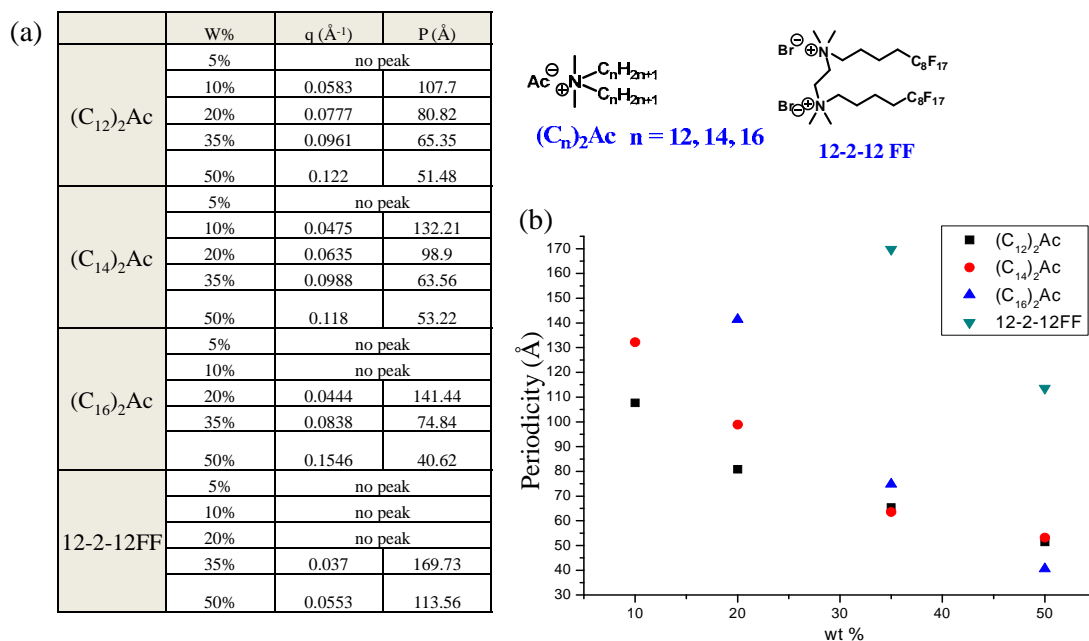


Figure 4.4 (a) Experimental q (\AA^{-1}) values by SAXs and the deduced periodicity p (\AA) values from $p = 2\pi/q$ of $(C_{12})_2Ac$, $(C_{14})_2Ac$, $(C_{16})_2Ac$, and **12-2-12 FF** at different concentrations in water; (b) diagram showing periodicity value vs. wt%

From the tendency of the MLV periodicity versus concentration in the Figure 4.4, the preliminary results can be concluded:

1. For these amphiphilic molecules, concentration increase leads to lower periodicity of MLVs.
2. At a fixed concentration, increasing the hydrocarbon chain length or changing hydrocarbon chain to fluorinated chain increase the periodicity

Besides, to further investigate the hydrophobic part of the $(C_n)_2Ac$ amphiphiles, infrared spectra were collected and shown in Figure 4.5.

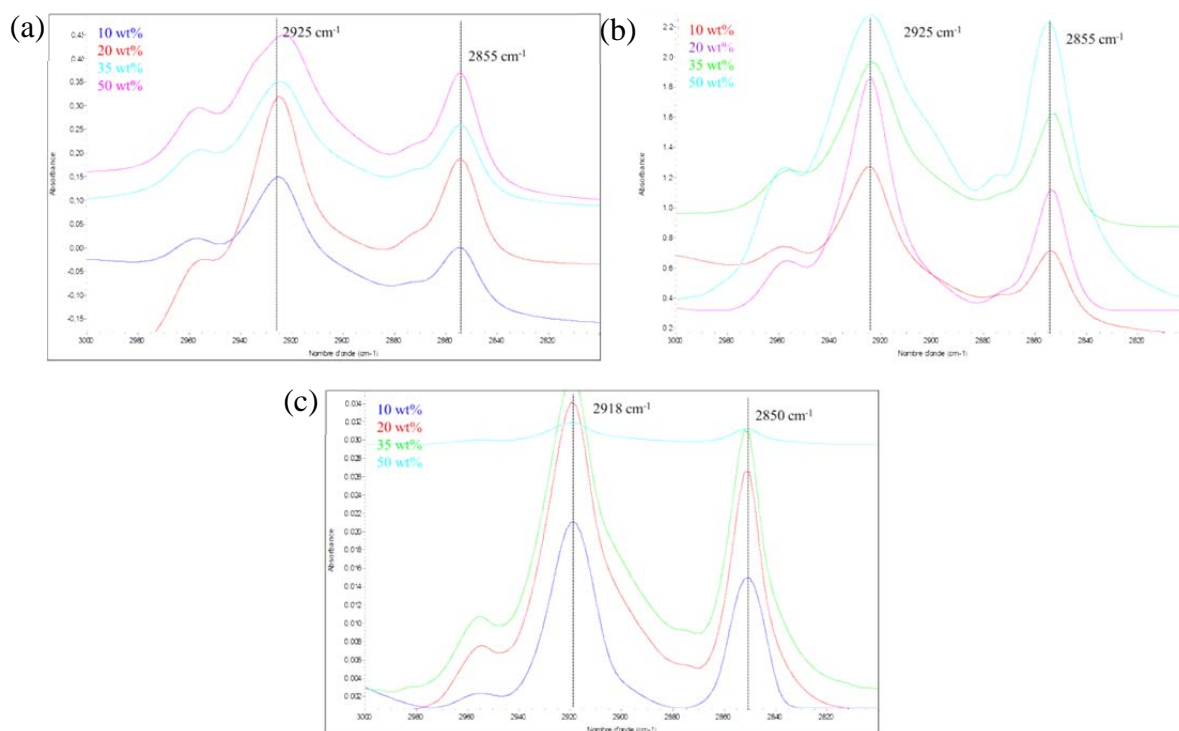


Figure 4.5 IR-spectra of CH₂ stretching modes of amphiphiles (a) $(C_{12})_2Ac$, (b) $(C_{14})_2Ac$, (c) $(C_{16})_2Ac$ in 10~50 wt% aqueous solution.

In the cases of $(C_{12})_2Ac$ and $(C_{14})_2Ac$ (Figure 4.5a & b), IR spectra show two major absorption bands centered at 2925 cm⁻¹ and 2855 cm⁻¹, corresponding to the asymmetric methylene ν_{as} (CH₂) and the symmetric methylene ν_a (CH₂) stretching modes, respectively. The frequencies of the CH₂ stretching modes indicate that hydrocarbon chains exhibit in a liquid disordered state, having a numerous of gauche conformations in the cases of $(C_{12})_2Ac$ and $(C_{14})_2Ac$. In the case of $(C_{16})_2Ac$ (Figure 4.5c), the wavenumbers of the asymmetric methylene ν_{as} (CH₂) and the symmetric methylene ν_a (CH₂) stretching modes are 2918 cm⁻¹ and 2850 cm⁻¹ respectively. The shifts indicate that the alkyl chains are in the gel phase.

As mentioned, our goal is to investigate the effect of the addition of organic compounds (model ion-chelators for fluoroionophore) in MLVs. Hence two added compounds, **N1** and **N2**, and their hydrolyzed analogues, **N1COOK** and **N2COOK**, were added to the aforesaid amphiphiles with fixed concentration (Figure 4.6). The results for 0.05 equivalent of additives

in the MLVs of 20 wt% $(C_n)_2Ac$ or 35 wt% **12-2-12 FF** are compiled in Table 4.1. And the data of SAXS are represented in Figure 4.7.

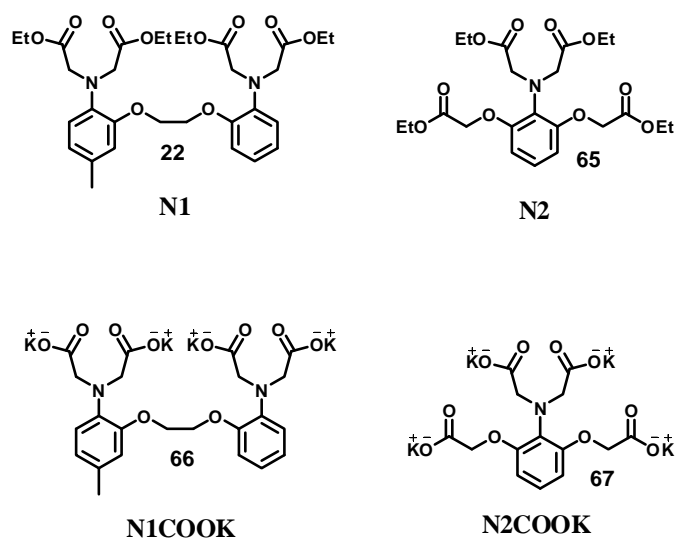
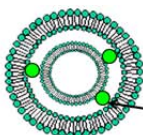


Figure 4.6 Structures of trial organic compounds, **N1**, **N2**, **N1COOK**, and **N2COOK** as additives in MLVs

0.05 eq. in H ₂ O	N1	N2	N1COOK	N2COOK
(C₁₂)₂Ac 20%	⊘	⊙	?	?
(C₁₄)₂Ac 20 %	⊘	⊙	⊙	⊙
(C₁₆)₂Ac 20%	⊘	⊙	?	⊙
12-2-12 FF 35%	⊘	⊘	⊘	⊙



⊘ : heterogeneous & precipitation

⊙ : with peak by SAXS

?: without peak by SAXS

Table 4.1 Experimental results of additives, **N1**, **N2**, **N1COOK**, and **N2COOK**, in MLVs with a given concentration of amphiphiles

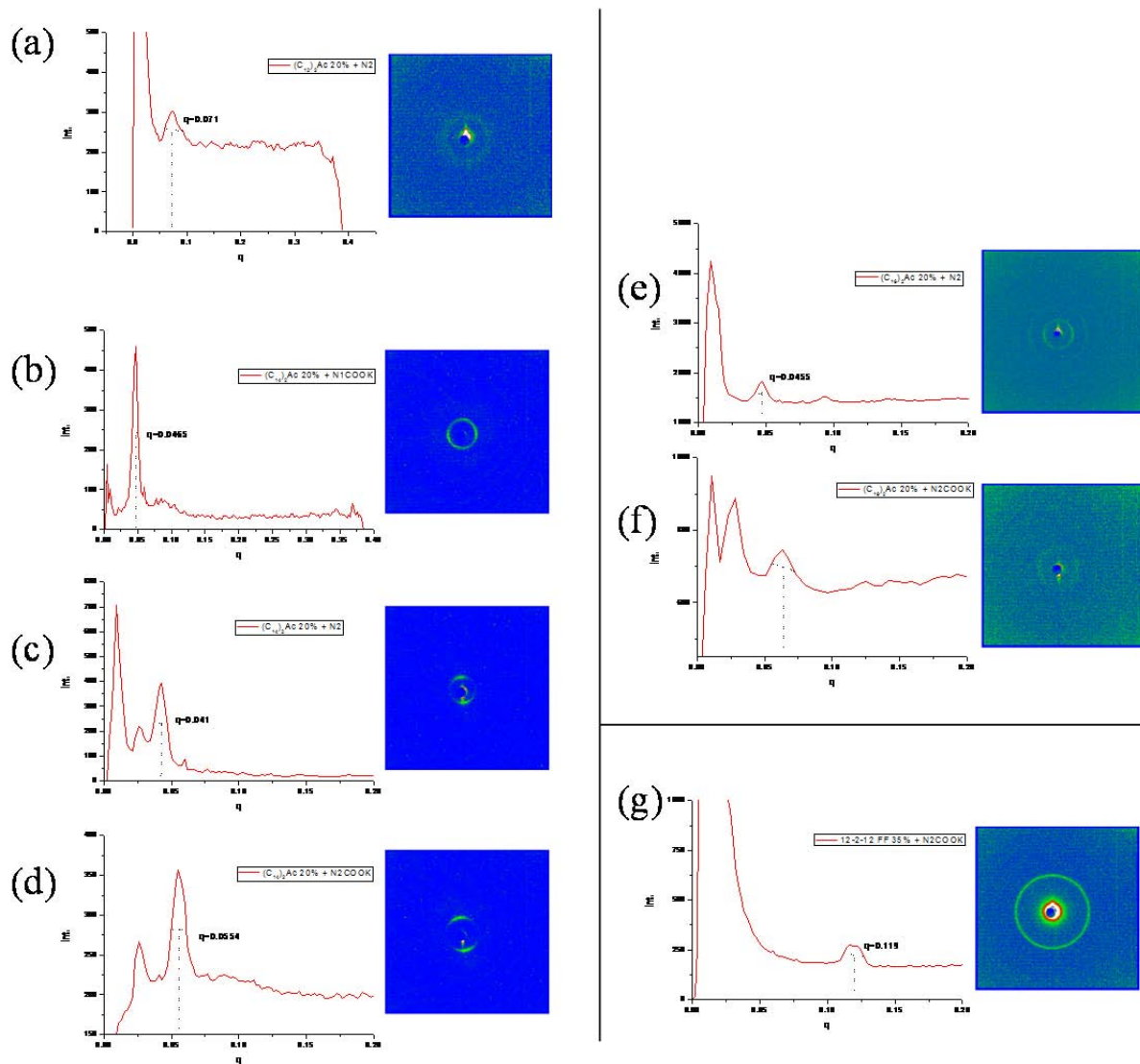


Figure 4.7 SAXS experiment: detectable condition of fixed concentration with 0.05 equivalent of additive, (a) $(C_{12})_2Ac$ 20 wt% with N_2 , (b) $(C_{14})_2Ac$ 20 wt% with $N1COOK$, (c) $(C_{14})_2Ac$ 20 wt% with N_2 , (d) $(C_{14})_2Ac$ 20 wt% with $N2COOK$, (e) $(C_{16})_2Ac$ 20 wt% with N_2 , (f) $(C_{16})_2Ac$ 20 wt% with $N2COOK$, (g) 12-2-12 FF 35 wt% with $N2COOK$.

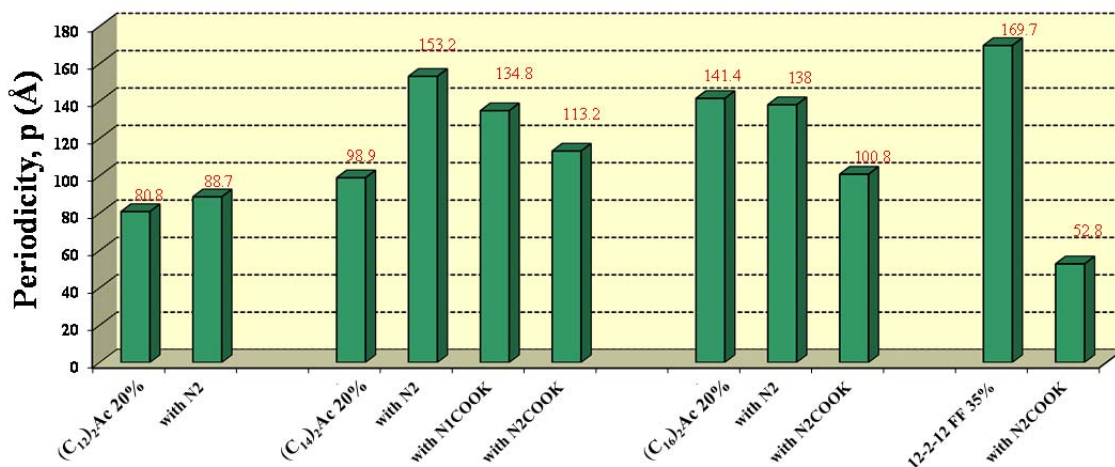


Figure 4.8 Affected periodicity values by adding additives of MLVs

To conclude the influence of adding model organic compounds into MLVs, the periodicity values of MLVs are shown in Figure 4.8. The observed results and explanation are:

1. For low periodicity amphiphilic compounds such as $(C_{12})_2Ac$ and $(C_{14})_2Ac$, adding a non-charged molecule such as **N2** will increase the periodicity.
2. For high periodicity amphiphilic compounds as $(C_{16})_2Ac$ and **12-2-12 FF**, inner space between layers is enough for non-charged molecules. As a result, the addition will not significantly increase the periodicity.
3. When the additive is hydrolyzed and charged, the electrostatic effect between carboxylate group of additives and ammonium head groups of amphiphiles will lower the periodicity as seen in $(C_{14})_2Ac$ and $(C_{16})_2Ac$ cases. Moreover, a notable periodicity decrease in the case of **12-2-12 FF** might be due to a stronger interaction with the two ammonium head groups of the gemini structure.
4. The spatial and electrostatic interaction between amphiphiles and confined compounds can affect the post-mix result in forming lamellar structure, periodicity, and vesicle size, etc.

4.2 Incorporation of synthesized Ca^{2+} -acceptors into GUVs

The results above show the hydrolyzed **N1** and **N2** interact with cationic vesicles. In this section, the GUVs (giant unilamellar vesicles) will be used to confine our synthesized Ca^{2+} -acceptor (**BANI** fluoroionophore). The method to fabricate GUVs (chapter 4.2.1), observe the mixture of GUVs and fluoroionophore, by means of fluorescence microscopy (Chapter 4.2.2) and confocal scanning laser microscopy with fluorescence-lifetime imaging microscopy (Chapter 4.3), will be introduced and discussed hereafter.

4.2.1 Introduction to GUV

GUVs (diameter ~5-100 μm) represent a potential model system for mimicking liposome membranes. In situ formation of mixture system on individual GUVs can be directly visualized and studied by optical microscopy due to the large, unilamellar structure. The dynamics of membrane domains, vesicle shape and morphology transformations can be clearly followed as well. They have been widely used to study lipid dynamics², lipid domain (raft) formation³, elastic properties of membranes and lipid-DNA interactions (Angelova et al.)^{4,5}, vesicle shape changes⁶, membrane tube formation⁷, and membrane fusion⁸.

The mechanism of formation and properties of GUVs have been studied since the 1980s. GUVs can be prepared by drying lipids dissolved in organic solvent (chloroform or chloroform/ methanol mixtures) followed by addition of distilled water. Water penetrates the dried lamellar structures, and GUVs are formed spontaneously due to membrane fusion processes. Formation appears to be optimal if a fraction of anionic lipids is incorporated or can be promoted by the addition of divalent cations (Ca^{2+} or Mg^{2+}) when using only neutral lipids.⁹ In addition, AC electric fields^{10,11} (electroformation) have been reported to facilitate or impede the formation process as represented in Figure 4.9, but with the drawback that electroformation tolerates low (~ 10 mM) ion concentrations during the GUV-formation process.¹² In order to test the effect of compartmentalization of **BANI** fluoroionophore by unilamellar vesicles, GUVs were used as a model system.

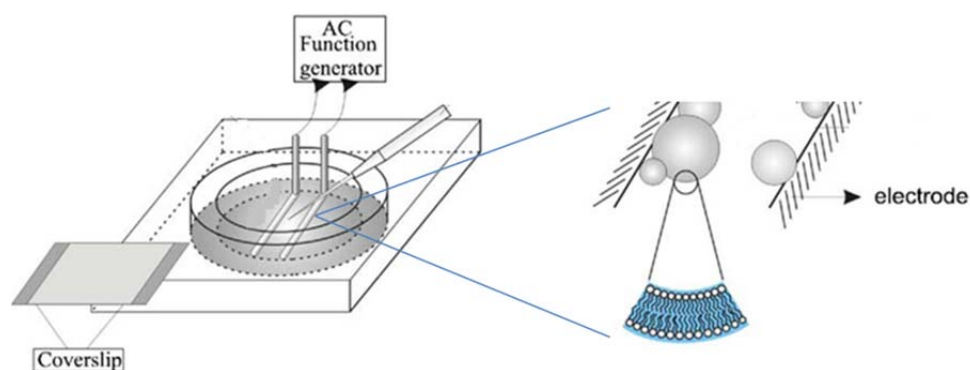


Figure 4.9 Schematic presentation of electroformation of GUVs¹³

The GUVs or SUVs can be formed from different phospholipids. For example, the DMPC or DOPC (neutral lipid), DOPG (anionic), and DOTAP (cationic) are common lipids and will be used in our unilamellar vesicle system. Some key physical properties and molecular structures are presented in Table 4.2 and Figure 4.10.

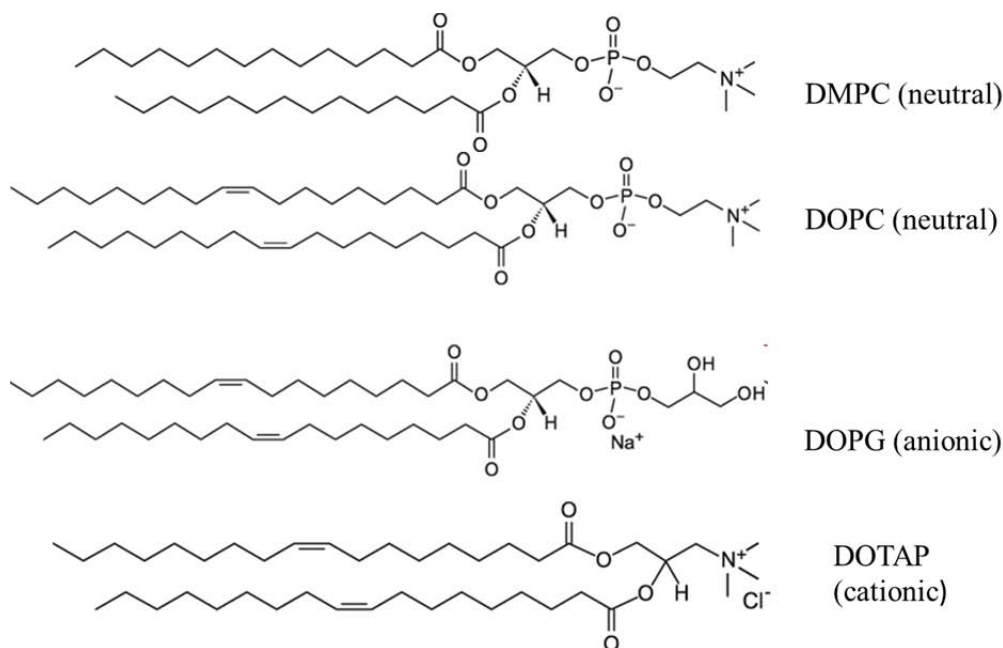


Figure 4.10 Structural formulae of used phospholipids

Name	Carbons: unsaturation	Transition temperature T_m (°C)	Net Charge at pH 7.4
1,2-ditetradecanoyl- <i>sn</i> -glycero-3-phosphocholine (DMPC)	14:0	23	0
1,2-dioleoyl- <i>sn</i> -glycero-3-phosphocholine (DOPC)	18:1	-20	0
1,2-di-(9Z-octadecenoyl)- <i>sn</i> -glycero-3-phospho-(1'- <i>rac</i> -glycerol) (DOPG)	18:1	-18	-1
1,2-di-(9Z-octadecenoyl)-3-trimethylammonium-propane (DOTAP)	18:1	~0	+1

Table 4.2 Utilized common phospholipids

4.2.2 Experimental results of blending GUVs with fluoroionophores

Before making use of electroformation of vesicles, simple drop cast formation was performed. After evaporation of 25 mg/ml DMPC in CHCl_3 onto the glass surface followed by re-hydration with 30 mM MOPS buffer solution, one can observe the multi-lamellar vesicles with a microscope as shown in Figure 4.11. Therefore, to obtain unilamellar vesicles special treatment is needed.

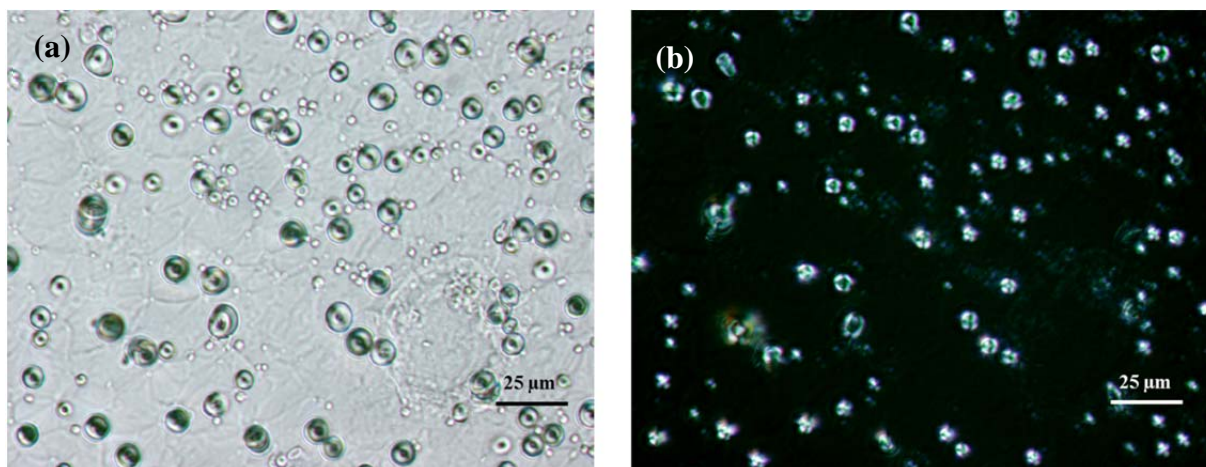


Figure 4.11 Microscope images of multilamellar vesicles formed by drop cast formation. $\sim 50 \mu\text{l}$ of 25 mg/ml DMPC was dried on the glass surface followed by rehydration with $\sim 200 \mu\text{l}$ of 30 mM MOPS solution. (a) DIC (differential interference contrast) observation to increase contrast with better shape; (b) polarized microscopy for visualization of multi-lamellar structure.

Using electroformation as described, the GUVs which are made of DMPC (Figure 4.12a) or DOPC (Figure 4.12b) were successfully formed.

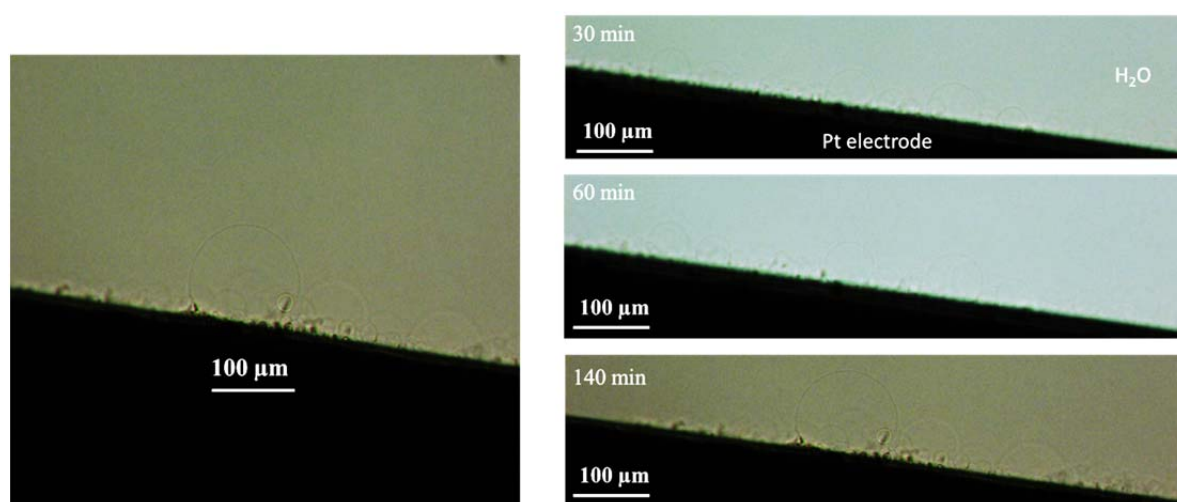


Figure 4.12 Electroformation of GUVs with (a) DMPC lipid, (b) DOPC lipid in the Milli-Q water

Here, the general electroformation procedure of fabricating giant unilamellar vesicles (GUVs) in a custom-made petri dish is summarized. $4 \mu\text{L}$ of 0.5 mM lipid mixture in chloroform was spotted onto the Pt electrode and dried under vacuum for at least 1h. An alternating electrical field of 10 Hz 0.5 V was applied to the electrodes which lie on a ITO glass (Indium Tin Oxide modified glass) at room temperature. $\sim 2.5 \text{ ml}$ of Milli-Q water was added (avoiding agitation). The applied voltage was gradually increased to 1 V (during 30 min) and applied for 2 hours. Finally the frequency and voltage are modified to 4 Hz and $2 \sim 3 \text{ V}$ for 30~60 minutes to detach the formed liposomes.

We then mixed the DOPC with **DPH**, (Figure 4.13, 1,6-diphenyl-1,3,5-hexatriene, a commonly used fluorescent protein probe, their quantum yields are significantly high in the liposome environment) to investigate if the mixture can form the fluorescent GUV. The growing process over time was recorded in Figure 4.14. Basically, the results showed the DOPC/ **DPH**= 300/1 mixture can only form the fiber or spiral fiber structures instead of GUVs.

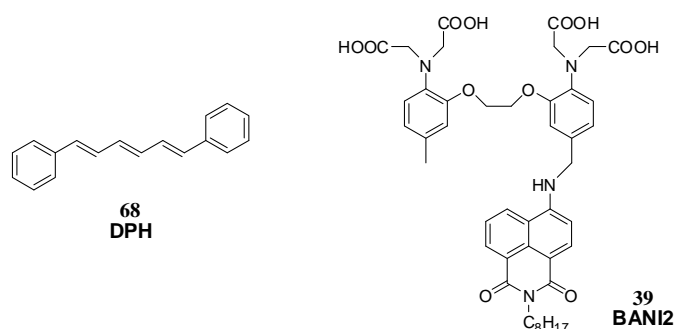


Figure 4.13 Molecular structure of fluorescent protein probe, **DPH**, and synthesized amphiphilic fluorophore, **BANI2**, for the test of fluorescent GUV fabrication

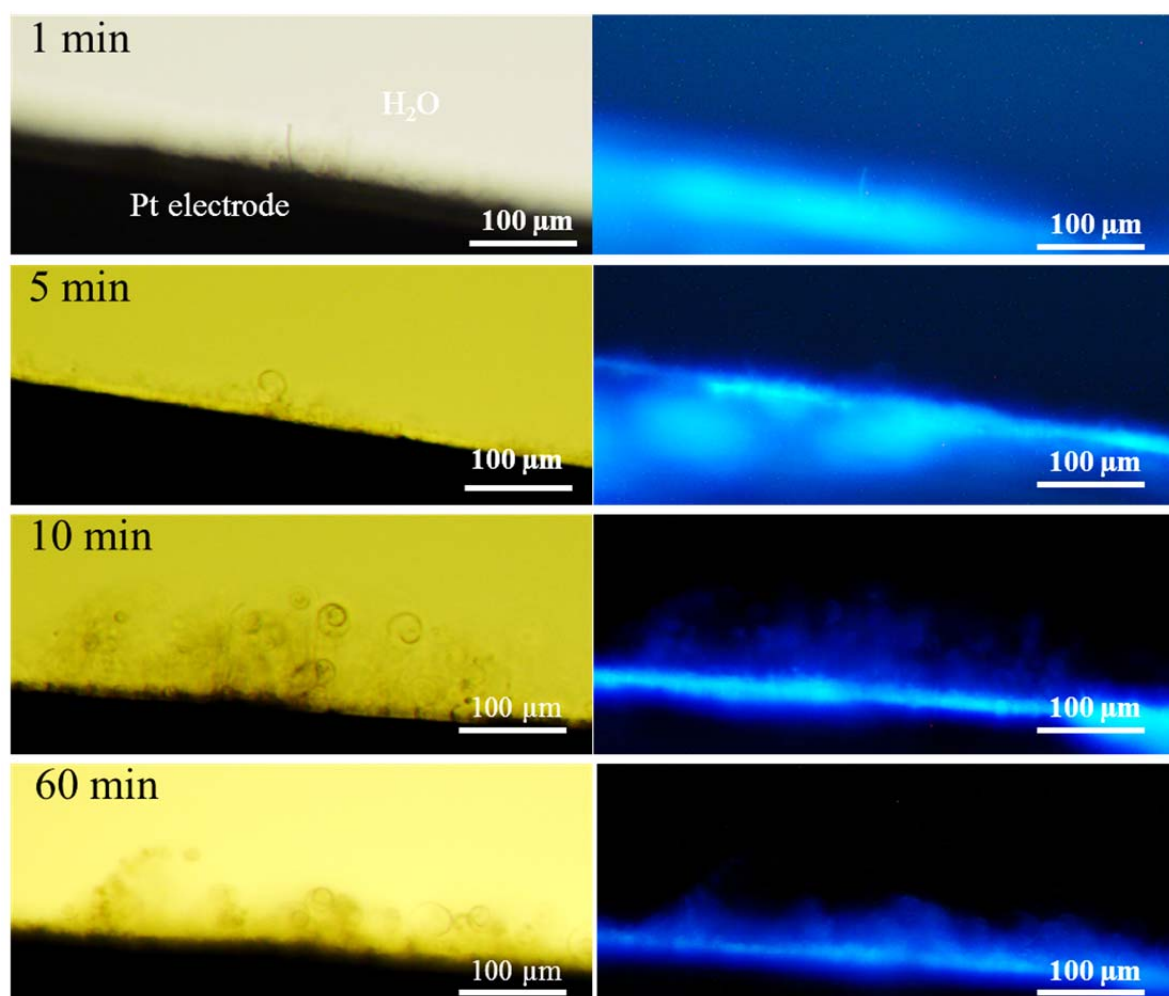


Figure 4.14 Test of fabricating fluorescent GUV by electroformation of DOPC: **DPH**= 300:1 on the Pt electrode in the Milli-Q water. The result shows the fiber or spiral fiber structures are formed instead of GUV

The **DPH** was then replaced by amphiphilic fluoroionophore, **BANI2**. The two amphiphiles, DOPC and **BANI2** were mixed to investigate if the amphiphilic additive (**BANI2**) would interfere with the aggregation process of DOPC to form GUV and if the hydrophobic long alkyl chain of **BANI2** could immobilize the **BANI2** on the liposome membrane bilayers. The growing process of fluorescent GUVs over time was recorded in Figure 4.15. As clearly seen in Figure 4.15, **BANI2** can be confined on the lipid bilayers without interfering with the formation of GUVs due to the amphiphilic character similar to lipids. After the higher voltage and lower frequency to detach the vesicles from the Pt electrodes, the fluorescent GUV solution can be transferred to a slide and observed by fluorescent microscopy, as shown in Figure 4.16.

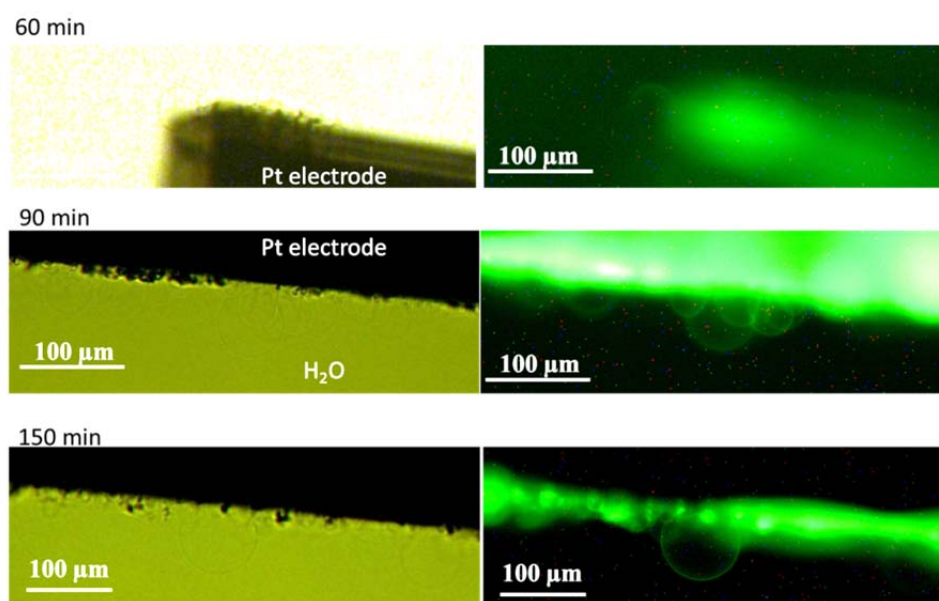


Figure 4.15 Microscope images (left) and its fluorescence microscope images (right) of electroformation growing process of fluorescent GUVs (DOPC: **BANI2** = 300:1) in the Milli-Q water

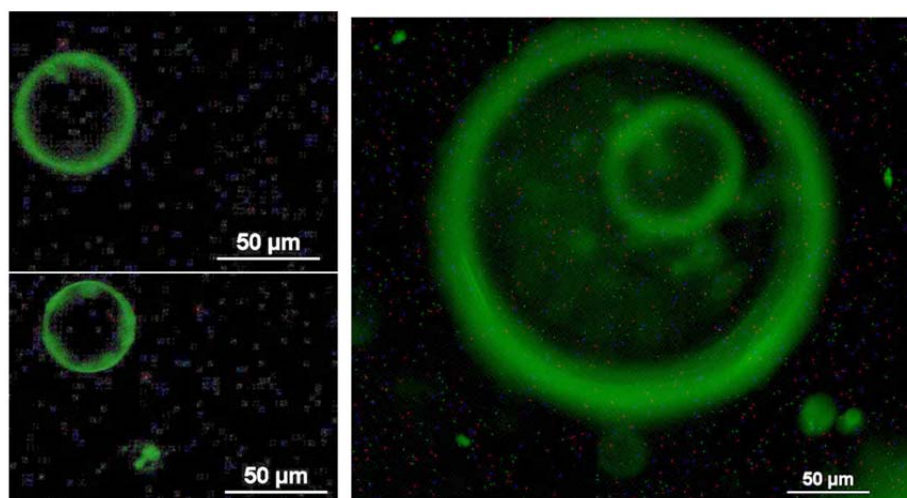


Figure 4.16 Fluorescence microscope images of detached fluorescent GUVs (DOPC: **BANI2** = 300:1) in Milli-Q water

The GUV formation was also tested through a simple drop cast method on the ITO glass without an applied AC field as shown in Figure 4.17. The result showed the fluorescent vesicles can be formed without applying AC voltage. In order to see if surface modification can facilitate vesicle formation, the OTS (octadecyltrichlorosilane) modified hydrophobic glass was further tested to compare with normal glass as shown in Figure 4.18. The result shows that the ITO or OTS modified glass surface can help vesicle formation, but not in the case of normal glass surfaces where the GUV yield is notably low.

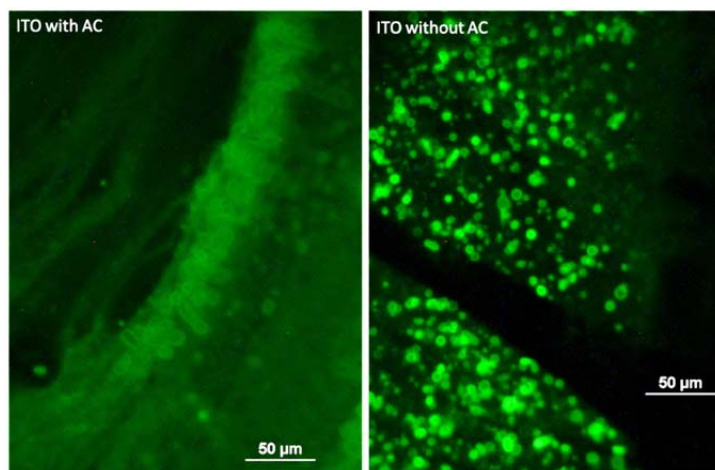


Figure 4.17 Fluorescence microscopy images of fluorescent GUV formation: drop cast DOPC: **BANI2** = 300:1 chloroform solution on the ITO glass (rather than Pt electrode), after the rehydration by the Milli-Q water the conductive surface was applied with AC electric field (a); without AC electric field (b)

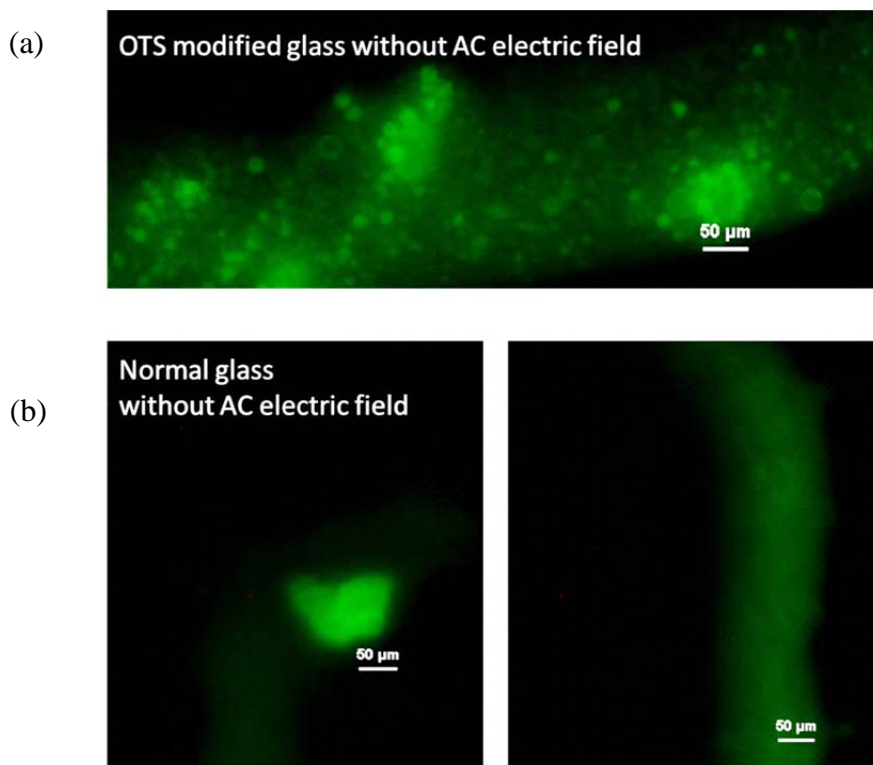


Figure 4.18 Fluorescence microscopy images of fluorescent GUV formation by drop cast method of DOPC: **BANI2** = 300:1 on the OTS modified glass (a), or normal glass (b), in Milli-Q water without AC electric field

After this series of comparisons, the tentative conclusions for GUV formation are:

1. GUVs can be formed with neutral lipid DOPC when AC electric field is applied (electroformation).
2. GUV formation is not altered by adding amphiphilic fluoroionophore **BANI2** (1/300~1/30) whereas the addition of **DPH** adding strongly perturbs the GUV formation.
3. Modified glass surface (ITO or OTS glass) can also promote vesicle formation owith the **BANI2**/DOPC system by the simple drop cast method, even without applying an AC electric field.

Finally, to see the switch-on/off ability of **BANI2** on the liposome bilayers, pre-complexation with Ca^{2+} then decomplexation by the addition of a large amount of EGTA was tested. As presented in Figure 4.19, the fluorescent vesicles (DOPC: **BANI2**=300:1 in 1 mM calcium formate and 30 mM MOPS solution at pH 7.2) are switched on initially. In this solution 100 μl of 0.06 M EGTA solution was carefully added with micro syringe without agitation, the fluorescence intensity decreased from mean grey= 0.247 to 0.149 levels within seconds (Figure 4.19, calculated by imageJ software). Therefore, the switch-on/off ability can be examined by fluorescence microscopy by comparing the fluorescence images before and after addition of EGTA. Besides, the careful addition of EGTA solution did not break the existing vesicles. We then performed more detailed experiments by using confocal microscopy in order to understand the fluorescence lifetime of **BANI2** on the liposome membrane.

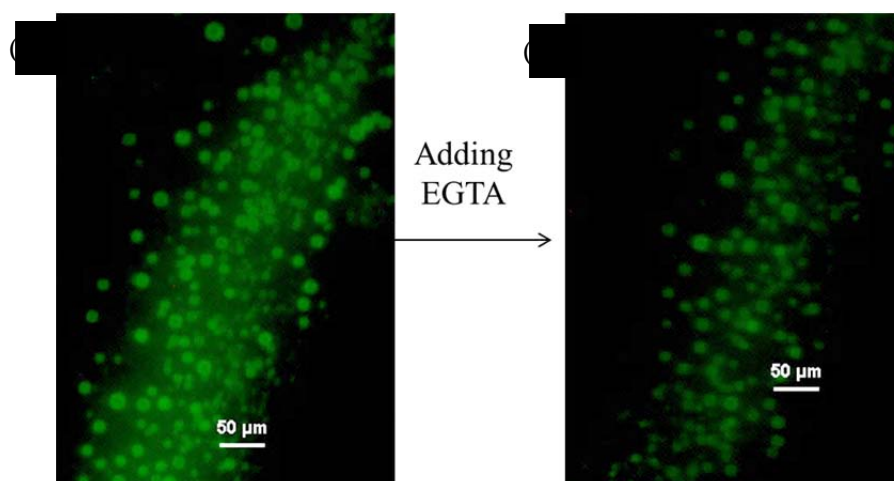


Figure 4.19 Fluorescence microscope images: drop cast formation of DOPC: **BANI2**=300:1 on ITO glass, rehydrated by MOPS (30 mM), calcium formate (1 mM), pH 7.2 solution for 2 hours without AC electric field (mean grey intensity= 0.247) (a); after carefully adding 100 μl of 0.06 M EGTA solution leading to 20 mM total concentration of EGTA in the bulk (mean grey intensity= 0.149) (b).

4.3 Confocal microscopy and fluorescence-lifetime imaging microscopy

Fluorescence wide field microspectroscopy has revealed that the green-light-emitting self-assembled GUVs are composed of **BANI2** and phospholipid. But the drawback of the fluorescence microscope is that the entire sample is flooded evenly in light from a light source. All parts of the sample in the optical path are excited at the same time and the resulting fluorescence is detected by the microscope's photodetector or camera including a large unfocused background part. In contrast, a *confocal microscope* (CFM) uses focused illumination and a pinhole in an optically conjugate plane in front of the detector to eliminate out-of-focus signal - the name "confocal" stems from this configuration (Figure 4.20).

Briefly, confocal microscopy is an optical imaging technique used to increase optical resolution and contrast of a micrograph by using focused light illumination and a pinhole to eliminate out-of-focus light in samples that are thicker ($\sim 10 \mu\text{m}$) than the focal plane. The key feature of confocal microscopy is its ability to acquire in-focus images from selected depths, a process known as optical sectioning. Images are acquired point-by-point and reconstructed with a computer, allowing three-dimensional reconstructions of topologically complex objects.¹⁴⁻¹⁶ Besides, combining CFM with TCSPC (time-correlated single photon counting) technique, the technique is known as *fluorescence-lifetime imaging microscopy* (FLIM) and allows us to know the lifetime variation in different conformational or structural environments.

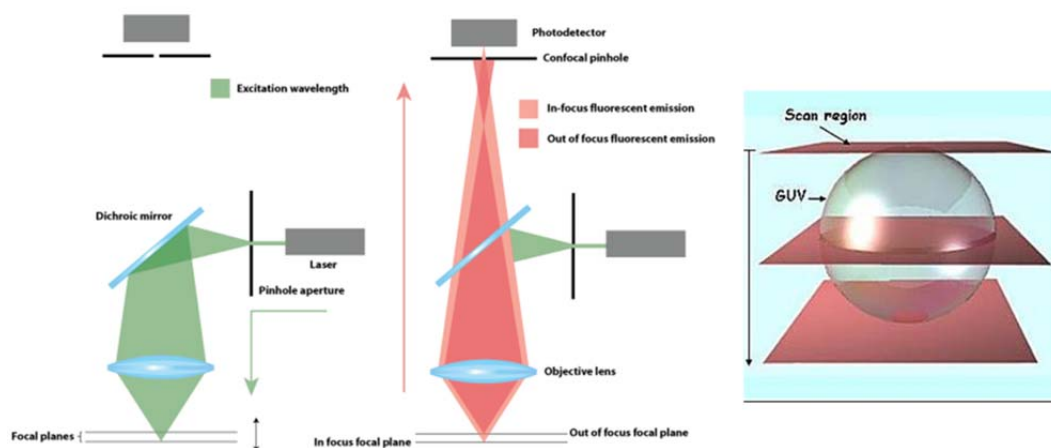


Figure 4.20 Simplified schematic representation of a confocal microscope¹⁷

4.3.1 Introduction to fluorescence-lifetime imaging microscopy (FLIM)

Fluorescence Lifetime Imaging Microscopy or FLIM is an imaging technique for producing an image based on both intensity and the differences in the exponential decay rate of the fluorescence from a sample. It can be coupled to confocal microscopy, two-photon

excitation microscopy, etc.¹⁸ The contrast in FLIM is determined by the lifetimes of local chemical composition of the sample, so the image contrast is not based on signal intensity or sample concentration. The local environment determines the fluorescence lifetime, which is then used to calculate an image that is independent of probe concentration.¹⁹

An example of the fluorescence-lifetime imaging principle is represented in Figure 4.21. Suppose that the cell (or an inhomogeneous surface) has two regions with equal steady-state fluorescence intensity, but the lifetime of the probe in the central region of the cell (τ_2) is longer than that in the outer region (τ_1). The longer lifetime in the central region could be due to the presence of an ionic species such as calcium, binding of the probe to a macromolecule, or other environmental factors. The quantum yields of the probe in the central and outer regions could be the same or different due to interactions of the probe with biomolecules. The concentrations of the probe could be different due to partial exclusion of the probe from some region of the cell. The intensity image will not reveal the different environments in regions 1 and 2 (Figure 4.21a). However, if the lifetimes were measured in regions 1 and 2 then the distinct environments would be detected (Figure 4.21b). FLIM allows image contrast to be based on the lifetimes in each region of the cell, which can be presented on a color scale or as a 3D surface in which the height represents the local decay times.

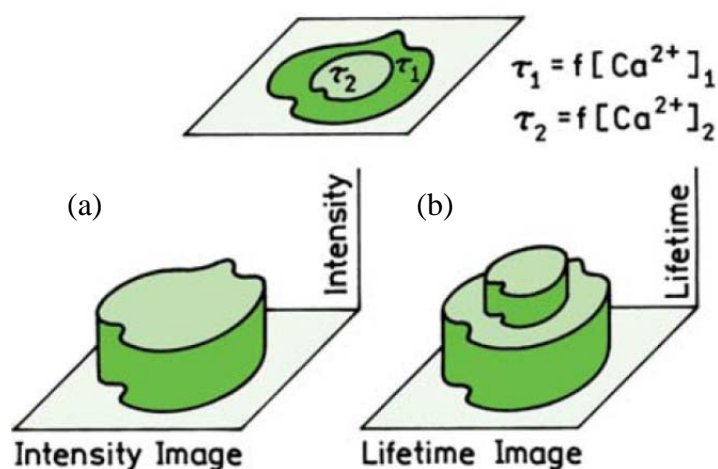


Figure 4.21 Illustration of the concept of fluorescence-lifetime imaging (FLIM). The object is assumed to have two regions that display the same fluorescence intensity but different decay times, $\tau_2 > \tau_1$.

Figure 4.22 shows a schematic for TCSPC coupled with CFM. TCSPC has many advantages for FLIM, it makes use of all the photons reaching the detector. Since individual photons are counted the measurements provide high efficiency.²⁰

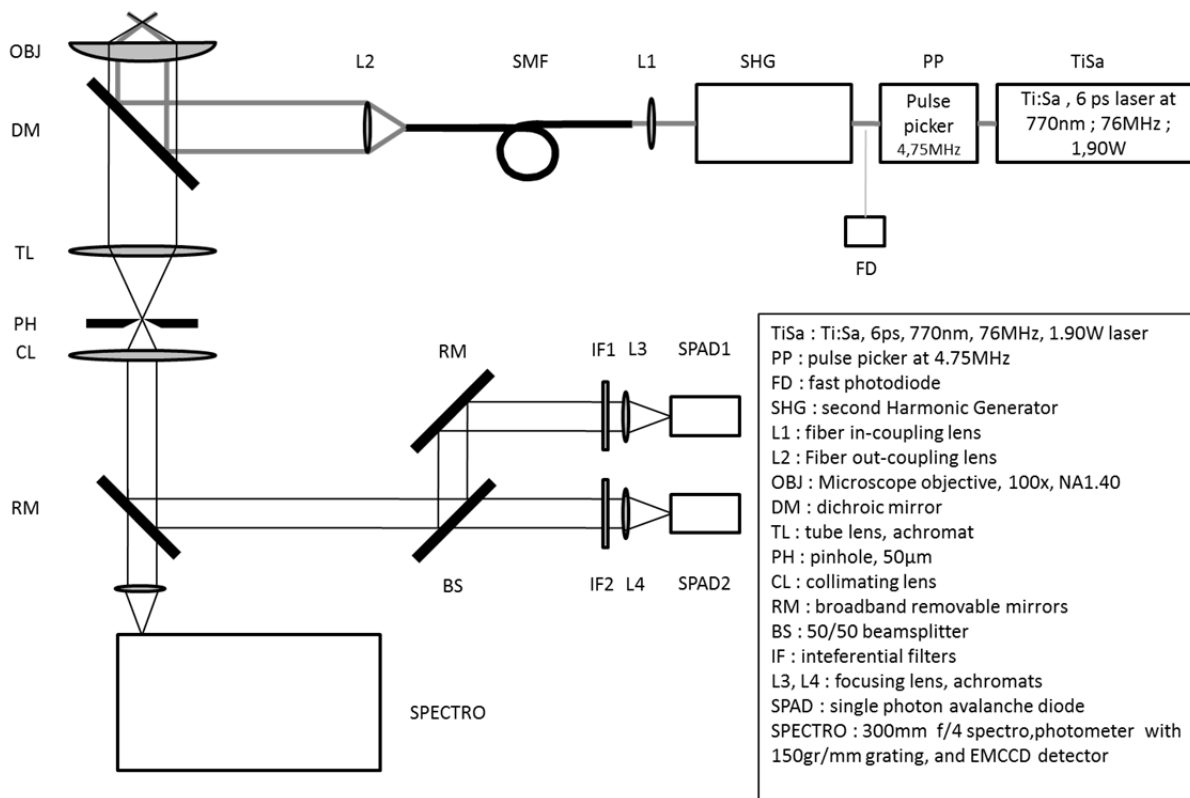


Figure 4.22 Schematic for FLIM using TCSPC

4.3.2 Experimental part

To observe **BANI2** in the vesicle by the FLIM technique, trial small unilamellar vesicles (SUVs) solution of 300 μ M DMPC and 1 μ M **BANI2** was prepared in 50 μ M CaCl₂ aqueous solution (preparation of SUVs in Chapter 5 Experimental section). The observed confocal images as samples, prepared by introducing one drop of solution on the glass slide, showed a thin film adhering on the glass with lifetime about 6.5 ns (Figure 4.23). Due to the detection limit (laser spot \sim 200 nm diameter) and the ease of adherence between the lipid vesicles and glass, in the highly concentrated sample it is hard to observe the separate, single SUVs. Measuring the fluorescence emitted from the SUV thin film showed the emission band is around 525 nm, which is correspondence to the fluorescence of BANI2 in the liposome domain. (Note. The fluorescence emission position and intensity are uncorrected; more precise fluorescence measurement will be shown in the next section, chapter 4.4 K_d measurement of probes in the SUVs matrix.)

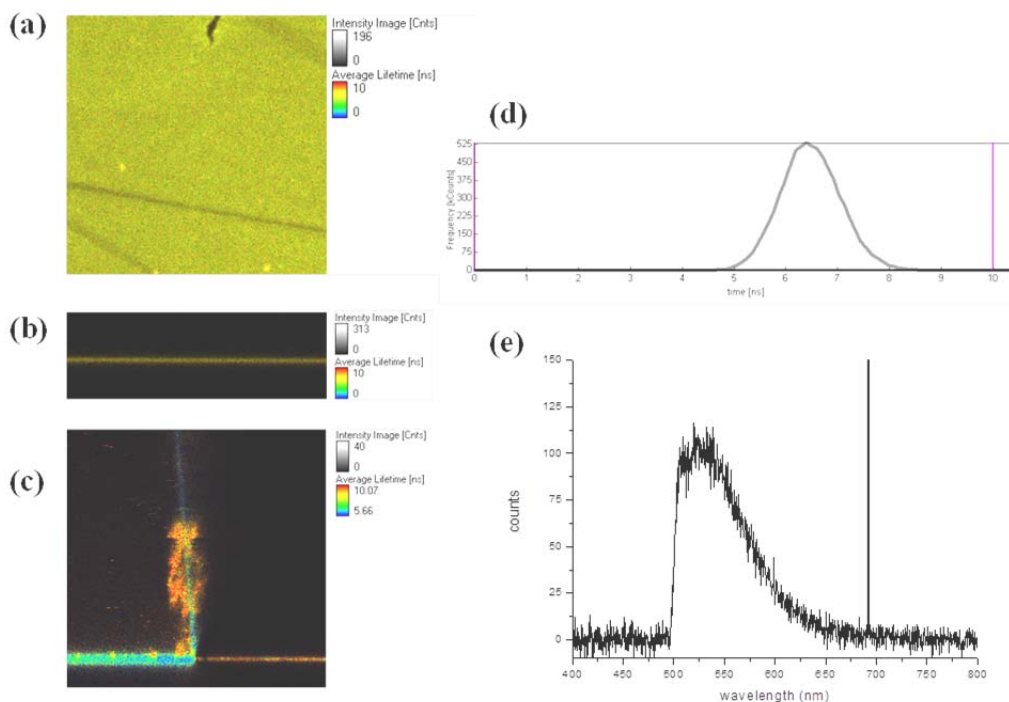


Figure 4.23 SUVs of DMPC (300 μM) and **BAN12** (1 μM) in CaCl_2 (50 μM) aqueous solution, one drop on a cover glass, $\lambda_{\text{ex}} = 430 \text{ nm}$: Confocal FLIM images of (a) $20 \times 20 \mu\text{m}$ XY scan, (b) $38 \times 13 \mu\text{m}$ XZ scan, and (c) $51.1 \times 51.1 \mu\text{m}$ XZ scan of droplet edge; (d) lifetime distribution profile; (e) non-corrected fluorescence spectrum of the film, a 500 nm filter was used.

To observe a single vesicle, the GUV electroformation method in the last section was utilized. With the successful preparation and observation by fluorescence microscopy having been effected, fluorescent GUVs (DOPC: **BAN12** = 300:1) in the 30 mM MOPS, 1 mM calcium formate, pH 7.2 solution were prepared and observed in Figure 4.24 and Figure 4.25. Thanks to the confocal FLIM technique, it is clear that the long alkyl chain equipped **BAN12** locates nowhere other than bilayer membrane, even if chelating with Ca^{2+} . Moreover, FLIM showed the slightly different environment can affect the lifetime of **BAN12** on the bilayer membrane (photobleaching could happen as well). Lifetime of **BAN12** differs from ~ 7.5 to 7 ns (Figure 4.24) from top to bottom of a fluorescent GUV (or LUV) with $\sim 2 \mu\text{m}$ diameter. In another fluorescent GUV lies on a collapsed one was observed and the lifetime values are ~ 9 ns and 8 ns respectively (Figure 4.25). This might be due to the environmental difference from the interaction between glass surface and fluorescent membrane. Despite the lifetime values are roughly estimated in these experiments, they show good evidence that fluorescence lifetime character of probes can be affected by different environments resulting from interaction with the glass surface or different hydrophobicity.

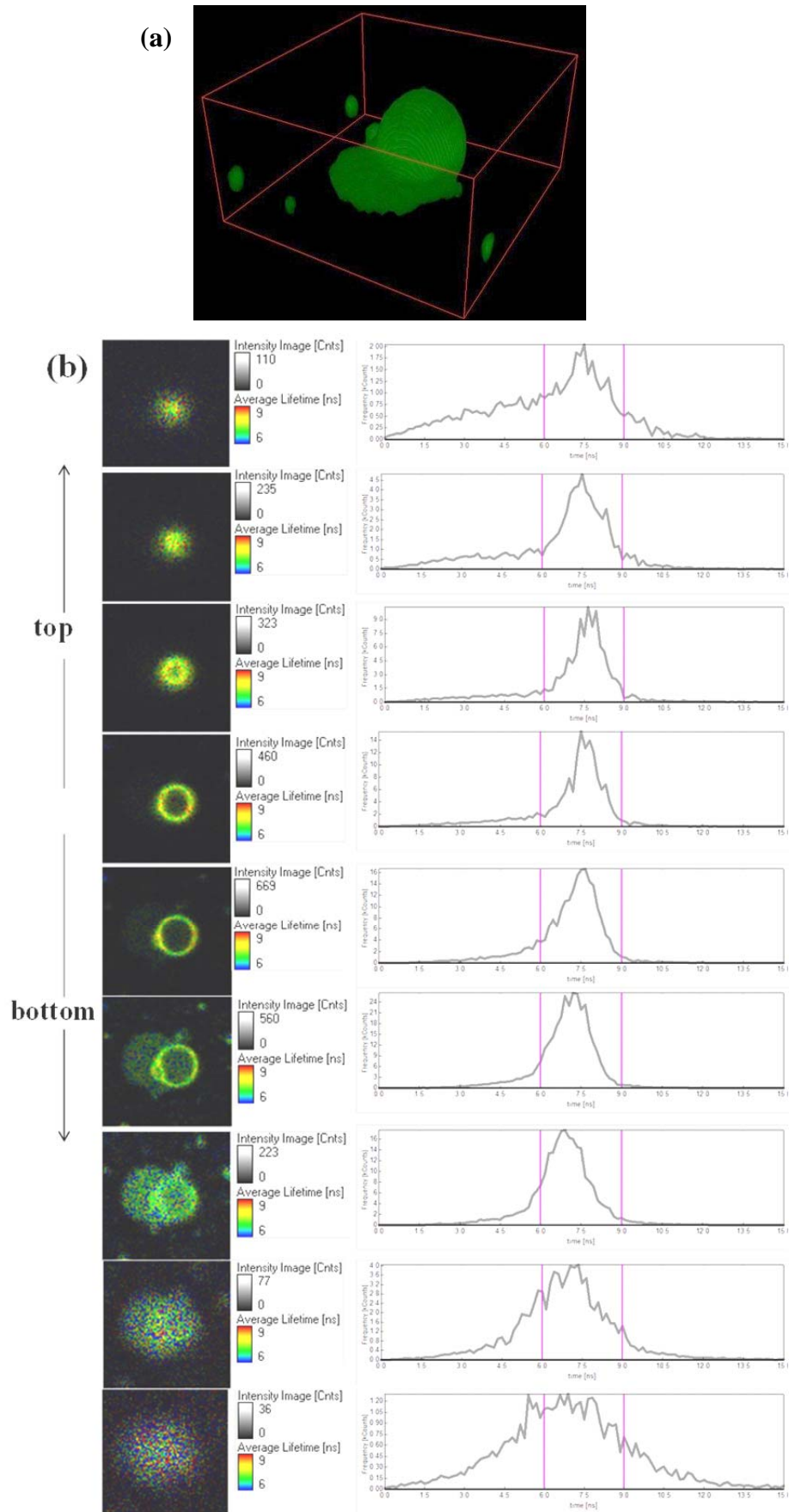


Figure 4.24 Fluorescent GUV (DOPC: **BANI2** = 300:1) in the 30 mM MOPS, 1 mM calcium formate, pH 7.2 solution. 3D image (a) stacked from confocal FLIM images of GUV to top to bottom (b), $\lambda_{\text{ex}} = 430 \text{ nm}$, $\lambda_{\text{em}} > 500 \text{ nm}$, $6.2 \times 6.2 \mu\text{m}$

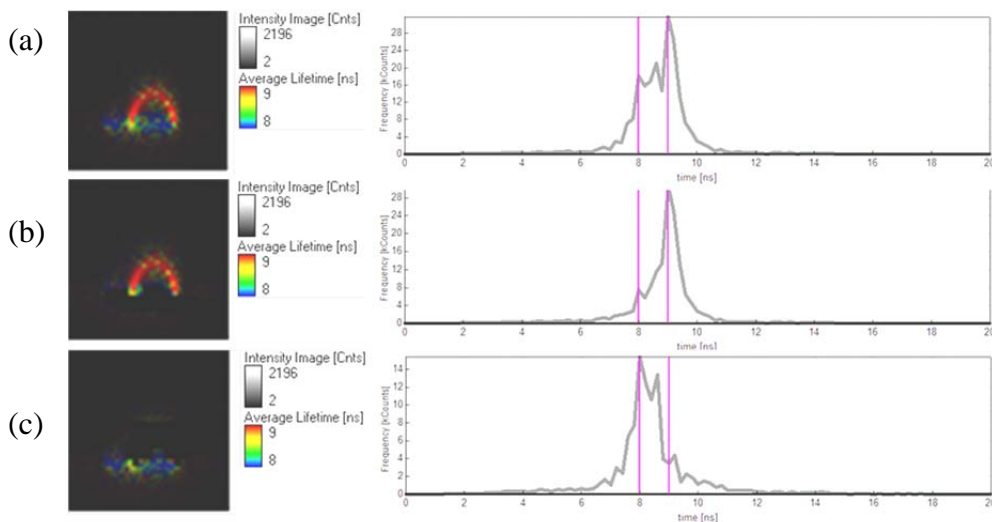


Figure 4.25 Confocal FLIM images of fluorescent GUV (DOPC: **BANI2** = 300:1) in the 30 mM MOPS, 1 mM calcium formate, pH 7.2 solution, $\lambda_{\text{ex}}=430$ nm, $\lambda_{\text{em}}>500$ nm, 7.44×7.44 μm XZ scan. (a) A fit GUV upon a collapsed one; (b) the fit GUV part; (c) the collapsed GUV part

The polarization of **BANI2** on the DOPC GUV bilayer was investigated. In this case the FLIM image and fluorescence emission spectrum (Figure 4.26a & c) are similar with aforesaid results, they showed a lifetime value about 9 ns and ~ 525 nm emission band. With regard to the image in Figure 4.26b, the observed polarization image is homogeneous at all angle of the GUV periphery which means the polarization of **BANI2** is angle independent on the bilayer. The image is uncorrected by G-factor:

$$P = \frac{I_{\parallel} - G \cdot I_{\perp}}{I_{\parallel} + G \cdot I_{\perp}} \quad \text{Equation 4.3}$$

The G-factor is used to compensate the difference of detection efficiency in the two detection channels (parallel or perpendicular). If not applied, the measurement remains sensitive to polarization variations exactly the same way.

Assuming an octyl chain equipped 4-amino-1,8-naphthalimide fluorophore lies on the lipid bilayer with a dipole moment parallel with the lipid chains, one should be able to see an angle dependent polarization effect. Therefore the result is unexpected and it may be because the measured vesicle is not big enough. The limitation of confocal focus light are ~ 200 nm and 600 nm diameter at XY and XZ scanning, respectively. In this case our detected vesicle size is ~ 2 μm diameter, which means $\sim 1/10$ to $1/3$ of bilayer are excited and detected at the same time. This might lead to the offset to opposite polarization angles. As a result, to observe the polarization effect a larger GUV might be needed.

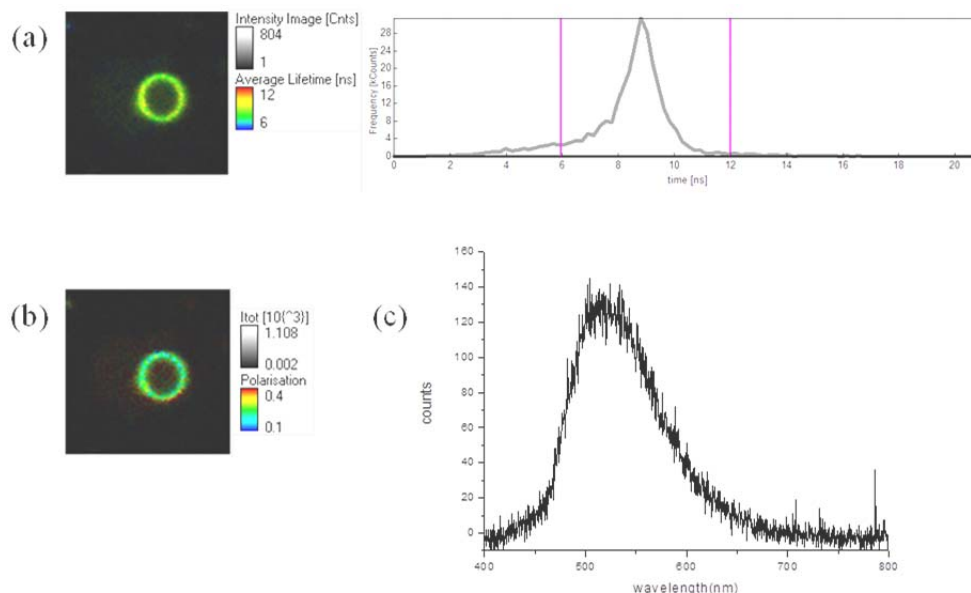


Figure 4.26 Fluorescent GUV (DOPC: **BAN12** = 300:1) in the 30 mM MOPS, 1 mM calcium formate, pH 7.2 solution. (a) confocal FLIM images and (b) fluorescence polarization confocal image ($6.2 \times 6.2 \mu\text{m}$, XY scan); (c) non-corrected fluorescence emission spectrum of **BAN12** on the liposome bilayer membrane ($\lambda_{\text{ex}} = 385 \text{ nm}$).

In the end, the switch-on/off ability of **BAN12** on the liposome bilayers was investigated by fluorescence microscopy of the confocal instrument set-up. As performed in the last section, pre-complexation with Ca^{2+} then decomplexation by adding a small amount of concentrated EGTA solution was tested again (Figure 4.27). The fluorescent giant vesicles (DOPC: **BAN12** = 300:1) were formed by drop-casting formation on ITO glass without an electric field in MOPS (30 mM), calcium formate (1 mM), pH 7.2 solution. These switched-on vesicles were followed by adding $\sim 50 \mu\text{l}$ of 0.06 M EGTA solution by microsyringe avoiding agitation at the 9th second in this total of 20 seconds observation (Figure 4.27c). The fluorescence intensity change was recorded by the mean grey and maximum grey of the sequential images. Mean grey was collected by the average intensity of the whole image, while maximum grey just extracts the brightest point of the image. Both of these intensity curves show the fluorescence intensity was fadeaway after the EGTA addition (at the 9th second). Moreover, the careful addition of EGTA solution did not break the existing vesicles. As a result, a tentative conclusion can be made that addition of an overdose of EGTA outside of vesicles in the solution is able to quench **BAN12** probes at outer periphery of bilayers by taking away the Ca^{2+} ion.

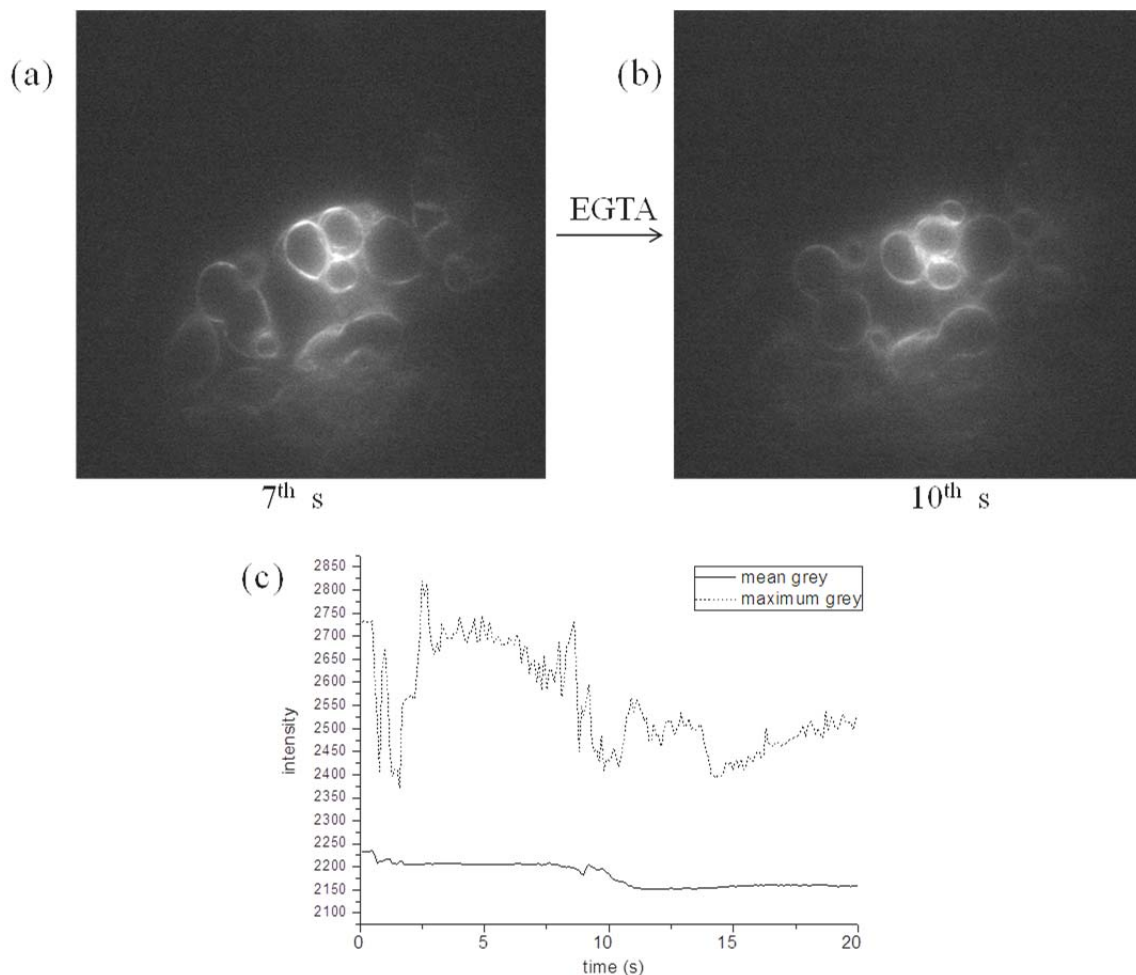


Figure 4.27 Switch-on/off ability of fluorescent vesicles (drop-cast formation on ITO glass, DOPC:**BANI2**= 300:1, rehydrated by MOPS (30 mM), calcium formate (1 mM), pH 7.2 solution) by carefully adding ~50 μ l of 0.06 M EGTA solution at the 9th second. Fluorescence intensity change is recorded as a function of time as mean grey and maximum grey. (a, b) Fluorescence microscope images of the 7th and 10th second, before and after EGTA addition respectively. (80 x 80 μ m) (c) Fluorescence intensity vs. time profiles.

4.4 Fluoroionophores within small unilamellar vesicles (SUVs)

In the last section, GUVs (giant unilamellar vesicles) proved to serve as well adapted containers for BAPTA-type fluoroionophores especially when the probe has amphiphilic character as **BANI2**. The goal of this section is to study the photophysical character of the fluoroionophores within, or confined in the small unilamellar vesicles (SUVs, ~20 nm in radius).

SUVs (or other unilamellar vesicles) are used for drug delivery due to their unique properties. A liposome encapsulates a region of aqueous solution inside a hydrophobic membrane; dissolved hydrophilic solutes cannot readily pass through the lipids. Hydrophobic chemicals can be dissolved into the membrane, and in this way liposome can carry both hydrophobic molecules and hydrophilic molecules. Therefore, for our purpose, with

well-prepared SUVs solution one can acquire the lifetime value, absorption / emission properties, and affinity change towards calcium (K_d value) for the probes on the liposome bilayers to compare with the free solution environment. Further utilization of SUVs as containers for the photoinduced ion-shuttle will be gradually established by basic research and understanding.

4.4.1 Pretest of EGTA additive in the SUVs solution

As described in Chapter 2, EGTA proved a crucial additive to fully switch on/off the fluorescence while Ca^{2+} is complexed or de-complexed by fluoroionophore in the free solution. With regard to the case in the SUVs environment, pretest by mixing **BANI2** with neutral lipid DMPC (1:300 equivalent, the preparation procedure is in Chapter 5, Experimental section) to obtain SUVs solution, followed by adding Ca^{2+} into the solutions with or without EGTA was performed to compare the switch-on/off abilities (Figure 4.28). As shown in the absorption spectra (Figure 4.28a), the baseline of EGTA containing solution is higher due to the larger vesicle size. The vesicle size was measured by dynamic laser scattering (DLS) and determined to be ~40 nm and ~85 nm for the non-EGTA containing and EGTA containing solution, respectively. Generally, the SUV preparation was performed using a microtip sonicator with a certain number of cycles. For example, the two solutions in Figure 4.1 are prepared using a microtip sonicator with four cycles sonication, but the vesicles size differed from each other due to the addition of EGTA in one of them. Hence we found the SUV preparation needs to be adjusted depending on the solution volume and additives. Notably, when Ca^{2+} was added into the EGTA containing SUVs solution the fluorescence could be switched on ~ 2-fold (Figure 4.28b), but not in the case without EGTA as additive (Figure 4.28c). As a result, even the switch-on/off ratio is not maximized but the EGTA is a crucial additive to switch off the fluorescence by eliminating the trace Ca^{2+} in the environment thereby letting the probes can be switched-on by adding Ca^{2+} afterwards.

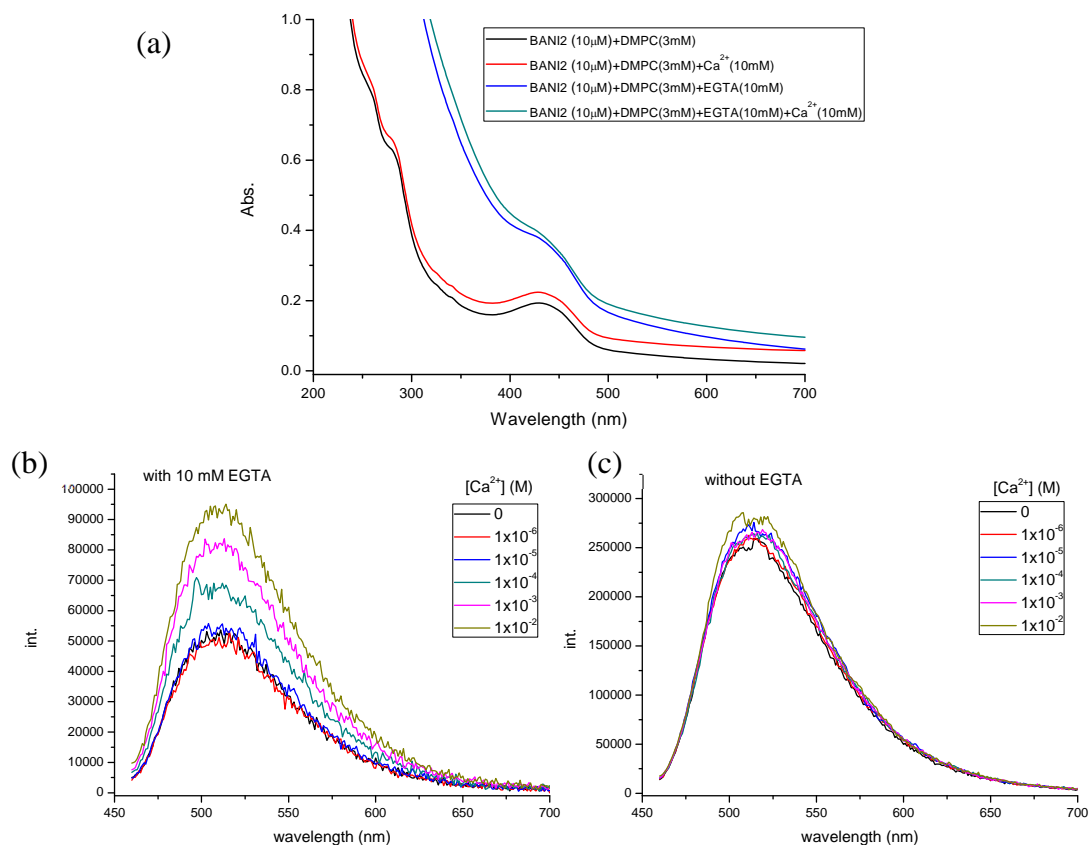


Figure 4.28 Calcium titration of **BAN12** ($10\mu\text{M}$) mixed with **DMPC** (3mM) with or without **EGTA** (10mM): (a) Electronic absorption spectra, (b, c) fluorescence emission spectra of solution with EGTA and without EGTA (emission spectra are not corrected by absorbance)

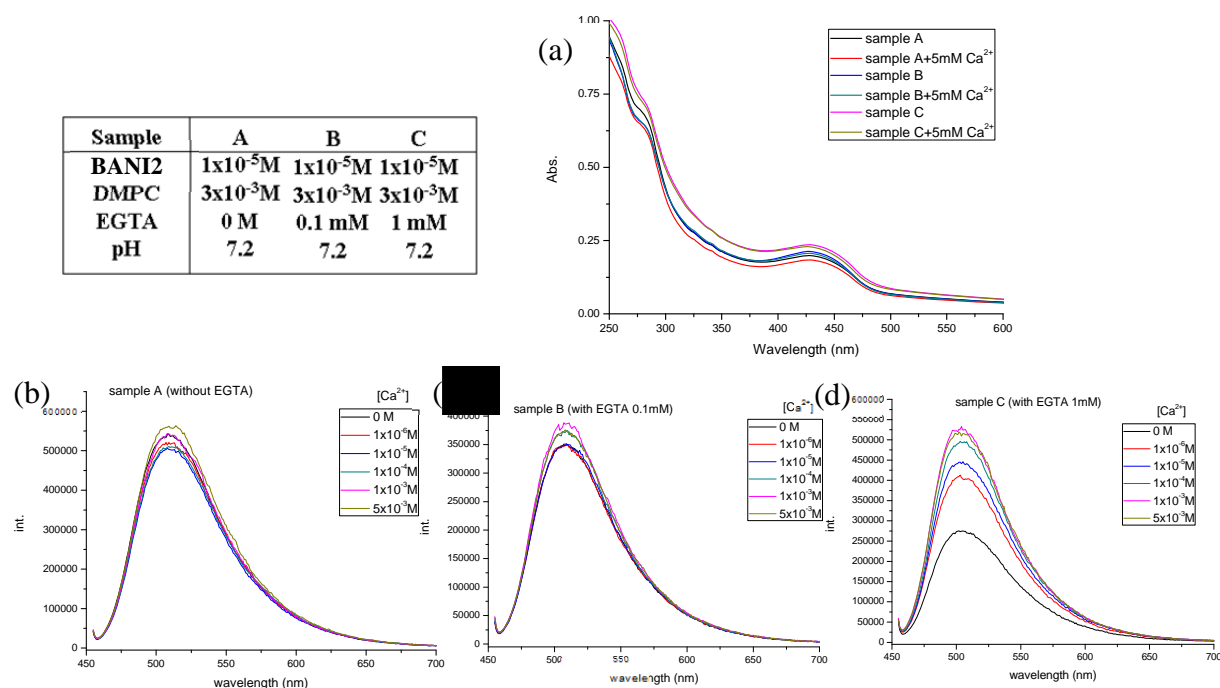


Figure 4.29 **BAN12** ($10\mu\text{M}$) in **DMPC** (3mM) solution with different concentrations of **EGTA** ($0\sim 1\text{mM}$ for sample A~C, respectively): electronic absorption spectra (a), and fluorescence emission spectra of sample A (b), sample B (c), and sample C (d)

Hence, the minimum needed dosage of EGTA in the vesicle solution was tested as shown and organized in Figure 4.29. To a 10 μM **BANI2** and 3 mM DMPC (1:300 equivalent) solution, a concentration of at least 1 mM EGTA is required to obtain a ~2-fold switch-on/off difference as shown in Figure 4.29d.

4.4.2 Dissociation constant (K_d) study of probes within different liposome environment

After having established the importance of EGTA in the SUVs solution or free solution (Chapter 2) with respect to fluorescence probe switch-on/off behavior, the concentration of additives was fixed (30 mM MOPS, 100 mM KCl and 10 mM EGTA) and pH at 7.2 for the K_d determination experiment as in chapter 2. Utilizing the Ca^{2+} titration allows us to calculate the K_d value when the probe molecules are in the lipid bilayer environment. The general way to perform the determination of K_d is described in the Chapter 5 Experimental section.

First, 1 μM **BANI2** with 300 μM neutral lipid (DMPC or DOPC), cationic lipid (DOTAP), anionic lipid (DOPG), as well as mixes of different ratios of aforementioned lipids were performed. The K_d measurements based on fluorescence in the aforesaid buffer solution with excitation wavelength at 450 nm were performed. The goal is to know the Ca^{2+} affinity of **BANI2** in different liposome environment thereby allowing us to estimate the suitable environment for photoinduced ion-shuttle systems. The SUVs size, K_d values, pCa, and switch-on ratio of the experimental results (Figure 4.31 ~ 4.39) are compiled in Table 4.3, and the K_d value changing diagram is shown in Figure 4.30.

liposome environment for BANI2	SUVs size (radius in nm)	K_d value (μM)	pCa	switch on/off factors (n-fold)	Figure
DOPC (neutral)	39	13.8	6.6	6.3	4.31
DMPC (neutral)	35	6.8×10^{-3}	6.47	5	4.32
DMPC:DOTAP = 3:1	26.5	0.91	6.23	3.7	4.33
DMPC:DOTAP = 1:1	22.4	1.68	5.76	4.6	4.34
DOTAP (cationic)	32	0.3	5.48	8	4.35
DMPC:DOPG = 3:1	52	0.112	6.61	6.4	4.36
DMPC:DOPG = 1:1	24.6	427	6.1	1.9	4.37
DMPC:DOPG = 2:3	26	1760.6	6.15	1.4	4.38
DOPG (anionic)	22	0.28	6.64	23	4.39
free solution	/	5.5×10^{-4}	6.13	110	2.46

Table 4.3 K_d determination experimental results for **BANI2** in different environments

Four cycles of microtip sonication is enough to prepare 10~20 ml of different SUVs solutions giving vesicles with a radius of ca. 30 nm. The SUVs confined environment can affect the K_d values from 0.3 to 1760 μM . Compared to **BANI2** in free solution ($K_d = 0.55$

nM), the affinity toward Ca^{2+} is dramatically lowered in a mixed lipid system but less lowered in the pure lipid system (Figure 4.30). This might be due to the lipid compression arrangement which resulted in spacial hindrance which agrees with the ATR-FTIR and PM-IRRAS experimental results in Chapter 3. As for the pCa values ($-\log[\text{Ca}^{2+}]_{\text{free}}$), in neutral and anionic SUVs, the values are ~ 6.5 , which means $1 \mu\text{M}$ of **BANI2** in the liposome environment can still be switched on when $[\text{Ca}^{2+}]_{\text{free}}$ is $\sim 1 \mu\text{M}$. But the pCa values in the cationic DOTAP liposome environment are decreased by increasing the ratio of cationic/neutral lipid, from 6.47 (pure DMPC), 6.23 (DOTAP/DMPC=1/3), 5.76 (DOTAP/DMPC=1:1) to 5.48 (pure DOTAP). Also, as seen in the fluorescence titration curve in Figure 4.32b~4.35b, the required $[\text{Ca}^{2+}]_{\text{free}}$ to reach maximum fluorescence intensity is increased from $\sim 1 \mu\text{M}$ to $\sim 20 \mu\text{M}$. It is probably attributed to the electrostatic repulsion between cationic lipid and Ca^{2+} leading to a more difficult approach of Ca^{2+} toward **BANI2**.

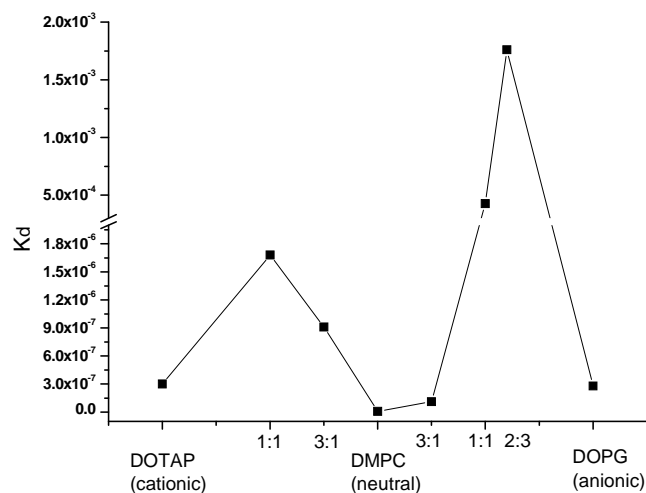


Figure 4.30 K_d value of **BANI2** in different SUVs solution environment

Comparing the switch-on/off ratio in the free solution (110-fold), the ratios in the liposome environment (4~23-fold) are greatly lowered. This is partly due to the fact that the added Ca^{2+} is outside of SUVs thereby only half probes are effective to catch Ca^{2+} (assuming the probes are equally distributed inside and outside the liposome membrane). Besides, by observing the fluorescence emission spectra (Figure 4.31a~4.39a) the emission bands are blue-shifted from 545 nm in the free solution to ~ 510 nm in all SUVs solution, implicating **BANI2** is fixed on the liposome bilayers in a more hydrophobic and lower polarity environment. The polarity of the SUVs environment is similar between acetone and methanol by comparing the emission wavelength of solvent effect which was performed and described in Chapter 2.3.1.5. **BANI2** has higher quantum yield in the lower polarity solvent such as methanol ($\Phi=0.046$) than that in water ($\Phi=2.4 \times 10^{-4}$) which is ca. 200-fold in difference. Therefore, **BANI2** already has certain fluorescence intensity before complexing with Ca^{2+} which leads to a lower overall fluorescence enhancement after cutting off the PET mechanism by complexing with Ca^{2+} .

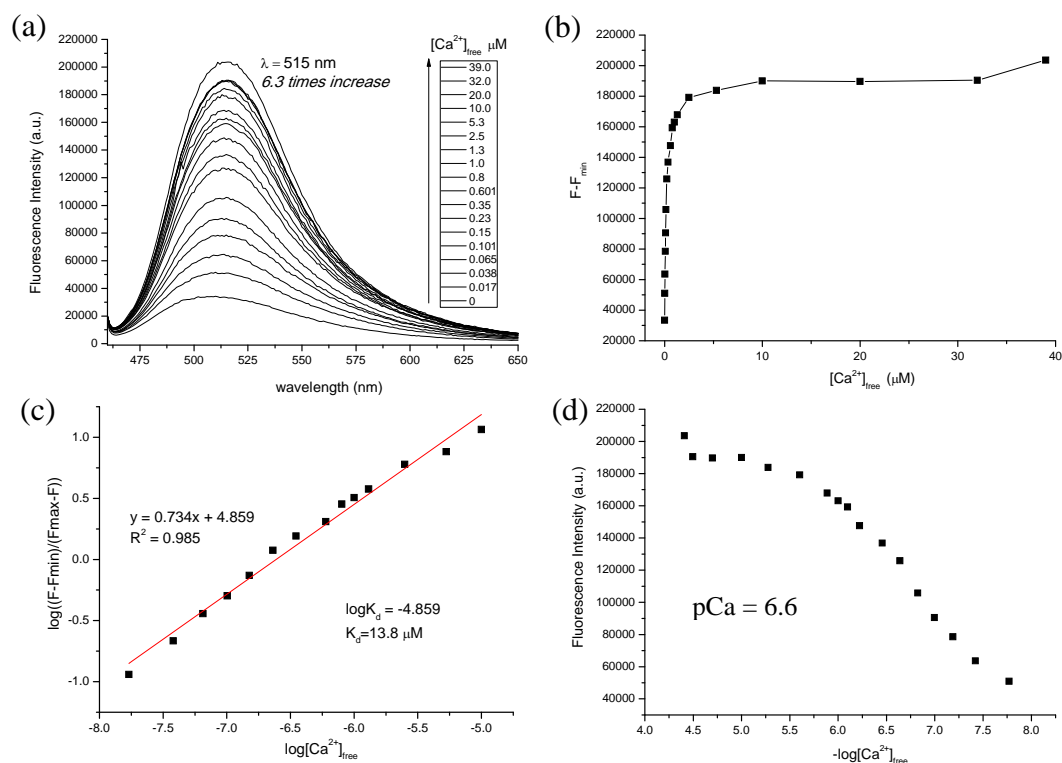


Figure 4.31 (a) Emission spectra of 1 μM **BAN12** and 300 μM DOPC (39 nm in radius SUVs) in MOPS (30 mM), KCl (100 mM), EGTA (10 mM) buffer at pH 7.2 solution in the presence of varying amounts of free Ca^{2+} . ($\lambda_{\text{ex}} = 450$ nm) (b) Fluorescence changes at 510 nm on complexing free Ca^{2+} . (c) Hill plot for the complexation of **BAN12** with free Ca^{2+} . (d) Fluorescence as a function of $-\log[\text{Ca}^{2+}]_{\text{free}}$.

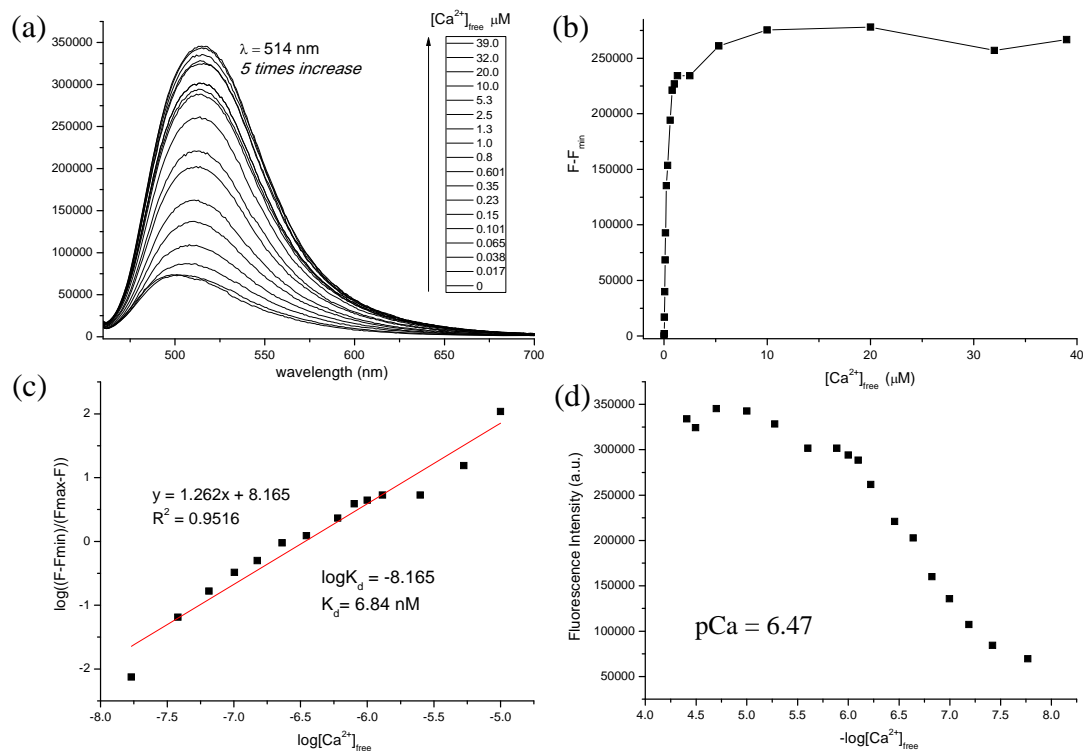


Figure 4.32 (a) Emission spectra of 1 μM **BAN12** and 300 μM DMPC (35 nm in radius SUVs) in MOPS (30 mM), KCl (100 mM), EGTA (10 mM) buffer at pH 7.2 solution in the presence of varying amounts of free Ca^{2+} . ($\lambda_{\text{ex}} = 450$ nm) (b) Fluorescence changes at 515 nm on complexing free Ca^{2+} . (c) Hill plot for the complexation of **BAN12** with free Ca^{2+} . (d) Fluorescence as a function of $-\log[\text{Ca}^{2+}]_{\text{free}}$.

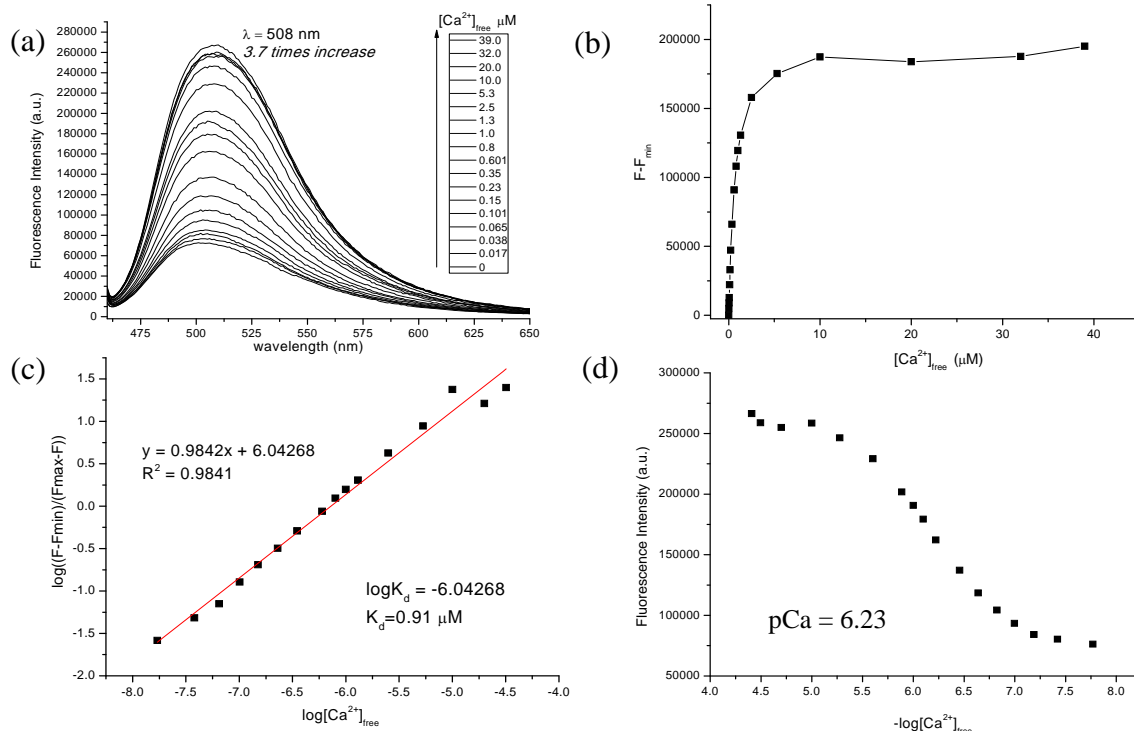


Figure 4.33 (a) Emission spectra of 1 μM **BANI2** and 300 μM DMPC:DOTAP = 3:1 (26.5 nm in radius SUVs) in MOPS (30 mM), KCl (100 mM), EGTA (10 mM) buffer at pH 7.2 solution in the presence of varying amounts of free Ca^{2+} . ($\lambda_{\text{ex}} = 450 \text{ nm}$) (b) Fluorescence changes at 510 nm on complexing free Ca^{2+} . (c) Hill plot for the complexation of **BANI2** with free Ca^{2+} . (d) Fluorescence as a function of $-\log[\text{Ca}^{2+}]_{\text{free}}$.

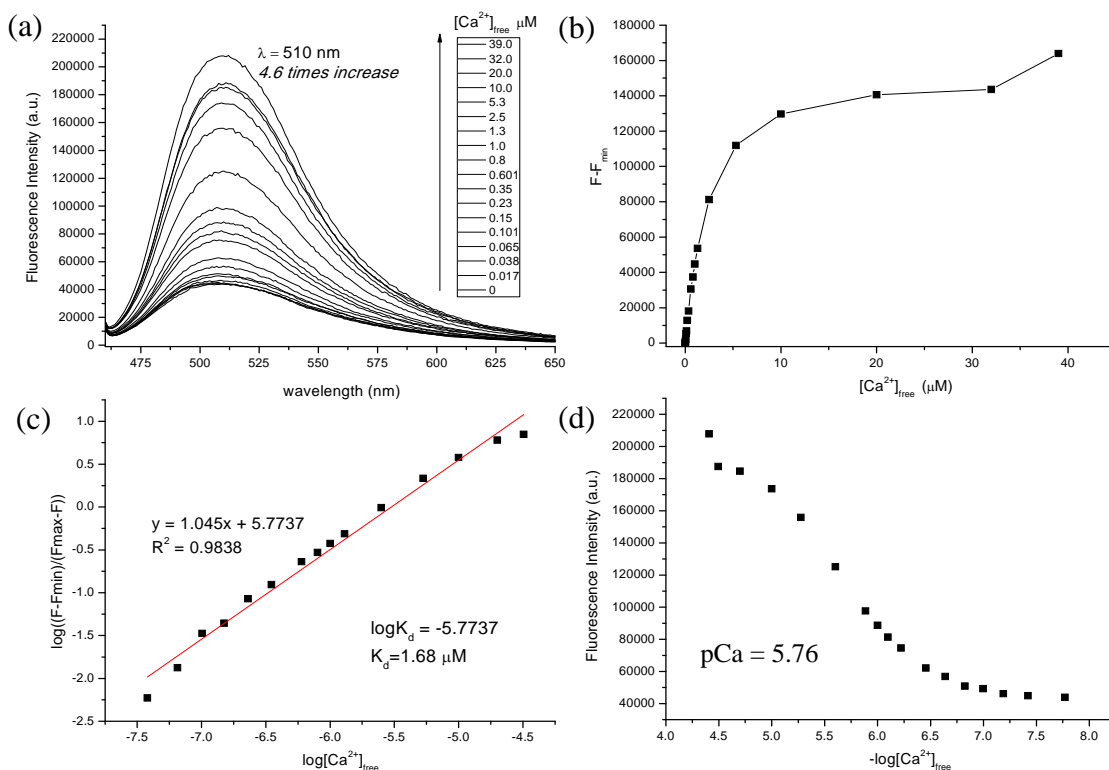


Figure 4.34 (a) Emission spectra of 1 μM **BANI2** and 300 μM DMPC:DOTAP = 1:1 (22.4 nm in radius SUVs) in MOPS (30 mM), KCl (100 mM), EGTA (10 mM) buffer at pH 7.2 solution in the presence of varying amounts of free Ca^{2+} . ($\lambda_{\text{ex}} = 450 \text{ nm}$) (b) Fluorescence changes at 510 nm on complexing free Ca^{2+} . (c) Hill plot for the complexation of **BANI2** with free Ca^{2+} . (d) Fluorescence as a function of $-\log[\text{Ca}^{2+}]_{\text{free}}$.

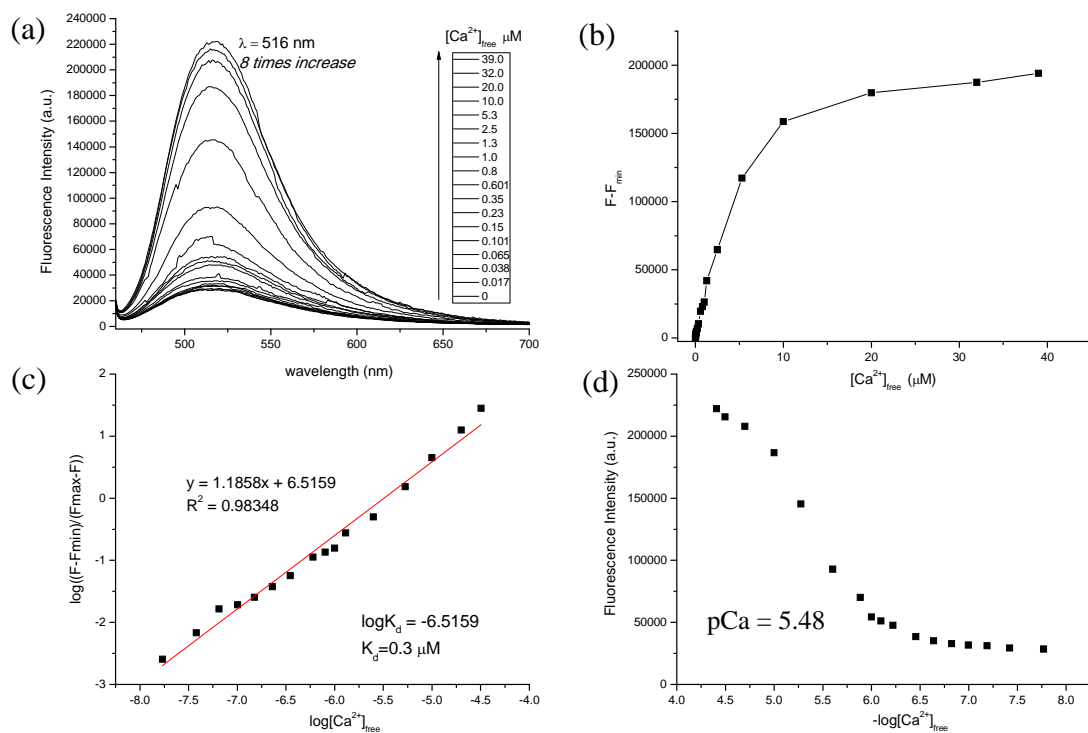


Figure 4.35 (a) Emission spectra of 1 μM **BAN12** and 300 μM DOTAP (32 nm in radius SUVs) in MOPS (30 mM), KCl (100 mM), EGTA (10 mM) buffer at pH 7.2 solution in the presence of varying amounts of free Ca²⁺. (λ_{ex} = 450 nm) (b) Fluorescence changes at 510 nm on complexing free Ca²⁺. (c) Hill plot for the complexation of **BAN12** with free Ca²⁺. (d) Fluorescence as a function of -log[Ca²⁺]_{free}.

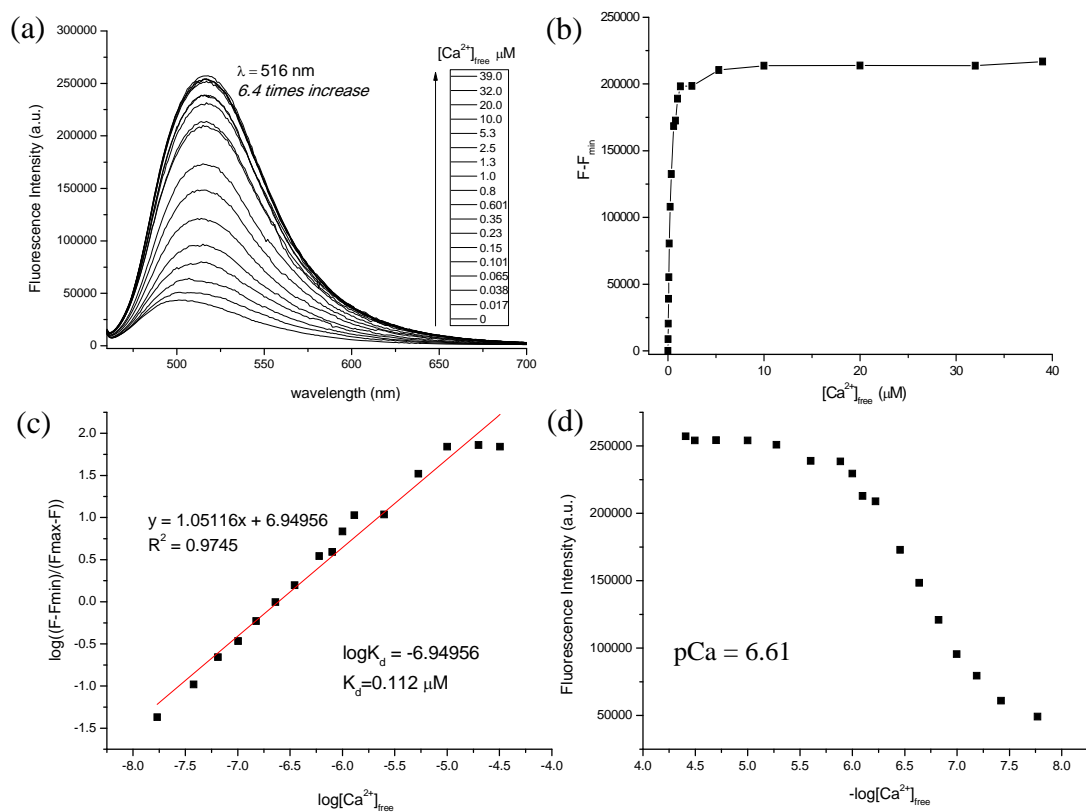


Figure 4.36 (a) Emission spectra of 1 μM **BAN12** and 300 μM DMPC:DOPG = 1:1 (52 nm in radius SUVs) in MOPS (30 mM), KCl (100 mM), EGTA (10 mM) buffer at pH 7.2 solution in the presence of varying amounts of free Ca²⁺. (λ_{ex} = 450 nm) (b) Fluorescence changes at 510 nm on complexing free Ca²⁺. (c) Hill plot for the complexation of **BAN12** with free Ca²⁺. (d) Fluorescence as a function of -log[Ca²⁺]_{free}.

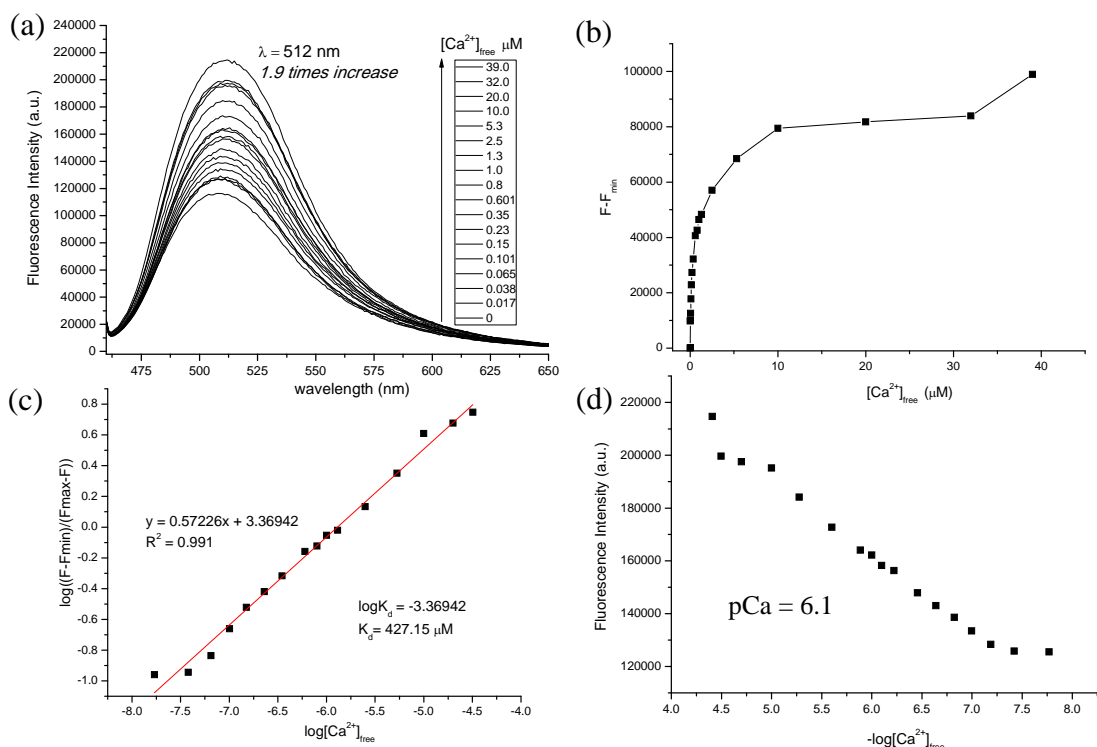


Figure 4.37 (a) Emission spectra of 1 μM **BAN12** and 300 μM DMPC:DOPG = 1:1 (24.6 nm in radius SUVs) in MOPS (30 mM), KCl (100 mM), EGTA (10 mM) buffer at pH 7.2 solution in the presence of varying amounts of free Ca^{2+} . ($\lambda_{\text{ex}} = 450$ nm) (b) Fluorescence changes at 510 nm on complexing free Ca^{2+} . (c) Hill plot for the complexation of **BAN12** with free Ca^{2+} . (d) Fluorescence as a function of $-\log[\text{Ca}^{2+}]_{\text{free}}$.

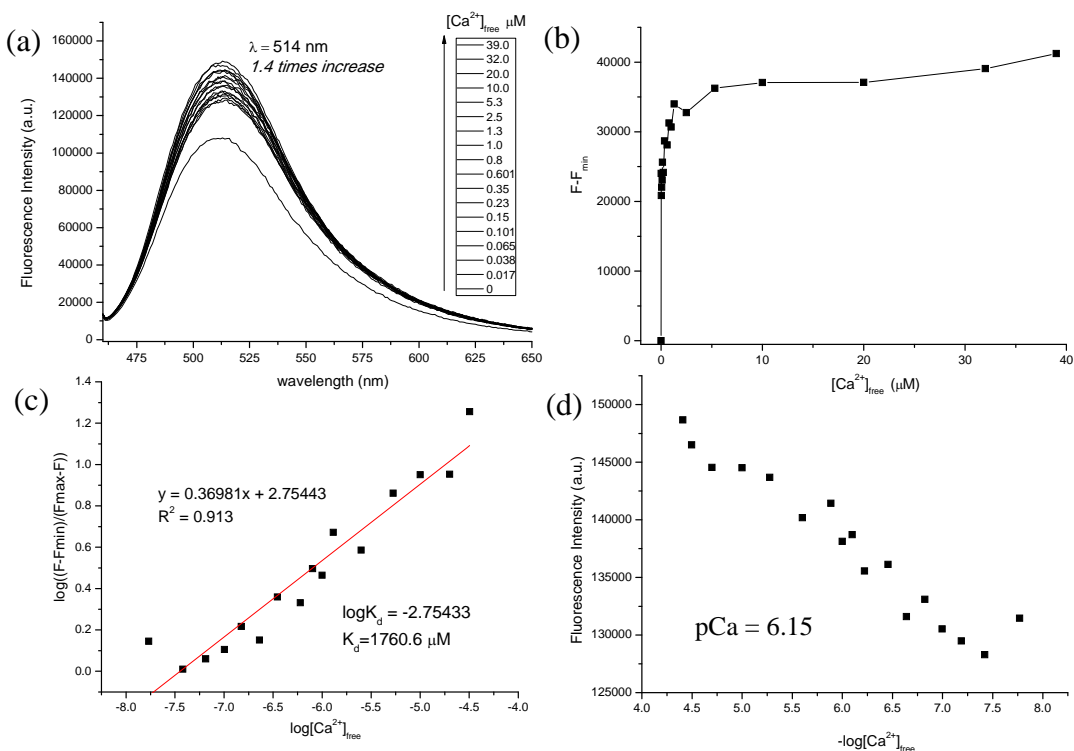


Figure 4.38 (a) Emission spectra of 1 μM **BAN12** and 300 μM DMPC:DOPG = 2:3 (26 nm in radius SUVs) in MOPS (30 mM), KCl (100 mM), EGTA (10 mM) buffer at pH 7.2 solution in the presence of varying amounts of free Ca^{2+} . ($\lambda_{\text{ex}} = 450$ nm) (b) Fluorescence changes at 510 nm on complexing free Ca^{2+} . (c) Hill plot for the complexation of **BAN12** with free Ca^{2+} . (d) Fluorescence as a function of $-\log[\text{Ca}^{2+}]_{\text{free}}$.

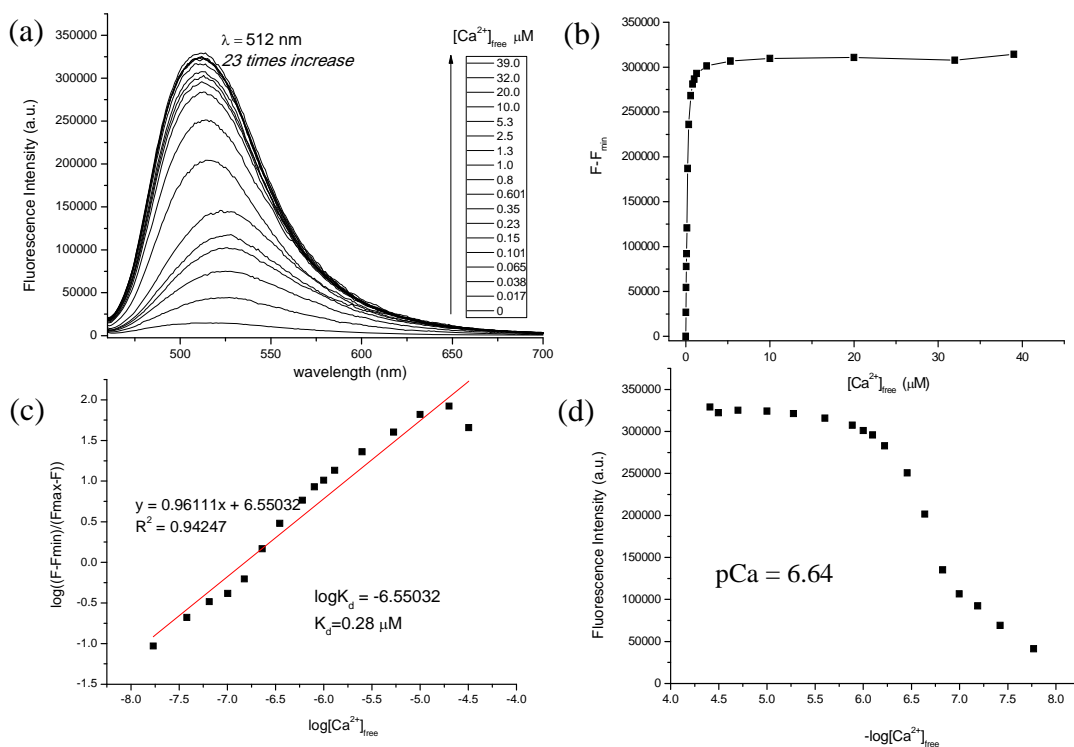


Figure 4.39 (a) Emission spectra of 1 μM **BAN12** and 300 μM DOPG (22 nm in radius SUVs) in MOPS (30 mM), KCl (100 mM), EGTA (10 mM) buffer at pH 7.2 solution in the presence of varying amounts of free Ca^{2+} . ($\lambda_{\text{ex}} = 450$ nm) (b) Fluorescence changes at 510 nm on complexing free Ca^{2+} . (c) Hill plot for the complexation of **BAN12** with free Ca^{2+} . (d) Fluorescence as a function of $-\log[\text{Ca}^{2+}]_{\text{free}}$.

In this series of K_d measurements, the lifetime of excited **BAN12** in the different liposome were measured separately with or without Ca^{2+} (Table 4.4). Lifetime defined by:

$$\tau = 1/k_F + k_{NR} \quad \text{Equation 4.4}$$

i.e. the reciprocal of the sum of rates of deexcitation.

As shown in the following equation, the decline of fluorescence intensity versus time at 515 nm, consistent with a biexponential model:

$$I_{(t)} = A + B1^* \cdot e^{-t/T1} + B2^* \cdot e^{-t/T2} \quad \text{Equation 4.5}$$

With the ratio of $B1^*$ and $B2^*$, the T1 and T2 percentage can be calculated and listed in the Table. Basically, in the SUVs solution the lifetime of non-complexed **BAN12** ($[\text{Ca}^{2+}]_{\text{free}} = 0$ μM) is shorter than the complexed $\text{Ca}^{2+}:\text{BAN12}$ ($[\text{Ca}^{2+}]_{\text{free}} = 39$ μM). This can mean that the PET mechanism in **BAN12** is still functional in the liposome environment but being quenched when $\text{Ca}^{2+}:\text{BAN12}$ complex formed. We also examined the lifetime of **BAN12** in the same condition buffer solution but without lipid, the result showed the reverse trend with

unapparent increase in lifetime when the Ca^{2+} :**BANI2** complex formed. This could be due to the **BANI2** aggregation-induced unusual behaviors as mentioned in Chapter 2. From the reasonable lifetime results in the liposome environment, **BANI2** aggregation seems diminished due to the good dispersion in the lipid membrane. On the other hand, at $[\text{Ca}^{2+}]_{\text{free}} = 0 \mu\text{M}$ situation, one can see the lifetime increase on raising the blend ratio of neutral lipid DMPC and anionic DOPG from 3:1 to 2:3. At the same time, the switch-on/off ratios decrease from 6.4, 1.9, to 1.4-fold as shown in Table 4.3. Therefore, combining these two trends implicate that blending anionic lipid into neutral lipid can quench the PET mechanism and lead to the fluorescence being switched-on at the first stage without complexing Ca^{2+} .

	switch off ($[\text{Ca}^{2+}]_{\text{free}} = 0 \mu\text{M}$)		switch on ($[\text{Ca}^{2+}]_{\text{free}} = 39 \mu\text{M}$)	
	T1/ns	T2/ns	T1/ns	T2/ns
DOPC	0.45 (71%)	5.5 (29%)	0.62 (27%)	7.97 (73%)
DMPC:DOTAP = 3:1	0.43 (60%)	7.1 (40%)	0.65 (18%)	10.1 (82%)
DMPC:DOTAP = 1:1	0.46 (61%)	7.8 (39%)	0.53 (19%)	9.5 (81%)
DMPC:DOPG = 3:1	0.34 (70%)	6.63 (30%)	1.27 (12%)	9.7 (88%)
DMPC:DOPG = 1:1	0.67 (33%)	9.6 (67%)	0.75 (23%)	9.5 (77%)
DMPC:DOPG = 2:3	0.9 (21%)	10 (78%)	0.92 (21%)	9.7 (78%)
free solution	1 (50%)	5.2 (50%)	0.38 (-15%)	3 (115%)

Table 4.4 Lifetime of **BANI2** in the different SUVs solution. $\lambda_{\text{ex}} = 460 \text{ nm}$, $\lambda_{\text{em}} = 510 \text{ nm}$ for liposome experiments. $\lambda_{\text{ex}} = 460 \text{ nm}$, $\lambda_{\text{em}} = 545 \text{ nm}$ for free solution measurement.

To compare the effect of alkyl chain length on the **BANI**-probes in the liposome environment, another new fluoroionophore **BANI3** with a shorter (ethyl) chain connected to the chromophore was also performed the K_d measurement in the DMPC SUVs solution (Figure 4.40). The experimental results of **BANI3** in the DMPC SUVs and in the free solution (see Chapter 2.1.3.4, Figure 2.49) were compiled in the Table 4.5.

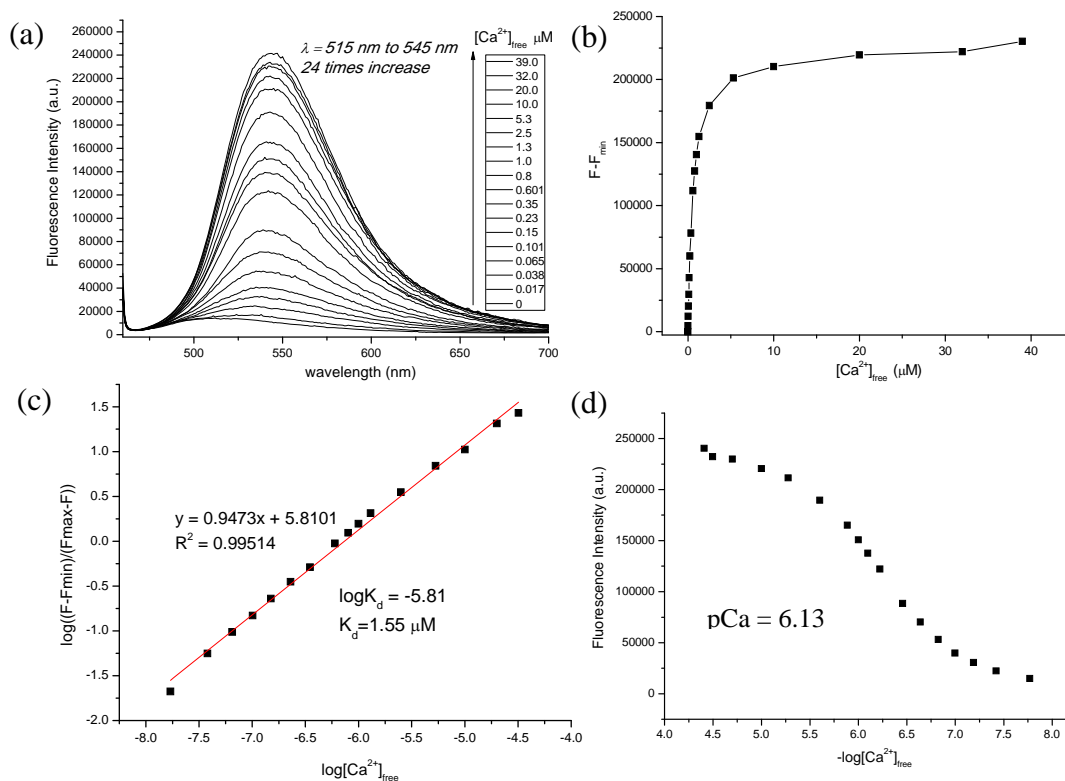


Figure 4.40 (a) Emission spectra of 1 μM **BANI3** and 300 μM DMPC (14 nm in radius SUVs) in MOPS (30 mM), KCl (100 mM), EGTA (10 mM) buffer at pH 7.2 solution in the presence of varying amounts of free Ca^{2+} . ($\lambda_{\text{ex}} = 450 \text{ nm}$) (b) Fluorescence changes at 510 nm on complexing free Ca^{2+} . (c) Hill plot for the complexation of **BANI3** with free Ca^{2+} . (d) Fluorescence as a function of $-\log[\text{Ca}^{2+}]_{\text{free}}$.

environment for BANI3	SUVs size (radius in nm)	K_d value (μM)	pCa	switch on/off factors (n-fold)	Figure
DMPC (neutral)	14	1.55	6.13	24	4.40
free solution	/	0.005	6.55	116	2.49

Table 4.5 K_d determination and experimental results for **BANI3** in different environments

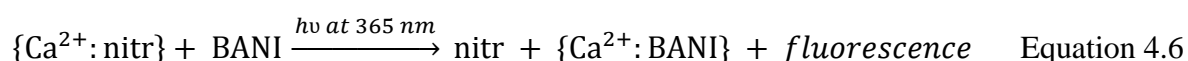
The results in the Table 4.5 show that the different environment could affect the K_d values and the fluorescence enhancement factor of **BANI3**. The K_d value and the switch-on/off factors are lower when **BANI3** is in the liposome environment (1.55 μM , 24-fold fluorescence enhancement) than in the free solution (5 nm, 116-fold). As for the similar tendency found in **BANI2**, the difference between **BANI3** in the liposome environment and free solution can be explained in the same way. On the other hand, comparing **BANI2** and **BANI3** in the DMPC SUVs solution with the same condition, the emission spectra of **BANI3** in Figure 4.40a show an apparent red-shift from 515 nm to 545 nm when $\text{Ca}^{2+}:\text{BANI3}$ is formed. But in the case of **BANI2** the emission spectra stay $\sim 515 \text{ nm}$ without shift when $\text{Ca}^{2+}:\text{BANI3}$ formed (Figure 4.32a). It means even **BANI3** is well mixed and fixed in the liposome bilayers in the beginning, but once $\text{Ca}^{2+}:\text{BANI3}$ is formed the complex does not prefer to stay in the hydrophobic environment and would be pulled out when Ca^{2+} was added.

On the contrary, the emission spectra of **BANI2** shows that the long alkyl chain can help the probe fix on the hydrophobic liposome membrane and not easily be isolated even when **Ca²⁺:BANI2** was formed. As a result, the smaller K_d value of **BANI2** (6.8 nM) than that of **BANI3** (1.55 μ M) can be attributed to the octyl group, which would stabilize the **Ca²⁺:BANI2** complex by inducing a more hydrophobic environment around BAPTA in the DMPC SUVs.

4.5 Photoinduced ion-shuttle in the free solution and SUVs nanodomains

As described in Chapter 1 General introduction, the goal of thesis is to build up the ion communication combining photoactive ion-shuttle and biomimetic host systems. With all the acquired information in mind, in this last section two Ca^{2+} -ejectors, **nitr-5** & **C15nitr-5**, and two Ca^{2+} -acceptors, **BANI2** & **BANI3** are employed, as model compounds to fabricate the Ca^{2+} -donor/acceptor pair as active components in the photoactivated ion-shuttle. One can notice that **nitr-5** and **BANI3** are without a long alkyl chain hence will be used in the free solution system; while **C15nitr-5** and **BANI2** are long alkyl chain equipped compounds so essentially were used in the SUVs matrix solution due to the stabilization on the liposome membrane by alkyl groups. The primary intention is represented in the cartoon graphic (Figure 4.41) for the two photoinduced ion-shuttle environments: free solution and SUVs matrix.

The photoinduced supramolecular system of Ca^{2+} -transport will be initiated by photolysis of **nitr-5** or **C15nitr-5** at 365 nm. The UV irradiation would lead to a 43-fold K_d difference for **nitr-5** and 13-fold for **C15nitr-5**, thereby the Ca^{2+} can be released and captured by Ca^{2+} -acceptors (**BANI2** or **BANI3**). Once the Ca^{2+} -acceptors catch the Ca^{2+} ion, the photon induced electron transfer (PET) process should be blocked and the fluorescence from naphthalimide chromophore could be enhanced and observed ($\lambda_{em} = 545$ nm or ~ 520 nm in free solution or SUVs matrix, respectively). Therefore, observing the fluorescence from switch-off to switch-on process allows us to confirm the Ca^{2+} -transport according to the following equation:



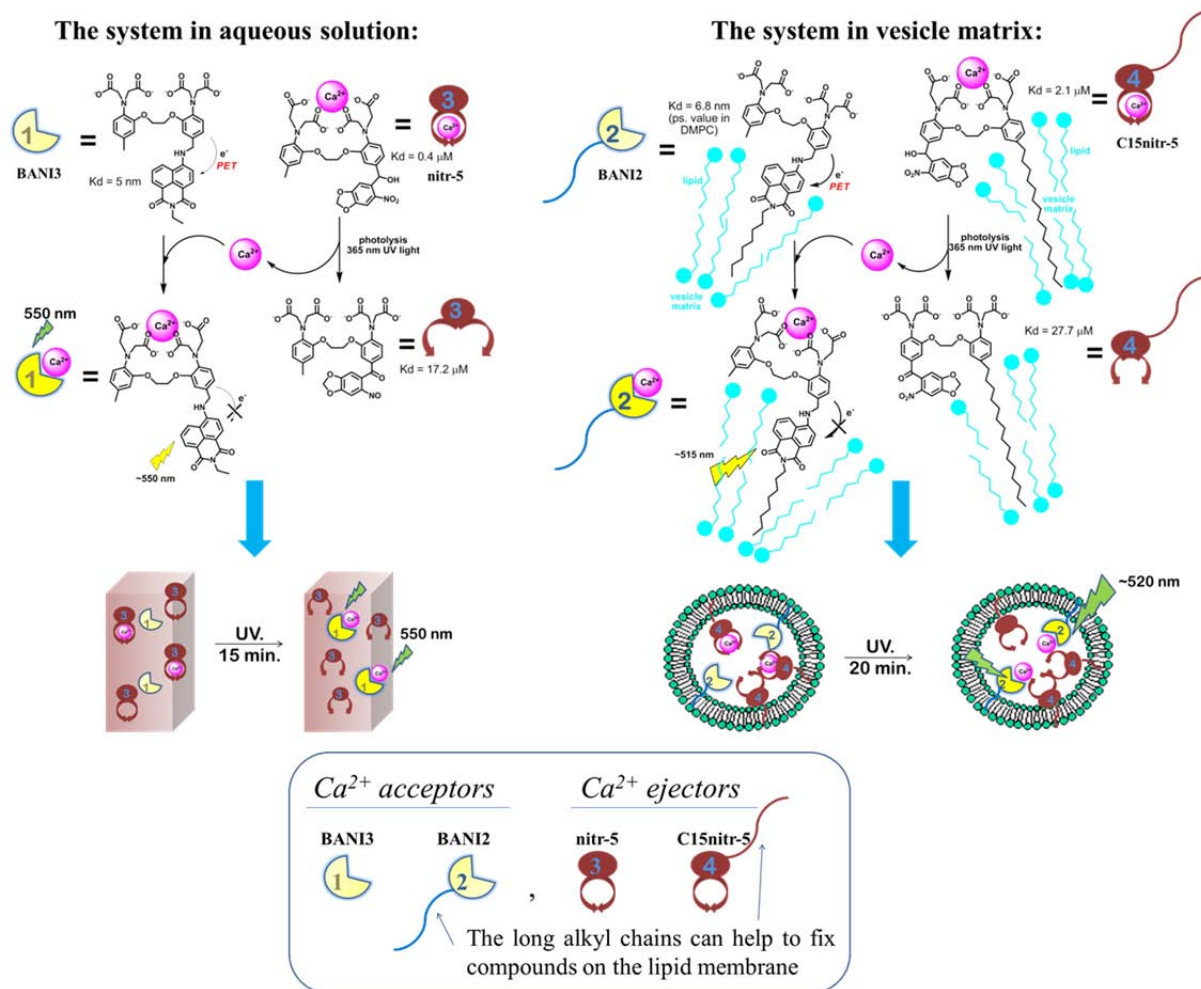


Figure 4.41 Graphical representative of photoactivated ion-shuttle in free solution and in a liposome environment

4.5.1 Photoinduced ion-shuttle in the free solution

First of all, since the K_d value of **nitr-5** is 80 times bigger than **BANI3**, the Ca^{2+} ion would prefer to complex with **BANI3** instead of **nitr-5**. So the trial solution containing **BANI3** (1 μM), MOPS (30 mM), KCl (100 mM), and Ca^{2+} (10 μM) at pH 7.2 was titrated by **nitr-5** to see how much **nitr-5** is needed to quench the fluorescence, i.e. Ca^{2+} is taken by **nitr-5** from **BANI3** (Figure 4.42a). Following UV irradiation at 365 nm to the solution ($[\text{nitr-5}] = 0 \mu\text{M}$ or 100 μM), the results showed the fluorescence decreased after the UV irradiation (Figure 4.42b)

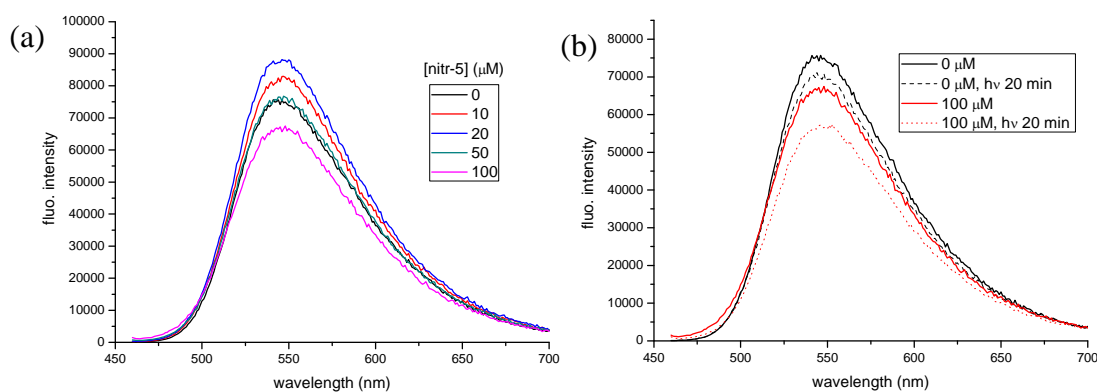


Figure 4.42 (a) Titration of **nitr-5** into **BAN13** (1 μM), MOPS (30 mM), KCl (100 mM), and Ca^{2+} (10 μM) pH 7.2 solution, (b) before and after UV irradiation at 365 nm to the non-titrated and titrated solution where $[\text{nitr-5}] = 0 \mu\text{M}$ and 100 μM , respectively. $\lambda_{\text{ex}} = 450 \text{ nm}$

After the failure of a trial experiment, the experiment was performed stepwise varying parameters systematically. First, we need to know how much Ca^{2+} is needed for **BAN13** to be fully switched-on and reaching the maximum fluorescence intensity without the additive of EGTA (basically, EGTA is a crucial additive to get good switch-on/off result as examined in Chapter 2 and all the K_d measurement experiments). As shown in Figure 4.43, 1: 1 equivalent ratio of **BAN13**: Ca^{2+} was found to reach the maximum intensity, but **BAN13** had a certain fluorescence intensity even at $[\text{Ca}^{2+}] = 0 \mu\text{M}$ due to the contamination of Ca^{2+} in the environment which generally can be eliminated by EGTA.

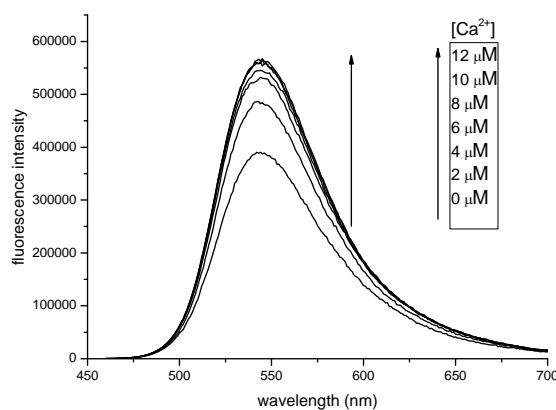


Figure 4.43 **BAN13** fluorescence switch-on test by titration of CaCl_2 into 10 μM **BAN13**, 30 mM MOPS, and 100 mM KCl solution at $\lambda_{\text{ex}} = 450 \text{ nm}$

After knowing the adequate Ca^{2+} concentration required to switch on the **BAN13** solution without help by EGTA, we tested the required photolysis time for the concentrated **nitr-5** solution (6 mM) which would be titrated into the **BAN13** solution (Figure 4.44). The irradiation process at 365 nm took ~ 4 hours to complete the **nitr-5** photolysis in such a concentrated case. It allowed us to use this fully photolyzed **nitr-5** solution to perform the

coming titration experiment.

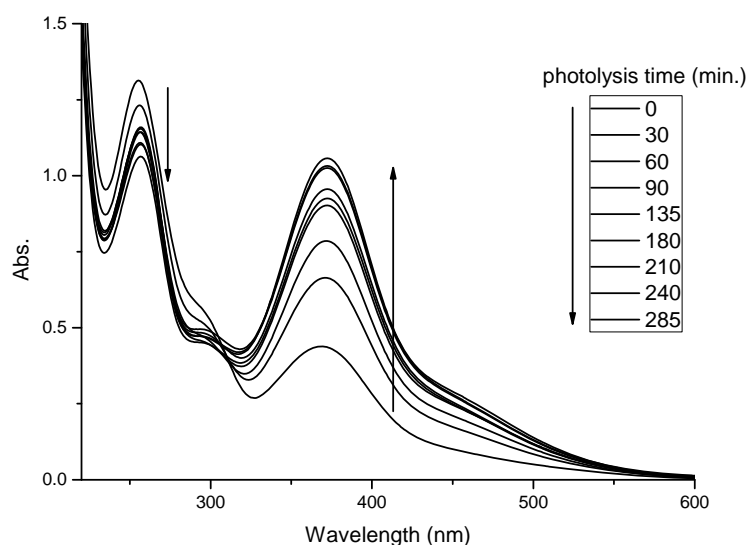


Figure 4.44 Electronic absorption spectra tracing the photolysis process of **BANI3** solution ($6 \times 10^{-3} \text{M}$), diluted and measured at $5 \times 10^{-5} \text{M}$, $\lambda_{\text{irrad.}} = 365 \text{ nm}$

With the required adequate concentration of Ca^{2+} at $10 \mu\text{M}$ to switch on $10 \mu\text{M}$ **BANI3** solution and concentrated **nitr-5**/photolyzed **nitr-5** in hand, the constitution of the switched-on solution was fixed with **BANI3**: $\text{CaCl}_2 = 1:1$ ($10 \mu\text{M}$) in 30 mM MOPS and 100 mM KCl at pH 7.2 followed by titrating this solution with concentrated **nitr-5** (Figure 4.45a,b) and pre-photolyzed **nitr-5** solution (Figure 4.45c,d). In this way, we tried to find the maximum fluorescence intensity difference of the two titration curves which could be a reference of switch-on/off difference of photoinduced ion-shuttle pair in one pot solution. As shown in Figure 4.45e, the two titration curves have maximum difference when the concentration of **nitr-5**/photolyzed **nitr-5** is $\sim 30 \mu\text{M}$. As a result, $30 \mu\text{M}$ **nitr-5** was used in a one-pot solution containing $10 \mu\text{M}$ **BANI3** and $10 \mu\text{M}$ CaCl_2 to test the Ca^{2+} -transport in the coming experiment.

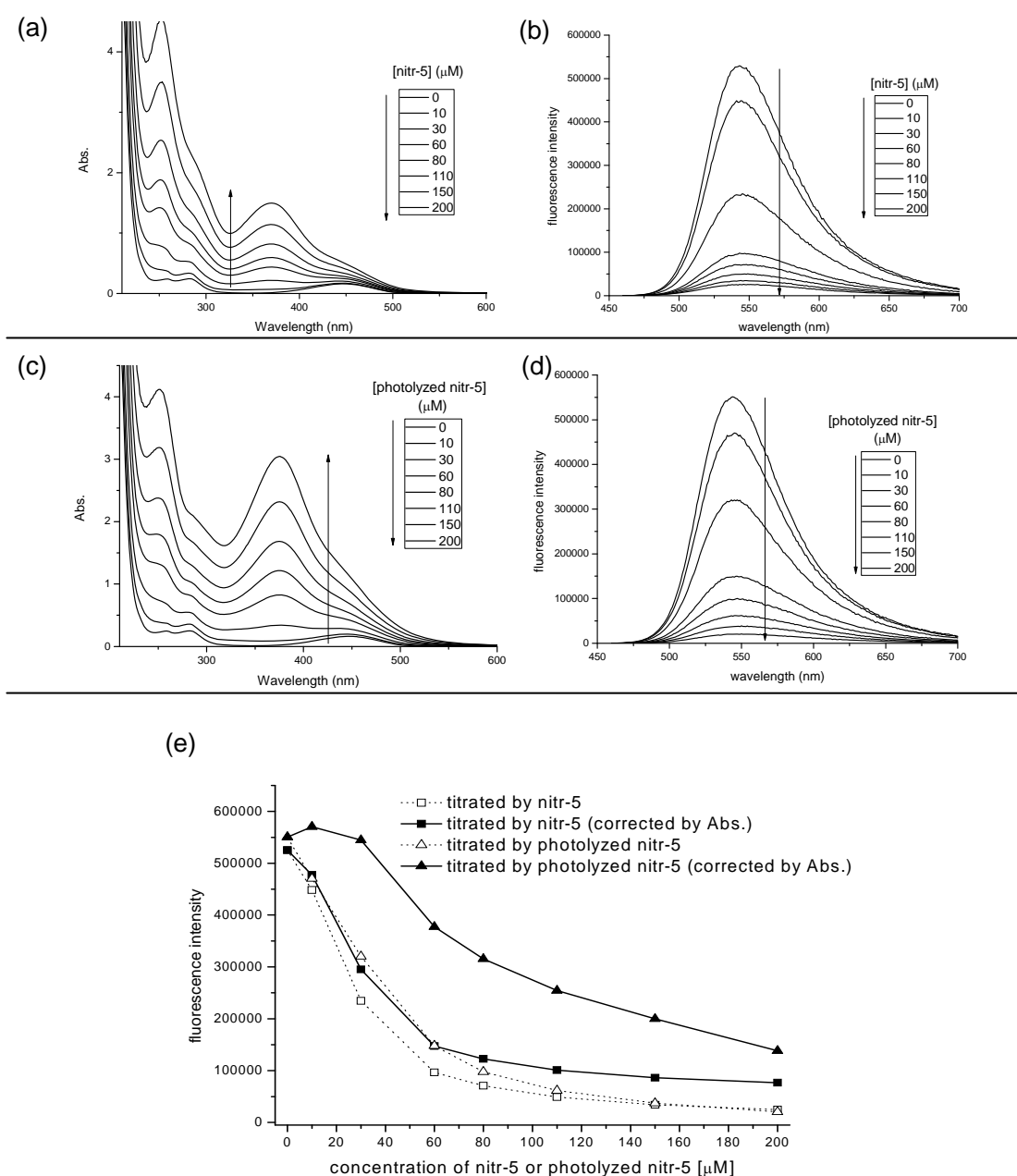


Figure 4.45 (a) Electronic absorption spectra and (b) fluorescence emission spectra on titrating **nitr-5** into the switched-on **BANI3** solution (10 μM **BANI3**, 10 μM CaCl_2 , 30 mM MOPS, and 100 mM KCl at pH 7.2) upon excitation at 450 nm; (c) Electronic absorption spectra and (d) fluorescence emission spectra of titrating pre-irradiated **nitr-5** into the switched-on **BANI3** solution at $\lambda_{\text{ex}} = 450$ nm. (e) Titration curves of fluorescence intensity versus concentration of **nitr-5** or photolyzed **nitr-5**.

Before directly testing the photolysis for the one pot ion-shuttle pair, it was necessary to ensure the emission intensity at 545 nm is mainly from **BANI3**. For this reason the blank experiment was performed to double check whether with/without Ca^{2+} or before/after photolysis **nitr-5** has no fluorescence intensity at 545 nm. The test was done in the same buffer solution as in the **nitr-5** titration experiments (30 mM MOPS, 100 mM KCl, pH 7.2), and the [**nitr-5**] are 10, 50, and 175 μM with or without 10 μM Ca^{2+} (Figure 4.46). As shown in Figure 4.46b & d, the fluorescence intensity at 545 nm is very weak in all conditions after

excitation at 450 nm. Therefore, the blank experiment shows in all conditions **nitr-5** has no fluorescence contribution at 545 nm. The fluorescence enhancement would therefore be due exclusively to the **BANI3** complexed with Ca^{2+} .

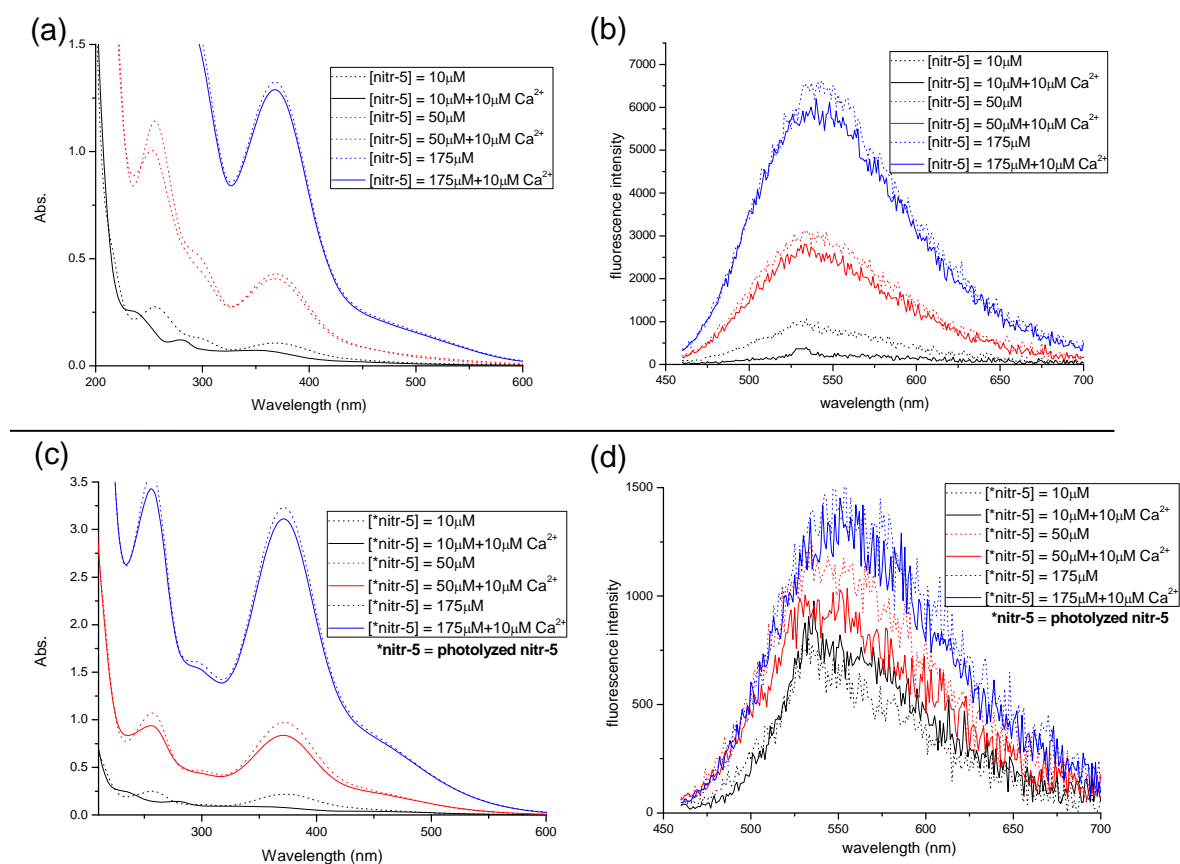


Figure 4.46 Electronic absorption spectra (a,c) and fluorescence emission spectra (b, d, $\lambda_{\text{ex}} = 450 \text{ nm}$) of $10 \mu\text{M}$, $50 \mu\text{M}$, $175 \mu\text{M}$ **nitr-5** solution (a, b) and photolyzed **nitr-5** solution (c, d) in 30 mM MOPS and 100 mM KCl at $\text{pH } 7.2$ solution with or without $10 \mu\text{M}$ Ca^{2+} .

With the constitution decided by titration curve experiment (Figure 4.45e) in mind, we decided to mix **BANI3** ($10 \mu\text{M}$), **nitr-5** ($30 \mu\text{M}$), CaCl_2 ($10 \mu\text{M}$) in the buffer solution (30 mM MOPS and 100 mM KCl). By adjusting stepwise all the components, one-pot photoinduced Ca^{2+} -transport experiment to improve the failed one (Figure 4.42) was achieved as shown in Figure 4.47. As mentioned, at certain concentrations **BANI3** can be fully switched on by one equivalent of Ca^{2+} , but 3 equivalent of **nitr-5** ($30 \mu\text{M}$) should be enough to switch it off by grabbing the Ca^{2+} from **BANI3** to form $\{\text{Ca}^{2+}:\text{nitr-5}\}$ and free **BANI3** at the first stage. Photolysis at 365 nm should be able to initiate the Ca^{2+} -transport to form $\{\text{Ca}^{2+}:\text{BANI3}\} + \text{nitr-5}$ by observing the fluorescence enhancement.

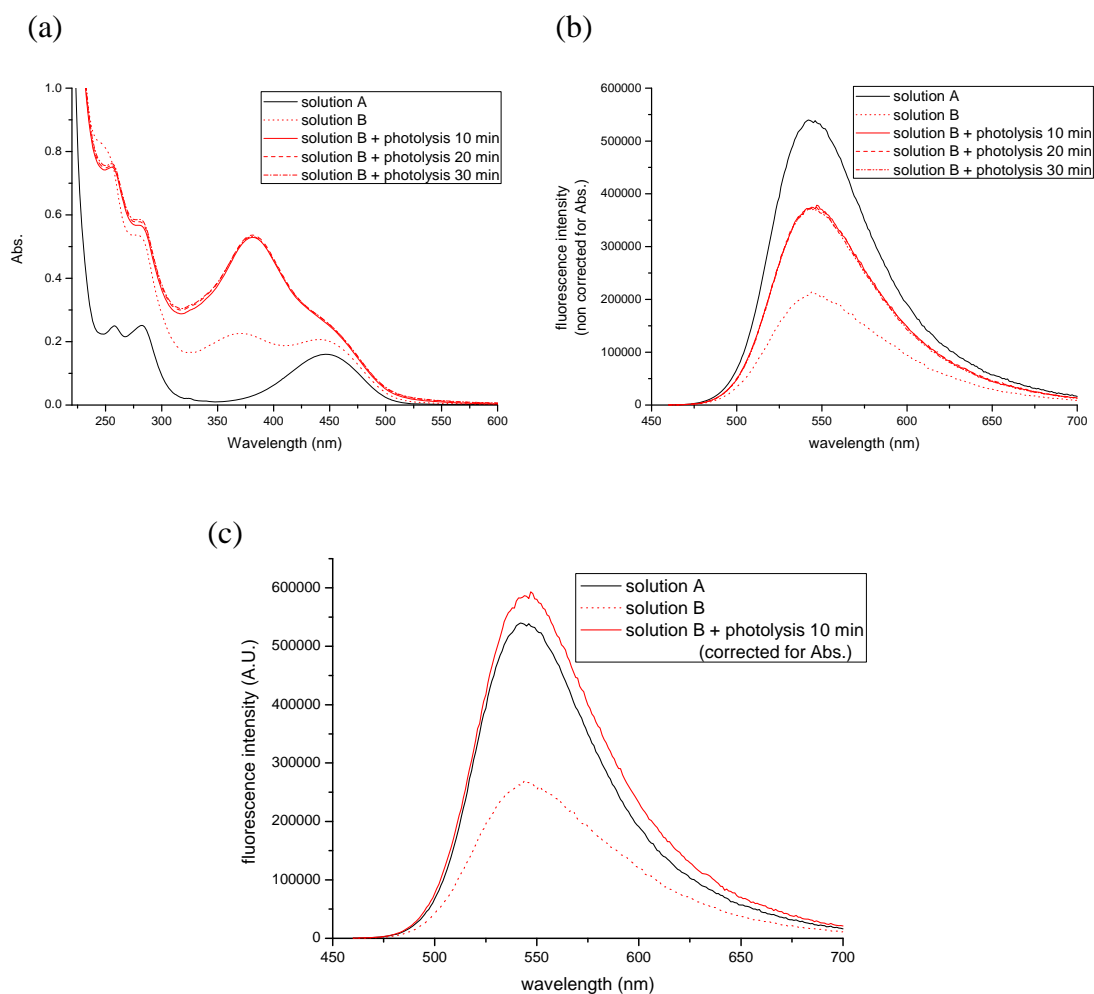


Figure 4.47 *Solution A*: control solution containing **BANI3** (10 μM), CaCl_2 (10 μM) in the KCl (100 mM), MOPS (30 mM) buffer; *solution B*: solution containing **BANI3** (10 μM), **nitr-5** (30 μM), CaCl_2 (10 μM) in KCl (100 mM), MOPS (30 mM) buffer. Electronic absorption spectra (a), fluorescence emission spectra (b), and fluorescence emission spectra corrected by absorption (c), of *solution A*, *B*, and photolyzed *solution B* 10~30 min. $\lambda_{\text{ex}} = 450$ nm

The result showed after adding 30 μM **nitr-5** into *control solution A* (**BANI3** 10 μM , CaCl_2 10 μM with buffer) to become *experimental solution B*, the absorption band at 370 nm emerged (Figure 4.47a), and the emission band of $\{\text{Ca}^{2+}:\text{BANI3}\}$ at ~ 550 nm decreased which was caused by forming $\{\text{Ca}^{2+}:\text{nitr-5}\} + \text{free BANI3}$ (Figure 4.47b). Photolysis would lead to the increase of **nitr-5** absorbance band at 375 nm implying the release of Ca^{2+} . The recovery of initial **BANI3** complex by regaining Ca^{2+} from **nitr-5** to form $\{\text{Ca}^{2+}:\text{BANI3}\}$ can be observed by fluorescence re-enhancement at 550 nm as shown in Figure 4.47b or absorption-corrected version in Figure 4.47c. In the absorption-corrected spectra we could clearly observe the one-pot photocontrolled ion-shuttle pair works quiet well as the description in Figure 4.41 cartoon representative and Equation 4.6 with three stages:

1. *Solution A* : **BANI3** + Ca^{2+} in 1 : 1 molar equivalents, emissive $\{\text{Ca}^{2+}:\text{BANI3}\}$

2. *Solution A* + **nitr-5** → *Solution B* : **BANI3** + Ca²⁺ + **nitr-5** in 1 : 1 : 3 molar equivalents, fluorescence decrease ~1/2 by forming {Ca²⁺:**nitr-5**} + free **BANI3**
3. 10 min photolysis for *Solution B* : fluorescence re-enhancement by reforming {Ca²⁺:**BANI3**} + photolyzed **nitr-5**

As a result, the photoactivated ion-shuttle system made of **BANI3** and **nitr-5** in the free solution was successfully demonstrated by these trial experiments. With the same method we further tested the switch-on/off ratio of one-pot solution with 1 μM **BANI3** which was the concentration in all of the K_d measurement experiment and will be compared with vesicle matrix solution in the next section. Thirteen solutions, each containing **BANI3** (1 μM), CaCl₂ (1 μM), MOPS (30 mM), and KCl (100 mM) at pH 7.2 with different concentrations of **nitr-5** (1 ~ 80 μM) were separately prepared and their photophysical properties tested before and after photolysis as shown in Figure 4.48.

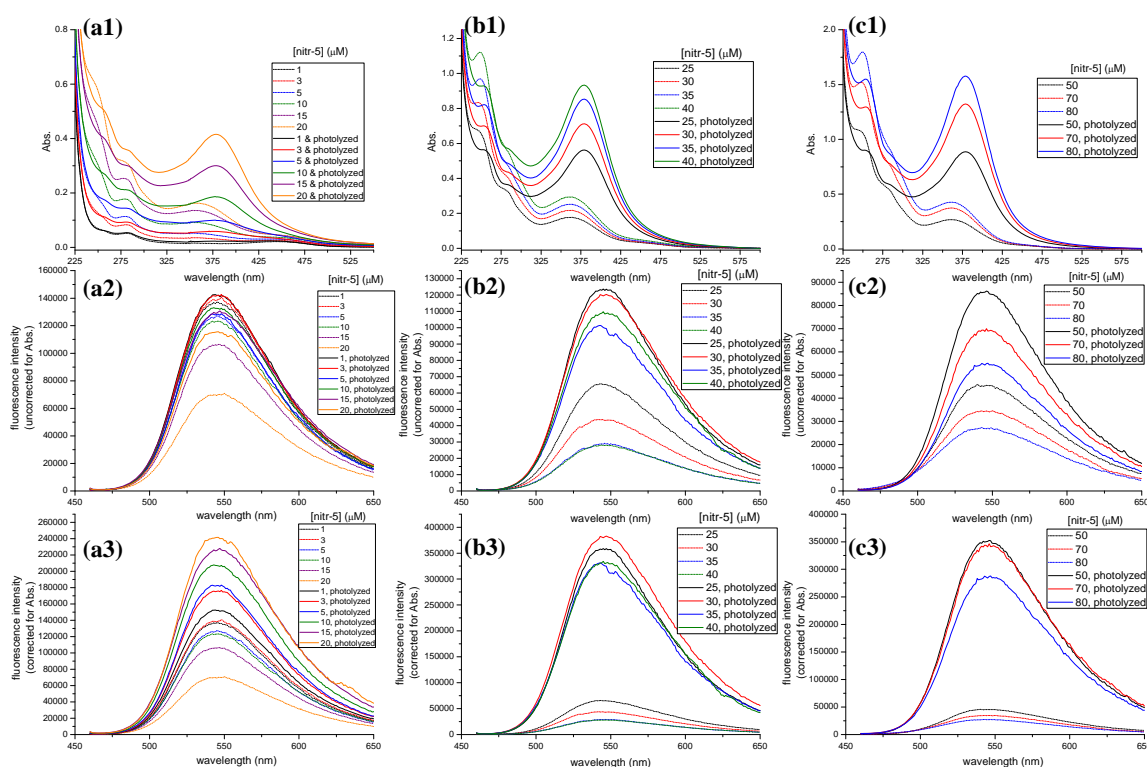


Figure 4.48 (a1, b1, c1) Electronic absorption spectra, (a2, b2, c2) original fluorescence emission spectra, and (a3, b3, c3) fluorescence emission spectra corrected by absorption at $\lambda_{\text{ex}} = 450$ nm of one-pot photolysis induced Ca²⁺-transport of thirteen solutions containing **BANI3** (1 μM), CaCl₂ (1 μM), MOPS (30 mM), and KCl (100 mM) at pH 7.2 with different concentration of **nitr-5** (1 ~ 80 μM). Note. The fluorescence intensity of a, and b series are incomparable due to the preparation and measurement on different days, hence needed to be put separately and their absolute fluorescence intensity cannot be compared.

In this way we tried to find the best **BANI3**: **nitr-5** blending ratio in these thirteen solutions to obtain the maximum fluorescence enhancement. i.e. the best ratio of ejector and acceptor for Ca²⁺-transport in the free solution. The fluorescence enhancement times are organized in

Table 4.6 and further compared with the **BANI2/ C15nitr-5** pair in Figure 4.50. It shows 1:40, **BANI3/nitr-5** molar equivalents in the 1 μM **BANI3** with 1 μM CaCl_2 buffered solution can reach the best fluorescence enhancement of about 12 times.

[nitr-5] (μM)	Fluo. enhancement factor at 550 nm	
	corrected by Abs.	uncorrected
1	1.11	1.03
3	1.27	1.02
5	1.44	1
10	1.68	1.07
15	2.13	1.22
20	3.49	1.66
25	5.5	1.9
30	8.7	2.74
35	11.4	3.5
40	12	3.95
50	7.7	1.94
60	8.8	1.9
70	9.9	2
80	10	2

Table 4.6 The corrected or uncorrected fluorescence enhancement by absorption at $\lambda_{\text{ex}} = 450$ nm of one-pot photolysis induced Ca^{2+} -transport solutions containing **BANI3** (1 μM), CaCl_2 (1 μM), MOPS (30 mM), and KCl (100 mM) at pH 7.2 with different concentrations of **nitr-5** (1 ~ 80 μM)

With this result in mind, the alkyl chain equipped Ca^{2+} -ejector, **C15nitr-5**, paired with **BANI3** was tested in the same way to compare with the last case using **nitr-5**. In order to make sure **C15nitr-5** functions in the free solution before directly using in the vesicle matrix environment the experiments shown in Figure 4.49 were performed. The pair of **BANI3/C15nitr-5** fluorescence enhancement is organized in Table 4.7 and shows 1:50 molar equivalents of **BANI3/C15nitr-5** ratio can reach the best fluorescence enhancement of about 13.5 times.

To compare the result of **BANI3** pairing with different Ca^{2+} -ejectors, **nitr-5** or **C15nitr-5**, profile of fluorescence enhancement times versus Ca^{2+} -ejector concentration is shown in Figure 4.50. The two curves show generally ~45 μM of Ca^{2+} -ejector (**nitr-5** or **C15nitr-5**) is needed to obtain the best switch-on/off ability for 1 μM **BANI3** as Ca^{2+} -acceptor in the free solution environment. The higher required number of equivalents of **C15nitr-5** (50 μM) to reach maximum fluorescence enhancement compared to **nitr-5** can be due to the lower photoinduced Ca^{2+} -affinity change of **C15nitr-5** (K_d increase factor = 13-fold cf. 43-fold for **nitr-5**). This result will serve as a reference of Ca^{2+} -transport efficiency and be compared with the ion-shuttle confined in the vesicle matrix presented in the next section.

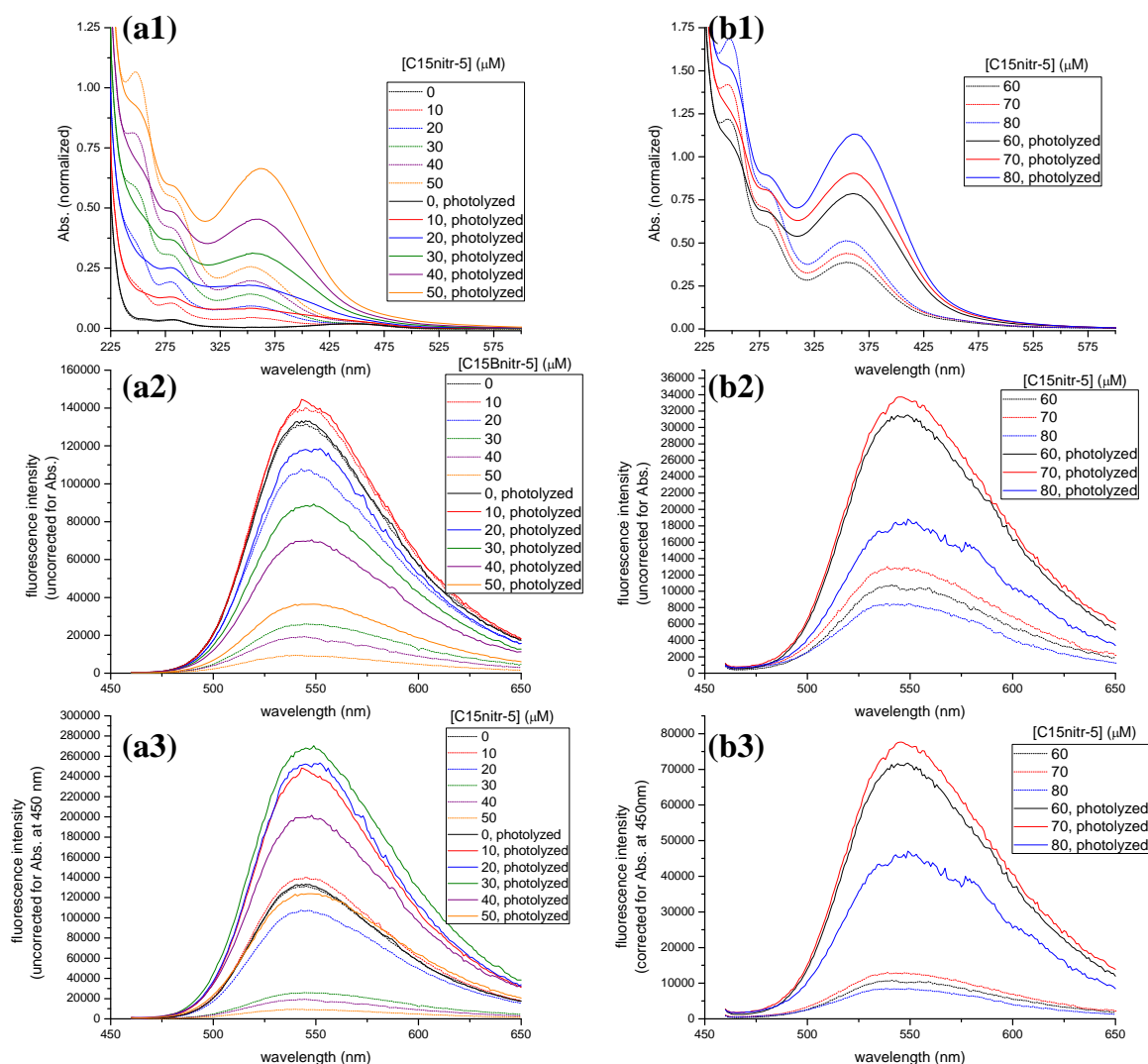


Figure 4.49 (a1, b1) Electronic absorption spectra, (a2, b2) original fluorescence emission spectra, and (a3, b3) fluorescence emission spectra corrected by absorption at $\lambda_{\text{ex}} = 450 \text{ nm}$ of one-pot photolysis induced Ca^{2+} -transport of nine solutions containing **BANI3** ($1 \mu\text{M}$), CaCl_2 ($1 \mu\text{M}$), MOPS (30 mM), and KCl (100 mM) at pH 7.2 with different concentration of **C15nitr-5** ($0 \sim 80 \mu\text{M}$). Note. The fluorescence intensity of a, and b series are incomparable due to the preparation and measurement on different days, hence needed to be put separately and their absolute fluorescence intensity cannot be compared.

[C15nitr-5] (μM)	Fluo. enhancement factor at 550 nm	
	corrected by Abs.	uncorrected
0	1	1
10	1.76	1.02
20	2.36	1.1
30	10.3	3.4
40	10.3	3.59
50	13.4	3.95
60	7	3.07
70	6	2.63
80	5.5	2.18

Table 4.7 The corrected or uncorrected fluorescence enhancement factor by absorption at $\lambda_{\text{ex}} = 450 \text{ nm}$ of one-pot photolysis induced Ca^{2+} -transport solutions containing **BANI3** ($1 \mu\text{M}$), CaCl_2 ($1 \mu\text{M}$), MOPS (30 mM), and KCl (100 mM) at pH 7.2 with different concentrations of **C15nitr-5** ($1 \sim 80 \mu\text{M}$)

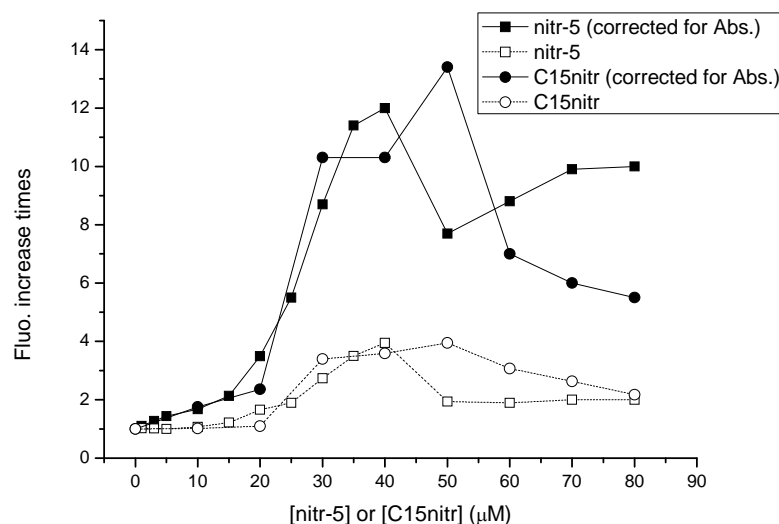


Figure 4.50 Profile of fluorescence enhancement factor versus Ca^{2+} -ejectors concentration in the **BANI3** (1 μM), CaCl_2 (1 μM), MOPS (30 mM), and KCl (100 mM) solution at pH 7.2

4.5.2 Photoactivated ion-shuttle confined in the vesicle matrix

After the establishment of Ca^{2+} -transport in the free solution, we further performed the more complicated system combining the photoactivated ion-shuttle with the SUVs matrix. In this way we anticipate enhancement of the Ca^{2+} -transport efficiency through the compartmentalization effect by liposome nanodomains.

As described in the Figure 4.41 cartoon graphic, the photoactivated supramolecular system in the vesicle matrix utilizes the long alkyl chain equipped **BANI2** and **C15nitr-5**. As the established process in the free solution system, first we need to know how much Ca^{2+} is needed to fully switch on the fluorescence of **BANI2** without the additive EGTA (basically, EGTA is a crucial additive to obtain a good switch-on/off ratio even in the SUV environment as described in Section 4.4.1). We found a 1:1 molar equivalent ratio of **BANI2**: Ca^{2+} is adequate, more Ca^{2+} would lead to the fluorescence decrease (Figure 4.51).

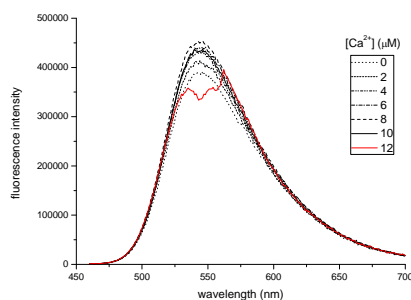


Figure 4.51 **BANI2** fluorescence switch-on test: 10 μM **BANI2** in 30 mM MOPS, 100 mM KCl buffer at pH 7.2

Before directly using the long alkyl chain equipped Ca^{2+} -ejector and Ca^{2+} -acceptor, we tested the simplified case using **BANI2** as Ca^{2+} -acceptor which bears an octyl group but keeping **nitr-5** (without long hydrocarbon chain) as Ca^{2+} -donor in the SUV solution made of neutral lipid DMPC. As the same strategy in the last section, making use of the fluorescence difference between titration curves allows us to find the best blending ratio of the **BANI2/nitr-5** pair in the vesicle environment. In this way, the maximum fluorescence intensity difference of the two titration curves which could be a reference of switch-on/off ability of photoinduced ion-shuttle pair in a one pot solution was sought (Figure 4.52).

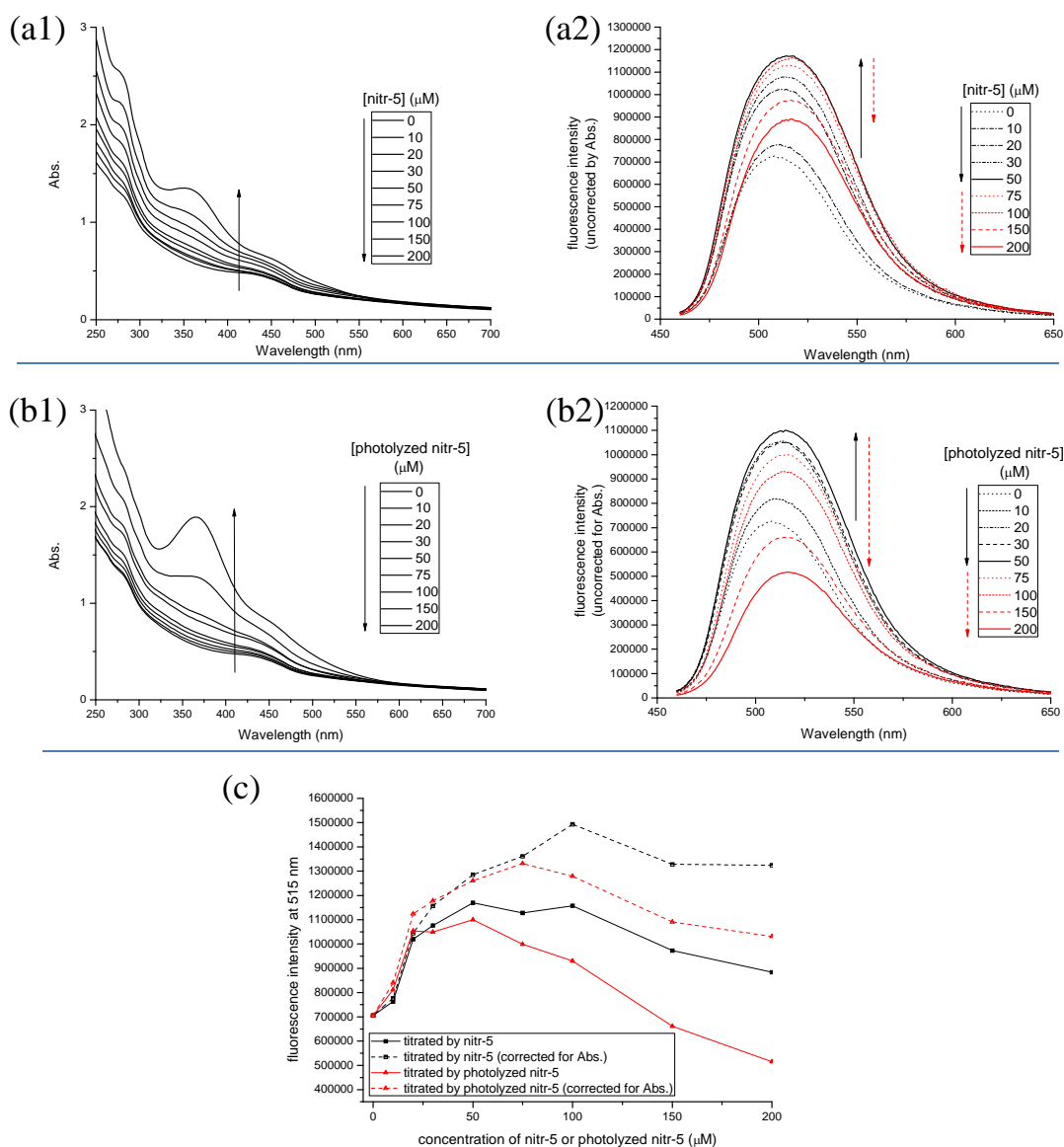


Figure 4.52 (a1, a2) Electronic absorption spectra and fluorescence emission spectra of titrating **nitr-5** into the switched-on **BANI2** vesicle solution (10 μM **BANI2**, 3 mM DMPC, 10 μM CaCl_2 , 30 mM MOPS, and 100 mM KCl at pH 7.2); (b1, b2) Electronic absorption spectra and fluorescence emission spectra of titrating pre-irradiated **nitr-5** into the switched-on **BANI2** vesicle solution. (c) Titration curves of fluorescence intensity versus concentration of **nitr-5** or photolyzed **nitr-5**.

As the experiment shows in Figure 4.52, a switched-on **BANI2** solution was obtained by adding adequate 1 equivalent CaCl_2 and mixing with 300 equivalent DMPC (3 mM) in the buffer solution (30 mM MOPS, 100 mM KCl at pH 7.2) titrated by concentrated **nitr-5** (Figure 4.52a) and pre-photolized **nitr-5** solution (Figure 4.52b).

The absorption spectra showed the normal trend of enhancement of 375 nm shoulder while **nitr-5** or photolized **nitr-5** were titrated into the solution. As for the emission spectra change, as organized in Figure 4.52c, the two titration curves increased at first then decreased. The decrease of fluorescence was expected by more and more **nitr-5** or photolyzed **nitr-5** in solution, but the increase in fluorescence at the first stage is probably due to the mixed **BANI2** in DMPC vesicles which had not been fully switched on with enough Ca^{2+} . This might be caused by the environmental changing to liposome matrix and the lower Ca^{2+} affinity of **BANI2**. As a result, we need to pre-mix **BANI2** with buffered SUVs solution then determine the required Ca^{2+} amount to fully switch on **BANI2** when it is in a more hydrophobic liposome environment again.

The procedure of making SUVs solution involves mixing the solutes with lipid compound in chloroform then obtaining a well-blended film by evaporating the solvent. Adding water or buffer solution to rehydrate the film followed by several cycles of microtip sonication allows us to get the small lamellar structure. As shown in Figure 4.53, the influence of Ca^{2+} addition timing was tested (before, after, or in the middle of the sonication process) on the fluorescence switch-on ability or the required Ca^{2+} amount. The timing of adding Ca^{2+} before sonication can be regarded as inside and outside of the vesicle are evenly distributed with Ca^{2+} ; on the contrary for the post-addition of Ca^{2+} , it can be imagined that access of the Ca^{2+} to enter the vesicle is prohibited hence cannot be utilized by probes on the inner membrane.

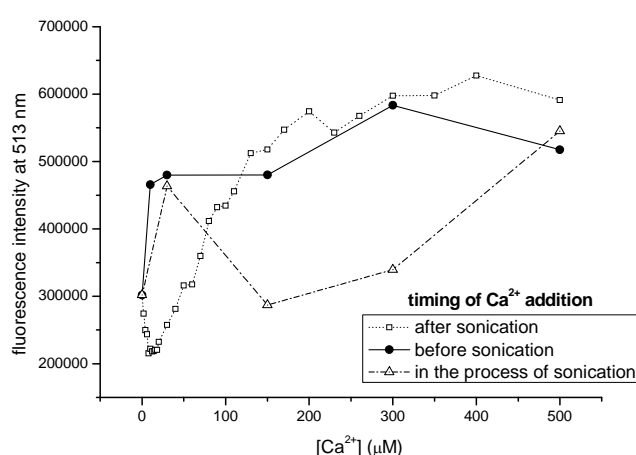


Figure 4.53 Ca^{2+} addition before, after, and in the middle of a 4 cycle microtip sonication for SUV preparation. A solution containing 10 μM **BANI2**, 3 mM DMPC, 30 mM MOPS, and 100 mM KCl at pH 7.2 was excited at 450 nm and the emission at 513 nm was observed.

The third timing of Ca^{2+} addition, in the middle of sonication cycles, was performed by

adding Ca^{2+} after 4 cycles sonication then one further cycle applied to see if the sonication can break the vesicle membrane and let the Ca^{2+} diffuse into the inner part of the vesicle.

The result shows the pre-addition of ~1 equivalent ($10\ \mu\text{M}$) Ca^{2+} is enough to switch on the fluorescence of **BANI2** in the SUVs environment, which means the Ca^{2+} can be utilized by **BANI2** which is located on the inner or outer vesicle membrane. If the Ca^{2+} -addition is performed during the sonication process, the fluorescence of **BANI2** can be increased to maximum by 1~3 equivalents (~ $30\ \mu\text{M}$) of Ca^{2+} but maximum fluorescence intensity does not seem to be lasting. This might be due to the possibility that Ca^{2+} can diffuse into the inner part of vesicle while sonication but is still not well distributed on the inner or outer vesicle, leading to **BANI2** cannot be fully switched on in all the tested samples. As regards the post-addition curve, the fluorescence intensity of **BANI2** decreases at first then increases to the maximum value when > 10 equivalents (~ $130\ \mu\text{M}$) of Ca^{2+} was added. The decrease then increase of **BANI2** fluorescence intensity in the beginning might be caused by the variation of hydrophobicity of the environment. As mentioned in the solvent effect for **BANI** compounds in the Chapter 2, **BANI**-series compounds have higher quantum yields in a more hydrophobic environment. Therefore the decrease of fluorescence intensity at first can be regarded as that **BANI2** moves a few nm from membrane towards bulk solution, but not yet be switched on by such low concentration of Ca^{2+} . Followed by more and more Ca^{2+} addition, the fluorescence can be fully switched on by forming the Ca^{2+} :**BANI2** complex. Notably, in the post-addition case it takes > 10 -fold Ca^{2+} (~ $130\ \mu\text{M}$) to obtain the same fluorescence intensity as the pre-addition case. It can explain the failure of the titration experiments in Figure 4.52 where the Ca^{2+} was outside of vesicles and not enough was present to switch on **BANI2** in the vesicle solution, leading to unexpected titration curves by adding **nitr-5** or photolyzed **nitr-5**.

After confirming the ratio of major components for the photoactivated ion-shuttle in the liposome matrix, the solutions containing $1\ \mu\text{M}$ **BANI2**, $1\ \mu\text{M}$ CaCl_2 , $300\ \mu\text{M}$ DOPC which can form more stable SUVs in room temperature, and different concentrations from 1 to $20\ \mu\text{M}$ of **C15nitr-5** were separately prepared in the $30\ \text{mM}$ MOPS and $100\ \text{mM}$ KCl at pH 7.2 buffer solution. Their absorption and emission behavior before and after photolysis are shown in Figure 4.54 to observe the fluorescence intensity change caused by Ca^{2+} -transport from **C15nitr-5** to **BANI2**. Unfortunately the result shows the photolysis upon **C15nitr-5** cannot increase the fluorescence intensity of **BANI2** in the liposome environment. Also, trying to use different lipids such as DOTAP (cationic) or DOPG (anionic) cannot improve the situation (Figure 4.55). In other words, observing the Ca^{2+} -transport in the liposome system another method or solution constitution is needed.

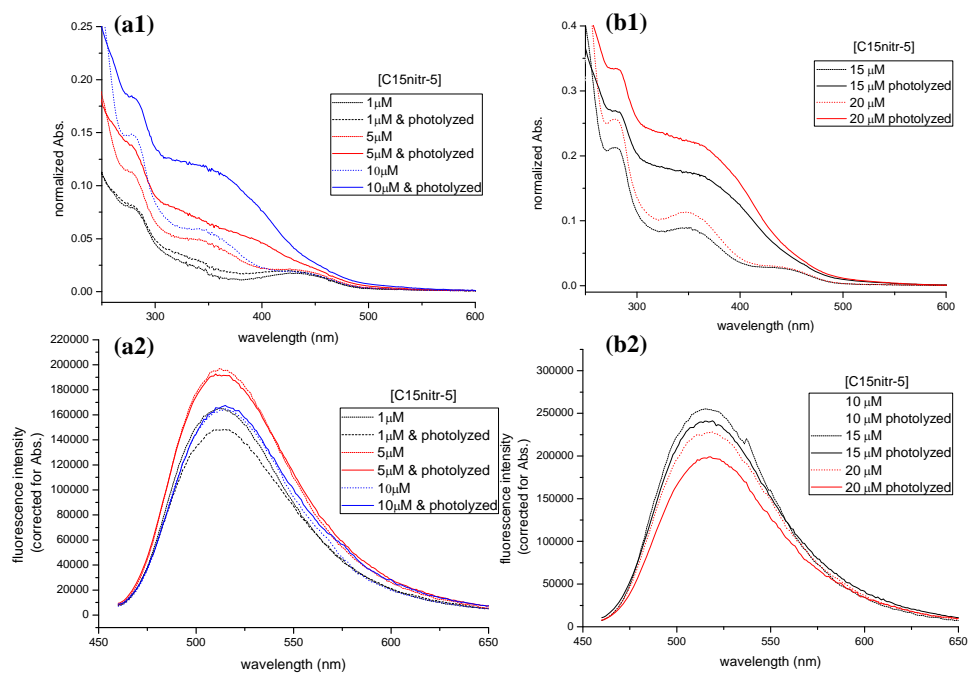


Figure 4.54 (a1, b1) Electronic absorption spectra, (a2, b2) fluorescence emission spectra corrected for absorption at $\lambda_{ex} = 450$ nm of one-pot photolysis induced Ca^{2+} -transport. Five solutions containing **BANI2** (1 μ M), $CaCl_2$ (1 μ M), DOPC (300 μ M), and different concentration of **C15nitr-5** (1, 5, 10, 15, 20 μ M) SUVs in MOPS (30 mM), and KCl (100 mM) buffer solution at pH 7.2 were separately measured before and after 15 min photolysis at 365 nm. Note. The fluorescence intensity of a and b series are incomparable due to the preparation and measurement on different days, hence needed to be put separately and their absolute fluorescence intensity cannot be compared.

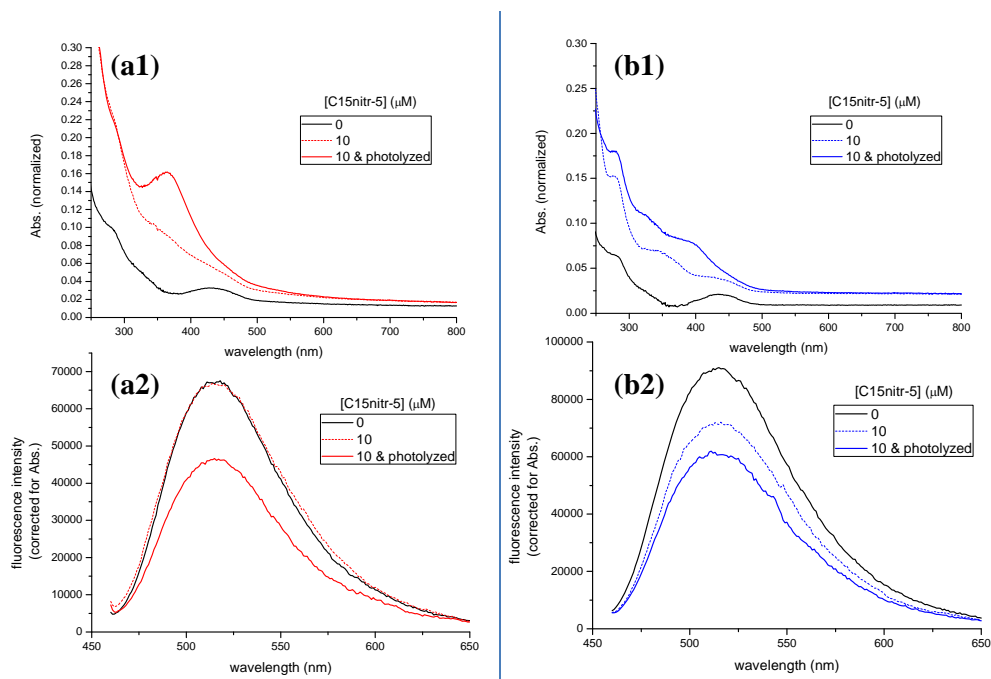


Figure 4.55 (a1, b1) Electronic absorption spectra, (a2, b2) fluorescence emission spectra corrected for absorption at $\lambda_{ex} = 450$ nm of one-pot photolysis-induced Ca^{2+} -transport. Solutions containing **BANI2** (1 μ M), $CaCl_2$ (1 μ M), **C15nitr-5** (0 or 10 μ M) in 300 μ M DOTAP (a1, a2) or 300 μ M DOPG (b1, b2) SUVs in MOPS (30 mM), and KCl (100 mM) buffer solution at pH 7.2 were measured before and after 15 min photolysis at 365 nm.

The goal is to observe the photoinduced Ca^{2+} -transport confined in the vesicle to compare with the one in the free solution, as evidenced by the fluorescence switch-on/off efficiency of Ca^{2+} -acceptors. An improved strategy to achieve this goal is using high concentration of EGTA to quench any Ca^{2+} -transport mechanism outside the vesicles or at outer liposome bilayer periphery part. In this way, the remains of inner vesicle photoinduced ion-shuttle would still function and could be observed. The procedure of this method was described in Figure 4.56a, and the tested results of **BANI2** and **BANI3** by emission spectra are reported in Figure 4.56b & c.

(a)

In the buffer* solution	Ca^{2+} -acceptor	$[\text{Ca}^{2+}]$ (μM)	$[\text{DOPC}]$ (μM)	$[\text{EGTA}]$ outside of vesicles (mM)
Solution A	2 μM BANI2	2	600	no
Solution X	2 μM BANI3	2	600	no

↓
1:1 volume mixed with EGTA (10 mM) buffer* solution
↓

Solution B	1 μM BANI2	1	300	5
Solution Y	1 μM BANI3	1	300	5

*buffer solution : MOPS (30mM), KCl (100mM), pH=7.2 solution

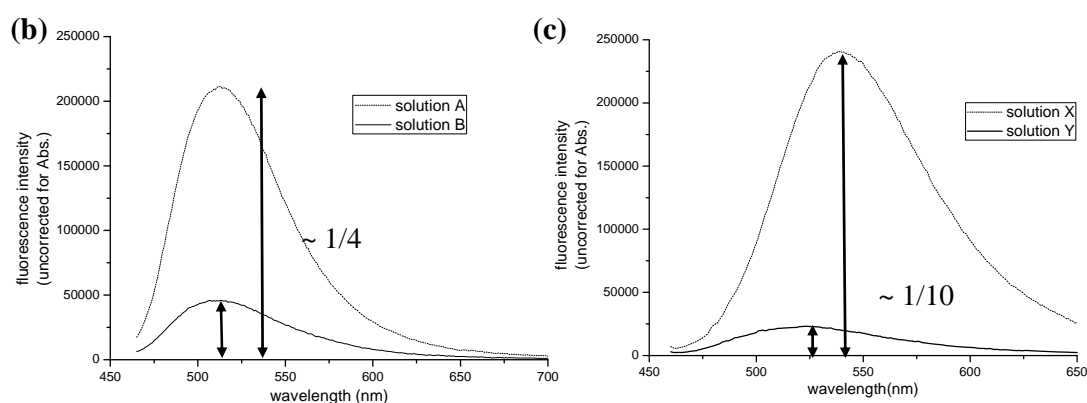


Figure 4.56 Procedure of quenching the Ca^{2+} -transport at the outer periphery of lipid membrane and outside of vesicles (a); fluorescence emission spectra of **BANI2** (b) and **BANI3** (c) before and after addition of EGTA outside of vesicle.

In the case of **BANI2** (Figure 4.56b), the fluorescence intensity decreased to $\sim 1/4$ when EGTA was added outside of vesicles in the solution. It is expected due to halving the concentration of all the solutes (leading 50% intensity decrease) and the inactivation of the **BANI2** which locates in the outer periphery of the vesicle bilayer (causing a further 2-fold fluorescence decrease). This result showed **BANI2** can be well-mixed with lipid and evenly distributed at the inner and outer bilayer membrane. As in the case of **BANI3** (Figure 4.56c), the residual fluorescence intensity was below the $1/4$ of the original amount and decreased to $\sim 1/10$ intensity. It can be imaged that **BANI3** is less hydrophobic than long alkyl chain equipped **BANI2**, hence less willing to be confined into the vesicle environment during the

SUV preparation process.

On the other hand, the volume for a molecule of DOPC is reported^{21,22} to be 1300 Å³, while the bilayer thickness is ~55 Å. For a lipid vesicle of 20 nm radius the aggregation number turns out to be 16000 and with a volume ~33500 nm³. For a 300 μM lipid concentration, using the aggregation number of 16000 the vesicle concentration would be ~19 nm. Therefore, the volume ratio of vesicle/solution is ~1/2700 according to the calculation. Since the observed fluorescence intensity did not decrease to such extent, the results implied that **BANI2** were mostly confined by liposome. In contrast, **BANI3** were partially confined meanwhile ~4/5 of them were exposed in the solution part.

Addition of outer EGTA allows us to uniquely observe the Ca²⁺-transport and fluorescence switch-on/off ability of photoactivated ion-shuttle inside the vesicle. Also, the fluorescence could be finally increased in the following photoactivated ion-shuttle experiments in the liposome matrix. First, DOPC (300 μM), **BANI2** (1μM), CaCl₂ (1μM), EGTA (5mM outside of vesicles), with different concentrations of **C15nitr-5** (1 to 55 μM) in MOPS buffer* were performed. It can be imagined that Ca²⁺ is moving upon 2D/ 2D dimensions (see Figure 4.58 cartoon representation) between both long alkyl chain equipped ejectors and acceptors inside the SUVs (Figure 4.57, Table 4.8).

*For briefly, MOPS buffer refers to a MOPS (30mM), KCl (100mM), pH 7.2 solution in the coming text.

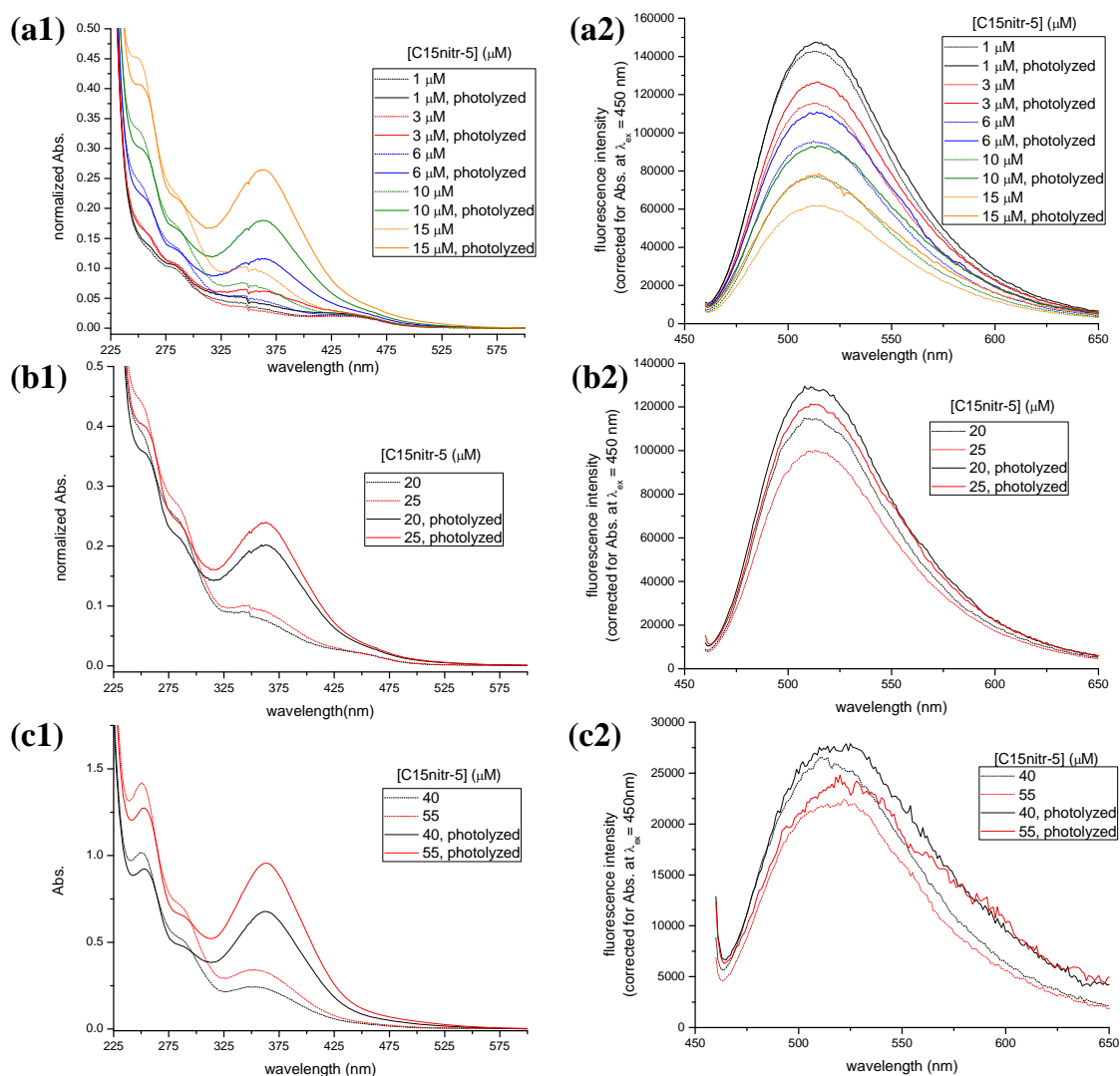


Figure 4.57 2D-2D photoinduced Ca^{2+} -transport inside DOPC SUVs. (a1, b1, c1) Electronic absorption spectra, (a2, b2, c2) fluorescence emission spectra corrected by absorption at $\lambda_{\text{ex}} = 450 \text{ nm}$ of one-pot photolysis induced Ca^{2+} -transport (UV irradiation at 365 nm for 20 min). Nine solutions used were: DOPC (300 μM), **BANI2** (1 μM), Ca^{2+} (1 μM), EGTA (5mM outside of vesicles), with different concentrations of **C15nitr-5** (1 to 55 μM) in MOPS buffer. Note. a, b, and c series are prepared and measured in different days, hence they need to be considered separately and their absolute fluorescence intensity cannot be compared.

[C15nitr-5] (μM)	BANI2 fluorescence enhancement factor
1	1.03
3	1.09
6	1.15
10	1.20
15	1.26
25	1.21
40	1.04
55	1.12

Table 4.8 Fluorescence enhancement factor of 2D-2D photoinduced Ca^{2+} -transport inside the DOPC SUVs

As seen in the emission spectra and the fluorescence enhancement factor in Table 4.8, *2D-2D* photoinduced Ca^{2+} -transport inside the DOPC SUVs has a maximum fluorescence enhancement factor at 1:15 blending ratio of **BANI2:C15nitr-5**. To the best of our knowledge, it is the first example to see the Ca^{2+} -transport between ion-shuttle pairs “inside” the vesicle. Even if the fluorescence enhancement value is low (1.26-fold) compared to the ~13-fold increase of ion-shuttle pairs in the free solution (last section, Chapter 4.5.1). The required equivalents of Ca^{2+} -ejector for Ca^{2+} -acceptor to reach the maximum fluorescence enhancement (**BANI2/C15nitr-5** = 1/15) is less than the system in free solution (**BANI3/C15nitr-5** \approx 1/45). To further understand if the efficiency can be improved by vesicle compartmentalization to reduce the number equivalents, another three supramolecular combinations with the previous one are graphically represented in Figure 4.58. The other three combinations are *2D-3D* (**BANI2/nitr-5**, Figure 4.59 & Table 4.9), *3D-2D* (**BANI3/C15nitr-5**, Figure 4.60 & Table 4.10), and *3D-3D* (**BANI3/nitr-5**, Figure 4.61 & Table 4.11) which were separately examined in the same way by using EGTA to deactivate the activities outside the vesicle membrane. Including the previous *2D-2D* case, the fluorescence enhancement factor versus Ca^{2+} -ejector concentration of these four combinations are compiled and plotted in the Figure 4.62 to investigate the compartmentalization effect.

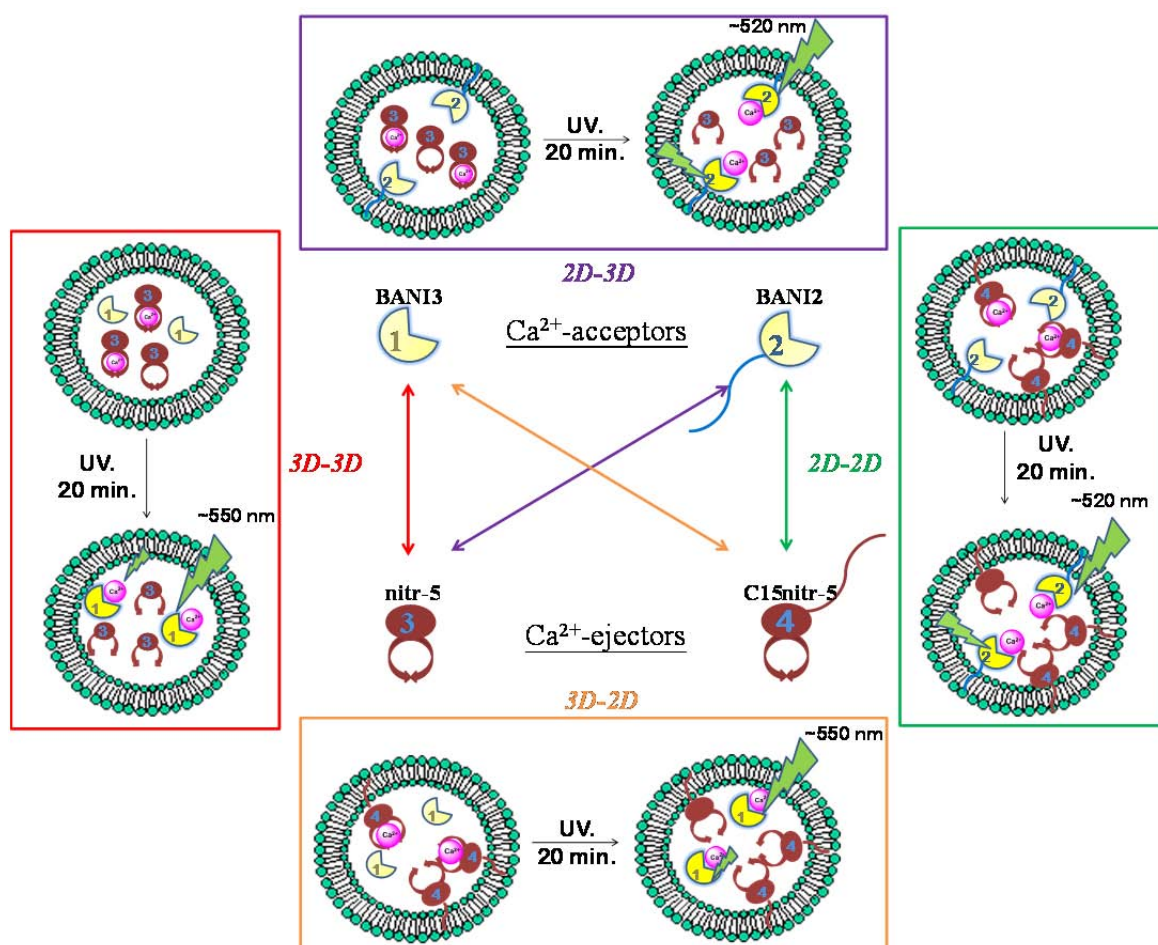


Figure 4.58 Cartoon representation of four supramolecular photoactivated ion-shuttle pairs inside vesicle nanodomains, with 5 mM EGTA outside of vesicles to quench any Ca^{2+} -transport outer on the liposome bilayers

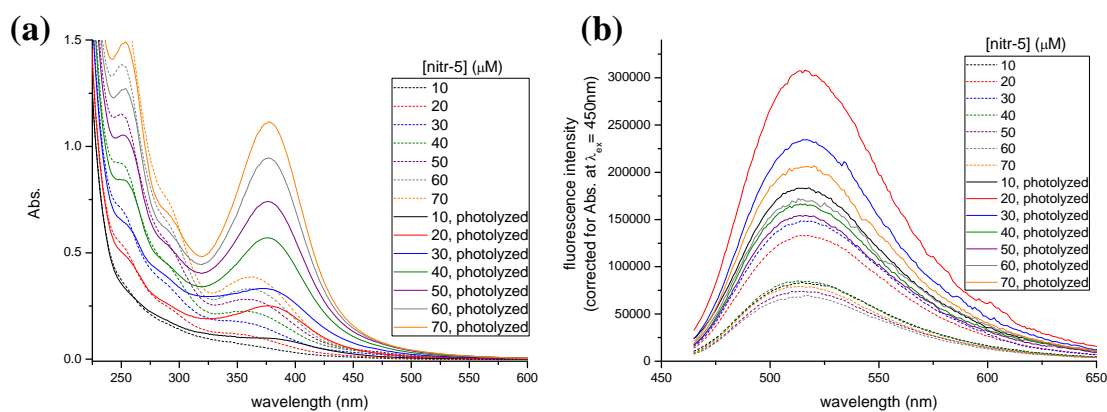


Figure 4.59 2D-3D photoinduced Ca^{2+} -transport inside DOPC SUVs. (a) Electronic absorption spectra, (b) fluorescence emission spectra corrected by absorption at $\lambda_{\text{ex}} = 450 \text{ nm}$ of one-pot photolysis (UV irradiation at 365 nm for 20 min) induced Ca^{2+} -transport. Seven solutions were used: DOPC (300 μM), **BANI2** (1 μM), Ca^{2+} (1 μM), EGTA (5mM outside of vesicles), with different concentrations of **nitr-5** (10 to 70 μM) in MOPS buffer.

[nitr-5] (μM)	BANI2 fluorescence enhancement factor
0	1
10	2.2
20	2.3
30	1.6
40	2
50	2.1
60	2.5
70	2.6

Table 4.9 Fluorescence enhancement factors of 2D-3D photoinduced Ca^{2+} -transport inside the DOPC SUVs

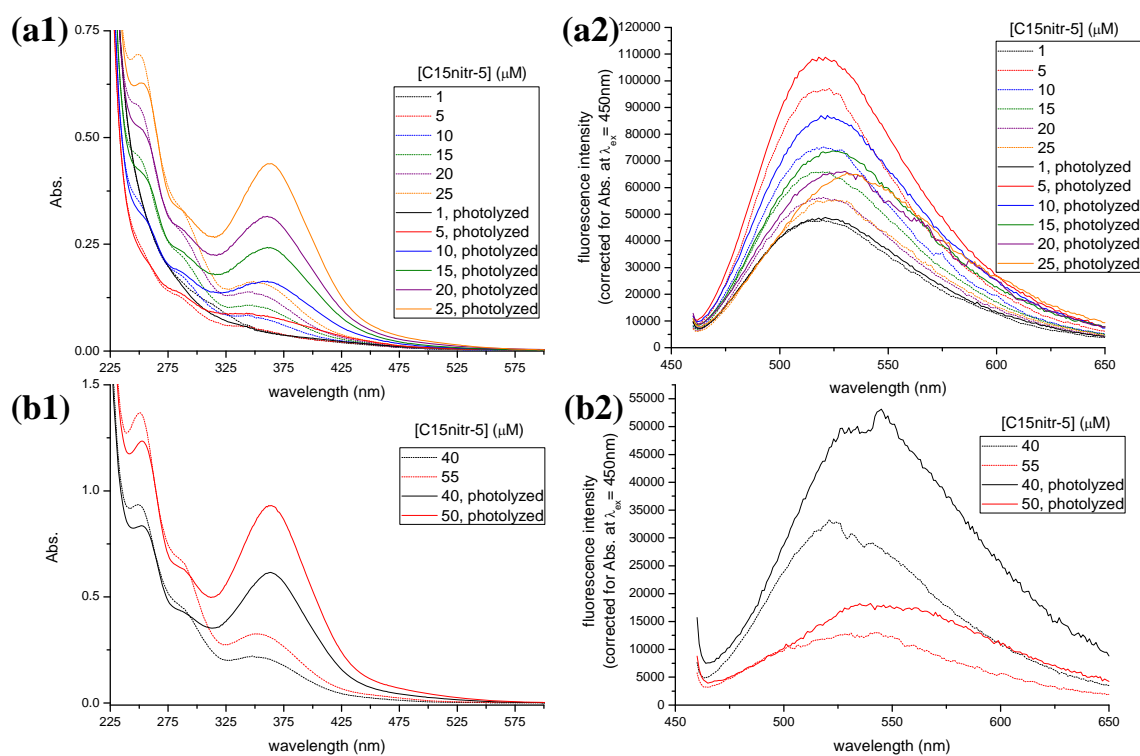


Figure 4.60 *3D-2D* photoinduced Ca^{2+} -transport inside DOPC SUVs. (a1, b1) Electronic absorption spectra, (a2, b2) fluorescence emission spectra corrected for absorption at $\lambda_{\text{ex}} = 450 \text{ nm}$ of one-pot photolysis (UV irradiation at 365 nm for 20 min) induced Ca^{2+} -transport. Eight solutions were used: DOPC (300 μM), **BANI3** (1 μM), Ca^{2+} (1 μM), EGTA (5mM outside of vesicles), with different concentrations of **C15nitr-5** (1 to 55 μM) in MOPS buffer.

[C15nitr-5] (μM)	BANI3 fluorescence enhancement factor
1	1.01
5	1.12
10	1.15
15	1.11
20	1.17
25	1.17
40	1.59
55	1.43

Table 4.10 Fluorescence enhancement factor of *3D-2D* photoinduced Ca^{2+} -transport inside the DOPC SUVs

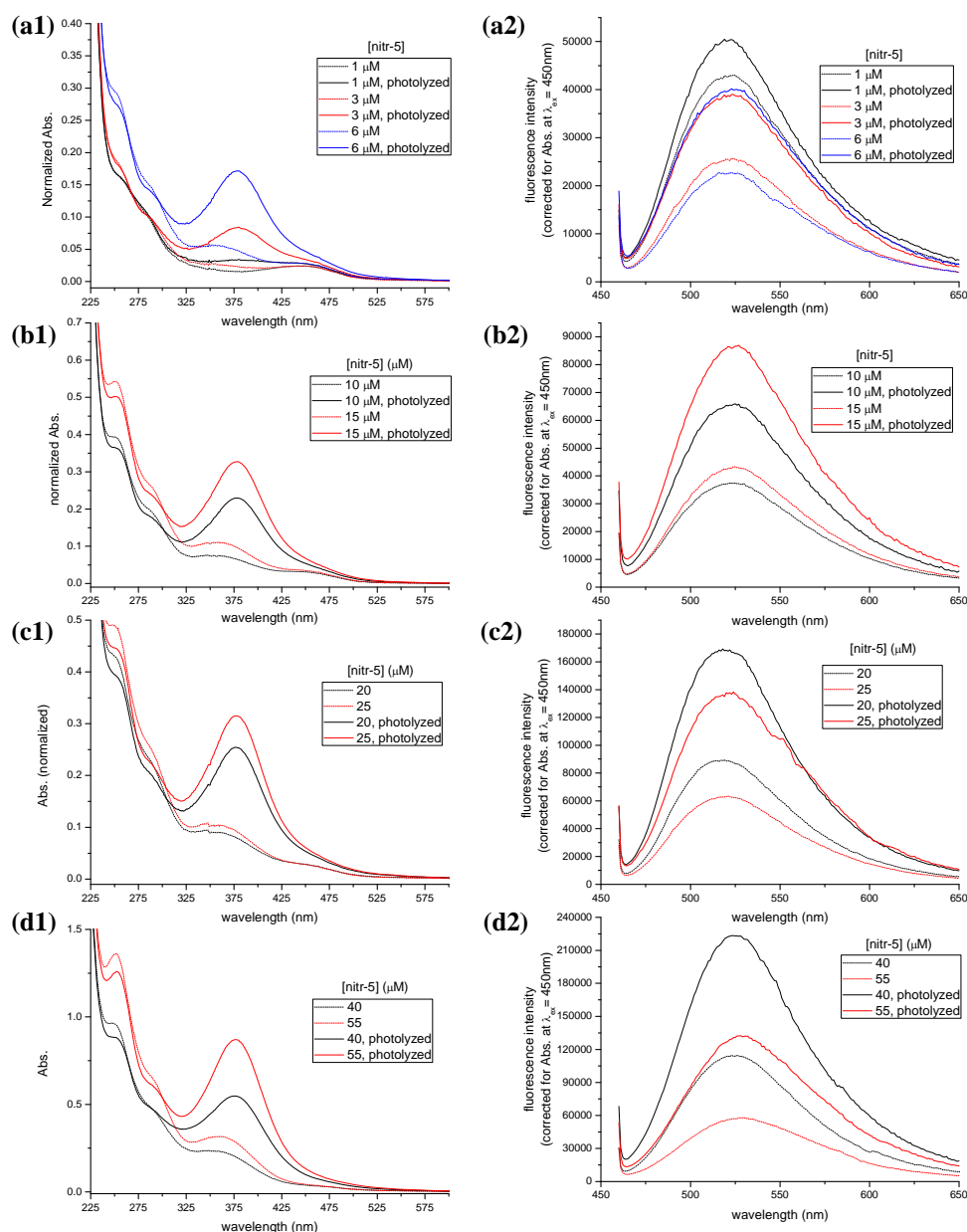


Figure 4.61 *3D-3D* photoinduced Ca^{2+} -transport inside DOPC SUVs. (a1-d1) Electronic absorption spectra, (a2-d2) fluorescence emission spectra corrected for absorption at $\lambda_{\text{ex}} = 450$ nm of one-pot photolysis (UV irradiation at 365 nm for 20 min) induced Ca^{2+} -transport. Nine solutions were used: DOPC (300 μM), **BANI3** (1 μM), Ca^{2+} (1 μM), EGTA (5mM outside of vesicles), with different concentrations of **nitr-5** (1 to 55 μM) in MOPS buffer.

[nitr-5] (μM)	BANI3 fluorescence enhancement factor
1	1.17
3	1.53
6	1.77
10	1.76
15	2
20	1.9
25	2.18
40	2
55	2.28

Table 4.11 Fluorescence enhancement factor of *3D-3D* photoinduced Ca^{2+} -transport inside the DOPC SUVs

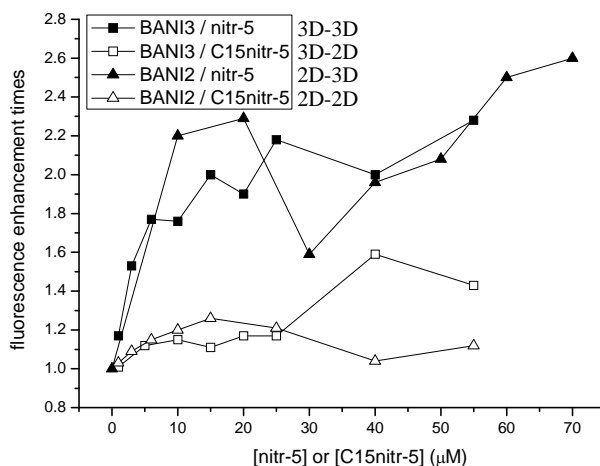


Figure 4.62 Fluorescence enhancement factor versus concentration of Ca^{2+} -ejectors (**nitr-5** or **C15nitr-5**) of four photoactivated Ca^{2+} -transport combinations inside vesicles

The photolysis increased the extinction coefficient of the 370 nm peak ~4-fold in the absorption spectra of these four combinations. As described in Chapter 2, this increase is from photolysis of **nitr-5** or **C15nitr-5** followed by generating a benzophenone whose carbonyl group is in direct conjugation with the bis(carboxymethyl)amino group para to it which is unmodified by Ca^{2+} . In the emission spectra, the maximum fluorescence enhancement factor was obtained when the number of equivalents of Ca^{2+} -acceptor (**BANI2** or **BANI3**) vs. Ca^{2+} -ejectors (**nitr-5** or **C15nitr-5**) was 1:15 to 1:20 as the profile plotted in Figure 4.62 indicates. The lower switch-on/off times in these four combinations (~ 2.5-fold) compared to the free solution (~13-fold), can be explained by the higher quantum yield of Ca^{2+} -free acceptors in a more hydrophobic environment as described in Chapter 4.4.2 (K_d measurements) and Chapter 2 (solvent effect of **BANI2** and **BANI3**).

One can notice that in the fluorescence enhancement curves (Figure 4.62), the *3D-3D* and *2D-3D* cases (■ and ▲ curves) have higher switch-on/off ratios compared to the *3D-2D* and *2D-2D* (□ and △ curves) cases where **C15nitr-5** is used. For this reason the stability of **C15nitr-5** in the DOPC bilayer membrane was tested by means of Langmuir film isotherm as shown in the Figure 4.63. LB-film composed of DOPC: **C15nitr-5** = 10:1 (molar ratio) was compressed, stopping at monolayer region ($P \sim 25$ mN/m). The surface pressure would gradually decrease due to the relaxation of the film. Followed by photolysis with UV irradiation at 365 nm, the surface pressure rapidly decreased as shown in Figure 4.63b. As a result, the conformational change during the photolysis process of **C15nitr-5** might destabilize the monolayer, or even break the SUVs of the liposome solutions as the similar phenomenon published by K. Kimura et al.²⁰

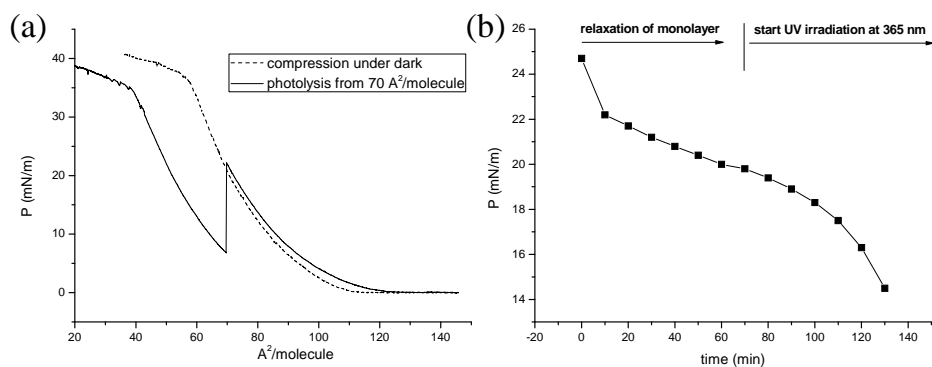


Figure 4.63 Langmuir isotherm experiments of DOPC: **C15nitr-5** = 10:1 (molar ratio) on the water subphase. (a) The two isotherms were performed in the dark (dash line), and in the dark until 70 Å²/molecular then compression was stopped for 70 min followed by photolysis with UV irradiation at 365 nm (solid line). (b) Surface pressure versus time of the relaxation and photolysis after monolayer reaching 70 Å²/molecule

The reason why only **C15nitr-5** can break the vesicles but not in the cases using **nitr-5** might be the fixation by long alkyl chain of **C15nitr-5**, while **nitr-5** could easily escape from the membrane surface after photolysis. Moreover, the absorption shift after photolysis indicate that **nitr-5** goes into a more hydrophilic environment with a 17 nm ($\Delta\omega = 1266 \text{ cm}^{-1}$) red-shift than **C15nitr-5** (14 nm, $\Delta\omega = 1099 \text{ cm}^{-1}$) as shown in the electronic absorption spectra in Figure 4.64 (abstract from Figure 4.60b1 and Figure 4.61d1).

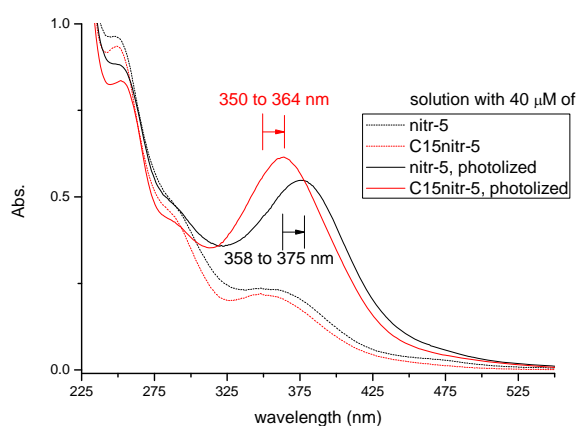


Figure 4.64 Electronic absorption spectra of one-pot photolysis (UV irradiation at 365 nm for 20 min) induced Ca²⁺-transport of solutions containing DOPC (300 μM), **BANI3** (1 μM), Ca²⁺ (1 μM), EGTA (5mM outside of vesicles), with 40 μM of **nitr-5** (black curve) or **C15nitr-5** (red curve) in MOPS buffer.

To conclude, the lower fluorescence enhancement factor of the cases using **C15nitr-5** (Figure 4.62 Δ and □) come from not only the smaller Ca²⁺-affinity decrease (K_d increase factor = 13-fold) but also the destabilization resulted from photolysis. The agitation of **C15nitr-5** probably breaks the vesicles. The resulting leakage of EGTA from outer part of vesicle into inner part could immediately quench the Ca²⁺-transport happening inside the vesicles. Fortunately, the destabilized bilayer can go through either rearrangement of bilayer

packing, disruption and transformation to smaller vesicle and micelle, or fusion together²³ as shown in Figure 4.65. These self-healing behaviors allow some Ca^{2+} ion can still survive and switch on the Ca^{2+} -acceptors, but in a lower fluorescence enhancement factor is observed.

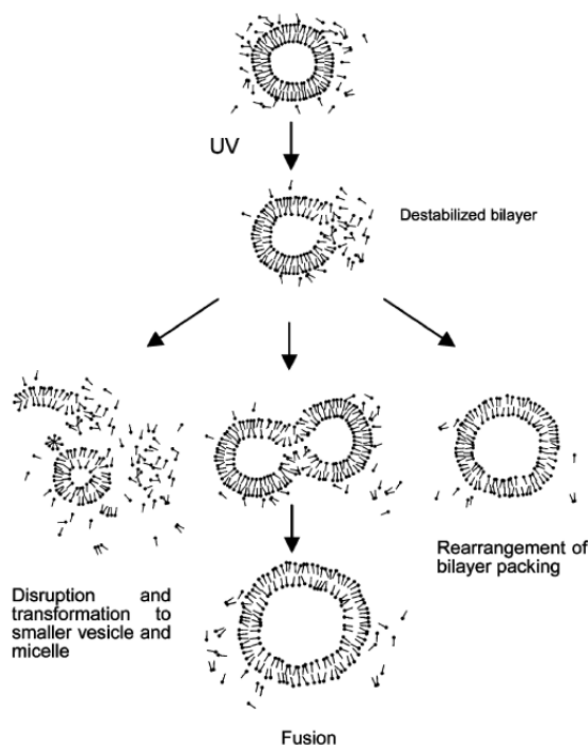


Figure 4.65 Conceptual representation of bilayer destabilization followed by changes in vesicle aggregation. [K. Kimura, *Langmuir*, 2007]²³

Since the compartmentalization effect in the cases using **nitr-5** instead of **C15nitr-5** as Ca^{2+} -ejector showed a better fluorescence enhancement, and the required Ca^{2+} -ejector amount can be reduced than the one in the free solution. In the end, the same strategy was repeated but doubling the number of DOPC equivalents without changing other constituents in order to obtain a better efficiency or less required Ca^{2+} -ejector, etc. DOPC (600 μM), **BANI2** (1 μM), CaCl_2 (1 μM), EGTA (5mM outside of vesicles), with a different concentration of **nitr-5** (0 to 70 μM) in MOPS solutions was performed and shown in Figure 4.66, while the same constitution but changing **BANI2** to **BANI3** was shown in Figure 4.67 with their fluorescence enhancement factors listed in Table 4.12. For easier comparison of all the results of photoinduced Ca^{2+} -transport in the free solution and in the vesicle matrix, their fluorescence increase times versus concentration of Ca^{2+} -ejectors are compiled in the last graph (Figure 4.68).

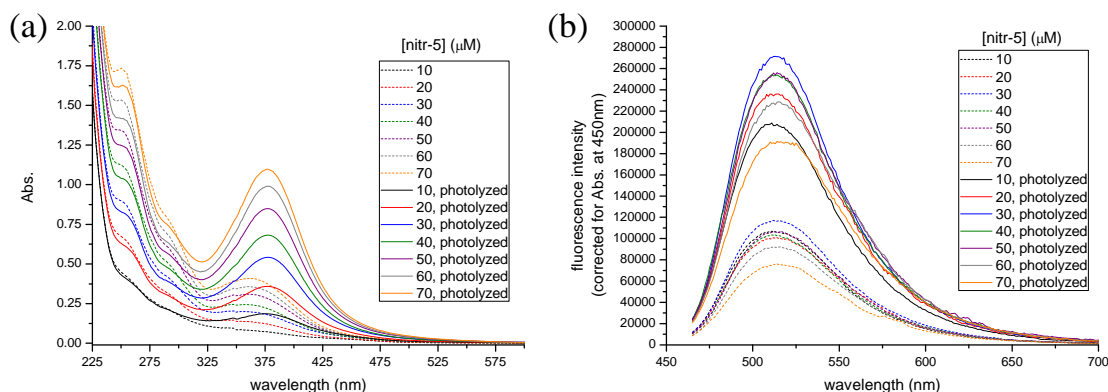


Figure 4.66 2D-3D photoinduced Ca^{2+} -transport in DOPC SUVs. (a) Electronic absorption spectra, (b) fluorescence emission spectra corrected for absorption at $\lambda_{\text{ex}} = 450 \text{ nm}$ of one-pot photolysis (UV irradiation at 365 nm for 20 min) induced Ca^{2+} -transport. Seven solutions were used: DOPC (600 μM), **BANI2** (1 μM), CaCl_2 (1 μM), EGTA (5mM outside of vesicles), with different concentrations of **nitr-5** (10 to 70 μM) in MOPS buffer.

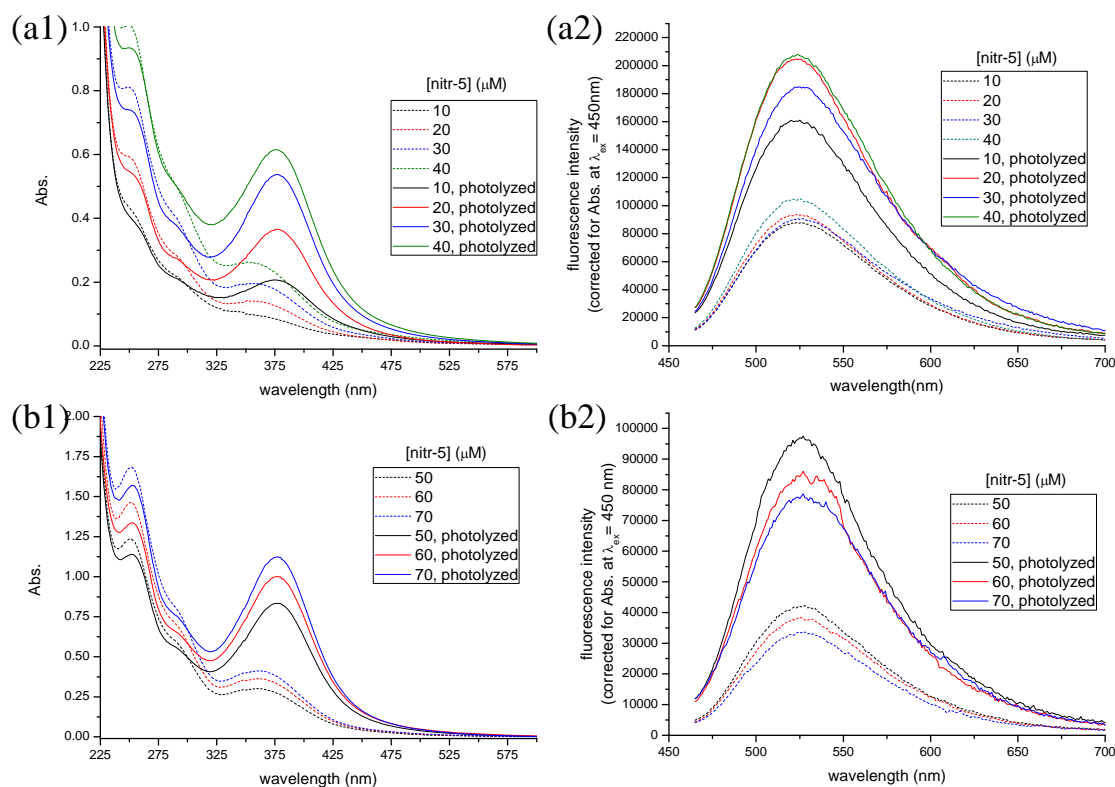


Figure 4.67 3D-3D photoinduced Ca^{2+} -transport in DOPC SUVs. (a1, b1) Electronic absorption spectra, (a2, b2) fluorescence emission spectra corrected for absorption at $\lambda_{\text{ex}} = 450 \text{ nm}$ of one-pot photolysis (UV irradiation at 365 nm for 20 min) induced Ca^{2+} -transport. Eight solutions were used: DOPC (600 μM), **BANI3** (1 μM), CaCl_2 (1 μM), EGTA (5mM outside of vesicles), with different concentrations of **nitr-5** (10 to 70 μM) in MOPS buffer.

[nitr-5] (μM)	fluorescence enhancement factor	
	BANI3	BANI2
10	1.8	2
20	2.2	2.3
30	2.3	2.3
40	2	2.5
50	2.3	2.4
60	2.2	2.5
70	2.3	2.5

Table 4.12 Fluorescence enhancement factor of 3D-3D (**BANI3/nitr-5**) and 2D-3D (**BANI2/nitr-5**) photoinduced Ca^{2+} -transport inside SUVs of 600 μM DOPC

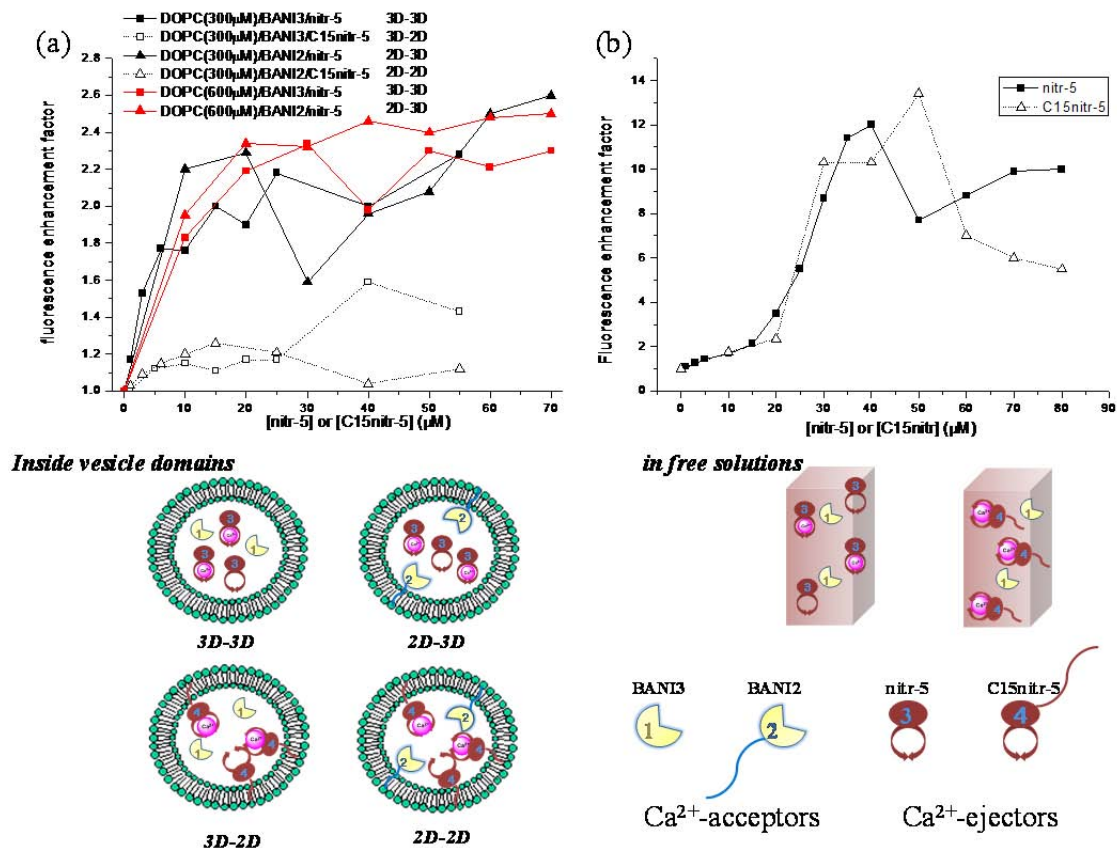


Figure 4.68 Fluorescence enhancement factor profiles by the factor of Ca^{2+} -ejectors (**nitr-5** or **C15nitr-5**) concentration. (a) SUVs matrix systems: DOPC (300 or 600 μM), Ca^{2+} -acceptors (**BANI2** or **BANI3**, 1 μM), CaCl_2 (1 μM), EGTA (5 mM outside of vesicles) in the MOPS buffer; (b) Free solutions system: **BANI3** (1 μM), CaCl_2 (1 μM) in the MOPS buffer. Note. all the data are corrected for absorption. <MOPS buffer: 30 mM MOPS, 100 mM KCl at pH 7.2>

As seen in Figure 4.68, the reason why the cases with **C15nitr-5** always have lower fluorescence enhancement factors has been discussed. Further, by comparing the two sets (Figure 4.68a & b) of profiles allows us to investigate the effect of changing the DOPC concentration and, the most important result from changing the environments where photoactivated ion-shuttles are in free solution or a vesicle matrix.

Doubling DOPC concentration can be assumed to increase the distance between the Ca^{2+} -ejectors and acceptors two times by diluting their concentration confined in a single vesicle. In Figure 4.68a, the compartmentalization effect shows unapparent difference between 600 μM (dashed curves) and 300 μM DOPC lipid (solid curves). This phenomenon indicates the fluorescence switch-on/off ability is independent of the distance between acceptor and ejector but can be dramatically affected by environment. For example, one can find the fluorescence enhancement slope is bigger in the SUVs matrix (Figure 4.68a) than in the free solution (Figure 4.68b), which means the efficiency of photoinduced Ca^{2+} -transport is more sensitive when the system is confined in the vesicles environment. The deduced reasons regarding environment difference could be:

1. **BANI2** or **BANI3** have strong interactions between themselves in the free solution as the unusual switch-on/off abilities caused by aggregation described in Chapter 2. Once mixed with lipid molecule, the compounds can be well distributed on the liposome membrane and the aggregation of **BANI** can be reduced.
2. As highlighted in the introduction for **nitr-5** compound (Chapter 2.1.2, Figure 2.10), photolyzed **nitr-5** would re-chelate the photoreleased Ca^{2+} due to the insufficient difference of K_d before and after irradiation. In the free solution system (Figure 4.68b) the profiles at low Ca^{2+} -ejector concentration show the insufficiency in donating Ca^{2+} , which leads to unapparent fluorescence enhancement until increasing their concentrations to $\sim 30 \mu\text{M}$. In contrast, the even-distribution of Ca^{2+} -ejectors and acceptors through blending in the SUVs matrix (Figure 4.68a) can reduce the recombination between photoreleased Ca^{2+} and photolyzed Ca^{2+} -ejectors (**nitr**-compounds), and enhance the possibility of combination between photoreleased Ca^{2+} and Ca^{2+} -acceptors (**BANI** compounds) right after photoinduced Ca^{2+} -release from Ca^{2+} -ejectors.

As a result, a better sensitivity is observed under the confinement of vesicle matrix which can produce a higher fluorescence enhancement slope even under the low Ca^{2+} -ejector concentration (0~20 μM) in Figure 4.68a. The ratio of *acceptor: ejector* to reach maximum switch-on/off ability can be reduced from $\sim 1:45$ in the free solution to $1:20$ in the SUVs matrix system. This is a distinctive example of compartmentalization effect which functions and enhances the Ca^{2+} -transport for the photoactivated supramolecular ion-shuttle systems.

4.6 Conclusion

1. Mixing the trial organic compounds within multi-lamellar vesicle (MLV) matrices has been investigated by small angle X-ray scattering. The success of confining the trial compounds by vesicles showed the spatial and electrostatic interaction between lipid amphiphiles, which changes the periodicity and vesicle size of the lamella structure.
2. Newly synthesized Ca^{2+} -acceptor, **octyl chain equipped BANI2** fluoroionophores was shown to integrate into giant unilamellar vesicle (GUV) by means of dropcasting or electroformation methods. The fluorescent GUVs obtained were observed by a fluorescence microscope and showed the fluorescence can be faded by adding EGTA to the subphase. Moreover, confocal scanning laser microscopy with the FLIM technique indicated the **BANI2** lifetime of the fluorescent GUVs can be slightly different in different environments with a homogeneous polarization (angle independent) character.
3. Dissociation constant (K_d value) of **BANI2** and **BANI3** Ca^{2+} -acceptors in small unilamellar vesicles (SUVs) were individually measured. Generally the K_d value in the vesicle matrices are higher (i.e. Ca^{2+} -affinity is decreased) than that in the free solution environment. Besides, the lower K_d value of **BANI2** in DMPC neutral liposome (6.8 nM) than that of **BANI3** (1.55 μM) can be attributed to the octyl group, which would stabilize the Ca^{2+} :**BANI2** complex by inducing a more hydrophobic environment around the BAPTA parent ionophore.
4. The molecular fluorescence switch-on/enhancement factors are lower in the vesicle nanodomains due to the higher quantum yield of Ca^{2+} -acceptors before being switched on by photoreleased Ca^{2+} , which is mainly caused by the more hydrophobic liposome surrounded environment.
5. Compared to the free solution environment, higher sensitivities of photoinduced ion-shuttle systems were observed under the confinement of vesicle matrix by means of reducing the recombination between photoreleased Ca^{2+} and photolyzed Ca^{2+} -ejectors. The ratio of *acceptor: ejector* to reach maximum switch-on/off ability thereby can be reduced from $\sim 1:45$ in the free solution to $1:20$ in the SUVs matrix system. These results implied that the compartmentalization effect by amphiphilic nanodomains functions and enhances the Ca^{2+} -transport for the photoinduced ion-shuttle supramolecular systems.

4.7 References

1. L. Pollack, *Annu. Rev. Biophys.* **2011**, *40*, 225.
2. J. Korlach, P. Schwille, W. W. Webb, and G. W. Feigenson. *Proc. Natl. Acad. Sci. USA.* **1999**, *96*, 8461.
3. L. A. Bagatolli, and E. Gratton. *Biophys. J.* **2000**, *78*, 290.
4. M. I. Angelova, S. Soléau, Ph. Méléard, J. F. Faucon, P. Bothorel, *Progr. Colloid Polym. Sci.* **1992**, *89*, 127.
5. M. I. Angelova and I. Tsoneva. *Chem. Phys. Lip.* **1999**, *101*, 123.
6. T. Tanaka, Y. Tamba, S. M. Masum, Y. Yamashita, and M. Yamazaki, *Biochim. Biophys. Acta*, **2002**, *1564*, 173.
7. A. Roux, G. Cappello, J. Cartaud, J. Prost, B. Goud, P. Bassereau. *Proc. Natl. Acad. Sci. US*, **2002**, *99*, 5394.
8. T. Tanaka, M. Yamazaki, *Langmuir*, **2004**, *20*, 5160.
9. K. Akashi, H. Miyata, H. Itoh, and K. Kinoshita Jr. *Biophys. J.* **1998**, *74*, 2973.
10. D. S. Dimitrov, and M. I. Angelova. *Stud. Biophys.* **1986**, *113*, 15.
11. D. S. Dimitrov, and M. I. Angelova. *Stud. Biophys.* **1987**, *119*, 61.
12. M. K. Doeven, J. H. A. Folgering, V. Krasnikov, E. R. Geertsma, G. V. D. Bogaart, B. Poolman, *Biophys. J.*, **2005**, *88*, 1134.
13. G. Staneva, M. I. Angelova, K. Koumanov, *Chemistry and Physics of Lipids*, **2004**, *129*, 53.
14. Pawley JB (editor), *Handbook of Biological Confocal Microscopy* (3rd ed.). Berlin: Springer. **2006**.
15. S. Ghosh, A. Adhikari, S. S. Mojumdar, and K. Bhattacharyya, *J. Phys. Chem. B* **2010**, *114*, 5736.
16. F. Gao, E. Mei, M. Lim, and R. M. Hochstrasser, *J. Am. Chem. Soc.*, **2006**, *128*, 4814.
17. Science in Your Eyes online image gallery, <http://www.scienceinyoureyes.com>
18. C. Giansante, G. Raffy, C. Schäfer, H. Rahma, M. T. Kao, A. G. L. Olive, and A. Del Guerso, *J. Am. Chem. Soc.*, **2011**, *133* (2), 316.
19. Joseph R. Lakowicz, *Principles of Fluorescence Spectroscopy*, 3rd edition , " 3rd edition, Springer, **2006**.
20. R. R. Duncan, A. Bergmann, M. A. Cousin, D. K. Apps, M. J. Shipston, *J. Microsc.* **2004**, *215*, 1.
21. K. Balali-Mood, T.A. Harroun, and J.P. Bradshaw, *Eur. Phys. J. E*, **2003**, *12*, s135.
22. S. Ghosh, A. Adhikari, S. S. Mojumdar, and K. Bhattacharyya, *J. Phys. Chem. B*, **2010**, *113*, 5736.
23. R. M. Uda, D. Yamashita, Y. Sakurai, and K. Kimura, *Langmuir*, **2007**, *23*, 7936.

Summary and Conclusion

A series of novel amphiphilic and non-amphiphilic photoactive molecules were synthesized, notably for use in photoinduced calcium ejection and recognition. Coupling processes of photocontrolled Ca^{2+} -transport supramolecular systems have been studied in order to assess the relative efficiency of intermolecular ion transfer in solution and confined vesicle capsules.

The photoactive Ca^{2+} -ejector and acceptor molecules of the photoactivated ion-shuttle system are based on the efficient BAPTA parent ionophore. ATR-FTIR and PM-IRRAS infrared techniques combined with Langmuir isotherms were utilized to study the octa-coordinated Ca^{2+} chelating behavior of BAPTA in solution and in monolayers (**C15BAPTAhyd**). Observing the BAPTA monolayer morphology by ellipsometry showed that the addition of calcium ions can deprotonate the carboxylic acid group and decrease the area per molecule which is accompanied with a film thickness increase. The results from these techniques showed the pK_a value of BAPTA is ~ 6 , and in monolayer environment the affinity towards Ca^{2+} is about 10~100-fold less. Interestingly, **C15BAPTAhyd** forms star-shape aggregation morphology while compressing the Langmuir film to the multilayer situation under the buffered subphase without calcium.

The fluorescence probes, fluoroionophores, serve as Ca^{2+} -acceptors in the detection part of the photoactivated ion-shuttle system. Two major compounds, **BANI2** and **BANI3**, have been investigated with respect to their photophysical properties. The dissociation constant K_d value of **BANI2** and **BANI3** are 0.55 nM and 5 nM in aqueous solution and a range of higher values in different liposome matrices. When chelating with Ca^{2+} , their fluorescence intensities can be switched on ~ 110 -fold but 5 to 20 times less in the vesicle matrix. This phenomenon was studied by their solvent effects which show these polar probes can have higher quantum yields in more hydrophobic environments, leading to relatively high initial fluorescence intensities before chelating Ca^{2+} in the liposome environments. The fluorescent properties of octyl hydrocarbon chain equipped **BANI2** was utilized and tested for the fluorescent giant unilamellar vesicles (GUVs). Fluorescence / confocal microscopy show the high stability and observable fluorescence switch of these fluorescent GUVs during Ca^{2+} -complexation and decomplexation by excess EGTA.

As regards the photosensitive Ca^{2+} -ejectors, **nitr-5** and **C15nitr-5**, photolysis at 365 nm can produce an acceptable decrease of calcium affinity. The measured K_d values before and after photolysis are 0.4 nM and 17.2 nM for **nitr-5** (K_d increase factor = 43-fold), while **C15nitr-5** has K_d increase factor = 13-fold from $K_d = 2.1$ nM to 27.7 nM. Not only the photoinduced K_d increase factor of **C15nitr-5** can impair the efficiency in donating photoreleased Ca^{2+} to fluorescence probes, but also the fixation by its long alkyl chain can

destabilize and break the vesicles during UV irradiation. These properties decrease the efficiency of photoinduced ion-shuttle systems inside the small unilamellar vesicles (SUVs).

BANI2 (or **BANI3**) can form strong interactions between themselves and auto-aggregate in aqueous solution, which happens for Ca^{2+} -ejectors as well. The aggregation can be diminished and the amphiphile receptors can be evenly distributed when the compounds are blended with lipids. As a result, the recombination between photoreleased Ca^{2+} and photolyzed Ca^{2+} -ejectors can be reduced due to the even-distribution and confinement in the SUV matrix. The compartmentalization effect allows a faster combination between the photoreleased Ca^{2+} and Ca^{2+} -acceptors right after irradiation of the Ca^{2+} -ejectors. Compared with the free solution environment, higher sensitivities of photoactivated ion-shuttle systems were observed under the confinement of the vesicle matrix. Adopting the improved strategy of using excess EGTA to quench the Ca^{2+} -transport outside the bilayer membrane, required fewer equivalent of Ca^{2+} -ejectors to switch on the Ca^{2+} -acceptors: the number of equivalents to reach maximum fluorescent intensity can be reduced from 45 equivalents for solution systems to 15~20 equivalents within the SUV matrix system. This result implied that the compartmentalization effect of amphiphilic nanodomains functions and enhances the Ca^{2+} -transport efficiency for the photocontrolled supramolecular ion-shuttle systems.

Future development

To improve the proof-of-principle examples in this thesis, improvements can be made in the molecular photoejection part (the molecular detection part is being highly efficient), as well as the self-assembled host matrices.

Concerning the molecular Ca^{2+} -ejector: Nitr-series Ca^{2+} -ejectors have advantages of pH and Mg^{2+} ion insensitivities, but they are not ideal photocontrolled Ca^{2+} -releasing compounds due to the (photo)chemical inefficiency. The K_d increase factor after photolysis is ca. 45-fold for **nitr-5** and 13-fold for **C15nitr-5**, which means the possibility of recombination between photoreleased Ca^{2+} and photolyzed ejectors cannot be ignored. This disadvantage could be diminished by using more efficient compounds such as DM-nitrophen (K_d increase factor = 600,000-fold), NP-EGTA (K_d increase factor = 12,500-fold), or azid-1 (K_d increase factor = 520-fold), etc. In this way, a lower required equivalent related to Ca^{2+} -acceptor is needed to reach maximum switch-off/on point with higher photocontrolled Ca^{2+} -transport efficiency.

As regards the container for photoinduced ion-shuttle, the aggregation of amphiphilic functional molecules can be decreased by blending with lipids but the hydrophobicity of environment can be affected as well. The solvent effects on Ca^{2+} -acceptors showed these polar probes can have higher quantum yields in more hydrophobic environments, leading to relatively high initial fluorescence intensities before chelating Ca^{2+} in the liposome environments. To improve this issue one could use hydrophilic polymer or inorganic nanocapsules. For example, using hydrophilic co-polymer covalent-connecting with alternate ejector and acceptor could be an interesting message transporting network without altering the hydrophobicity. In the other way, confining the photoactive compounds into inorganic tubular hosts which can be made from templates of organic gemini compounds could diminish the undesired aggregation but also avoid the hydrophobicity change.

In the end, developing reversible and multicycle ion-shuttle systems will be a promising goal to construct message communication, information processing, molecular switches, and logic gate networks. Certainly, confining these reversible ion-messenger systems inside nanocapsules, nanotubes, or other containers will be potential and interesting to build up photochromic systems upon 1-D to 3-D structures.

Chapter 5
Experimental Section

5.1 Materials

Commercially-available starting materials were obtained from Aldrich, Lancaster, Avocado, or Avanti lipid unless other mentioned. Anhydrous solvents, such as absolute ethanol, chlorobenzene, DMSO and DMF were used as received. Dichloromethane, toluene and acetonitrile were distilled over calcium hydride (CaH_2). Tetrahydrofuran (THF) and diethyl ether were dried over sodium/benzophenone and distilled immediately before use.

5.2 Thin-layer chromatography and column

The thin-layer chromatography was performed on Merck 60 silica plate F254. The plates are visualized under UV at 254 nm and 365 nm. The column chromatography was performed on silica gel (silica gel Merck, particle size of 63-200 microns, 230-400 mesh or size from 40 to 63 microns).

5.3 Nuclear magnetic resonance (NMR)

The ^1H and ^{13}C NMR spectra were recorded by Bruker DPX200 (^1H : 200 MHz), AC-250 (^1H : 250 MHz, ^{13}C : 62.9 MHz), Avance 300 (^1H : 300 MHz, ^{13}C : 75 MHz). Chemical shifts δ are expressed relative to tetramethylsilane (TMS) using the residual signals of deuterated solvents (CDCl_3 , CD_2Cl_2 , D_2O , d_6 -DMSO, CD_3OD) as internal reference. The coupling constants are calculated in Hertz (Hz). For the assignment of signals, the following abbreviations are used: s = singlet, d = doublet, t = triplet, q = quartet, dd = doublet doublet, m = multiplet.

5.4 Mass Spectrometry

The mass spectra were produced by the Centre of Study and Structural Analysis Organic Molecules (CESAMO) at the University Bordeaux I. The impact spectra (EI) ($E = 70$ eV) and LSIMS + ($E = 35$ keV) were performed on a spectrometer Micromass VG Autospec-Q. Electrospray spectra were performed on a spectrometer Varian Saturn-4D. The high resolution spectra were recorded using the method of LSIMS + with a resolution of 10000.

5.5 UV-visible absorption Spectroscopy

The electronic absorption spectra were recorded on a double beam Varian Cary 5000 spectrophotometer whose wavelength range extends from 170 to 3300 nm. As for the sample with vesicles, electronic absorption spectra were obtained using a Varian Cary 1 spectrophotometer equipped with the DRA-CA-30I sphere.

5.6 Fluorescence spectroscopy

Emission spectra, fluorescence excitation and lifetimes have been recorded by HORIBA Jobin Yvon spectrometer Fluorolog-3 with a Xenon lamp of 450 W of nanoled excitation. The detector used is HAMAMATSU 2658P PMT in single photon counting mode.

5.7 Irradiation systems

Irradiation at 365 nm in sealed quartz cuvettes were performed with a portable lamp (type "TLC") Turner Designs VL LC-6 with a power of 12 watts.

5.8 Calculation of fluorescence quantum yield

The fluorescence quantum yield were determined by comparison with standard: Ru(bipy)₃Cl₂ (bpy: 2,2'-bipyridine) in air-equilibrated water solution, $\Phi_F = 0.028^1$ The quantum yield fluorescence was determined by the equation:

$$\Phi_F = \frac{\Phi_{ST} \times A_{ST} \times I \times \eta^2}{A \times I_{ST} \times \eta_{ST}^2}$$

Φ_F = Quantum yield

Φ_{ST} = Quantum yield of the standard

A = Absorbance at the excitation wavelength

A_{ST} = Absorbance of standard at the excitation wavelength

I = Emission intensity (integrated)

I_{ST} = Emission intensity of standard (Integrated)

η = refractive index of the solvent

η_{ST} = refractive index of the standard solvent

5.9 Determination of dissociation constants (K_d) with fluorimeter^{2,3}

A series of calibration solutions containing various $[Ca^{2+}]$ was prepared by mixing two solutions (*solution A* containing 10 mM K₂EGTA and *solution B* containing 10 mM CaEGTA) in various ratios. Both solutions contained 1 μ M Ca²⁺-probe molecular, 100 mM KCl, 30 mM MOPS and they were adjusted to pH 7.2.

To determine the K_d for Ca²⁺-probe molecular, the fluorescence spectrum was recorded with 2.0 mL of *solution A* (0 μ M free Ca²⁺) at 20 °C. Then 203 μ L of this solution was discarded and replaced by 203 μ L of *solution B* (39 μ M free Ca²⁺), and the spectrum was recorded. This brings the CaEGTA concentration to 1.00 mM and the $[Ca^{2+}]_{free}$ to about 0.017 μ M with no change in the concentration of the probe or of the total EGTA. The $[Ca^{2+}]_{free}$ is

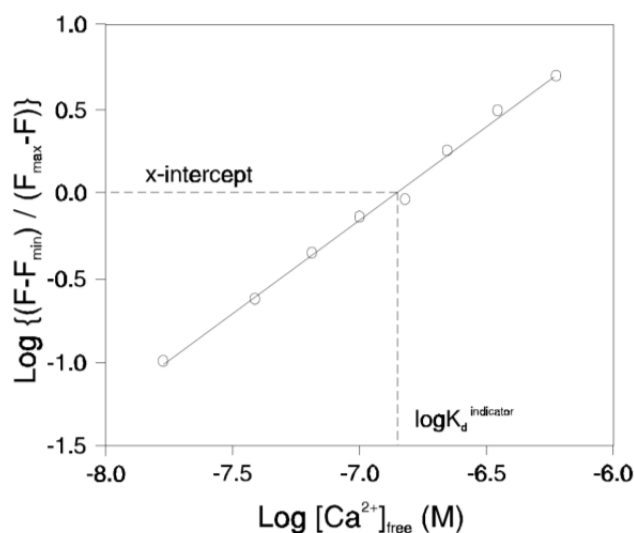
calculated from the K_d of EGTA for Ca^{2+} (150.5 nM) using the following equation:

$$[\text{Ca}^{2+}]_{\text{free}} = K_d^{\text{EGTA}} \times \frac{[\text{CaEGTA}]}{[\text{K}_2\text{EGTA}]}$$

Further iterations attained 0.038, 0.065, 0.101, 0.150, 0.230, 0.350, 0.601, 0.800, 1.00, 1.30, 2.50, 5.30, 10.0, 20.0 and 32.0 μM free Ca^{2+} by successively discarding 223, 251, 285, 327, 421, 479, 667, 420, 350, 412, 905, 1028, 926, 992, and 747 μL of *solution A* and replacing each with an equal volume of *solution B*.

Once the spectra have all been recorded, emission at a single wavelength can be plotted against $[\text{Ca}^{2+}]_{\text{free}}$ to give a calibration curve that can be used to determine the $[\text{Ca}^{2+}]_{\text{free}}$ of an unknown solution. Similarly, for ratiometric indicators such as fura-2 or indo-1, the ratio of the absorption, excitation or emission at two wavelengths can be plotted against $[\text{Ca}^{2+}]_{\text{free}}$.

Raw spectral data and the accompanying data analysis are shown in the figure below. The data is plotted as the log of the $[\text{Ca}^{2+}]_{\text{free}}$ (x-axis) versus the log $\{(F - F_{\text{min}})/(F_{\text{max}} - F)\}$ (y-axis). This double log plot gives an x-intercept that is the log of the K_d expressed in moles/liter. In the example, the x-intercept is -6.84. The inverse log of this number is 145×10^{-9} M (145 nM). The slope of the plot is 1.0, which reflects the 1:1 binding of each probe with a single Ca^{2+} ion. The first dilution (from “zero” Ca^{2+} to 0.017 μM) has the greatest error due to contaminating ions from glassware, reagents, etc. and may sometimes be unreliable.



5.10 Determination of dissociation constants (K_d) with UV/Visible absorption spectrometer

If absorption data are used while the compound is non-emissive, the $[\text{Ca}^{2+}]_{\text{free}}$ is calculated

from the K_d of HEEDTA for Ca^{2+} ($5.43 \mu\text{M}$ at pH 7.3, $20 \text{ }^\circ\text{C}$).^{4,5} A series of calibration solutions containing various $[\text{Ca}^{2+}]$ was prepared by mixing two solutions (*solution A* containing 10 mM HEEDTA and *solution B* containing 10 mM Ca^{2+} and 10 mM HEEDTA) in various ratios. Both solutions contained $30 \mu\text{M}$ Ca^{2+} -ejector molecular, 100 mM KCl, 30 mM MOPS and they were adjusted to pH 7.3. As the similar way, 0.61, 1.37, 2.35, 3.64, 5.41, 8.3, 12.6, 21.7, 28.9, 36.1, 46.9, 90.2, 191.3, 361, 721.5, 1155 μM free Ca^{2+} was used by discarding 203, 223, 251, 285, 327, 421, 479, 667, 420, 350, 412, 905, 1028, 926, 992 and 747 μL of *solution A* and replacing each with an equal volume of *solution B*.

5.11 ATR-FTIR

The ATR spectra were recorded by Nicolet Nexus 6700 spectrometer equipped with an MCT detector cooled at 77 K and diamond three reflection ATR crystals. 800 to 1000 scan for 5 mg/ml BAPTAhyd sample were recorded at resolution of 8 cm^{-1} .

5.12 Langmuir isotherms

The surface pressure measurement were performed on a computer controlled Langmuir film balance (Nima Technology, Coventry, UK), and the surface pressure (π) was measured by the Wilhelmy method using a filter paper plate. During the measurement, the bottom edge of the well soaked plate is always just at the water meniscus surface.

For the surface pressure isotherms, a rectangular Teflon trough with computer-controlled barriers in a compression rate of $5 \text{ cm}^2/\text{min}$. The experiment temperature is controlled at $21 \pm 2 \text{ }^\circ\text{C}$. Amphiphiles were dissolved in the chloroform solvent in a concentration about 10^{-4} mol/L . A carefully measured quantity with Hamilton syringes for 50 μL of the sample was spread at the air-water interface. After waiting for 15 min to let the solvent evaporate, the compression curves were recorded.

5.13 PM-IRRAS⁶

PM-IRRAS spectra were recorded on a Nicolet 870 Fourier transform infrared (FTIR) spectrometer by the co-addition of 800 scans at a resolution of 8 cm^{-1} , scan speed= 0.46 cm/s , slit= 30. For the experiment recording different stages of Langmuir film, the Langmuir trough of NIMA516 (Nima Technology, Coventry, UK) was equipped with the above-mentioned method.

When desired surface pressure and sample volume is pre-calculated. The round-like trough with 5.2 cm inside-diameter was used without need of further compression process. A solution of molecules in CHCl_3 was directly injected with the calculated volume on the subphase in

the round-like trough in order to obtain the pre-calculated surface pressure.

5.14 Ellipsometry measurement⁷

The thickness of the films formed was determined using a NFT IELli2000 ellipsometer (Göttingen, Germany) equipped with a frequency doubled Nd:YAG laser (532 nm, 50 mW), a polarizer, a compensating plate, an analyzer, and a CCD camera. It operates on the principle of classical null ellipsometry.⁸ This parameter has been obtained from the ellipsometric angles (ψ and Δ) measured with an incidence angle of 54.58, which give the null conditions. The morphology of films at the air-water interface was observed by the CCD camera. The spatial resolution was about 2 μm , and the size of images was 450 x 670 μm with a x10 magnification lens. The angles of the polarizer, compensator, and analyzer that obtained the null condition allow one to obtain the (Δ , Ψ) angles, which are related to the optical properties of the sample. For ultrathin films, Δ is proportional to the film thickness. Application of the measured data with computerized optical modeling included in the ellipsometric software leads to a deduction of film thickness for a given refractive index. The value of the film thickness mainly depends on the refractive index used. Since it is difficult to determine an accurate experimental refractive index value, we therefore decided to use the same average value of the refractive index 1.45 for both lipid layers to reduce the number of parameters introduced in our model.^{9,10}

5.15 Small angle X-ray scattering (SAXS)

A Rigaku Nanoviewer (Micro-source generator, MicroMax 007, 800W rotating anode coupled with a Confocal Maxflux Mirror) was used. Samples were put in the sealed glass capillary with 1 mm in diameter by means of centrifuge. The temperature of the sample was regulated at 18 °C unless indicated differently. Integration of the spectra was performed with a program delivered with the apparatus.

5.16 Electroformation of giant unilamellar vesicles (GUVs)^{11,12}

Giant unilamellar vesicles (GUVs) are prepared in a custom made petri dish. 4 μl of 0.5 mM lipid mixture in chloroform was spotted onto the Pt electrode and dried under vacuum for at least 1h. An alternating electrical field of 10 Hz 0.5 V was applied to the electrodes at room temperature. ~2.5 ml of Milli-Q water was added (avoiding agitation). The applied voltage was gradually increased to 1 V (during 30 min) and applied for 2 hours, followed by 30 ~60 min of 4 Hz and 2 ~3 V to detach the formed liposomes.

For preparation directly on the glass surface instead of on the Pt electrode, ITO glass (Indium Tin Oxide modified glass) was used with carefully applied AC fields on the ITO glass

edges. These electroformation methods can increase the yield of simple dropcast and standing for a long time on the glass.

5.17 Preparation of small unilamellar vesicles (SUVs)

Small unilamellar vesicles (SUVs) are prepared by mixing the solutes with lipid compound (generally 1:300 molar ratio for our experiments) in chloroform, followed by carefully evaporating the solvent with air flow to obtain a well-blended film. After at least one hour high vacuum to remove the remaining solvent, adding water or buffer solution to rehydrate the film followed by several cycles of microtip sonication (4 cycles, each cycle is at amplitude = 40, pulse = 3, with 10 min sonication then standing for 5 min) allows us to get the small lamellar structure. If DLS is used to measure the vesicle size, further centrifugation to remove the metal pollutants from the microtip is required.

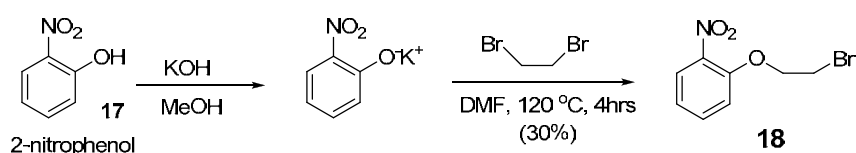
5.18 Optical / fluorescence Microscopy

Samples were sealed between a glass slide and cover glass or directly observed when GUVs grow in the petri dish. NIKON Eclipse Physio Station E600FN equipped with HAMAMATSU C4742-95 digital CCD camera was used with 10x/0.3, 20x/0.5, 40x/0.75 Plan Fluor objective with an adequate condenser and a prism for DIC (differential interferential contrast) observation.

5.19 Confocal fluorescence microscope

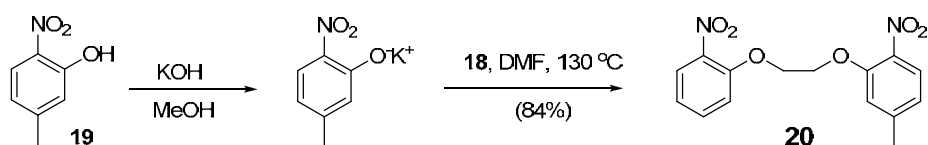
A Picoquant Microtime 200 was used with two MPD SPADs and a Ti-Sa laser chain (Coherent) yielding 4-6 ps pulses at 4.75 MHz. An 80% T/20% R spectrally flat beam splitter was used in combination with a microscope objective (100× UPLSAPO, NA 1.4), suitable interferential filters, a 50 μm pinhole, and, when specified, a polarizing beam splitter and two Glan-Thompson polarizers. Spectroscopy was performed with an Andor system, collecting after the pinhole. FLIM results were obtained using FastFLIM algorithm.

5.20 Synthesis procedure

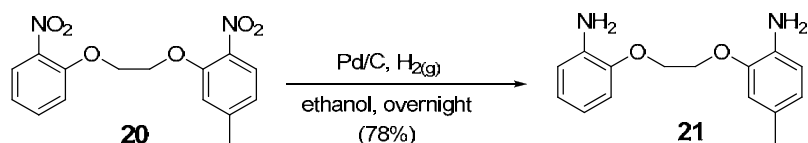


2-nitrophenol (50 g, 0.36 mol, 1 eq) was stirred in methanol and heated until dissolved. A solution of potassium hydroxide (22.2 g, 0.4 mol, 1.1 eq) dissolved in hot methanol was slowly added. Within a few minutes the reaction was completed. After removing the solvent,

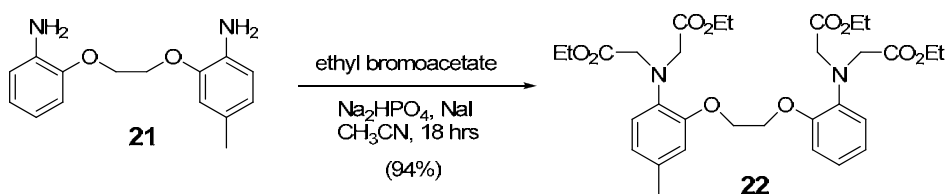
270 g 1, 2-dibromoethane (1.44 mol, 4 eq), and DMF (200 ml) were added and heated together to 120 °C for 4 hours. The mixture was cooled, extracted with water and dichloromethane, then washed with 10 % aqueous NaOH three times and then sat. aqueous NaCl. The combined organic extracts were dried with MgSO₄, filtered and evaporated. The crude was washed by ethyl ether to remove the insoluble byproduct. The solution part was evaporated to dryness and the residue recrystallized from ethanol containing a small quantity of water. The yield of **18** was 26.5 g (30 %).



2-nitro-5-methylphenol (**19**, 13.7 g, 89 mmol, 1.1 eq) was dissolved in warm methanol. A solution of potassium hydroxide (5.23 g, 93 mmol, 1.15 eq) dissolved in hot methanol was slowly added. Within a few minutes the reaction was completed. After removing the solvent, **18** (20 g, 81 mmol, 1 eq), and DMF (40 ml) were added and heated together to 130 °C for 3 hours. The mixture was cooled, diluted to 300 ml with water, and filtered; the precipitate was washed repeatedly with aqueous Na₂CO₃ and then water. After drying, it was recrystallized from hot ethanol with 4 % acetic acid. The yield of **20** was 21.7 g (84 %).



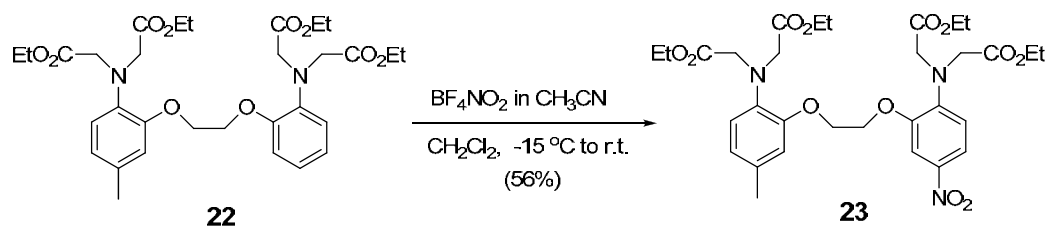
20 (10 g, 31 mmol) was hydrogenated at room temperature and atmospheric pressure with palladium (1 g, 10% on charcoal) catalyst in ethanol overnight. The mixture was filtered through celite and washed with hot ethanol. The solvent was removed and the residue was washed with ethyl ether and filtered to remove impurities. The ether phase was dried and get 6.33 g white powder **21** (78 %).



21 (6.33 g, 25 mmol, 1 eq), ethyl bromoacetate (15 ml, 135 mmol, 5.5eq), dried Na₂HPO₄ (17.4 g, 125 mmol, 5 eq), NaI (1.84 g, 12 mmol), and dried CH₃CN (35 ml) were refluxed under nitrogen for 18 hours. The cooled solution was extracted with toluene and water. The organic phase was dried with MgSO₄ then recrystallized from ethanol. The yield of **22** was 13.9 g (94 %).

¹H NMR (250 MHz, CDCl₃) δ 6.88-6.82 (m, 4H), 6.7-6.66 (m, 3H), 4.26 (s, 4H), 4.2-3.98 (m,

16H), 2.26 (s, 3H), 1.18-1.1 (m, 12H)

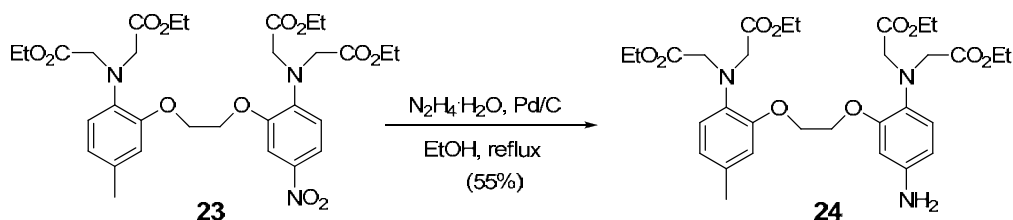


A solution of **22** (1 g, 1.66 mmol, 1 eq) in dry dichloromethane (20 ml) was cooled to -20 °C before nitronium tetrafluoroborate (0.25 g, 1.9 mmol, 1.1eq) in dry CH₃CN was added dropwise, maintaining the temperature of the bath below -10 °C. After the addition was complete, the reaction was stirred at room temperature overnight. Water was added to quench any remaining nitronium salts, extracted with CH₂Cl₂, and then sat. aqueous NaCl. The organic phase was dried with MgSO₄, filtered, and the solvent evaporated. The crude product was then purified by column chromatography on silica gel eluting with ethyl acetate / petroleum ether (1:10). Further recrystallization from CH₂Cl₂ / petroleum ether gave 0.6 g of **23** (56 %).¹³

¹H NMR (250 MHz, CDCl₃) δ 7.83-7.8 (m, 1H), 7.7 (d, *J* = 2.4 Hz, 1H), 6.76-6.64 (m, 4H), 4.34-4.00 (m, 20H), 2.25 (s, 3H), 1.24-1.11 (m, 12H).

¹³C NMR (75 MHz, CDCl₃) δ 171.43, 170.44, 150, 148.57, 145.33, 140.78, 137, 132.03, 122.13, 119.37, 118.24, 115.78, 114.61, 107.9, 67.77, 66.63, 61.27, 60.61, 53.75, 53.49, 20.85, 14.02, 13.92

HRMS (m/z %) Calcd. for C₃₁H₄₁N₃O₁₂Na 670.2582, Found 670.2603

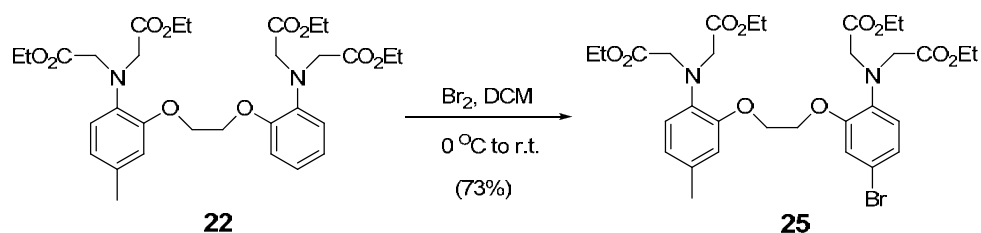


23 (0.2 g, 0.31 mmol, 1 eq), Pd/C (20 mg, 10 % on charcoal), and ethanol (8 ml) were stirred under argon and to this solution hydrazine hydrate (75 μl, 0.0015 mmol, 5 eq) was added dropwise via a syringe and the resulting solution was refluxed overnight. The mixture was filtered through celite with ethyl acetate. After removing the solvent, the residue was purified by column chromatography on silica gel eluting with ethyl acetate / triethylamine (100:1 v/v). The yield of **24** was 105 mg (55 %).¹⁴

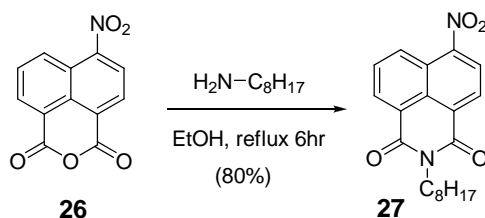
¹H NMR (250 MHz, CDCl₃) δ 6.77-6.65 (m, 4H), 6.3-6.2 (m, 2H), 4.26 (s, 4H), 4.12-4.03 (m, 16H), 3.55 (s, 2H), 2.25 (s, 3H), 1.19-1.12 (m, 12H)

¹³C NMR (75 MHz, CDCl₃) δ 171.69, 171.59, 152.01, 150.31, 142.34, 136.79, 132.1, 131.42, 121.68, 121.62, 119.30, 114.36, 107.72, 102.12, 67.11, 67.05, 60.62, 60.49, 53.92, 53.54, 20.91, 14.05

HRMS (m/z %) Calcd. for C₃₁H₄₃N₃O₁₀Na 640.28, Found 670.284

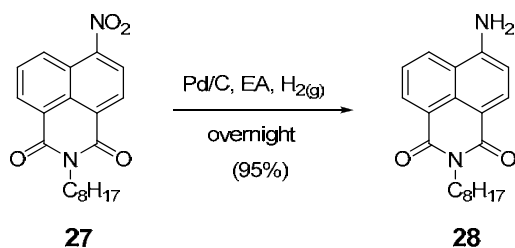


22 (1.5 g, 2.5 mmol, 1 eq) was dissolved in dried CH_2Cl_2 (60 ml) under argon cooled to 0 °C. To this solution bromine (0.25 ml, 4.9 mmol, 2 eq) in dried CH_2Cl_2 (10 ml) was added dropwise via a syringe and the resulting solution was stirred at room temperature overnight. The reaction was quenched by 10 % aqueous NaOH, then extracted with CH_2Cl_2 , washed by water then sat. aqueous NaCl. The combined organic phase was dried with MgSO_4 , filtered, and solvent evaporated. The crude product was recrystallized from ethanol. The yield of **25** was 1.23 g (73%).



4-nitro-1,8-naphthalic anhydride (**26**, 5 g, 21 mmol, 1 eq), *n*-octylamine (3.75 ml, 23 mmol, 1.1 eq), and ethanol (100 ml) were refluxed under nitrogen for 6 hours. The reaction was cooled to room temperature and let to stand for an additional hour. The resulting precipitate was filtered and washed with ethanol / water (1:3 v/v) twice. The yield of **27** was 5.8 g (80 %).

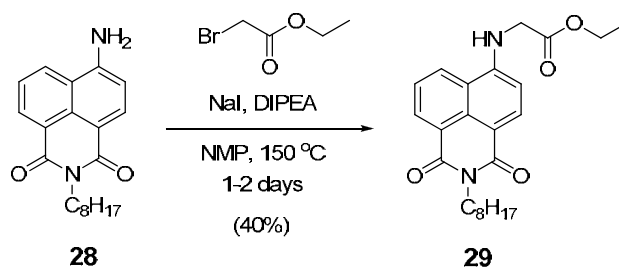
^1H NMR (250 MHz, CDCl_3) δ 8.84 (d, $J = 8.7$ Hz, 1H), 8.71 (q, $J = 6.3$ Hz, 2H), 8.41 (d, $J = 7.9$ Hz, 1H), 7.99 (t, $J = 8$ Hz 1H), 4.17 (t, $J = 7.5$ Hz, 2H), 1.73 (m, 2H), 1.37-1.27 (m, 10H), 0.86-0.84 (m, 3H)



27 (5.5 g, 31 mmol) were hydrogenated at room temperature and atmospheric pressure with palladium (0.6 g, 10% on charcoal) catalyst in ethyl acetate (500 ml) for overnight. The mixture was filtered through celite and rinsed by hot ethyl acetate. Then removing the solvent and the residue was washed by pentane containing a few percent by volume CHCl_3 . The yield of **28** was 4.77 g (95 %).

^1H NMR (250 MHz, CDCl_3) δ 8.59 (q, $J = 7.3$ Hz, 1H), 8.4 (d, $J = 8.1$ Hz, 1H), 8.1, (d, $J =$

8.3 Hz, 1H), 7.64 (t, $J = 7.8$ Hz, 1H), 6.88 (d, $J = 8.1$ Hz, 1H), 5.00 (s, 2H), 4.14 (t, $J = 7.6$ Hz, 2H), 1.7 (m, 2H), 1.35-1.25 (m, 10H), 0.83 (m, 3H)

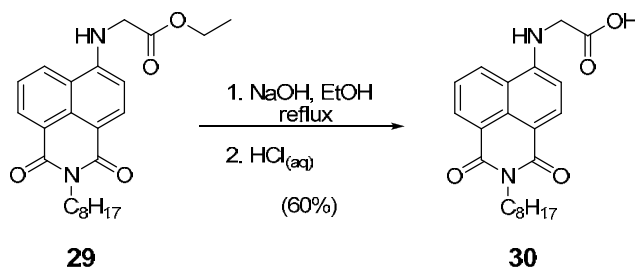


28 (2 g, 6.2 mmol, 1 eq), ethyl bromoacetate (4.2 ml, 37.9 mmol, 6 eq), NaI (2.8 g, 18.7 mmol, 3 eq), and N,N-diisopropylethylamine (6.2 ml, 37.5 mmol, 6 eq) were refluxed together in N-Methyl-2-Pyrrolidone (NMP, 70 ml). After checking TLC, the reaction was cooled to room temperature, water was added and then the precipitate was filtered. The solid crude was purified by column chromatography on silica gel eluting with ethyl acetate / petroleum ether (1:3). The yield of **29** was 1 g (40 %).

^1H NMR (250 MHz, CDCl_3) δ 8.52 (q, $J = 7.1$ Hz, 1H), 8.4 (d, $J = 8.3$ Hz, 1H), 8.13, (d, $J = 8.3$ Hz, 1H), 7.58 (t, $J = 7.8$ Hz, 1H), 6.53 (d, $J = 8.3$ Hz, 1H), 6.01 (s, 1H), 4.34, (q, $J = 7.1$ Hz, 2H), 4.15-4.09 (m, 4H), 1.7 (m, 2H), 1.38-1.25 (m, 15H), 0.83 (m, 3H)

^{13}C NMR (75 MHz, CDCl_3) δ 169.9, 164.44, 163.99, 147.75, 134, 131.1, 129.45, 125.93, 125.05, 123.06, 120.21, 111.51, 104.57, 62.13, 44.93, 40.23, 31.78, 29.33, 29.21, 28.15, 27.16, 22.6, 14.15, 14.06

HRMS (m/z %) Calcd. for $\text{C}_{24}\text{H}_{31}\text{N}_2\text{O}_4$ 411.2278, Found 411.2282



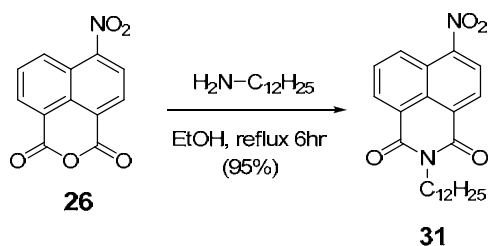
29 (0.2 g, 0.49 mmol, 1 eq) and NaOH (0.2 g, 5 mmol, 10 eq) were refluxed in ethanol (15 ml) overnight. After adding 10 % aqueous NaOH, the solution was washed by CH_2Cl_2 for 3 times to remove the impurity. The aqueous phase was collected and neutralized by concentrated HCl to $\text{pH} < 3$. The yellow precipitate was collected and washed several times with petroleum ether and then ethyl acetate / petroleum ether (1:5). The yield of **30** was 0.11 g (60 %).

^1H NMR (300 MHz, CD_3OD) δ 8.39 (q, $J = 7.5$ Hz, 2H), 8.26 (d, $J = 8.6$ Hz, 1H), 7.5 (t, $J = 7.7$ Hz, 1H), 6.58 (d, $J = 8.7$ Hz, 1H), 4.06 (t, $J = 7.5$ Hz, 2H), 3.92 (s, 2H), 1.67 (m, 2H), 1.36-1.26 (m, 10H), 0.88 (t, $J = 6.6$ Hz, 3H)

^{13}C NMR (75 MHz, CD_3OD) δ 171.26, 163.63, 162.84, 150.33, 133.84, 130.61, 129.13, 128.23, 124.53, 121.9, 120.09, 108.59, 104.24, 44.25, 39.45, 31.19, 28.69, 28.55, 27.54, 26.52,

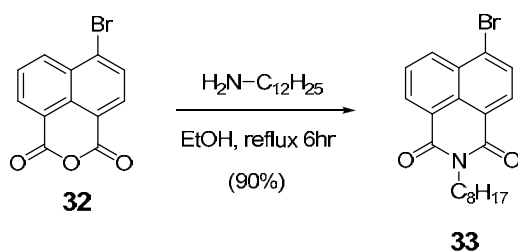
22.02, 13.88

HRMS (m/z %) Calcd. for C₂₂H₂₅N₂O₄ 381.1819, Found 381.1802



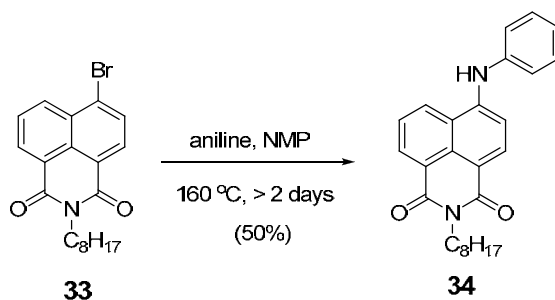
4-nitro-1,8-naphthalic anhydride (**26**, 2 g, 8.2 mmol, 1 eq), dodecylamine (1.68 g, 9.1 mmol, 1.1 eq), and ethanol (40 ml) were refluxed overnight. The reaction was cooled to 0 °C, and resulting precipitate was filtered and washed by water then ethanol / water (1:1 v/v). The yield of **31** was 3.2 g (95 %).

¹H NMR (300 MHz, CDCl₃) δ 8.83 (d, *J* = 8.4 Hz, 1H), 8.71 (q, *J* = 7.2 Hz, 2H), 8.4 (d, *J* = 8.1 Hz, 1H), 7.98 (t, *J* = 7.95 Hz, 1H), 4.17 (t, *J* = 7.7 Hz, 2H), 1.73 (m, 2H), 1.24 (m, 18H), 0.87 (m, 3H)



4-bromo-1,8-naphthalic anhydride (**32**, 0.5 g, 1.8 mmol, 1 eq), *n*-octylamine (0.33 ml, 2 mmol, 1.1 eq), and ethanol (10 ml) were refluxed for 6 hours. The mixture was poured into water, and the resulting precipitate was filtered and washed by water then ethanol. The yield of **33** was 0.63 g (90 %).

¹H NMR (250 MHz, CD₃OD) δ 8.65 (d, *J* = 7.3 Hz, 1H), 8.56 (d, *J* = 8.5 Hz, 1H), 8.41 (d, *J* = 7.9 Hz, 1H), 8.03 (d, *J* = 7.9 Hz, 1H), 7.84 (m, 1H), 4.15 (t, *J* = 7.4 Hz, 2H), 1.70 (m, 2H), 1.36-1.26 (m, 10H), 0.85 (m, 3H)



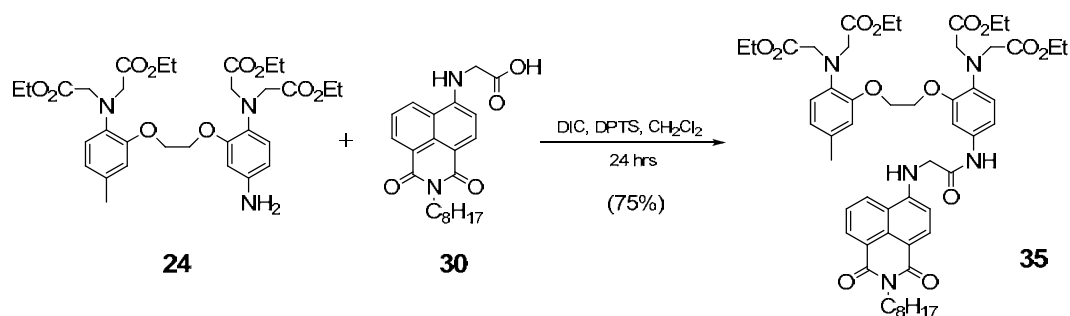
33 (0.1 g, 0.26 mmol, 1 eq) and aniline (0.12 ml, 1.28 mmol, 5 eq) were refluxed together in N-Methyl-2-Pyrrolidone (NMP, 3 ml). After checking TLC, the reaction was cooled to

room temperature, then evaporated. The solid crude was purified by column chromatography on silica gel eluting with ethyl acetate / petroleum ether (1:3 v/v). The yield of **34** was 52 mg (50 %).

^1H NMR (250 MHz, CD_3OD) δ 8.59 (q, $J = 8.6$ Hz, 1H), 8.37 (m, 2H), 7.65 (m, 1H), 7.47-7.09 (m, 6H), 4.15 (t, $J = 7.4$ Hz, 2H), 1.72 (m, 2H), 1.27 (m, 10H), 0.87 (m, 3H)

^{13}C NMR (75 MHz, CD_3OD) δ 164.47, 163.87, 146.55, 139.85, 133.41, 131.36, 129.83, 126.32, 125.48, 124.78, 123.28, 122.37, 121.87, 113.41, 108.93, 40.32, 31.8, 29.34, 29.22, 28.16, 27.16, 22.61, 14.07

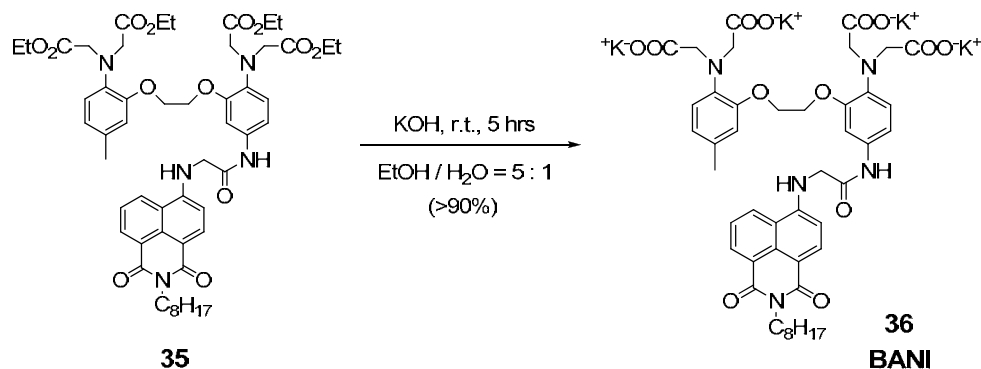
HRMS (m/z %) Calcd. for $\text{C}_{26}\text{H}_{29}\text{N}_2\text{O}_2$ 401.2232, Found 401.2223



24 (200 mg, 0.32 mmol, 1 eq), **30** (136 mg, 36 mmol, 1.1 eq), and 4-(dimethylamino)-pyridinium 4-toluenesulfonate (DPTS, 0.19 g, 0.64 mmol, 2 eq) were mixed in 10 ml dried CH_2Cl_2 under argon. To this solution $\text{N,N}'$ -Diisopropylcarbodiimide (DIC, 0.1 ml, 0.64 mmol, 2 eq) were dropwise added and the resulting solution was stirred at room temperature for 24 hours. The reaction was quenched by water, extracted with CH_2Cl_2 , and then washed by sat. aqueous NaCl. The combined organic phase was dried with MgSO_4 , filtered, and the solvent evaporated. The crude product was dissolved in ethyl ether then filtered to remove solid byproduct. After removing the solvent the crude was recrystallized from ethyl acetate and petroleum ether two times. The yield of **35** was 0.24 g (75%).

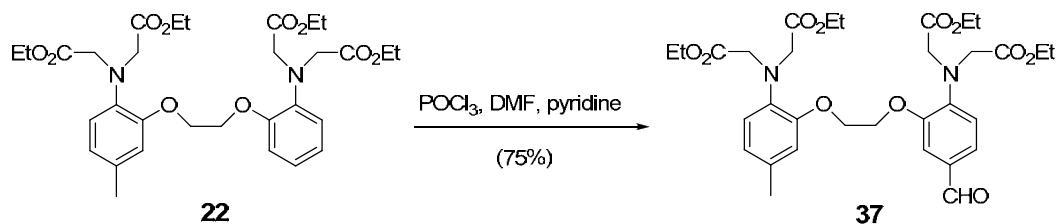
^1H NMR (300 MHz, CD_3OD) δ 9.00 (s, 1H), 8.5 (d, $J = 7.1$ Hz, 1H), 8.35 (d, $J = 8.4$ Hz, 1H), 8.25 (d, $J = 8.3$ Hz, 1H), 7.53 (t, $J = 7.1$ Hz, 1H), 7.21 (s, 1H), 7.07 (d, $J = 7.9$ Hz, 1H), 6.72 (t, $J = 7.5$ Hz, 3H), 6.65-6.52 (m, 3H), 4.47 (d, $J = 7.9$ Hz, 2H), 4.18-3.89 (m, 20H), 3.87-3.78 (m, 2H), 2.16 (s, 3H), 1.69 (s, 2H), 1.33-1.09 (m, 22H), 0.83 (t, $J = 5.3$ Hz, 3H)

^{13}C NMR (75 MHz, CD_3OD) δ 171.62, 171.43, 166.81, 164.47, 164, 157.24, 150.28, 150.13, 148.58, 136.38, 135.63, 134.1, 132.69, 132.31, 131.02, 129.49, 126.57, 124.81, 122.82, 121.71, 120.4, 119.3, 118.85, 114, 112.68, 110.93, 106.23, 104.63, 67.24, 66.66, 60.79, 60.73, 53.73, 53.6, 46.9, 42.02, 40.2, 31.74, 29.3, 29.16, 28.15, 27.15, 23.4, 22.55, 20.81, 14, 13.97



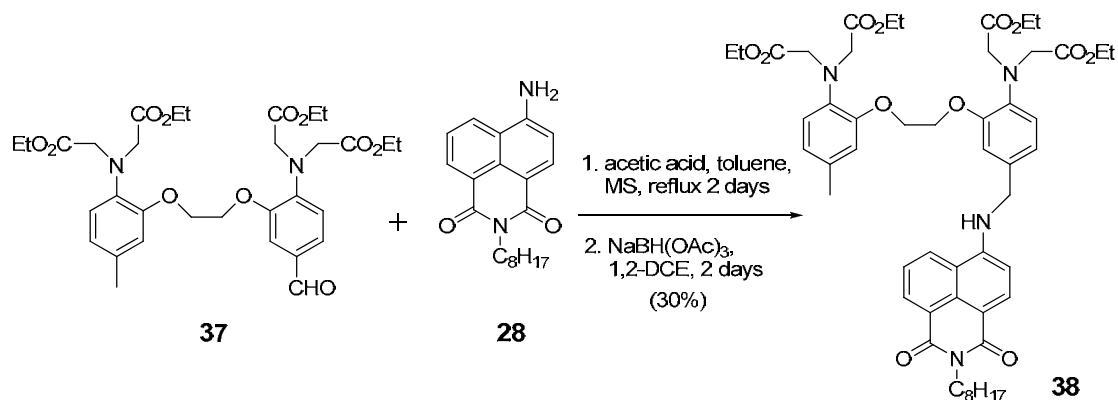
A mixture of **35** (50 mg, 0.05 mmol) and KOH (25 mg, 0.45 mmol) in EtOH/H₂O (1.25/0.25 ml) was stirred for 5h. The resultant solution was diluted with ice-water (1 ml) and 10 % HCl_(aq) was added slowly at 0 °C until pH = 7. The solvents were removed by freeze drying. The yield was 97.6 mg (52.5 w % of **36** with KCl).

¹H NMR (300 MHz, CD₃OD) δ 8.49 (d, *J* = 8.4 Hz, 1H), 8.43 (d, *J* = 7.2 Hz, 1H), 8.3 (d, *J* = 8.4 Hz, 1H), 7.61 (t, *J* = 8 Hz, 1H), 7.35 (s, 1H), 7.1 (d, *J* = 8.7 Hz, 1H), 6.98 (d, *J* = 8.4 Hz, 1H), 6.91 (d, *J* = 7.8 Hz, 1H), 6.8 (s, 1H), 6.67 (t, *J* = 6.9 Hz, 2H), 4.34 (s, 4H), 4.25 (s, 2H), 4.06 (t, *J* = 7.4 Hz, 2H), 3.54 (s, 4H), 3.52 (s, 4H), 2.27 (s, 3H), 1.67 (s, 2H), 1.35-1.29 (m, 10H), 0.88 (t, *J* = 5.3 Hz, 3H)



22 (1 g) was dissolved in dry dimethylformamide (2 ml) containing dry pyridine (0.2 ml). The mixture was cooled in an ice bath and phosphorus oxychloride (1.5 ml) was added dropwise. The reaction was stirred at 60 °C for 1 hour and then overnight at room temperature. The mixture was dissolved in CH₂Cl₂ (10 ml) and poured onto crushed ice mixed with 10% NaOH_(aq). The aqueous layer was extracted with CH₂Cl₂ several times. The combined organic phase were dried with MgSO₄, filtered and evaporated. The partially crystalline residue was triturated with isopropyl alcohol (5 ml), filtered, washed with ether/pet. ether 1:1 solution and dried. The yield of **37** was 0.8 g (75 %)

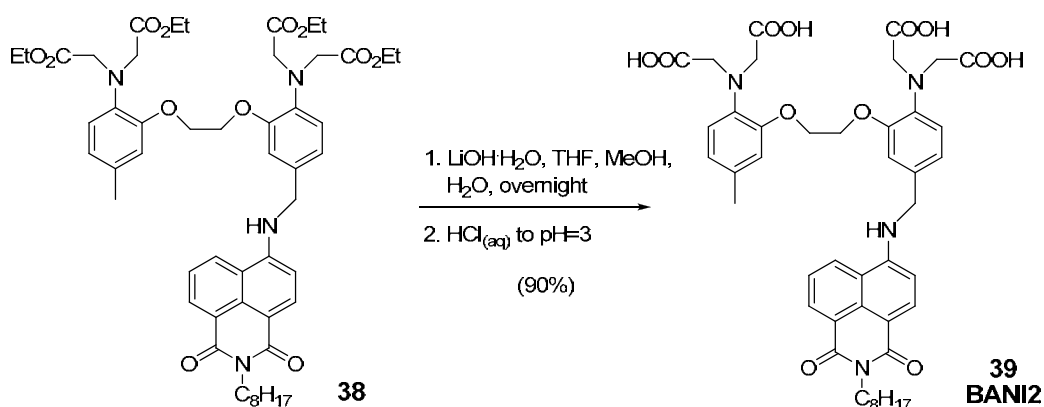
¹H NMR (300 MHz, CDCl₃) δ 9.79 (s, 1H), 7.37 (s, 2H), 6.74-6.65 (m, 4H), 4.32- 4.02 (m, 20H), 2.25 (s, 3H), 1.17-1.12 (m, 12H)



A mixture of **37** (0.35 g, 0.55 mmol, 1eq), **28** (0.2 g, 0.61 mmol, 1.1eq) in toluene (20 ml) containing acetic acid (0.063 ml) and some molecular sieves was refluxed for 2 days. Then the solvent was removed and NaBH(OAc)_3 (1.18 g) and 1,2-dichloroethane (20 ml) were added. The mixture was stirred more 2 days. After checked by TLC, $\text{NaHCO}_3(\text{aq})$ was added to quench the reaction and CH_2Cl_2 (30 ml) was added. The mixture passed through celite then extracted with CH_2Cl_2 and then sat. $\text{NaCl}(\text{aq})$. The organic phase was dried with MgSO_4 and concentrated. The residue was chromatographed on silica gel with ethyl acetate / CH_2Cl_2 / pet. ether (3:1:3 v/v), then further recrystallized with ethyl acetate with pet. ether. The yield of **38** was 0.15g (30 %).

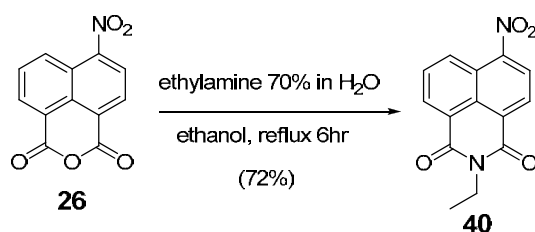
^1H NMR (300 MHz, CDCl_3) δ 8.58 (d, $J = 7.2$ Hz, 1H), 8.44 (d, $J = 8.4$ Hz, 1H), 8.11 (d, $J = 8.3$ Hz, 1H), 7.59 (t, $J = 7.9$ Hz, 1H), 7.02 – 6.89 (m, 2H), 6.87 – 6.59 (m, 5H), 5.59 (s, 1H), 4.49 (d, $J = 4.7$ Hz, 2H), 4.28 (d, $J = 5.0$ Hz, 4H), 4.07 (m, 18H), 2.24 (s, 3H), 1.70 (d, $J = 7.1$ Hz, 2H), 1.50 – 1.07 (m, 22H), 0.86 (s, 3H). ^{13}C NMR (75 MHz, CDCl_3) δ 171.48, 171.33, 164.64, 164.07, 150.70, 150.31, 148.99, 139.38, 136.87, 134.26, 132.24, 131.05, 130.75, 129.72, 125.92, 124.81, 123.26, 121.99, 121.00, 120.32, 119.61, 119.19, 114.74, 113.65, 110.95, 104.80, 67.60, 67.15, 60.79, 60.57, 53.61, 47.80, 40.25, 31.82, 29.38, 29.23, 28.21, 27.20, 22.62, 20.90, 14.09.

HRMS (m/z %) Calcd. for $\text{C}_{52}\text{H}_{66}\text{N}_4\text{O}_{12}\text{Na}$ 961.4569, Found 961.4562



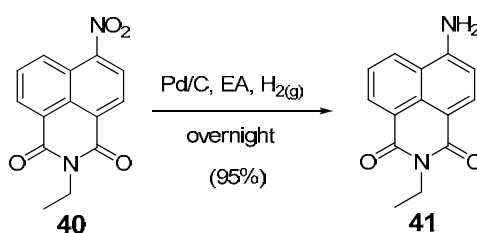
A mixture of **38** (50 mg, 0.053 mmol, 1eq) and $\text{LiOH.H}_2\text{O}$ (53 mg, 1.26 mmol, 22eq) in THF (4 ml), MeOH (4 ml), H_2O (1 ml) was stirred at room temperature overnight. After confirmation by RP-TLC, the solvent was removed and the crude was washed and sonicated

in dichloromethane and ethyl acetate then filtered. The crude solid was dissolved in Milli-Q water and filtered to obtain the clear yellow solution. The solution was slowly acidified at 0°C with 10 % HCl_(aq) until pH = 3. The precipitate was collected by centrifugation and washed by water once then freeze dried to get a yellow powder. The yield of **39** was 40 mg (90%). ¹H NMR (300 MHz, DMSO) δ 8.76 (d, *J* = 8.1 Hz, 1H), 8.51 – 8.30 (m, 2H), 8.19 (d, *J* = 8.5 Hz, 1H), 7.69 (t, *J* = 7.7 Hz, 1H), 7.09 (s, 1H), 6.96 – 6.55 (m, 7H), 4.55 (s, 2H), 4.24 (s, 4H), 4.00 (d, *J* = 6.4 Hz, 10H), 2.19 (s, 3H), 1.57 (s, 2H), 1.26 (d, *J* = 15.7 Hz, 10H), 0.83 (s, 3H). ¹³C NMR (75 MHz, DMSO) δ 172.65, 172.52, 163.47, 162.62, 150.22, 149.30, 149.18, 137.80, 136.31, 133.81, 130.61, 130.38, 130.09, 129.09, 128.37, 128.32, 124.15, 121.63, 120.00, 119.59, 118.38, 117.85, 115.12, 113.54, 107.73, 104.30, 67.06, 66.88, 54.07, 45.49, 30.96, 28.47, 28.32, 27.35, 26.30, 21.80, 20.17, 13.68.

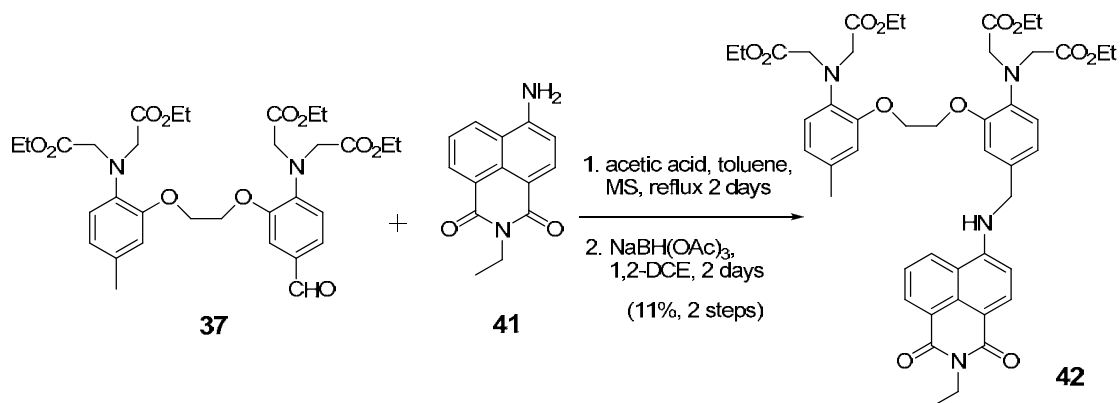


4-nitro-1,8-naphthalic anhydride (**26**, 1 g, 4.1 mmol, 1 eq), ethyl amine 70% aqueous solution (0.4 ml, 4.9 mmol, 1.2 eq), and ethanol (25 ml) were refluxed under nitrogen for 6 hours. The reaction was cooled to room temperature and standing for another 1 hour. The resulting precipitate was filtered and washed with ethanol / water (1:3 v/v) twice. The yield of **40** was 0.8 g (72 %).

¹H NMR (250 MHz, CDCl₃) δ 8.84 (d, *J* = 8.9 Hz, 1H), 8.76-8.69 (m, 2H), 8.41 (d, *J* = 7.9 Hz, 1H), 8.02-7.96(m, 1H), 4.26 (q, *J* = 4.1 Hz, 2H), 1.35 (t, *J* = 7.1 Hz, 3H)



40 (0.8 g, 3 mmol) were hydrogenated at room temperature and atmospheric pressure with palladium (0.1 g, 10% on charcoal) catalyst in ethyl acetate (80 ml) for overnight. The mixture was filtered through celite and rinsed by hot ethyl acetate. The solvent was removed and the residue was washed by pentane with a small quantity CHCl₃. The yield of **41** was 0.66 g (95 %).

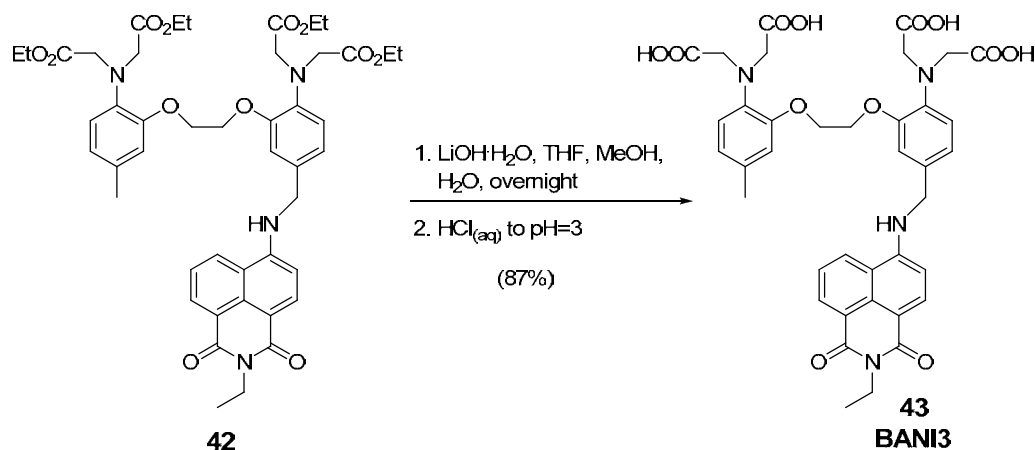


A mixture of **37** (1.06 g, 1.68 mmol, 1eq), **41** (0.6 g, 1.85 mmol, 1.1eq) in toluene (60 ml) containing acetic acid (0.2 ml) and some molecular sieves was refluxed for 2 days. Then the solvent was removed and of NaBH(OAc)_3 (3.6 g) and 1,2-dichloroethane (60 ml) were added. The mixture was stirred more 2 days. After checked by TLC, $\text{NaHCO}_3(\text{aq})$ was added to quench the reaction and 30 ml of CH_2Cl_2 was added. The mixture passed through celite then extracted with CH_2Cl_2 and then sat. $\text{NaCl}(\text{aq})$. The organic phase was dried with MgSO_4 and concentrated. The residue was chromatographed on silica gel with ethyl acetate / pet. ether (1:1 v/v), then further recrystallized with ethyl acetate with pet. ether. The yield of **42** was 0.16g (11 %).

$^1\text{H NMR}$ (200 MHz, CDCl_3) δ 8.55 (d, $J = 8$ Hz, 1H), 8.43 (d, $J = 8.4$ Hz, 1H), 8.12 (d, $J = 8.4$ Hz, 1H), 7.56 (t, $J = 8.1$ Hz, 1H), 6.96 – 6.65 (m, 7H), 5.65 (s, 1H), 4.48 (d, $J = 4.9$ Hz, 2H), 4.27-4.00 (m, 22H), 2.24 (s, 3H), 1.34-1.10 (m, 15H).

$^{13}\text{C NMR}$ (75 MHz, CDCl_3) δ 171.48, 171.34, 164.46, 163.87, 150.64, 149.04, 139.3, 136.81, 134.22, 132.18, 130.99, 130.72, 129.68, 126.01, 124.76, 123.18, 121.93, 120.89, 120.29, 119.52, 119.1, 114.58, 113.45, 110.83, 104.76, 67.51, 67.07, 60.77, 60.56, 53.55, 47.73, 35.14, 20.88, 14.05, 13.39.

HRMS (m/z %) Calcd. for $\text{C}_{46}\text{H}_{54}\text{N}_4\text{O}_{12}\text{Na}$ 877.363, Found 877.3655

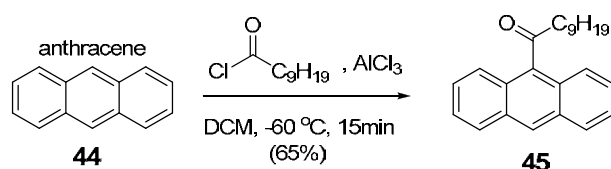


A mixture of **42** (50 mg, 0.058 mmol, 1eq) and $\text{LiOH}\cdot\text{H}_2\text{O}$ (53 mg, 1.26 mmol, 22eq) in THF (4 ml), MeOH (4 ml), H_2O (1 ml) was stirred under room temperature overnight. After

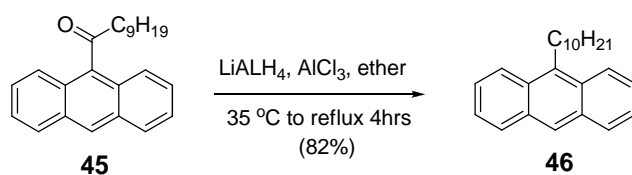
confirmed by RP-TLC, the solvent was removed and the crude was washed and sonicated in dichloromethane and ethyl acetate, then filtered. The crude solid was dissolved in Milli-Q water and filtered to obtain a clear yellow solution. The solution was slowly acidified under 0°C with 10 % HCl_(aq) to pH = 3. The precipitate was collected by centrifugation and washed by water once then freeze dried to get a yellow powder. The yield of **43** was 38 mg (87%).

¹H NMR (300 MHz, DMSO) δ 8.79 (d, *J* = 8.0 Hz, 1H), 8.43 (d, *J* = 6.4 Hz, 2H), 8.19 (d, *J* = 8.3 Hz, 1H), 7.68 (t, *J* = 7.5 Hz, 1H), 7.10 (s, 1H), 6.95 – 6.51 (m, 7H), 4.54 (s, 2H), 4.24 (s, 4H), 4.00 (d, *J* = 6.0 Hz, 10H), 2.19 (s, 3H), 1.15 (d, *J* = 6.5 Hz, 3H).

¹³C NMR (75 MHz, DMSO) δ 172.59, 172.48, 163.29, 162.43, 150.25, 149.30, 149.18, 137.82, 136.33, 133.77, 130.65, 130.34, 130.11, 129.09, 128.40, 124.13, 121.65, 121.37, 120.02, 119.62, 118.38, 117.85, 115.12, 113.58, 107.75, 104.28, 67.05, 66.84, 53.90, 45.45, 33.99, 20.17, 13.05.



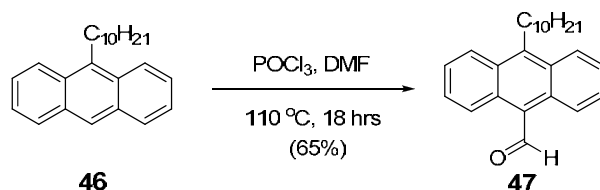
A solution of decanoyl chloride (35 ml, 0.17 mmol, 2 eq) in dried CH₂Cl₂ (450 ml) was added via syringe to AlCl₃ (22.5 g) followed by addition of anthracene (**44**, 15 g, 84 mmol, 1 eq) at -60°C, and the mixture was stirred for 15 minutes. After hydrolysis with 2N HCl, the organic phase was separated, washed with sat. aqueous NaHCO₃, water then sat. aqueous NaCl. The combined organic phase was dried with MgSO₄, filtered, and the solvent was evaporated. After removing the excess decanoyl chloride by distillation, the crude product was purified by column chromatography on silica gel eluting with ethyl acetate / petroleum ether (1:20). The yield of **45** was 17.6 g (65 %).¹⁵



At 35°C a solution of AlCl₃ (0.54 g, 4 mmol, 1.3eq) in dried ethyl ether (8 ml) was rapidly added to LiAlH₄ (0.27 g, 7.1 mmol, 2.3eq) in dried ethyl ether (8 ml) and stirred for 15 min. A solution of **45** (1 g, 3.1 mmol, 1 eq) in dried ethyl ether (24 ml) was added AlCl₃ (0.54, 4 mmol, 1.3eq), then the solution was slowly added to the previous solution and the mixture was refluxed for 2 hours. After cooling to room temperature, hydrolysis with 35% H₂SO₄, the organic phase was separated and the aqueous phase was washed with sat. NaHCO₃ solution and water. The combined organic phase was dried with MgSO₄, filtered, and solvent evaporated. The crude was purified by column chromatography on silica gel eluting with

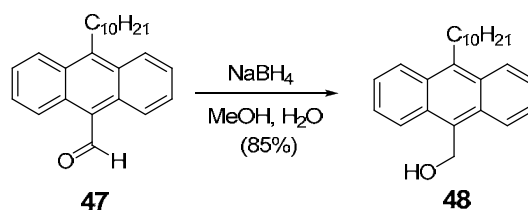
petroleum ether. The yield of **46** was 0.81 g (82 %).¹⁵

¹H NMR (300 MHz, CD₃Cl) δ 8.33 (d, *J* = 8.7 Hz, 3H), 8.02 (d, *J* = 1.8 Hz, 2H), 7.52 (m, 4H), 3.64 (t, *J* = 8.3 Hz, 2H), 1.86 (m, 2H), 1.63-1.34 (m, 14H), 0.96 (t, 3H)



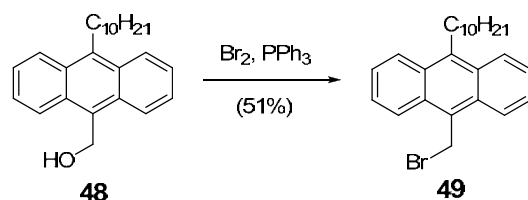
DMF (10 ml) and POCl₃ (1.12 ml, 12 mmol, 3.8 eq) were added via syringe to **46** (1 g, 3.1 mmol, 1 eq) and the mixture was heated to 110°C for 18 hours. After hydrolysis with sat. Na₂CO₃(aq) then water, the organic phase was separated and the aqueous phase extracted with CH₂Cl₂. The combined organic phase was washed with dil. HCl, sat. NaHCO₃(aq) then water, dried with MgSO₄ and concentrated. The residue was chromatographed on silica gel with ethyl acetate / petroleum ether (1:20 v/v). The yield of **47** was 0.7 g (65 %).¹⁵

¹H NMR (300 MHz, CD₃Cl) δ 11.51 (s, 1H), 8.99 (d, *J* = 8.7 Hz, 2H), 8.37 (d, *J* = 8.7 Hz, 2H), 7.67 (qn, *J* = 3.8 Hz, 4H), 3.66 (t, *J* = 8.3 Hz, 2H), 1.84 (m, 2H), 1.55-1.28 (m, 14H), 0.89 (t, 3H)



A solution of **47** (0.2 g) in MeOH (50 ml) was refluxing at 65°C. NaBH₄ (35 mg, 0.93 mmol, 1.6 eq) in MeOH / H₂O (1 ml, 5:1 v/v) was slowly added via syringe. After another 2.5 hours refluxing, the mixture was quenched by water, filtered, and the solid crude product was recrystallized from MeOH. The yield of **48** was 0.17 g (85 %).¹⁵

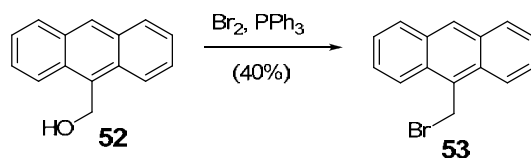
¹H NMR (300 MHz, CD₃Cl) δ 8.47 (d, *J* = 8.4 Hz, 2H), 8.33 (d, *J* = 8.1 Hz, 2H), 7.55 (qn, *J* = 6.6 Hz, 4H), 5.68 (d, *J* = 3.3 Hz, 2H), 4.85 (d, *J* = 6.6 Hz, 1H), 3.62 (t, *J* = 8.3 Hz, 2H), 1.82 (m, 2H), 1.55-1.28 (m, 14H), 0.89 (t, 3H)



A solution of PPh₃ (82 mg, 0.31 mmol, 1.08 eq) was dissolved in warm CH₃CN (3 ml) then cooled to room temperature. Br₂ (16 μl, 0.32 mmol, 1.1 eq) was slowly added via syringe, then **48** (0.1 g, 0.29 mmol, 1 eq) was added two times. After 1 hour stirring, the solution was

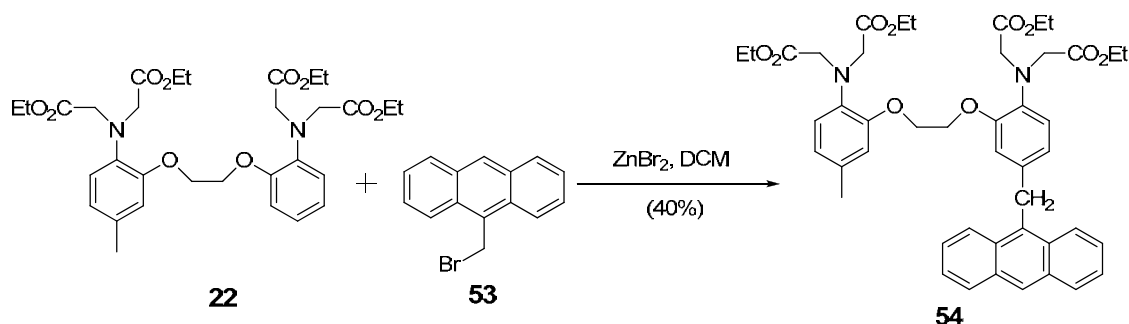
cooled to 0°C and the precipitate was filtered. The solid crude was washed by water then recrystallized from methanol. The yield of **49** was 60 mg (51 %).¹⁵

¹H NMR (300 MHz, CD₃Cl) δ 8.42 (d, *J* = 8.3 Hz, 2H), 8.31 (d, *J* = 8.3 Hz, 2H), 7.53 (qn, *J* = 2.5 Hz, 4H), 5.43 (s, 2H), 3.61 (t, *J* = 8.1 Hz, 2H), 1.81 (m, 2H), 1.55-1.29 (m, 14H), 0.89 (t, 3H)



A solution of PPh₃ (4.08g, 15.5 mmol, 1.08 eq) was dissolved in warm CH₃CN (60 ml) then cooled to room temperature. Br₂ (0.81 ml, 15.8 mmol, 1.1 eq) was slowly added via syringe, then 9-anthracenemethanol (**52**, 3 g, 14.4 mmol, 1eq) was added in two times. After 1 hour stirring, the solution was cooled to 0°C and the precipitate was filtered. The solid crude was washed by water then recrystallized from methanol. The yield of **53** was 1.5g (40 %)¹⁶

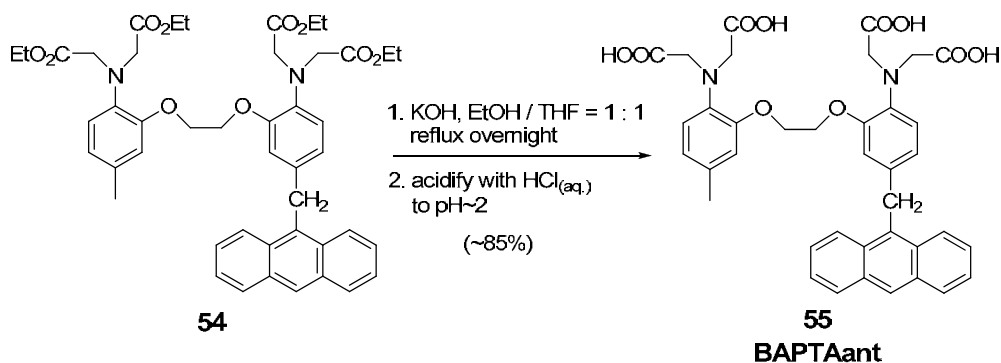
¹H NMR (CDCl₃, 300 MHz) : δ (ppm) = 8,51 (s, 1H) ; 8,31 (d, *J* = 8,5 Hz, 2H) ; 8,05 (d, *J* = 8,5 Hz, 4H) ; 7,66 (t, *J* = 7,5 Hz, 2H) ; 7,51 (t, *J* = 8 Hz, 2H) ; 5,56 (s, 2H).



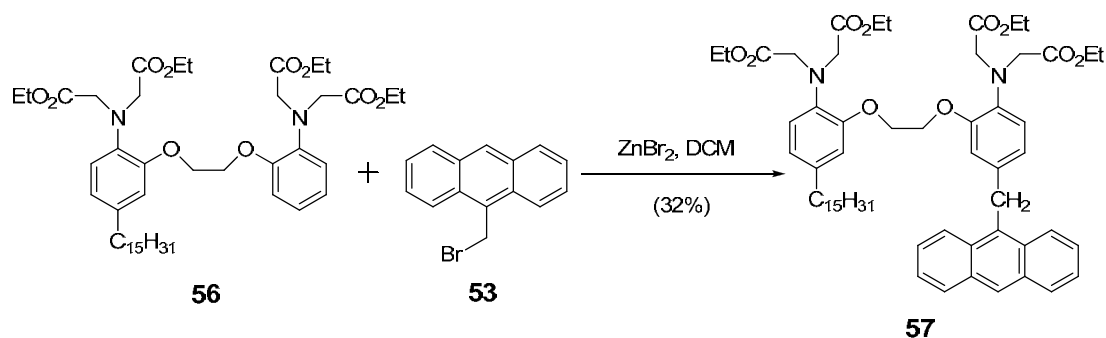
A solution of **22** (200 mg, 0.33 mmol, 1 eq), **53** (100 mg, 0.36 mmol, 1.1 eq) and CH₂Cl₂ (6 ml) was added to ZnBr₂ (75 mg, 0.33 mmol, 1 eq) under Ar_(g). After 18 hours reaction at room temperature without light, water was added to quench the reaction and then extracted with CH₂Cl₂. The organic phase was dried with MgSO₄ and concentrated. The residue was chromatographed on silica gel with ethyl acetate / CH₂Cl₂ (1:25 v/v), then further recrystallized from ethanol. The yield of **54** was 100 mg (40 %).

¹H NMR (300 MHz, CDCl₃) δ 8.40 (s, 1H), 8.21 (dd, *J* = 5.8, 4.3 Hz, 2H), 8.09 – 7.94 (m, 2H), 7.52 – 7.37 (m, 4H), 6.81 – 6.46 (m, 6H), 4.91 (s, 2H), 4.36 – 3.81 (m, 20H), 2.26 (s, 3H), 1.23 – 0.94 (m, 12H).

¹³C NMR (75 MHz, CDCl₃) δ 171.48, 171.44, 150.14, 150.08, 137.21, 136.69, 134.74, 131.92, 131.72, 131.49, 130.27, 128.96, 126.32, 125.65, 124.73, 124.60, 121.45, 120.69, 118.84, 118.73, 113.82, 112.99, 66.78, 66.72, 60.49, 60.45, 53.39, 53.29, 32.81, 20.80, 13.89, 13.84.



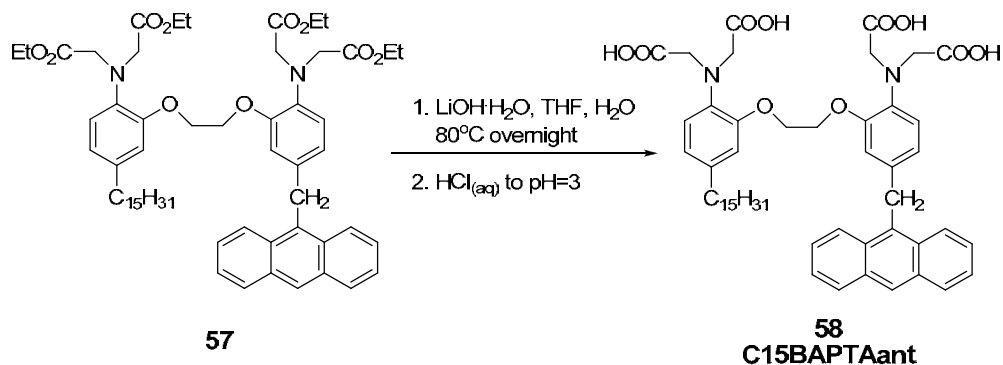
A mixture of this **54** (50 mg, 0.063 mmol, 1eq) and KOH (53 mg, 0.95 mmol, 15eq) in EtOH: THF: H₂O (1: 1: 0.1) was refluxed overnight in the absence of light. After cooling to room temperature, the solvent was removed then washed with dichloromethane. The crude product was dissolved in water and acidified with 10 % HCl_(aq) until pH = 3. The precipitate was filtered and washed by water giving a yield >85%.



A solution of **56** (1 g, 1.25 mmol, 1 eq), **53** (0.4 g, 1.5 mmol, 1.2 eq) and CH₂Cl₂ (60 ml) was added to ZnBr₂ (0.37 g, 1.64 mmol, 1.3 eq) under Ar_(g). After 18 hours reaction at room temperature without light, water was added to quench the reaction and then extracted with CH₂Cl₂. The organic phase dried with MgSO₄ and concentrated. The residue was chromatographed on silica gel with ethyl acetate / pet. ether (1:4 v/v). The yield of **57** was 400 mg (32 %).

¹H NMR (300 MHz, CDCl₃) δ 8.40 (s, 1H), 8.32 – 8.13 (m, 2H), 8.10 – 7.94 (m, 2H), 7.56 – 7.36 (m, 4H), 6.95 – 6.46 (m, 6H), 4.92 (s, 2H), 4.37 – 3.82 (m, 20H), 2.52 (t, *J* = 7.4 Hz, 2H), 1.50 (d, *J* = 36.7 Hz, 2H), 1.28 (s, 24H), 1.19 – 0.97 (m, 12H), 0.90 (s, 3H).

¹³C NMR (75 MHz, CDCl₃) δ 171.52, 171.45, 150.14, 150.06, 137.24, 136.87, 134.67, 131.94, 131.51, 130.28, 128.98, 126.33, 125.65, 124.73, 124.60, 120.76, 120.64, 118.60, 112.94, 112.81, 66.77, 66.67, 60.48, 60.44, 53.35, 53.27, 35.39, 32.82, 31.79, 31.54, 29.57, 29.53, 29.44, 29.23, 29.18, 22.56, 14.00, 13.88, 13.83.

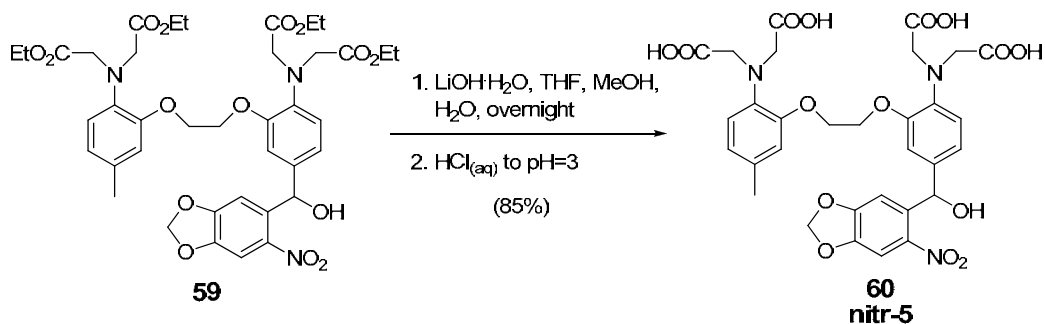


A mixture of **57** (50 mg, 0.058 mmol, 1eq) and LiOH·H₂O (53 mg, 1.26 mmol, 22eq) in 5 ml THF:H₂O (1:1 v/v) was refluxed overnight. After cooling to room temperature, the solvent was removed then washed by dichloromethane and ethyl acetate. The crude solid was dissolved in water and filtered. The clear yellow solution was slowly acidified with 10 % HCl_(aq) to pH = 3. The precipitate was collected by centrifugation and washed by water once then freeze dried to get a yellow powder. The yield of **58** was 23.3 mg (53%).

¹H NMR (300 MHz, CDCl₃) δ 8.41 (s, 1H), 8.26 (d, *J* = 8.3 Hz, 2H), 8.01 (d, *J* = 7.3 Hz, 2H), 7.48-7.39 (m, 4H), 6.84 (qi, *J* = 9 Hz, 3H), 6.66 (d, *J* = 10 Hz, 2H), 6.47 (*J* = 8.1 Hz, 1H), 4.16 (s, 2H), 4.13 (s, 2H), 3.47 (s, 4H), 3.41 (s, 4H), 2.5 (t, *J* = 7.7 Hz, 2H), 1.55 (s, 2H), 1.29-1.23 (m, 24H), 0.85 (t, *J* = 6.6 Hz, 3H).



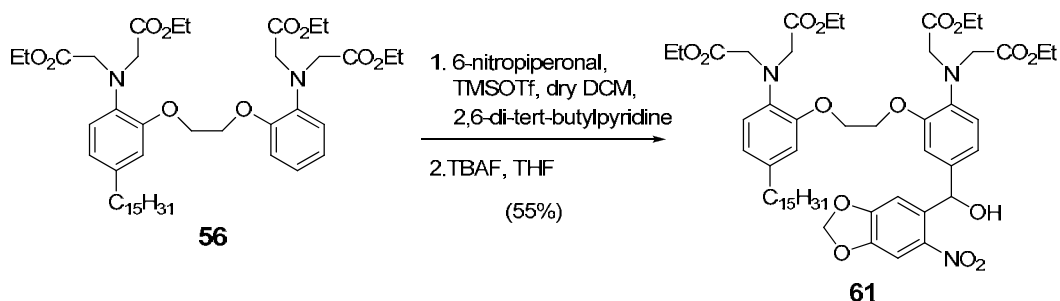
Trimethylsilyl trifluoromethanesulfonate (TMS OTf) (0.77 ml, 4.25 mmol, 5.1eq) was added dropwise to a solution of **22** (0.5 g, 0.83 mmol, 1 eq), 6-nitropiperonal (210 mg, 1.08 mmol, 1.3 eq), and 2,6-di-tert-butylpyridine (1.1 ml, 4.98 mmol, 6eq) in 7 ml dry dichloromethane at room temperature under N₂ atmosphere. After reaction overnight, the solution was diluted with dichloromethane (10 ml), poured into saturated aqueous NaHCO₃ (50 ml), and separated, and the aqueous layer was extracted with dichloromethane then H₂O and NaCl_(sat.), dried by MgSO₄, and evaporated to dryness. The crude product was dissolved in 8 ml THF, and tetrabutylammonium fluoride trihydrate (1M in THF solution, 2 ml) was added. After stirring 30 min at room temperature, the solution was evaporated to dryness, dissolved in ethyl acetate then extracted with H₂O and NaCl_(sat.), dried by MgSO₄, and evaporated to dryness. The residue was chromatographed on silica gel with ethyl acetate / petroleum ether (2:3 to 1:1 v/v). The yield of **59** is 272 mg (41%).¹⁷



A mixture of **59** (50 mg, 0.062 mmol, 1eq) and LiOH·H₂O (58 mg, 1.36 mmol, 22eq) in THF (4 ml), MeOH (4 ml), H₂O (1 ml) was stirred at room temperature overnight. After the reaction was complete as confirmed by RP-TLC, the solvent was removed and the crude product was washed and sonicated in dichloromethane and ethyl acetate then filtered. The crude solid was dissolved in Milli-Q water and filtered to obtain the clear yellow solution. The solution was slowly acidified under 0°C bath with 10 % HCl_(aq) to pH = 3. The precipitate was collected by centrifugation and washed by water once then freeze dried to get a yellow powder. The yield of **60** was 37 mg (85%).

¹H NMR (300 MHz, MeOD) δ 7.43 (s, 1H), 7.31 (s, 1H), 6.98 (s, 1H), 6.81 (d, *J* = 11.1 Hz, 4H), 6.69 (s, 1H), 6.36 (s, 1H), 6.11 (d, *J* = 10.7 Hz, 2H), 4.30 (s, 4H), 4.06 (d, *J* = 14.7 Hz, 8H), 2.26 (s, 3H).

¹³C NMR (75 MHz, MeOD) δ 175.91, 175.66, 153.46, 152.20, 151.44, 148.47, 143.23, 139.99, 138.09, 137.80, 134.15, 127.15, 122.78, 121.39, 121.01, 119.59, 115.95, 114.60, 108.45, 105.90, 104.61, 71.41, 68.78, 68.40, 56.05, 55.52, 21.01.

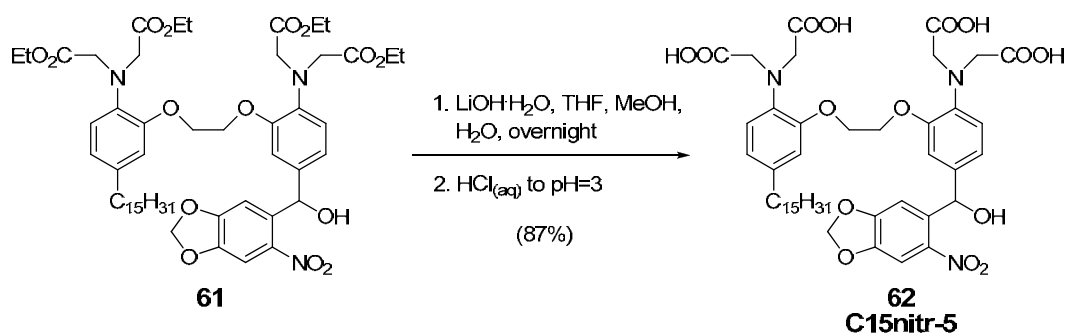


Trimethylsilyl trifluoromethanesulfonate (TMS OTf) (0.35 ml, 1.92 mmol, 5eq) was added dropwise to a solution of **56** (0.3 g, 0.38 mmol, 1 eq), 6-nitropiperonal (95 mg, 0.49 mmol, 1.3 eq), and 2,6-di-tert-butylpyridine (0.5 ml, 2.3 mmol, 6eq) in 3 ml dry dichloromethane at room temperature under N₂ atmosphere. After reaction overnight, the solution was diluted with dichloromethane (10 ml), poured into saturated aqueous NaHCO₃ (50 ml), and separated, and the aqueous layer was extracted with dichloromethane then H₂O and NaCl_(sat.), dried by MgSO₄, and evaporated to dryness. The crude was dissolved in 5 ml THF, and tetrabutylammonium fluoride trihydrate (1M in THF solution, 0.5 ml) was added. After 15 min at room temperature, the solution was evaporated to dryness, dissolved in ethyl acetate then extracted with H₂O and NaCl_(sat.), dried by MgSO₄, and evaporated to dryness. The residue was chromatographed on silica gel with ethyl acetate / petroleum ether (1:2 v/v). The

yield of **61** is 200 mg (55%).

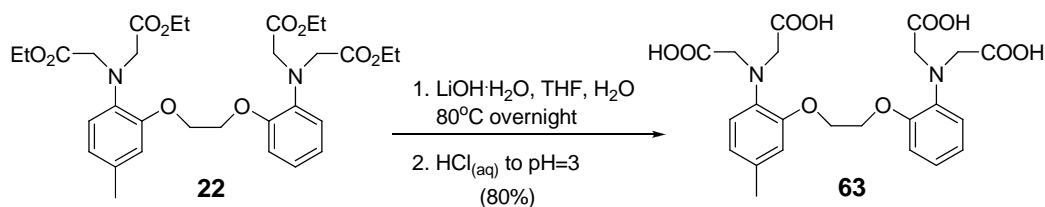
^1H NMR (300 MHz, CDCl_3) δ 7.46 (s, 1H), 7.13 (s, 1H), 6.89 (s, 1H), 6.74-6.63 (m, 5H), 6.35 (s, 1H), 6.09 (d, $J = 3.4$ Hz, 2H), 4.23 (s, 4H), 4.11-3.98 (m, 16H), 2.49 ($J = 7.6$ Hz, 2H), 1.52 (s, 2H), 1.24-1.09 (m, 39H), 0.86 (t, 3H)

^{13}C NMR (75 MHz, CDCl_3) δ 171.68, 171.49, 152.06, 152.21, 150.11, 147.04, 142.03, 139.01, 137.21, 136.98, 136.56, 135.51, 121.01, 119.74, 118.97, 118.26, 113.35, 111.99, 108.10, 105.41, 102.95, 70.85, 67.27, 66.94, 60.75, 60.64, 53.48, 35.48, 31.88, 31.64, 29.65, 29.53, 29.32, 22.64, 14.07, 13.99.



A mixture of **61** (50 mg, 0.05 mmol, 1eq) and $\text{LiOH}\cdot\text{H}_2\text{O}$ (32 mg, 1.1 mmol, 22eq) in THF (4 ml), MeOH (4 ml), H_2O (1 ml) was stirred at room temperature overnight. After confirmation that the reaction was complete by RP-TLC, the solvent was removed and the crude product was washed and sonicated in dichloromethane and ethyl acetate then filtered. The crude solid was dissolved in Milli-Q water and filtered to obtain the clear yellow solution. The solution was slowly acidified under 0°C bath with 10 % $\text{HCl}_{(\text{aq})}$ to $\text{pH} = 3$. The precipitate was collected by centrifugation and washed once by water then freeze dried to get a yellow powder. The yield of **62** was 38 mg (87%). ^1H NMR (300 MHz, MeOD) δ 7.42 (s, 1H), 7.30 (s, 1H), 6.99 (s, 1H), 6.89 – 6.60 (m, 5H), 6.36 (s, 1H), 6.09 (d, $J = 11.6$ Hz, 2H), 4.29 (s, 4H), 4.06 (d, $J = 11.1$ Hz, 8H), 2.52 (s, 2H), 1.56 (s, 2H), 1.27 (s, 24H), 0.89 (s, 3H).

^{13}C NMR (75 MHz, MeOD) δ 175.96, 175.70, 158.71, 153.45, 152.14, 151.46, 148.44, 143.19, 139.93, 139.29, 138.14, 138.01, 122.18, 121.36, 120.89, 119.70, 115.44, 114.62, 108.46, 105.89, 104.59, 71.40, 68.78, 68.44, 56.09, 55.64, 36.49, 33.06, 32.69, 30.77, 30.63, 30.46, 23.72, 14.44.

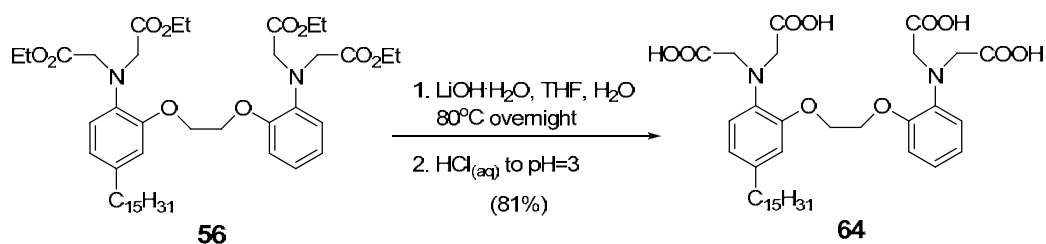


A mixture of **22** (50 mg, 0.083 mmol, 1eq) and $\text{LiOH}\cdot\text{H}_2\text{O}$ (53 mg, 1.83 mmol, 22eq) in 5 ml THF: H_2O (1:1 v/v) was refluxed overnight. After cooling to room temperature, the solvent was removed then washed by dichloromethane and ethyl acetate. The crude solid was dissolved in water and filtered. The clear yellow solution was slowly acidified with 10 %

HCl_(aq) to pH = 3. The precipitate was collected by centrifugation and washed once by water then freeze dried get a yellow powder. The yield of **63** was 42.7 mg (80%).

¹H NMR (300 MHz, MeOD) δ 6.97 (m, 6H), 6.71 (d, *J* = 7.7 Hz, 1H), 4.40 (s, 4H), 3.54 (ss, 8H), 2.31 (s, 3H).

¹³C NMR (75 MHz, MeOD) δ 178.47, 178.37, 152.01, 151.81, 141.94, 139.29, 133.97, 123.99, 122.36, 122.17, 119.40, 119.17, 113.50, 112.52, 67.33, 67.24, 59.30, 59.18, 21.19, -15.52, -15.54, -15.57, -15.59, -15.62, -15.64.



A mixture of **56** (50 mg, 0.083 mmol, 1eq) and LiOH·H₂O (53 mg, 1.83 mmol, 22eq) in 5 ml THF:H₂O (1:1 v/v) was refluxed overnight. After cooling to room temperature, the solvent was removed then washed by dichloromethane and ethyl acetate. The crude solid was dissolved in water and filtered. The clear yellow solution was slowly acidified with 10 % HCl_(aq) to pH = 3. The precipitate was collected by centrifugation and washed once by water then freeze dried get a yellow powder. The yield of **64** was 35 mg (81 %).

5.21 References

1. A. Juris, V. Balzani, F. Barigelletti, S. Campagna, P. Belser, A. von Zelewsky, *Coord. Chem. Rev.*, **1998**, *84*, 85
2. P.S. Mohan, C.S. Lim, Y.S. Tian, W.Y. Roh, J.H. Lee, B.R. Cho, *Chem. Commun.*, **2009**, 5365.
3. Molecular Probes, Inc. Product Information of Calcium Calibration Buffer Kits
4. M. Tsukioka, M. Jino, M. Endo, *Journal of Physiology*, **1994**, *475* (3), 369
5. R. Y. Tsien, R. S. Zucker, *Biophysical J.* **1986**, *50*, 843
6. D. Blaudez, J. M. Turllet, J. Dufourcq, D. Bard, T. Buffeteau, B. Desbat, *J. Chem. Soc. Faraday Trans.*, **1996**, *92* (4), 525
7. H. P. Ta, K. Berthelot, B. Couлары-Salin, B. Desbat, J. Géan, L. Servant, C. Cullin, S. Lecomte, *Langmuir* **2011**, *27*, 4797
8. R. M. A. Azzam, N. M. Bashara, *North-Holland Physics Publishing: New York*, **1977**.
9. D. Ducharme, J. J. Max, C. Salesse, R. M. Leblanc, *J. Phys. Chem.* **1990**, *94*, 1925
10. J. Saccani, S. Castano, F. Beaurain, M. Laguerre, B. Desbat, *Langmuir* **2004**, *20*, 9190
11. J. M. Holopainen, M. I. Angelova, P. K. J. Kinnunen, *Biophysical Journal*, **2000**, *78*(2) 830
12. G. Staneva, M. I. Angelova, K. Koumanov, *Chemistry and Physics of Lipids*, **2004**, *129*, 53
13. O. Reany, T. Gunnlaugsson, D. Parker, *Perkin Trans.* **2000**, *2*, 1819
14. S. Kemp, N.J. Wheate, D.P. Buck, M. Nikac, J.G. Collins, J.R. Aldrich-Wright, *J. Inorg. Biochem.*, **2007**, *101*, 1049
15. F.H.C. Stewart, *Aust. J. Chem.*, **1960**, *13* (4), 478
16. F. Effenberger, S. Heid, R. Merkle, P. Zimmermann, *Synthesis*, **1995**, 1115
17. S.R. Adams, J. P. Y. Kao, G. Grynkiewicz, A. Minta, R.Y. Tsien, *J. Am. Chem. Soc.* **1988**, *110*, 3212.

Synthesized compound list

